

Characterisation of fungicidal and non-fungicidal effects of Inatreq[™] active

Stuart Bagley BSc MRes

Thesis submitted to the University of Nottingham for the
degree of Doctor of Philosophy.

March 2021



The University of
Nottingham

UNITED KINGDOM • CHINA • MALAYSIA

Acknowledgements

I would like to thank my supervisor Dr. Darren Wells and co-supervisor Dr Ranjan Swarup for their invaluable guidance and support throughout my project. Darren as my main supervisor, who pushed me to explore outside of my comfort zone and instilled the importance of approaching problems from a multidisciplinary standpoint. As well as emotional support we offered each other throughout Arsenal's tumultuous seasons...

To everyone at Corteva Agriscience, who were so welcoming throughout my placement. The Wellesbourne field team, for your friendship and all those hot days in spray suits. I would like to thank Mike Ashworth and John Fraser for your continual support and insight, as well as supervision throughout.

To the Integrated Phenomics team members Dr Jon Atkinson and Dr Michael Wilson, for their support throughout, and in particular towards our paper and all 3d printing needs. Also, thanks to Michael for your essential support with all bioinformatics work that was carried out.

To the Glasshouse Team for their essential assistance throughout in helping experimental set up and maintenance – often overlooked but I appreciated all your friendship and support throughout, and without you much of the work would not have been possible.

To my friends I have made throughout my PhD studies, particularly Fletch, Heather, Rosie, Connie, Sam, Izzy and Steve. Postgraduate studies would have been a far duller place, and Bodega a far worse financed establishment.

To Rachael, for the continuous support over these last two years, particularly in this last year during Covid-19. You started your first year in medicine, amid a global pandemic, and took it in your stride so much so that you offered me your unwavering support, motivation, and love throughout, and I am unsure I could have achieved this without you. But then you made me buy a dog that is Satan incarnate.

Finally, to my family. Stephen, even when I did not offer you the support I should have growing up, you always guided me in the right direction, and served as a constant inspiration to me (even if I did not say as much). Mum and Dad, I would not be where I am now without you pushing me forwards and supporting me no matter what. I dedicate this thesis to you, for everything you have sacrificed to provide Stephen and I with all the opportunities we have had and acting as a constant reminder of the importance of hard work.

Abstract

With growing demand for increased crop yields, mitigating losses due to abiotic and biotic stresses is of paramount importance. A new fungicide with a novel mode of action effective in wheat against the pathogen responsible for *Septoria tritici* blotch (*Zymoseptoria tritici*), has recently been released by Corteva Agriscience. Inatreq™ active (active ingredient fenpicoxamid) is the first commercially available picolinamide fungicide. Preliminary observations of this fungicide suggest that it may also have biostimulant-like properties, unrelated to its fungicidal activity. The aim of this study is to further characterise the fungicidal activity of Inatreq when applied as a curative application, using traditional and image-based assessment techniques. This work also aims to characterise the beneficial non-fungicidal effects associated with the application of Inatreq, and to begin to understand the mechanisms underlying this activity.

It was found that when the curative efficacy of Inatreq was compared to a panel of commercially available fungicides also used to manage *Septoria tritici* blotch, it performed excellently, outperforming all alternatives. This work was also used to validate an image-based assessment tool against traditional manual scoring methods. This tool aims to eliminate the influence of bias from the process of scoring disease severity and was found to be reliable and accurate, providing more consistent scores, that were more specific in the mid-range of disease severity, and closer to the accepted ground truths than traditional methods.

Inatreq application was associated with improvements in biomass accumulation, a reduction in stomatal conductance and improvement of water use efficiency, in both well-watered plants and plants experiencing drought. These effects were observed in controlled environment growth room conditions, as well as in a large-scale glasshouse trial, across multiple wheat varieties. These effects were also observed in the model plant species *A. thaliana*. However, this conserved response was not observed in *A. thaliana* plants that had mutations in their abscisic acid (ABA) signalling and biosynthesis pathways. RNA sequencing data revealed an array of biological processes and genes that were upregulated following the application of Inatreq, with many related to ABA, stomatal regulation, and a variety of other stress responses, providing targets for future research.

The findings of this project highlight the amenability of Inatreq to a variety of crop protection strategies, as well as characterising its biostimulant-like activity. This research utilised a range of phenotyping technologies, as well as developing some bespoke tools, with a particular emphasis on low-cost phenotyping approaches with wider applicability.

Table of contents

Acknowledgements.....	i
Abstract.....	ii
Table of contents.....	iii
List of figures.....	vii
List of tables.....	xiii
Chapter 1. Introduction, background and aims.....	2
1.1. Introduction.....	1
1.2. Wheat (<i>Triticum aestivum</i>).....	5
1.3. Causes for losses in wheat yield.....	8
1.3.1. Drought.....	8
1.3.2. Disease - <i>Septoria tritici</i> blotch (STB).....	10
1.4. Disease control – fungicides.....	13
1.4.1. Fenpicoxamid - Inatreq™ active.....	15
1.4. Aims and objectives.....	17
Chapter 2. Assessing the curative fungicidal efficacy of Inatreq™ active using traditional techniques and image analysis.....	19
2.1. Introduction and aims.....	20
2.1.1. Introduction.....	20
2.1.2. Aims.....	22
2.2. Methods.....	22
2.2.1. General methods.....	22
2.2.2. Fungicide application – Curative application of Inatreq to plants previously inoculated with <i>Zymoseptoria tritici</i>	23
2.2.3. Disease scoring.....	24
2.2.4. Confocal laser scanning microscopy to assess asymptomatic fungal colonization.....	27
2.3. Results.....	29
2.3.1. Assessment of image analysis tool.....	29

2.3.2.	Curative fungicidal efficacy of Inatreq.	36
2.3.4.	Microscopy.	36
2.4.	Discussion.....	37
2.4.1.	Development of a tool for disease assessment from images.	37
2.4.2.	Fungicidal efficacy.....	39
Chapter 3.	Characterising the non-fungicidal effects of Inatreq on wheat.	43
3.1.	Introduction and aims.	44
3.1.1.	Introduction.	44
3.1.2.	Aims.....	47
3.2.	Methods.....	47
3.2.1.	General plant material and growing conditions.	47
3.2.2.	Comparing the root/ shoot biomass of mature plants treated with Inatreq under well-watered conditions.....	48
3.2.3.	Effects of Inatreq on wheat grown under differential watering.	50
3.2.4.	Identifying if Inatreq reduces transpiration in a dose dependent manner.	52
3.3.	Results.....	52
3.3.1.	Root/shoot biomass of mature wheat plants.....	52
3.3.2.	Characterising the effects of Inatreq on wheat grown under differential watering	53
3.3.3.	Identifying if Inatreq reduces transpiration in a dose dependent manner. 56	
3.4.	Discussion.....	56
Chapter 4.	High throughput glasshouse and field phenotyping.....	61
4.1.	Introduction and aims.	62
4.1.1.	Introduction.	62
4.1.2.	Aims.....	64
4.2.	Methods.....	65
4.2.1.	High-throughput glasshouse phenotyping.....	65
4.2.2.	Field trial.	70

54.3.	Results.....	75
4.3.1.	High-throughput glasshouse phenotyping.....	75
4.3.2.	Field trial.....	86
4.4.	Discussion.....	89
4.4.1.	High-throughput glasshouse phenotyping.....	89
4.4.2.	Field trial.....	92
Chapter 5.	Studies using the model plant <i>Arabidopsis thaliana</i>	93
5.1	Introduction and aims.....	94
5.1.1.	Introduction.....	94
5.1.2.	Aims.....	96
5.2.	Methods.....	97
5.2.1.	Plant material and growth conditions.....	97
5.2.2.	Fungicide application.....	98
5.2.3.	Development of a high throughput thermal imaging platform.....	98
5.2.4.	Observing the effect of application of Inatreq on stomatal conductance.....	103
5.2.5.	Identifying the underlying genetic response to the application of Inatreq in <i>Arabidopsis</i>	104
5.3.	Results.....	105
5.3.1.	HTP thermal imaging platform.....	105
5.3.2.	Effects of Inatreq on transpiration rate in <i>Arabidopsis thaliana</i>	107
5.3.3.	RNA sequencing analysis.....	109
5.4	Discussion.....	116
5.4.1.	Development of a HTP thermal imaging platform.....	116
5.4.2.	Non-fungicidal effects of Inatreq upon <i>A. thaliana</i>	116
5.4.3.	RNA sequencing.....	117
Chapter 6.	Conclusions and Future Work.....	120
6.1.	Fungicidal activity of Inatreq.....	122
6.2.	Non-fungicidal effects of Inatreq.....	123
6.3.	Model plant studies.....	124

6.4. Phenotyping.....	124
6.5. Future work.....	126
References	128
Appendices	153
Appendix 1.....	154
A1.1 Image analysis symptom selection macro.....	154
A1.2 Total leaf area selection macro	155
A1.3 First disease severity scoring questionnaire.....	157
A1.4 Expert disease severity questionnaire 2.....	163
Questionnaire 2 results	168
Appendix 2.....	169
A2.1 FvFm protocol.....	169
Appendix 3.....	170
A3.1 Contrast list.....	170
A3.2 Complete gene list.....	171
Appendix 4.....	181
A4.1 Publication.....	181

List of figures

- Figure 1.1: Required yield increases to reach 2050 targets. Circles represent the observed global yield of each crop between 1961-2008, the solid lines are their current projections up to 2050. The dashed lines represent a trend of ~2.4% increase in yield annually that will be required to double crop production by 2050 without acquiring additional land for cultivation. Figure from (Ray *et al.*, 2013) 3
- Figure 1.2: Proportion of the EU wheat production. France: 25.9%, Germany: 14.7%, UK: 9.8%, Remaining EU states: 49.6%. Total wheat production: 138 million tonnes. Source FAOstat 2018..... 7
- Figure 1.3: Infection and colonization process of *Z. tritici*. a) Diagram of the infection and pycnidia formation process (taken from (Steinberg, 2015)). b) Confocal microscope image of the surface of an infected leaf. Blue: *Z. tritici* hyphae growing towards a stomatal pore; red: leaf mesophyll cells; green: leaf epidermal cells (scale bar = 50µm). c) Cross-section of infected leaf. Red: *Z. tritici* colonisation of the substomatal and mesophyll space, blue: plant cell walls (scale bar = 50µm). d) Symptomatic leaf material with mature pycnidia (scale bar = 5mm). 12
- Figure 1.4: a) chemical structure of fempicoxamid IUPAC: [2-[[[(3S,7R,8R,9S)-7-benzyl-9-methyl-8-(2-methylpropanoyloxy)-2,6-dioxo-1,5-dioxonan-3-yl]carbamoyl]-4-methoxy-pyridin-3-yl]oxymethyl 2-methylpropanoate. Bracket represents R group added to UK2A (b) to improve photostability. 15
- Figure 2.1: Disease symptom image analysis. a) Colour thresholding tool in FIJI used to select for areas of disease, b) raw image of infected leaves, c) image with diseased regions of the leaves segmented (in red) using colour thresholding. Scale bars = 10 mm. 25
- Figure 2.2: a) Confocal image of wheat leaf samples (black) inoculated with *Zymoseptoria tritici* (white). b) Images following colour thresholding where parameters were set to only select for the *Zymoseptoria tritici* mycelium and was used to calculate the total area covered by fungal mycelium. Scale bars = 150 µm..... 28
- Figure 2.3: Comparison between the individual scores given by 7 industry experts (grey crosses), the mean score of the experts (black circle), and the score calculated using the image analysis tool (red circle). Error bars for mean expert score are $\pm 2SE$. Fungicides were applied either 6 days post-inoculation (dpi) or 10 days dpi. Analysed images taken from curative treatment data set (Section 2.2.2). 30

Figure 2.4: Linear regression matrix comparing all expert estimates to each other vertically and horizontally, as well as to the image analysis tools scores along the bottom (I.A). All linear regressions feature R^2 values. Symptom severity scored as percentage coverage (0-100 %). 31

Figure 2.5: Intra-rater reliability comparing biologists first score (x-axis) to their second score (y-axis). Due to the automation of the image analysis tool, all repeats returned a score of 1.00..... 32

Figure 2.6: ● = Estimated disease symptom severity by individual experts plotted against the mean of all expert scores. ▲ = Image analysis symptom severity score plotted against mean expert score. — = solid line is the concordance line representing perfect agreement between the estimated and true value. Experts estimate and image analysis score each feature a red or black best fitting line by linear regression, respectively..... 34

Figure 2.7: Bland-Altman plot visualising the difference in variance between the image analysis tool and Expert \bar{x} . The average difference in score coverage throughout was 2.7%, reflecting that the image analysis tool scored slightly higher than that of the experts mean score (Seen in Figure 2.5). The variance in scores from the mean error always fell within the 1.96 standard deviation. 35

Figure 2.8: Percentage symptomatic leaf area, following the curative application of Inatreq active. Fungicides were applied at two time points: 6 days post-inoculation (dpi) or 10 dpi with *Z. tritici*. Each image had 8-12 leaves in, and the disease severity was calculated as a score of severity across all the leaves in the image. 36

Figure 2.9: Total area of *Z. tritici* imaged on wheat samples treated with their respective fungicides. Error bars = SE, $*=P<0.05$, $n=10$ 37

Figure 3.1: Hydroleca column experimental set up. a) columns in-situ, b) a split column revealing the root system grown amongst the hydroleca, c) the root and shoot system following removal of the remaining hydroleca. A 1m rule is used for scale. 49

Figure 3.2: Mean root (a) and shoot (b) dry weights of two winter wheat varieties: Skyfall and Extase. $n=8$ Error bars = $\pm SE$, $* = P<0.05$ 53

Figure 3.3: Comparison of transpiration rate in wheat plants (var. Skyfall) where (a) the water was withheld, and (b) where watering was maintained. Measurements were observed for 4 days following fungicide application (red line). $n = 30$, error bars = $\pm SE$, $* = P<0.05$, $** = P<0.01$ 54

Figure 3.4: Mean relative water content (RWC) of mature wheat plants (var. Skyfall) treated with either Inatreq, or a control solution. The plants were grown under two different watering regimens, the drought condition where prior to the fungicide application watering was completely withheld (a), or the watered condition where regular watering to ensure the plants had a consistently high level of water availability throughout (b). $n= 30$, Error bars = \pm SE, * = $P<0.05$ 55

Figure 3.5: Dose response of transpiration rates of well-watered wheat plants (var. Skyfall) treated with either a control solution, 100 % field rate of Inatreq, or 200% field rate of Inatreq. Transpiration rates were observed prior to fungicide application, and subsequently each day for thereafter (red line represents fungicide application). $n=20$, error bars = \pm SE, * = $P<0.05$ 56

Figure 4.1: Weather data at Wellesbourne field trial site. Data collected daily over the course of the trial. Grey line represents fungicide application date (15/06/2020)..... 71

Figure 4.2: Annual spring rainfall and temperatures in the west-midlands, from 1862-2020. Red dot represents 2020 data. (Source: Met Office ‘UK and Regional series’ weather data). 71

Figure 4.3: Experimental design of field trials at the Wellesbourne field station 2020. 4 blocks, 12 treatments (listed in Table 4.5)..... 72

Figure 4.4: Comparison of untreated wheat PSA. Plants were grown until GS 33 (BBCH) with high water availability, before initiating differential watering to achieve three levels of water availabilities: low, medium, and high. This was observed in two different varieties: a) Extase and b) Skyfall. Initiation of differential watering represented by dashed red line (---). $n = 10$, error bars = \pm SE, a,b and c represent significant subsets ($P<0.05$). 76

Figure 4.5: Comparison of untreated wheat height. Plants were grown until GS 33 (BBCH) with high water availability, before then initiating differential watering to achieve three levels of water availabilities: low, medium, and high. This was observed in two different varieties: a) Extase and b) Skyfall. Initiation of differential watering represented by dashed red line (---). $n = 10$, error bars = \pm SE, a, b, and c represent significant subsets ($P<0.05$). 77

Figure 4.6: Projected shoot area (PSA) measurements in wheat variety Extase, treated with either: a water control spray, blank solution or Inatreq. a) Plants grown under low water availability, b) plants grown under medium water availability, c) plants grown

under high water availability. Spray date and drought initiation represented by dashed red line (---), $*=P<0.05$, error bars = $\pm SE$, $n=10$ 79

Figure 4.7: Raw images of wheat variety Extase, throughout growing season. Treated with the control solution or Inatreq, and grown under either low, medium, or high-water availability conditions. Spray date and drought initiation represented by dashed red line (---)..... 80

Figure 4.8: Projected shoot area (PSA) measurements in wheat variety Skyfall, treated with either: a water control spray, blank solution, Revystar or Inatreq. a) Plants grown under low water availability, b) plants grown under medium water availability, c) plants grown under high water availability. Spray date and drought initiation represented by dashed red line (---), Error bars = $\pm SE$, $n=10$ 81

Figure 4.9: Height measurements in wheat variety Extase, treated with either: a water control spray, blank solution, or Inatreq. a) Plants grown under low water availability, b) plants grown under medium water availability, c) plants grown under high water availability. Spray date and drought initiation represented by dashed red line (---), error bars = $\pm SE$, $n=10$ 82

Figure 4.10: Height measurements in wheat variety Skyfall, treated with either: a water control spray, blank solution, Revystar, or Inatreq. a) Plants grown under low water availability, b) plants grown under medium water availability, c) plants grown under high water availability. Spray date and drought initiation represented by dashed red line (---), error bars = $\pm SE$, $n=10$ 83

Figure 4.11: Inflorescence count for Extase plants treated with their respective fungicide application protocol. These plants were then grown under conditions of either high, medium, or low water availability. Error bars = $\pm SE$, $n = 10$ 84

Figure 4.12: Yield data from the Wellesbourne field trial, comparing. a) Average total grain weight per plot, b) average 1000 grain weight, c) average total ear number per plot. Error bars = $\pm SE$ 88

Figure 5.1: Bespoke HTP thermal imaging robot, *in situ*. 98

Figure 5.2: Belt-and-Pinion drive system 100

Figure 5.3: Wiring schematic of HTP thermal imaging platform 101

Figure 5.4: LabVIEW graphical interface for control of imaging vector with controls over various parameters..... 102

Figure 5.5: a) Comparison of thermal measurements between light/dark-adapted <i>A. thaliana</i> (Col-0) plants. b) Comparison of transpiration measurements derived from porometer measurements, between light-/dark-adapted plants, $*= P<0.05$. $n=12$ error bars = 2SE	106
Figure 5.6: Regression analysis of thermal measurements compared to their respective transpiration score derived from porometer measurement. R^2 values are calculated for both light and dark groups individually as well as the combination between the two. $n=11$	107
Figure 5.7: Comparison of surface temperatures following the application of Inatreq on four <i>Arabidopsis</i> lines: Wildtypes Col-0, and <i>Ler</i> , as well as ABA mutants <i>ost1</i> and <i>aba2</i> . a) 2 hours prior to Inatreq application, b) 24 hours after Inatreq application, c) relative water content (RWC) 48 hours after fungicide application. $*=P<0.05$, $** = P<0.01$. $n=8$, all error bars = $\pm 2SE$	108
Figure 5.8: Comparison of surface temperatures of the WT ecotype Col-0. Plants were either grown under well-watered conditions or had water completely withheld 24 hours prior to their respective fungicide applications. $n=8$, error bars = SE, $*=P<0.05$	109
Figure 5.9: Principal components analysis. Data represents the pre-treated plants (p) ($n=4$), as well as the plants treated with either the control solution (c) or Inatreq (tr) at four timepoints: +1 hour after application ($n=4,2$), +4 hours ($n=5,4$), +8 hours ($n=4,3$), +24 hours ($n=3,3$). Treated samples have their timepoints indicated.....	110
Figure 5.10: Heatmap and hierarchical clustering of 4810 <i>A. thaliana</i> genes showing differential expression, compared between 9 groups. These groups had either no treatment (pre-treated), treated with the control solution (C) or Inatreq (TR) and were analysed at 5 separate timepoints: 0 (pre-treatment group only), 1, 4,8, and 24 hours after treatment application. Data was standardised to ensure a zero mean and unit variance. The scaled value (z-score) is plotted across a red-blue colour scale, red indicating a high score, and blue a low score.....	111
Figure 6.1: Time course of canopy temperatures taken using the Thermal Imager.....	125
Figure 6.2: The networking of phytohormones involved in plant immune response, highlighting the role ABA plays and its interactions with other phytohormones. SA: Salicylic, JA: Jasmonates, ET: Ethylene. Figure taken from (Pieterse <i>et al.</i> , 2009)	127

List of tables

Table 1.1: Global harvest area of 3 major cereal crops, production total and yield, compared between 1966-2018 (FAOSTAT, 2014)	2
Table 1.2: Actual and potential losses due to abiotic factors. Adapted from (Oerke, 2006). Potential losses in square brackets.....	4
Table 2.1: Commercial fungicides, their active ingredients, and their respective application rates. All fungicides were applied at a dilution rate equivalent to 200 L/ha in water.....	24
Table 2.2: Confocal microscope imaging parameters.....	28
Table 2.3: Mean R ² values from Figure 2.4 where each expert, or the scores from the image analysis tool, were compared to each other.....	31
Table 2.4: Coefficients of determination (R ² , testing reliability) and concordance correlation coefficient (ρ_c , measuring accuracy) compared between expert disease scores and image analysis scores, and between individual expert scores compared to the mean expert score (Expert x). Assessments compared symptom coverage scores of leaves inoculated with <i>Z. tritici</i> , before being treated with a range of commercial fungicides at two separate timepoints.....	35
Table 3.1: Fungicides with observed non-fungicidal effects in the absence of disease....	46
Table 4.1: Fungicide treatments for image-based phenotyping of the effects of fungicide application under varying water availability. Inatreq provided by Corteva Agriscience, Inatreq blank provided by Corteva Agriscience and Revystar ® XE provided by BASF..	67
Table 4.2: Experimental conditions and respective replicate numbers in HTP glasshouse trial.....	68
Table 4.3: Workflow of HTP glasshouse trial conducted at the NaPPI facility, part of The University of Helsinki.....	68
Table 4.4: Workflow of field experiment conducted at the Wellesbourne field station..	72
Table 4.5: Panel of fungicides applied as part of the field trial at Wellesbourne field station, with respective application rates, and active ingredient content.	73
Table 4.6: Commercial fungicide details, including active ingredient class, product name, and producer.	73

Table 4.7: Chlorophyll fluorescence parameters of dark-adapted plants under differential watering and fungicidal treatments. Table a) Extase variety, table b) Skyfall variety. \pm SE, a, b, and c = homogenous subsets derived by Tukey's post-hoc test for significance ($p < 0.05$).....	85
Table 4.8: Mean effects of a panel of fungicides on wheat plants quantum yield (QY max, F_v'/F_m'), normalised difference vegetation index (NDVI), and relative water content (RWC %). Values with the same letter in the same column do not significantly differ from one another according to Tukey's post-hoc test ($P < 0.05$, $n=8$).....	87
Table 5.1: <i>A. thaliana</i> used in this study, including mutants with their genetic backgrounds listed.....	97
Table 5.2: Components of the HTP thermal imaging platform	99
Table 5.3: Description of differential expression (DE) within hierarchal clusters.....	112
Table 5.4: Number of differentially expressed (DE) genes found to be in contrast, using an unbiased pair-wise <i>t</i> -test.....	113
Table 5.5: GO analysis of genes in each cluster of interest that were overrepresented in biological processes. Numbers of annotated genes associated with the process in brackets.	114
Table 5.6: The ten genes with the largest, most significant response (FDR $P \leq 0.0000001$, except for 24hr where FDR $P \leq 0.05$), in each of the four contrast sets at $t=1$ hr, $t=4$ hr, $t=8$ hr and $t=24$ hr (Table has gene AGI code, \log_2 fold change, False Discovery Rate (FDR) corrected <i>p</i> -value, cluster membership and brief gene description (appendix 3.2 includes a larger set of genes ~ 100)) Genes were filtered to show only contrasts with an average expression greater than the set mean.....	115
Table 5.7: Lists the ten genes with the largest, most significant response (cont.)	116
Table 6.1: List of specifications and cost of the HTP thermal imaging platform and commercial/research "off the shelf" alternatives. Taken from (Bagley <i>et al.</i> , 2020)	125

Chapter 1. Introduction, background and aims.

1.1. Introduction.

The global demand for food is continually increasing in-line with the growing population. It is predicted that the global population will reach approximately 9.7 billion people by 2050 (Godfray *et al.*, 2010; United Nations, 2015). At present there are already 800 million individuals living in extreme poverty and experiencing both malnutrition and/or food insecurity (Green *et al.*, 2016; Tian *et al.*, 2016). Compounding the challenge of feeding an ever-increasing global population, past agricultural practices have often been detrimental to the environment resulting in soil erosion, increased accumulation of sediment in the waterways, increased pollution as well as reductions in biodiversity and damage to ecosystems (Foley *et al.*, 2005, 2011; Dale and Polasky, 2007; Power, 2010). Furthermore, the land available for agricultural practice is finite, and any ill-management will therefore impact future production capabilities, and in some areas this has meant that the area of available agricultural land is reducing (Wuepper *et al.*, 2020).

Three cereal crops; wheat, maize and rice account for the majority of human calorific intake, and this is not likely to change in the near future (FAOSTAT, 2014). In the 1950s there was a disconnect between the agricultural output of these three crops and the global dietary requirement. This food crisis was largely averted by the advent of the “Green-Revolution” (Borlaug, 1972). This revolution was characterized by three key changes to traditional agriculture: (i) the development of new crop ‘ideotypes’ which generally had a much-improved harvest index (HI: the ratio of grain yield to total biomass); (ii) increased application of fertilizers, most notably nitrogen and phosphorus fertilizers, as well as crop protection chemicals; (iii) large scale investment in on-farm infrastructure, such as improved irrigation systems, and increased mechanization. These changes in practice and intensification led to increases in production of all three of the main cereals, with either minimal increases in land area under cultivation, or in the case of wheat, a reduction (Table 1.1). The total cereal production in the 50 years preceding the Green Revolution tripled, requiring only a 30% increase in cultivated land. During this time the global population more than doubled (Pingali, 2012).

Table 1.1: Global harvest area of 3 major cereal crops, production total and yield, compared between 1966-2018 (FAOSTAT, 2014)

	Area harvested (million ha)			Production (million tonnes)			Yield (hg/ha x 100)		
	1966	2018	Fold Increase	1966	2018	Fold increase	1966	2018	Fold increase
Maize	111	194	1.75	246	1148	4.67	221	592	2.68
Rice	126	167	1.33	261	782	3.00	208	468	2.25
Wheat	216	214	0.99	304	734	2.41	141	343	2.43

It is indisputable that the Green Revolution was successful in achieving many of its goals, but many of the changes it initiated have contributed to the environmental concerns we are faced with today. Since the 1960s nitrogen and phosphorus fertilization has seen an almost 7 and 1.5 fold increase respectively (Tilman, 1999). Nitrogen fertilizers are largely applied in the form of ammoniacal fertilizers derived from the Haber-Bosch process. This process requires significant amounts of energy, approximately 1% of the global energy supply (Wang and Meyer, 2019), the majority of which is supplied from fossil fuels. In addition to this, the process produces 1.87 tons of CO₂ for every ton of ammonia produced (Wang and Meyer, 2019), substantially contributing to carbon emissions. Phosphorus fertilizers are derived from finite phosphate rock reserves that are beginning to dwindle, which is limiting the accessibility of phosphorus fertilizers in many regions and constraining productivity (Nziguheba *et al.*, 2016). Due to this, interest in recycling and retaining phosphorus is increasing, but it is not yet at a level to sustain production of phosphorus fertilizers alone. In addition to this, fertilisers as well as agrochemicals can leach and contaminate water sources. Leaching of N and P fertilisers not only represents a direct loss of nutrients that have been applied but they can also pollute the ground waters which may result in adverse health effects on humans, as well as the environmental effects (Evenson and Gollin, 2003; Foley *et al.*, 2005; Eliazar Nelson *et al.*, 2019). In addition to the damage caused by increased inputs, the design of an ideal ideotype has meant that cereal production is often dominated by monocultures, with limited biodiversity and genetic variety (Smale, 1997; Tilman, 1998; Evenson and Gollin, 2003; Eliazar Nelson *et al.*, 2019). Finally, the large-scale adoption of on-farm infrastructure has led to issues such as diversion of natural waterways and accumulation of salts in soils due to irrigation (Wichelns and Oster, 2006), and the negative

consequences of exhaust emissions, and further soil erosion due to mechanised agriculture (Bakker *et al.*, 2007; Lovarelli *et al.*, 2018).

We are now currently facing a similar impasse to that seen in the 1960s, with current forecasts of agricultural production not aligning with the required output. To feed the growing population, it is predicted that crop production yields will have to increase by approximately 2.4% per annum. However, at present the annual yield increase in maize, rice and wheat is around 1.6%, 1% and 1.3% respectively (Figure 1.1) (Ray *et al.*, 2013). If the current trends in agricultural intensification are continued ~1 billion ha of additional land would instead need to be cleared by 2050 to reach production targets (Tilman *et al.*, 2011). However, learning from the previous Green Revolution, it is now understood that the environmental sustainability of any improvements may be as important as the improvements themselves (Hunter *et al.*, 2017). Therefore, a new Green Revolution will need to incorporate environmentally sustainable strategies.

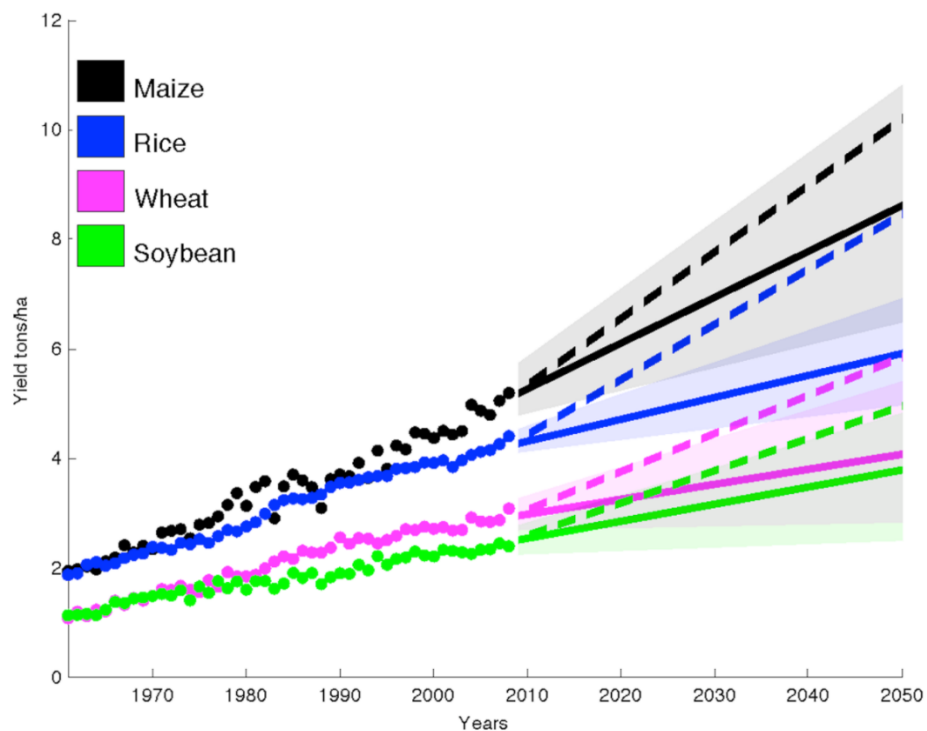


Figure 1.1: Required yield increases to reach 2050 targets. Circles represent the observed global yield of each crop between 1961-2008, the solid lines are their current projections up to 2050. The dashed lines represent a trend of ~2.4% increase in yield annually that will be required to double crop production by 2050 without acquiring additional land for cultivation. Figure from (Ray *et al.*, 2013)

One area that needs to be managed to reach future yield goals is to reduce crop losses because of disease. Due to the scale of the production of wheat, maize, and rice, they are

the predominant source of calories in global diet composition accounting for 46% (Pingali, 2015). As a result of their demand these cereals are generally grown as complete monocultures. Monocultures have very little genetic diversity across whole populations and are a promising proposition to farmers as plants have a standardized life cycle, where they may be planted at the same time, grow at similar rates, and can be harvested at the same time. However, despite the benefits of monocultures, the lack of genetic diversity leaves the populations at risk of new pest outbreaks and diseases. The severity and extent of damage a disease outbreak may cause is directly related to the genetic diversity and density of the host populations. In a monoculture, where the diversity is extremely low and the population density high, disease and pests can spread rapidly through the population, whereas in more “natural” scenarios with more increased diversity within the population, the incidence of the disease is often much lower (Newton, 2016). With the increasing intensification of agriculture, the number of diseases and pests, as well as their incidence and densities will continue to increase.

Table 1.2: Actual and potential losses due to biotic factors. Adapted from (Oerke, 2006). Potential losses in square brackets.

Crop	Loss (%), [Potential losses]				
	Weeds	Animal	Pathogens	Virus	Total
Maize	10.5, [40.3]	9.6, [15.9]	8.5, [9.4]	2.7, [2.9]	31.2, [68.5]
Rice	10.2, [37.1]	15.1, [24.7]	10.8, [13.5]	1.4, [1.7]	37.4, [77]
Wheat	7.7, [23]	7.9, [8.7]	10.2, [15.6]	2.4, [2.5]	28.2, [49.8]

One of the most important facets of modern agriculture is crop protection, and how to mitigate the losses that may result due to pests and diseases (Table 1.2). This has led to the widespread use of chemical pesticides, which have been highly successful in protecting crops, even when grown as monocultures. However, the mismanagement of many of these pesticides has led to the development of resistant pests and inefficient pesticides. Going forward it is the focus of the crop protection industry to develop effective and sustainable crop protection products, whilst also developing management schemes that preserve the action of the products in the long term.

1.2. Wheat (*Triticum aestivum*).

Wheat (*Triticum aestivum*) is one of the three main cereal crops grown globally with over 700 million tonnes harvested annually (Table. 1), and it represents the source of approximately 20% of all calories in the global diet (Shiferaw *et al.*, 2013). Unlike the other two cereals that make up the “big 3”, wheat is much more flexible in its climatic requirements owing to its rich genetic diversity, with over 30000 varieties. Wheat can be cultivated between 61° N, in the northern regions of Scandinavia and Russia, and 45° S in Argentina, Chile and New Zealand (Shewry, 2009).

There are two main types of cultivated wheat: winter, and spring wheat. Winter wheat is the most produced, making up 97% of production in the UK, and requires a vernalising period which usually occurs over winter, where it is exposed to a prolonged period (2-6 weeks) of cold temperature (~4 °C). Spring wheat is much lower yielding and is often produced for animal feed. Although lower yielding, it requires lower inputs compared to winter wheat (Watson *et al.*, 1963).

Wheat domestication.

Modern day wheat is the result of intense selection pressure driven by humans for preferred agronomic traits. Wheat cultivation began ~10,000 years ago, during the Neolithic revolution where humans made the transition from nomadic hunter gatherers, to settled populations who cultivated their food. The early stages of wheat domestication took place in the Fertile Crescent near modern day south-east Turkey.

It was here that early farmers began domesticating three main cereal crops: emmer wheat, einkorn wheat, and barley. From here, domesticated forms of each of these cereals began being disseminated across Eurasia and Africa. The dissemination of these cereals such as emmer wheat, meant that regions began forming their own subdivisions, but the free gene exchanges with wild emmer or domesticated emmer from other regions meant that the centre for emmer genetic diversity formed in Levant and South eastern Turkey (Luo *et al.*, 2007). Durum wheat (*Triticum durum*) makes up ~5% of the global wheat crop, with common wheat (*Triticum aestivum*) making up the remaining 95%. Durum is a harder wheat, often used for production of pasta whereas common wheat is used to produce things such as bread, and pastry. Emmer wheat and durum wheat have a tetraploid genome ($2n = 4x = 28$ AABB genome), comprising of two genomes from a past hybridization, whereas common wheat has a hexaploid genome ($2n = 6x = 42$ AABBDD) (Akpınar *et al.*, 2015). Common wheat originates from a hybridization event between

another domesticated emmer wheat variety that was grown in sympatry with goat grass (*Aegilops tauschii*) which has a diploid genome (DD). It is believed this event occurred primarily in Armenia and south west Caspian Iran, based upon the DD genomes of *A. tauschii* and its gene pool (Dvorak *et al.*, 1998). It has been previously postulated that there is a correlation between the ploidy level of cereal crop species and its success as a crop (Dubcovsky and Dvorak, 2007). In early stages of domestication of crop species, the tetraploid crop emmer wheat would generally prevail over einkorn, a diploid species, as the primary cereal. This remained the case until new forms of tetraploid cereals such as durum wheat began to develop and become the primary cereal crop. However, these tetraploid species were soon superseded by the arrival of the hexaploid wheat species, *T. aestivum*, which remains the dominant species today over the likes of durum wheat. On the face of it, it may seem odd that production of common wheat outweighs durum wheat so much, when durum wheat has similar yield capabilities and larger grain size compared to common wheat, when under optimal conditions. However, owing to increased ploidy representing an increasing number of hybridizations, and therefore convergence of multiple genomes, this increased ploidy level means that the crop is increasing its adaptability to a wider range of conditions, such as climate, photoperiods, and stresses. As well as this, owing to polyploid species containing more genomic DNA, and much of it being duplicate DNA, they are more likely to accumulate mutations. This includes both negative and positive mutations, but due to the higher number of duplicate genes they are better equipped to tolerate these mutations. This process is called subfunctionalisation and means that these polyploid species can withstand many more detrimental mutations, until a favourable one occurs and is able to become fixed (Charmet, 2011).

Despite the various benefits of the domestication of wheat, there have also been bottlenecks that have led to the exclusion of alleles that may have been potentially beneficial. As the plants became more domesticated and polyploidisation occurred, the effective population size continued to reduce. This effect is referred to as a domestication bottleneck. The bottleneck effect was then worsened by the modern selection of varieties, with the reduction of diversity being most pronounced for the alleles that have had the strongest positive selection. For example, the *Q* allele in wheat influences glume tenacity as well as glume/spike shape, which allows for more flowers per spikelet and therefore enables an increased potential for yield. It is thought that the mutation in the *Q* allele that caused this change in spike morphology only appeared once. This is an example where a positive allele has been selected for so strongly in breeding strategies, that there is extremely low variation in this allele (Charmet, 2011).

Presently, selective breeding of wheat has been extremely successful with yields increasing significantly over the last century. However, this has come at a cost in the narrowing of the availability of genetic diversity, and accordingly reduced the prevalence of potentially new adaptive alleles (Reif *et al.*, 2005; Haudry *et al.*, 2007). To combat this, wild relatives and landraces have been identified as sources of these potentially adaptive alleles, and therefore these will be used in introgressive breeding strategies to introduce alleles will improve crop yields in this new and changing environment (Ortiz *et al.*, 2007).

An EU perspective.

Wheat is the most important cereal grown in the EU, making up over 50% of the total cereal produced (FAOSTAT, 2014). In total, the EU produced approximately 138 million tonnes of wheat, with over half the production coming from France, Germany, and the UK (Figure 1.2).

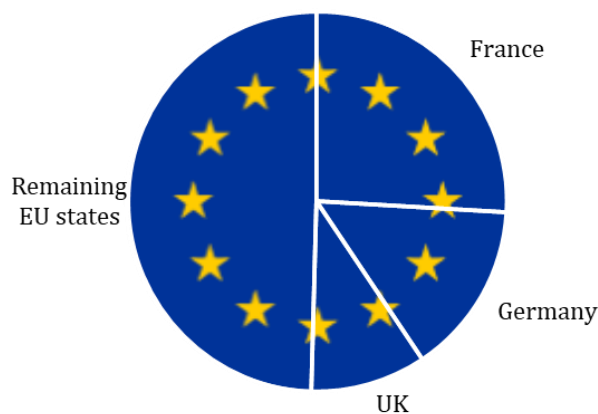


Figure 1.2: Proportion of the EU wheat production. France: 25.9%, Germany: 14.7%, UK: 9.8%, Remaining EU states: 49.6%. Total wheat production: 138 million tonnes. Source FAOstat 2018

Of the wheat that is produced, 20% is exported (<https://ec.europa.eu/info/food-farming-fisheries/plants-and-plant-products/plant-products/cereals>), whilst the remaining wheat is mostly shared between human (~33%) and animal consumption (~66%). Small percentages of the wheat is used for alcohol distilling, as well as biofuel production, whilst secondary products from wheat include straw for animal bedding and fodder (Fones and Gurr, 2015).

Currently in Europe, the rate of yield increase is not fast enough, and therefore will not be able to increase enough to reach the projections required for the future population size

(Brisson *et al.*, 2010). This is not a trend that is mirrored globally, where countries such as Mexico continue to accelerate the rate of increasing yields (Lobell *et al.*, 2005). Research suggests that despite the genetic improvement of cereal crops, the changing climate in temperate regions such as those in northern Europe has become unfavourable to cereal production. General warming in regions like France has been accompanied by increased incidence of winter and spring droughts. These droughts occur during the stem elongation stage of wheat growth which accelerates growth stages, and therefore shortens the growing period before reaching maturity. Furthermore, high temperatures (>25 °C) have been shown to reduce individual grain weight during grain filling (Gate *et al.*, 2009). This again highlights the need for the introgression of potentially adaptive alleles to the gene pool.

1.3. Causes for losses in wheat yield.

Wheat will continually need to increase its yield in line with growing demand. For wheat to achieve its 2050 yield goal it is predicted its rate of increasing yields will need to improve annually by 1.6%, and therefore by 2050 yields will need to be up to 5 t/ha of grain, rather than the 3 t/ha produced at present (Singh *et al.*, 2016). Therefore, to ensure the demand for wheat is met, any sources of potential loss must be managed. Drought and disease are two factors that have been highlighted as major threats to production, having the potential to devastate yields, and therefore are continuing to require attention going forward to minimize their effects as much as possible.

1.3.1. Drought.

Impacts of drought stress (like some diseases) can remain asymptomatic for long periods of time, and when the symptoms do become apparent, they are often the result of a longer-term stress than is immediately obvious (Ault, 2020). Drought is one of the major abiotic stresses effecting modern agriculture and, in terms of agricultural drought, can be defined as moisture deficits in the root zone, resulting from environmental conditions that are different to that of the climatological norm, which prevents crops from growing normally or completing their lifecycle (Zhu, 2002; Solomon, 2007). Drought is becoming one of the most widespread global climatic disasters, impacting agricultural yields (Ludlow and Muchow, 1990; Helmer and Hilhorst, 2006) and can now be considered one of the major determinants of global food security (Schmidhuber and Tubiello, 2007). It is predicted that, under a scenario where high greenhouse gas emissions are maintained, the global

dryland area may increase by 10% more than it would under the climatic conditions in 1961-1990 (Feng and Fu, 2013). Furthermore it is reported that over the next 30-90 years there will be severe and widespread drought across large land areas due to reductions in precipitation and increases in evaporation (Dai, 2013).

Drought is caused by a multitude of factors and is not entirely the result of negative anthropogenic impacts upon the environment. Droughts have been common throughout history and are accepted as a natural occurrence caused by climatological and hydrological patterns. Drought is generally caused by disruptions to the normal flow of moisture in and out of moisture sinks such as glaciers and lakes, as well as through systems such as soil rivers and plants (Ault, 2020). These naturally occurring disruptions to hydrological cycles may occur during events such as during El Niño where precipitation in areas of Brazil may be displaced to other regions, leaving Brazil and regions of Central America in a state of drought (Dai and Wigley, 2000). Humans do however influence the incidence and severity of drought, due to factors such as their roles in climate change, poor environmental practices, and excess demand for water. Increases in global temperatures by 1.5 – 2 °C would significantly increase the risk of drought in Central Europe as well as parts of the Mediterranean (Lehner *et al.*, 2017) with the difference between 1.5 – 2 leading to an even more significantly increased chance of consecutive years of drought. Alongside the effects of climate change, increasing demand for water for agriculture. Almost 65% of the global freshwater withdrawal is for agricultural purposes (Abunnour *et al.*, 2016) and if crop production is to reach its goals by 2050 it is predicted that water consumption must increase by 70-90% (de Fraiture and Wichelns, 2010).

Plant responses to drought.

Drought affects the growth of grain crops, and therefore their productivity by firstly reducing canopy absorption of photosynthetically active radiation (PAR), reducing radiation use efficiency (RUE) and reduced harvest index (HI) (Earl and Davis, 2003; Farooq *et al.*, 2009). To avoid these negative effects of drought, plants have developed drought mitigation responses to low levels of water availability such as reduction of stomatal conductance and an increase in root-shoot ratio (Sharp, 2002). These responses enable the plant to better search for sources of water in the soil with increased growth focused towards the rooting system, as well as conserving the water in the soil itself, by reduction of excess evapotranspiration (Verslues, 2016). The central regulator in the plants drought response is the phytohormone abscisic acid (ABA). ABA responds to reduced water potential and dehydration of plant tissue during limited water availability.

It is suggested that drought is perceived by membrane based mechanosensing proteins in the root cell membranes, such as mechanosensitive channels or receptor kinases (Hamilton *et al.*, 2015; Haswell and Verslues, 2015; Bacete and Hamann, 2020). Once low water availability is perceived the accumulation of ABA may increase by as much as 100-fold from unstressed leaves (Verslues, 2016), relative to the level of stress. When ABA accumulates in the guard cells of the leaves, it directly induces the efflux of potassium ions via potassium ion channels, leading to the loss of cell turgor due to osmosis and then closure of the stomatal guard cells (Raghavendra *et al.*, 2010).

1.3.2. Disease - *Septoria tritici* blotch (STB).

The most economically important wheat disease in temperate regions, and in particular Northwestern Europe, is *Septoria tritici* blotch (STB), caused by the ascomycete *Zymoseptoria tritici* (formerly *Mycosphaerella graminicola* or *Septoria tritici*) (Fones and Gurr, 2015; Savary *et al.*, 2019). In seasons that experience particularly severe epidemics of STB, there is the potential of losses reaching up to 50% (Eyal, 1973; Eyal *et al.*, 1987) and therefore, in the EU up to 70% of the annual fungicide usage may be directed towards the management of STB (Fones and Gurr, 2015).

Life cycle and infection process.

Z. tritici is classified as a blotch pathogen, like *Septoria nodorum* blotch, and tan spot (causal agents: *Parastagonospora nodorum* and *Pyrenophora tritici-repentis* respectively), however, it undergoes a relatively unique colonization and life cycle pattern, which has meant that *Z. tritici* has remained under-studied in comparison to other pathogens. *Z. tritici* is initially propagated by two types of spore: pycnidiospores and ascospores, both of which are pathogenic. Pycnidiospores are replicated asexually and are normally associated with the spread of STB short distances, such as from leaf to leaf or between plants in proximity. Pycnidiospores are contained within the pycnidia fruiting bodies which appear as black specks within necrotic tissue and develop in substomatal space. These pycnidia can range in size based on fungal strain or severity of the infection but usually range within 60 – 200 µm. Pycnidiospores are thread-like spores approximately 2.6 x 62.5 µm in size and are exuded from the pycnidia in response to wet and humid conditions where they are then spread from leaf to leaf by splash distribution (Steinberg, 2015). It has been estimated (Fones and Gurr, 2015) that across a season, a single hectare of wheat can generate an asexual spore load of 10¹⁰⁻¹¹ Ascospores on the other hand are

sexually reproduced, depending on the meeting of strains of differing mating types (Kema *et al.*, 1996). Unlike the pycnidiospores, ascospores are associated with being progenitor of STB in new emerging crops and spreading *Z. tritici* over larger distances by the wind. The source of these ascospores is generally from leftover harvest stubble from previous crops. Ascospores are therefore more often associated with disease immediate disease progression across a plant, whilst ascospores are associated with disease introduction (Royle, 1994). The movement of these ascospores is so free that a single field may contain 90% of the global genetic diversity at one time (Zhan *et al.*, 2003). Ascospores are formed in perithecia, which are also sub-epidermal and form after the pycnidia. These spores are smaller than the pycnidiospores, approximately 10 – 15 x 2 – 3 µm (Bockus *et al.*, 2010).

Pycnidiospores or ascospores will germinate on wheat leaves in cool and humid conditions after which they will switch to hyphal growth, with the fungal hyphae extending across the surface of the leaf, and entering the leaf through stomatal pores (Steinberg, 2015). The process by which hyphae can locate the stomata is not conclusively defined. One hypothesis suggests that it is a random process (Kema, 1996; Shetty *et al.*, 2003), whilst it has also been suggested that there may be an unknown thigmotropic stimulus (Duncan and Howard, 2000) similar to those seen in rust species (Hoch *et al.*, 1987), but there is no conclusive evidence to support this. Importantly, once the hyphae enter the substomatal and mesophyll space, no appressoria or feeding structures form. *Z. tritici* instead begins to colonize the substomatal and intracellular space, whilst the plant remains asymptomatic. This latent phase may remain this way for up to 9-15 days. It has been found that *Z. tritici* can remain undetected, and therefore avoid triggering a host defense response, by secreting a chitin-binding effector Mg3LysM (Marshall *et al.*, 2011). *Mg3LysM* is strongly up-regulated during the symptomless colonization of the intracellular space, and MgLysM has been found to bind to the chitin, therefore blocking recognition and activation of chitin-induced plant response. *Mg3LysM* mutant varieties of *Z. tritici* were found to have a significantly impaired ability to colonize the leaf and initiated a more rapid and pronounced expression of wheat defense genes than the wild type. 7-11 days after the onset of the protracted latent phase, *Z. tritici* induces programmed cell death (PCD) leading to the rapid development of lesions which can spread to cover large portions of the leaf if not controlled. The onset of PCD leads to the breakdown of leaf cells and leakage, offering nutritional sustenance to the pathogen which fuels the production of sexual/ asexual spores and their respective fruiting bodies.

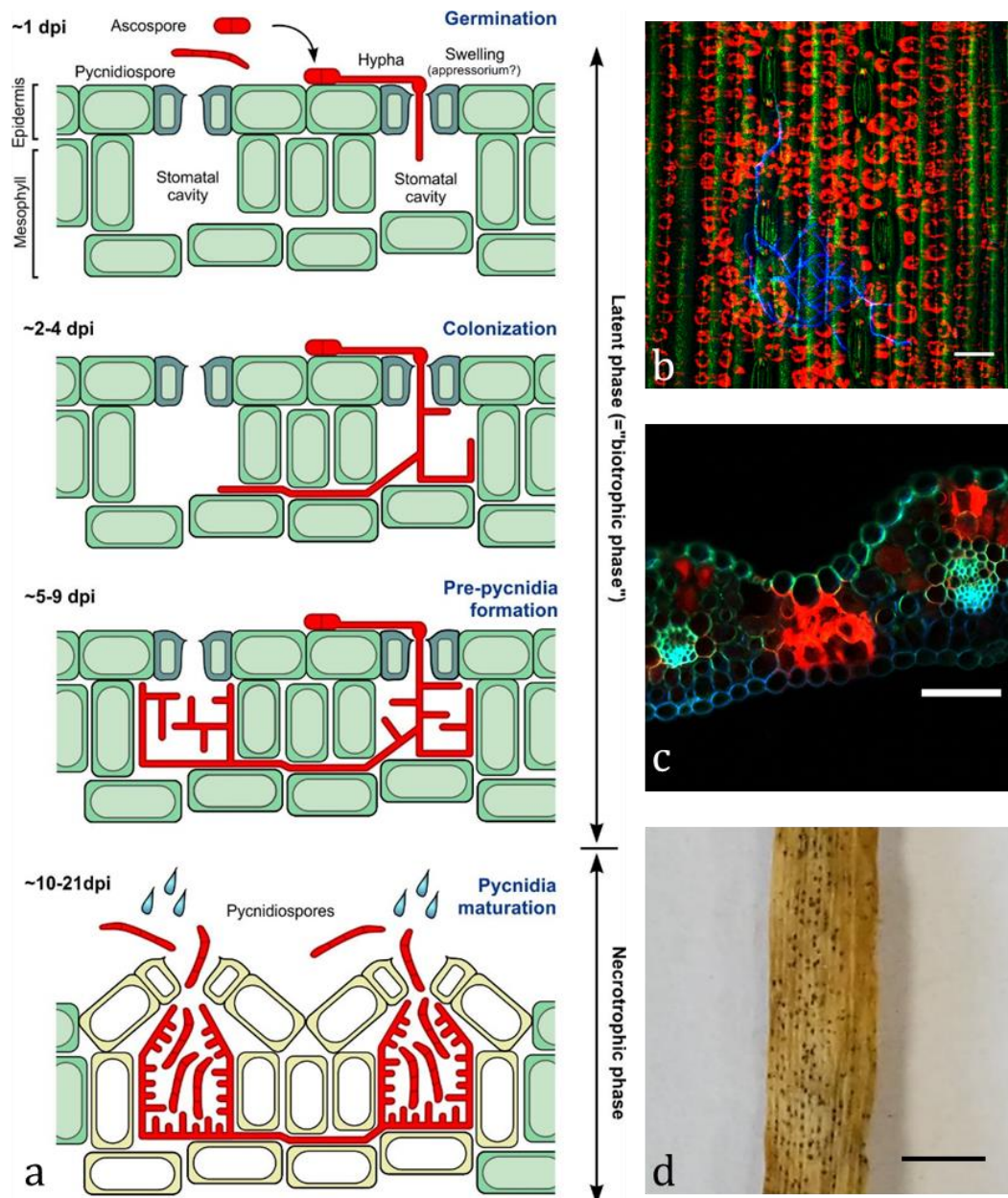


Figure 1.3: Infection and colonization process of *Z. tritici*. a) Diagram of the infection and pycnidia formation process (taken from (Steinberg, 2015)). b) Confocal microscope image of the surface of an infected leaf. Blue: *Z. tritici* hyphae growing towards a stomatal pore; red: leaf mesophyll cells; green: leaf epidermal cells (scale bar = 50 μ m). c) Cross-section of infected leaf. Red: *Z. tritici* colonisation of the substomatal and mesophyll space, blue: plant cell walls (scale bar = 50 μ m). d) Symptomatic leaf material with mature pycnidia (scale bar = 5mm).

Z. tritici's genetic plasticity enables it to be a continuous threat, even in the face of fungicide applications and management. Significant gene-flow can occur between strains of septoria, with up to 20-30% of the population at the end of a season likely originating from sexual reproduction (Eriksen *et al.*, 2001). As previously mentioned these

ascospores will be unlikely to influence the severity of disease that season, but they will introduce new strains and therefore may start new infections. This potentially high-turnover of genetic traits therefore mean that *Z. tritici* has the capability to maintain pace with control measures, as well as the development of new ones. On top of this quick turnover of traits through sexual reproduction, *Z. tritici* has 21 chromosomes, 8 of which are “dispensable”, highlighting the plasticity of its genome. 17% of the genome is repetitive, and of this repetitive portion, 70% is enriched with class 1 transposable elements. Class one transposable elements, also known as retrotransposons, move through RNA intermediates. This added intermediary introduces a new point where mutations may be appear. Its also believed that having 8 dispensable chromosomes, means that loss of fungicide target genes may be accelerated quickly with minimal detriment

The impact of these lesions can be severe, particularly when present on the flag leaf or second leaf where every 1% incremental increase in disease severity, yield is reduced by 1% and 0.6% respectively (King *et al.*, 1983).

Z. tritici is particularly troublesome in Northern European regions, due to their cool and wet climate which allows it to thrive (Eyal *et al.*, 1987; Hardwick *et al.*, 2001; Palmer and Skinner, 2002; Orton *et al.*, 2011; Dean *et al.*, 2012). Wheat is grown across this area in large-scale monocultures, with little differentiation between the varieties used, and often only have moderate resistance to STB. This lack of genetic resistance to the pathogen highlights the importance of effective crop protection strategies across Europe.

1.4. Disease control – fungicides.

As previously highlighted, modern agriculture has created the perfect storm for the emergence of many pathogens, with crops being more intensely grown on the limited land available, and the pool of genetic diversity ever decreasing as breeding has instead pursued high yielding monocultures. Therefore, chemical intervention has become the norm, and is now critical to ensure current yields are maintained, and future targets are reached. Using *Z. tritici* in the UK as an example, losses in varieties with low levels of resistance are ~20% and in varieties selected for improved resistance, and treated with fungicides this reduction in yield decreases to 5-10% (Fones and Gurr, 2015). It has been estimated that the yield response in UK wheat to effective fungicide strategies can equate to a 2.5 tonne increase in yield per hectare, further demonstrating the benefits of fungicide use (Torriani *et al.*, 2015). It is important to note that this 2.5 tonne increase per

hectare equates to \$520/ha (UK prices in 2019, FAOSTAT), whereas the cost of an intensive 3 spray fungicide strategy costs around \$120/ha highlighting the financial incentive fungicides may pose to growers.

Over the last century chemical crop protection has advanced substantially, from predominantly self-prepared mixes of inorganic chemicals in the early 1900s to fungicides now having a global market value of over \$18 billion USD (Sparks *et al.*, 2017). The control of crop disease using inorganic chemicals can be dated as far back as 1802, with Bénédict Prévost identifying that wheat bunt was caused by the basidiomycete *Tilletia caries*, which in-turn may be controlled, to a degree, by copper sulphate (Ainsworth, 2009). However, up until the 1940s many of these “fungicides” were D.I.Y concoctions of inorganic chemicals produced by the user and were mostly ineffective. Following the conclusion of World War two, which brought substantial innovation and advancement in the chemical industry, resources began being directed toward the agricultural industry, and development of effective chemical protectants (Robinson and Sutherland, 2002). Fungicidal chemistries such as dithiocarbamates began being introduced, acting as protectants, meaning their application timing was critical, and any application outside of this narrow window may be ineffective (Russell, 2005). But despite the short fallings of these early chemistries, they had moved the fungicide industry forward, changing farmers’ attitudes to chemical treatments, from home produced mixes, to commercially manufactured chemical products, produced by mainstream chemical companies, such as Dupont. With the foundations set in the two preceding decades, the fungicide market grew substantially from the 1960s and 1970s, coinciding with the beginning of the Green Revolution, which championed increasing chemical inputs. There were now many agrochemical companies, researching and producing new chemicals, driven by market competition for new crop protection products. With the increase in market competition for crop protectants, the targets of these chemicals became much more focused on large hectareage field crops such as wheat and barley, rather than horticultural crops. This led to the need for the development of new and more sophisticated fungicide application systems. The improvement in these systems, as well as improvement in the chemicals that were applied, meant that applications could be effective with much lower dosages, and were much safer. The introduction of systemic single site fungicides began in the 1970s and continued to be the predominant type of fungicidal compound up until the present. At present there are approximately 55 classes of fungicide compounds (FRAC, 2017), but sterol 14 α -demethylation inhibitors (DMIs), quinone outside inhibitors (QoIs) and succinate dehydrogenase inhibitors (SDHI) are the three predominant classes of fungicides, with over two thirds of the fungicide treated area

in the UK being treated with one or more of the three (Hawkins and Fraaije, 2018). Single-site fungicides generally have a desirable low toxicological profile, with minimal effects on humans or other animals, but are especially susceptible to the formation of resistance. Previously, growers would often rely exclusively on the most effective, newly released fungicides, and apply them on their own which becomes easy for pathogens to overcome and develop resistance as resistance to single site compound may only require a simple genetic change (Brent and Hollomon, 2007). This meant that often fungicides would be released to market and within a couple of seasons their efficacy would be severely impaired (Russell, 1995). The cyclical introduction of compounds, mismanagement and consequent development of resistance, paired with increasing pressure from the EU, as well as withdrawal of products from the market under the EU directive 2009/128/EC, which encourages improved Integrated Pest Management schemes, has meant that there is a reducing pool of products available for growers to use. To combat this and preserve the efficacy of products currently available to us, there is increasing advocacy for management strategies utilizing mixtures of fungicides, variable dose rates, and the addition of multi-site fungicides as mixing partners to currently effective single site compounds.

1.4.1. Fenpicoxamid - Inatreq™ active.

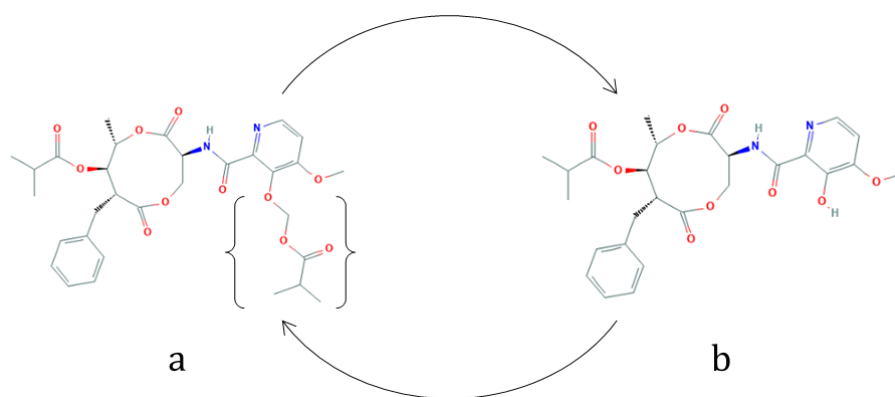


Figure 1.4: a) chemical structure of fenpicoxamid IUPAC: [2-[[[(3S,7R,8R,9S)-7-benzyl-9-methyl-8-(2-methylpropanoyloxy)-2,6-dioxo-1,5-dioxonan-3-yl]carbonyl]-4-methoxy-pyridin-3-yl]oxymethyl 2-methylpropanoate. Bracket represents R group added to UK2A (b) to improve photostability.

Fenpicoxamid, the active ingredient (a.i) in Inatreq™ active (note: future references to “Inatreq” refer to the commercial product “Inatreq™ active”), is a novel picolinamide developed in collaboration between Dow Agriscience (now Corteva Agriscience) and Meiji Seika Pharma, and is primarily effective against the wheat pathogen *Zymoseptoria tritici* (Loiseleur, 2017). Picolinamides are a new class of fungicides that competitively bind

with the mitochondrial ubiquinol-cytochrome *c* oxidoreductase cytochrome *bc*₁ complex at the ubiquinone reduction site (Qi) site, as opposed to the Qo site that QoIs bind to (Young *et al.*, 2018). Fenpicoxamid is a derivative of the natural occurring UK-2A, which is structurally related to antimycin A and was isolated from *Streptomyces* sp. 517-02 (Ueki *et al.*, 1996).

Fenpicoxamid's pathway from discovery through to development and commercial production began almost 25 years ago with the collection of soil samples by Osaka City University in Japan. These samples contained *Streptomyces* sp. 517-02 which was found to naturally produce UK-2A, a compound that had natural fungicidal activity (Ueki *et al.*, 1996; Machida *et al.*, 1999). This could be produced on a large scale using conventional fermentation within a bioreactor, with conditions which may be optimised for maximal production from the streptomyces species. UK-2A was extensively characterised in a collaborative effort between Dow AgroSciences LLC and Meiji Seika Pharma Co. Ltd, testing its glasshouse and field efficacy as a fungicide, as well as its *in planta* stability. Initially, UK-2A performed well against pathogens such as *Z. tritici* in *in vitro* assays but performed poorly in a field context. This lack of efficacy within a field context was found to be due to inherent properties of the molecule, such as photo-instability, nullifying its activity. Considerable effort was then directed towards a simple one-step post fermentation modification of UK-2A to rectify these issues, which resulted in over 300 potential analogues being prepared. A minor modification of the picolinamide hydroxyl group of UK-2A, adding an isopropylcarboxymethyl ether masking group, forming fenpicoxamid, was found not only to redress issues of photo-stability, but also improved efficacy at low doses, and allowed the development of a novel formulation for delivery, improving uptake as well as retention within the leaf (Owen *et al.*, 2017). Commercial production of fenpicoxamid now consists of two stages: fermentation of *Streptomyces* optimised for the maximal production of UK-2A, which is recovered, purified, and then undergoes a one-step modification, adding a stabilising group.

It has been found using metabolism studies, that when cells uptake fenpicoxamid, it is almost all converted immediately back to UK-2A by carboxylesterases removing the isopropylcarboxymethyl ether masking group that was added in the post fermentation modification stage (Owen *et al.*, 2017). UK-2A is the active moiety in the fenpicoxamid molecule, and further to this fungitoxicity assessments suggest that fenpicoxamid itself is less active than UK-2A, but is still comparable to that of commercial comparison standards (Owen *et al.*, 2017; Young *et al.*, 2018).

Fenpicoxamid is a particularly efficacious fungicidal compound when applied preventatively but has also been found to have curative activity when applied with the accompanying surfactants in Inatreq active. When fenpicoxamid is applied to the surface of the leaf, deposits bind to the surface of the leaf and act as reservoirs of fenpicoxamid. When these are then absorbed by fungal hyphae, it is converted to UK-2A and acts in a fungicidal manner (preventative application). Small amounts of fenpicoxamid is also known to penetrate the cuticle and leaf tissue, which then is again converted to UK-2A and kills *Z. tritici* present within the leaf (curative application).

Non-fungicidal activity.

In preliminary trials at Corteva Agriscience it has been found that the application of Inatreq was associated with potential drought benefits, such as extension of green leaf duration, increased chlorophyll content and delay of wilting (Walker, unpublished). Previously traits such as these have been observed in other commercial fungicides (Berdugo *et al.*, 2012; Dal Cortivo *et al.*, 2017; Kuznetsov *et al.*, 2018), but the mechanism for these effects are poorly understood or characterized.

1.4. Aims and objectives.

Inatreq (a.i: Fenpicoxamid) is a new fungicidal compound and is the first new fungicidal mode of action to be released in the last 10 years. The work described in this thesis aims to characterize aspects of its fungicidal and non-fungicidal activity by:

- Investigating the curative fungicidal activity of Inatreq, using traditional and non-traditional, lab-based assessment methodologies (Chapter 2).
- Characterising the non-fungicidal effects of Inatreq on wheat grown in glasshouses and controlled environment chambers (Chapter 3).
- Confirming the effects observed in Chapter 3 in large scale field and automated glasshouse trials (Chapter 4).
- Developing a high-throughput tool for assessment of non-fungicidal effects of Inatreq on a model species and investigate the underlying genetic basis of the response (Chapter 5).

Chapter 2. Assessing the curative fungicidal efficacy of Inatreq™ active using traditional techniques and image analysis.

2.1. Introduction and aims.

2.1.1. Introduction.

In modern agriculture, production has become dependent upon the benefits associated with fungicide applications, preventing losses resulting from the spread of disease. Most crop protection products are applied at a homogenous rate, across entire fields, targeting a broad spectrum of pathogens, and acting in a preventative manner.

However, there is increasing interest in applying fungicides in a more precise, and targeted manner with encouragement from pressure to reduce pesticide inputs. The EU is increasing this pressure to reduce pesticide inputs, by withdrawing the use of many previously-available synthetic pesticides, and encouraging the use of Integrated Pest Management (IPM) schemes under EU directive 2009/128/EC. Interest in a reduced rate of pesticide application is driven by concerns over the effects of pesticides on the environment in terms of soil health and erosion (Pimentel *et al.*, 1995), reductions in biodiversity (Wu and Chen, 2004; Hole *et al.*, 2005; Geiger *et al.*, 2010; Heick *et al.*, 2017; Brühl and Zaller, 2019) as well as the reduced efficacy of pesticides as a result of improper/over use (Leroux *et al.*, 2007; Cools and Fraaije, 2008; Torriani *et al.*, 2009, 2015; Cools *et al.*, 2011a; Fraaije *et al.*, 2012; Miles *et al.*, 2013).

Many pathogens that are common in the field are not distributed across the field homogeneously, and instead they can appear as sporadic blooms – spreading out from single points of pathogen introduction. For example, following the initial infection of *Z. tritici*, which is often the result of an airborne ascospore, the disease will then be widely propagated by splash-dispersed pycnidiospores, progressing from the lower leaves of plants towards the top of the same plant, as well as to plants in its immediate vicinity. Site specific, targeted applications of fungicides are being proposed as a solution, only applying fungicides to the plants that need it (Tackenberg *et al.*, 2016). These systems utilise either remote sensors within the field (Tackenberg *et al.*, 2016), or with the current increasing technological advancement of remote sensors and autonomous agricultural machinery, can be mounted upon the spraying machinery (Faïçal *et al.*, 2014, 2017; Talaviya *et al.*, 2020).

The assessment of plant disease is complex, and it is not only important to be able to accurately quantify disease severity for the discovery and development of new fungicides, but also for farmers and producers making decisions on crop management, seed breeders aiming to produce new crop varieties with improved disease resistance, and research on fundamental biological processes. In many of these cases, disease severity is assessed

using visual estimates with the assistance of keys (Horsfall and Barratt, 1945), or with specific training (Nutter and Schultz, 1995; Nutter and Esker, 2006). In plant disease measurement, disease severity refers to the proportion of a sample unit that is symptomatic (Nutter *et al.*, 1991). A widely accepted and accurate method for measuring true disease severity is to develop prints of the sample unit, cut out the symptomatic areas and weigh them as a proportion of the total sample unit (Nita *et al.*, 2003). Measurements utilising image analysis now allow for accurate scores to be given more easily and conveniently. These allow users to select areas of disease by identifying pixels within a pre-specified colour range and measure these as a proportion of the total area, giving the percentage leaf area covered by necrosis/ lesions (PLACN/ PLACL). These measurements can usually be carried out on inexpensive or free image processing tools such as ImageJ (Stewart and McDonald, 2014b) and Mesurim Pro (Leplat *et al.*, 2018). It is of note that when using these image analysis systems, the selection of diseased area is still subjective as the assessor sets the segmentation parameters. As well as discerning disease based upon the visible colour spectrum, image analysis has further advanced in disease recognition with the introduction of more sophisticated imaging modalities such as thermography, multi/hyper-spectral cameras, and chlorophyll fluorescence (Rolfe and Scholes, 2010). For a comprehensive review of further advances in image based disease assessment, see (Oerke *et al.*, 2014; Mahlein, 2016) and references therein. These tools can further improve the recognition of disease and recognise infection without visual symptoms. Visual estimates of disease severity without the aid of image analysis are still in widespread use. This is often because it can be extremely fast, carried out easily with minimal requirements other than an assessor and is therefore inexpensive, and can offer relatively accurate measurements with the appropriate training (Nutter and Schultz, 1995; Godoy *et al.*, 2006). Despite these benefits visual estimates can be inaccurate and have extremely variable reliability and repeatability (Sherwood *et al.*, 1983; Chiang *et al.*, 2016). In disease measurement “repeatability” or “reproducibility” is a measure of the statistical relationship between multiple disease assessments of the same sampling units by the same individual/instrument (intra-rater repeatability, (Nutter *et al.*, 1991)). “Reliability” or “replicability” is a measure of the consistency of disease assessment between scorers and therefore is a measure of the closeness of inter-rater scoring (Nutter *et al.*, 1991). The usage of these terms in the literature is not always consistent, requiring definition prior to use. For example, in a review by Barba (2018), it was outlined that these terms were generally used in three manners: either interchangeably, as outlined above, or even in the inverse manner to how it is defined above. Any future use of these terms is used with the former definition in mind. Both repeatability and reliability

may be influenced by a myriad of factors, such as lighting, bias based upon treatments, poor training, or even difficulties scoring diseases that present with a variety of symptoms. As well as being repeatable and reliable, the disease scoring method being used must be “accurate”. These results inform and influence various actions so must be as close as possible to the exact value, or in terms of disease assessment where an exact figure of severity is subjective, a value that is recognised as a “true value”.

With the growing interest in targeted, precise fungicide application, image analysis tools are potentially of great benefit. These need to reflect the scores that would be obtained by visual assessment, or even offer the ability to recognise disease in asymptomatic plants, to direct fungicide application. Symptoms of *Septoria tritici* Blotch (STB) are characterised by blotches of chlorotic and necrotic tissue that exhibit small black specks (pycnidia). These clear chlorotic regions have meant that STB has been an exemplar disease for automated image analysis (Stewart and McDonald, 2014b).

2.1.2. Aims.

The work presented in this Chapter compares traditional disease severity scoring of STB on wheat leaves by experts to a simple to use, easily customisable image analysis tool based on the open-source image processing software Fiji (Schindelin *et al.*, 2012). If this tool proves to be effective it will be used to analyse the curative activity of Inatreq against *Z. tritici*. This curative activity of will be compared in parallel to a panel of commercially available fungicides, with varying modes of action, that are commonly used to manage *Z. tritici*.

The potential to use confocal microscopy as a predictor of future disease severity, during *Z. tritici*'s asymptomatic stage was also assessed. This may potentially inform the efficacy of fungicide application before visual symptoms are apparent.

2.2. Methods.

2.2.1. General methods.

Plant material and growth conditions.

A commercial winter wheat cultivar (*Triticum aestivum* cv. 'KWS Trinity') was used in all pathology experiments. This cultivar was selected as it has both relatively low resistance to *Zymoseptoria tritici* and good resistance to *Blumeria graminis* (powdery mildew). 7-12 seeds were sown into 10 cm outside diameter (OD) pots filled with compost (John Innes

M3) and grown in a controlled environment growth room set on a 12/12-hour photoperiod at 20/16 °C. Plants were irrigated daily and then supplemented with a commercial NPK fertiliser (O-MIX 20-8-20 NPK feed, OMEX) once a week.

Fungal culturing and inoculation.

Zymoseptoria tritici fungal isolates (field isolates, supplied by Corteva Agriscience) were cultured in 10 cm petri dishes filled with 50 mL of potato dextrose agarose (PDA) containing penicillin and streptomycin (both 25 mg/L). Isolates were cultured in darkness at approximately 18 °C. Once the fungal cultures were sporulating (5 – 7 days after inoculation), 10 mL non-ionic surfactant solution (5 µL/mL Tween-20 (Sigma-Aldrich) in sterile dH₂O) was added. Spores were disrupted using a sterile spreader and the spore solution pipetted through a muslin cloth into a 50 mL conical centrifuge tube. A further 5 mL of sterile dH₂O was added to the plate before using the spreader again to dislodge remaining spores which were then added to the centrifuge tube. This process was repeated for three fungal plates. The spore suspension was vortexed before being centrifuged at 224 RCF for 10 minutes to remove any remaining agar or mycelia. Following centrifugation, the supernatant was removed, being careful not to disrupt the pellet, and replaced with 20 mL dH₂O. This solution was then vortexed again before being centrifuged for a further 10 minutes at 224 RCF. The supernatant was carefully removed, and the pellet resuspended in 20 mL of dH₂O by vortexing. The spore concentration of the final suspension was estimated using a haemocytometer and adjusted to a concentration of approximately 1 × 10⁶ spores/mL by dilution in a solution of 50 % (w/v) potato dextrose broth supplemented with 1.5 g/L gelatin, 0.5 g/L sodium oleate and 100 µL/L of Tween-20.

Spore solutions were applied using a handheld sprayer until surface run-off. Plants were then transferred to a propagator tank with the lid closed to maintain 100% humidity for 3 days to facilitate infection, before the lid was then removed.

2.2.2. Fungicide application – Curative application of Inatreq to plants previously inoculated with *Zymoseptoria tritici*.

Wheat seedlings were inoculated with *Z. tritici* 12 days after sowing when the first two leaves were fully unrolled (BBCH growth stage 12). These plants were then treated with a panel of four commercial fungicides, alongside Inatreq at two application rates (see Table 2.1 for fungicide list and application rates) at either 6 days post-inoculation (6 dpi) or 10 dpi.

Fungicides were applied using a handheld calibrated sprayer. All fungicides were diluted in water and applied at a rate equivalent to 200 L/ha

Table 2.1: Commercial fungicides, their active ingredients, and their respective application rates. All fungicides were applied at a dilution rate equivalent to 200 L/ha in water.

Fungicide	Active ingredient	Application rate (L/ha)	Active ingredient per hectare
Elatus Era (Syngenta, UK)	75 gai/L Benzovindiflupyr 150 g/L Prothioconazole	1	75 gai/ha Benzovindiflupyr 150g/ha Prothioconazole
Imtrex (BASF plc, UK)	62.5 gai/L Fluxapyroxad	2	125 gai/ha Fluxapyroxad
Inatreq™ active (Corteva Agriscience, UK)	50 gai/L Fenpicoxamid	2	100 gai/ha Fenpicoxamid
Inatreq™ active	50 gai/L Fenpicoxamid	1.5	75 gai/ha Fenpicoxamid
Librax (BASF plc, UK)	45 gai/L Metconazole 62.5 g/L Fluxapyroxad	2	90 gai/ha Metconazole 125 gai/ha Fluxapyroxad
Proline 250 (Bayer Crop Science, UK)	250 gai/L Prothioconazole	0.72	180 gai/ha Prothioconazole

2.2.3. Disease scoring.

Automated image analysis tool.

Plants were assessed for disease symptoms 21 days after inoculation. Whole leaves, present at both inoculation and fungicide application, were randomly selected and excised 10 – 15 mm from the ligule and transferred to a copy stand for imaging using a Nikon D5100 DSLR camera. Leaves were arranged flat and fixed onto a black background, adaxial side up and with all images also featuring a reference scale. Leaves were evenly illuminated, to minimise shadowing and reflections. For each fungicidal treatment images of 8-12 representative leaves were taken. All images were captured whilst the camera was in manual mode, to ensure settings remained consistent across images. Images were

processed using the open-source image software package FIJI (Schindelin et al., 2012). Images were cropped and their backgrounds removed so they only featured the central portion of the leaves (Figure 2.1b). Using FIJI's image adjustment tool "Threshold Colour" (Figure 2.1a), it was then possible to segment sections of the leaves that were demonstrating STB symptoms using the hue-saturation-brightness (HSB) colour space and quantify the segmented area. Firstly, a suitable combination of thresholds was found for selecting symptoms by comparing between plants that were either infected or not, with no fungicidal applications. The total area of the leaves was then calculated using the same technique but with the thresholding parameters being adjusted to segment the complete leaf. These two sets of parameters were then used across all image sets to prevent user bias influencing scores. Both stages of image thresholding were then integrated into separate macros for multiple image processing (Appendix 1.). Multiple image processing allows for the total leaf area and the total symptomatic area to be calculated at ~1 image/second.

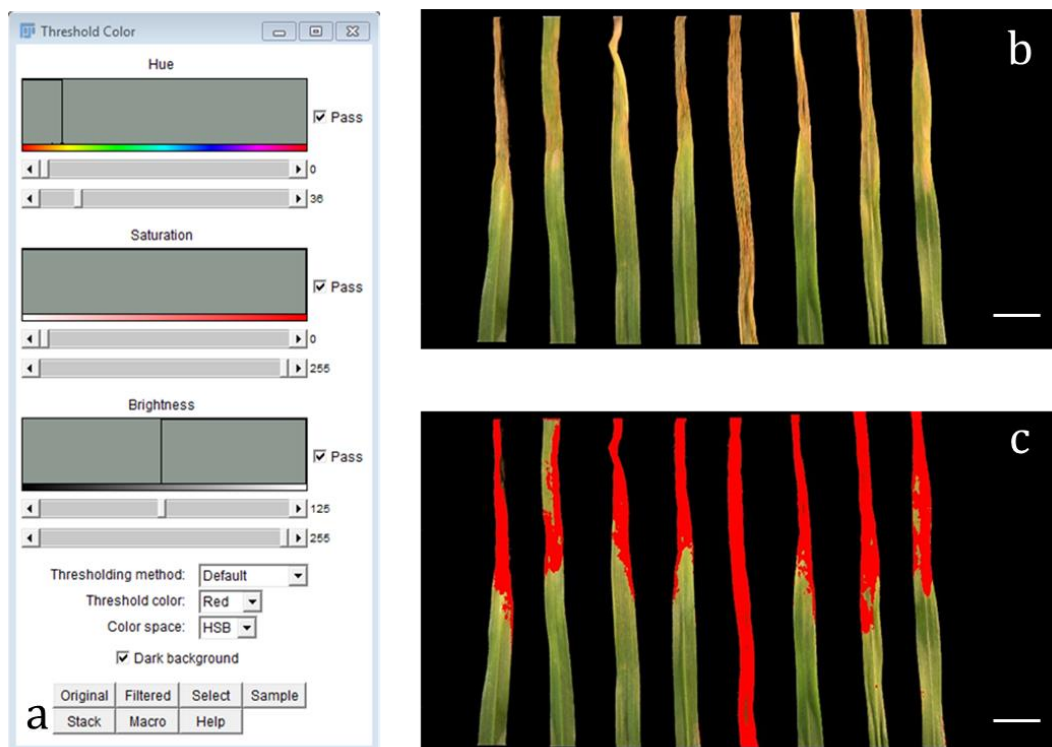


Figure 2.1: Disease symptom image analysis. a) Colour thresholding tool in FIJI used to select for areas of disease, b) raw image of infected leaves, c) image with diseased regions of the leaves segmented (in red) using colour thresholding. Scale bars = 10 mm.

Validation of image analysis technique by comparison with visual scores from industry experts.

Image analysis results using the macros were directly compared to disease area scores provided by trained and experienced field scientists who specialise in fungicide research and development. The scientists were asked to assess a randomised panel of images showing leaves with varying disease coverage (see Section 3.2.2)(Appendix 1) and score the symptom coverage using the nearest percent estimates (NPE) method (Chiang *et al.*, 2016). The estimation of percentage coverage is preferred to a categorised disease scale which have been found to be less reliable (Forbes and Korva, 1994; Nita *et al.*, 2003). Fungicide treatments were not disclosed, only the identities of the inoculated control (with no fungicide) group and uninoculated control groups were disclosed, to give the scorers a reference for the least and most infected samples. All scorings were conducted individually, and the participants were not allowed to confer.

To assess intra-rater reliability a second set of assessments were conducted using the same expert panel 3 months later. For this assessment, the leaves in each image had their position rearranged, and the order of images in the questionnaire was randomised. Experts were instructed to assess the new images under the same conditions as before and not to refer to the previous results (Appendix 1).

Data analysis.

Regression analysis was used to investigate the relationships between individual experts' scores, the mean score between the experts, and the score given using the image analysis tool. Values of the coefficients of determination (R^2) closer to 1 represent techniques that have similar scores, and are therefore interchangeable, whereas scores that were closer to 0, represent scoring techniques that vary greatly from each other, and their scores are not comparable. Inter-rater reliability was tested by using linear regressions, which compared each expert's estimate or image analysis score amongst each other. The mean R^2 value of each systems individual interactions were then compared using a one-way ANOVA to test for significant differences amongst experts scores and the image analysis tool. If required, a Tukey's post-hoc test for significance was performed. Intra-rater reliability of the expert's assessments were analysed using correlational coefficients, comparing the scores given by the same expert for the repeated assessments.

To test the accuracy of both individual experts and the image analysis tool, scores were compared to a mean expert score (Expert \bar{x}). For this, the Expert \bar{x} was regarded as the "ground truth" score (true value), as it is commonly used and is the generally accepted

methodology for assessment in industry. The results between the expert panel and the image analysis tool were compared by linear regression and using Lin's concordance correlation coefficient (Lin, 1989). Regression analysis can often pass data that is accurate but scattered (i.e., lacking precision), whereas data that is very precise but slightly biased out may be rejected. Lin's concordance coefficient combines the measure of accuracy and precision.

Bland-Altman plots (Bland and Altman, 2010) are commonly used in clinical assays to test reproducibility of pharmaceutical tests and compare their degree of agreement. They have also been used to compare disease severity scoring in plants (Bock *et al.*, 2008) and were used to compare the level of agreement between the image analysis score and the Expert \bar{x} score, testing the accuracy of the new methodology. Bland-Altman plots compare the difference between each score and plot it against the actual score. The plot includes the upper and lower levels of 95% agreement (the mean \pm 1.96* standard deviation). A Bland-Altman plot showing acceptable levels of agreement and reproducibility shows the mean difference line near to 0 and all points plotted within the 95% level of agreement.

2.2.4. Confocal laser scanning microscopy to assess asymptomatic fungal colonization.

Staining.

14 days after inoculation, leaves were excised for staining and imaging using confocal laser scanning microscopy. For each treatment group, 9 leaves were sampled which had been fully unrolled at the time of both inoculation and fungicide spray. These samples were cut into 1.5 - 2 cm lengths from the centre section of the leaves and stored in 1.5 mL microcentrifuge tubes, filled with 1 mL 100% ethanol, and kept in darkness at 4 °C. Samples were kept in ethanol for a minimum of 4 days to undergo bleaching and removal of chlorophyll.

Following the initial bleaching, the ethanol was removed and replaced with 1 mL of 10% w/v KOH and incubated for 4 hours at 80 °C. Tubes were sealed closed using plastic sealing film to prevent any popping open. Following incubation, samples were washed at least 4 times in 1x PBS solution to neutralise sample PH prior to staining.

Samples were incubated at room temperature in staining solution (20 μ g/mL propidium iodide (Sigma-Aldrich); 10 μ g/mL FITC-conjugated lectin from *Triticum vulgare* (Sigma-Aldrich), in PBS. To aid penetration into deeper tissues, the solution was vacuum infiltrated using a desktop desiccator at 250 mbar for 4 cycles of 4-5 minutes under

vacuum followed by 5-minute intervals at atmospheric pressure. Following this, the samples were stored in PBS in darkness at 4 °C for a maximum of 7 days until ready to image.

Confocal Laser Scanning Microscopy.

All confocal microscopy was conducted using a Leica SP8 laser scanning confocal microscope (Leica, Wetzlar, Germany). The laser channels, excitation/ detection wavelengths and laser/ detector types are listed in Table 2.2. A representative image of the surface of each leaf was taken, 2 cm from the tip of the leaf.

Table 2.2: Confocal microscope imaging parameters.

Fluorescent target	Laser type	Excitation wavelength	Detector	Peak detection wavelength
FIT-C conjugated lectin	Argon (20% power)	500-540 nm	Photomultiplier tube (PMT)	488 nm
Propidium iodide	561 DPSS	580-630 nm	Hybrid Detector (HyD)	561 nm

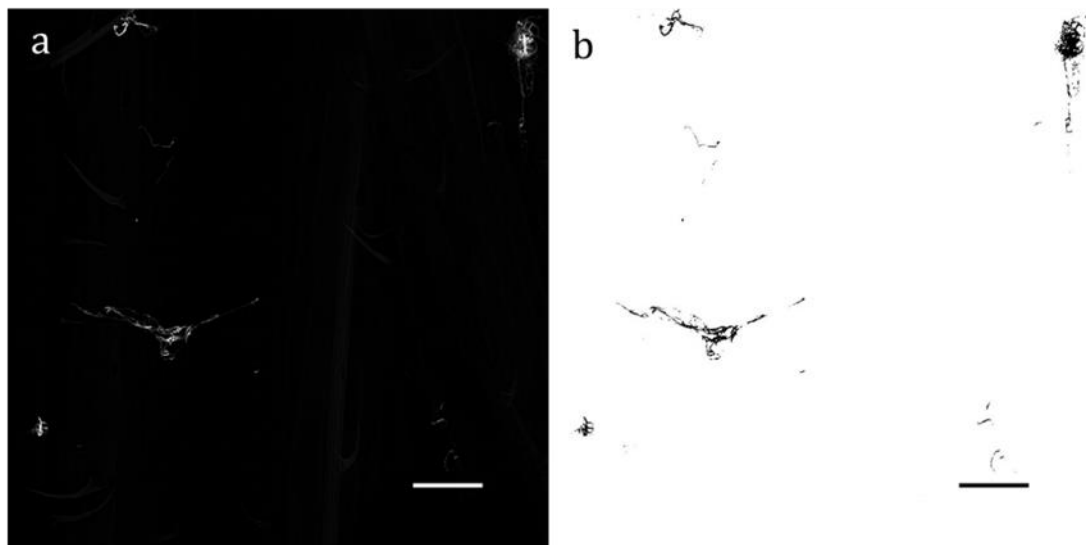


Figure 2.2: a) Confocal image of wheat leaf samples (black) inoculated with *Zymoseptoria tritici* (white). b) Images following colour thresholding where parameters were set to only select for the *Zymoseptoria tritici* mycelium and was used to calculate the total area covered by fungal mycelium. Scale bars = 150 µm

Analysis.

All confocal images were analysed using the open source image software package FIJI (Schindelin *et al.*, 2012). To analyse fungal population size in the confocal images, only the channel displaying fluorescence from the FIT-C conjugated lectin was observed. This channel was then adjusted using the colour thresholding tool as in Section 2.2.3 to select for just the fungal mycelium such as in Figure 2.2. All images were a 1160 μm x 1160 μm area of the leaf surface, and the total area occupied by fungal mycelium was calculated. These results were then further analysed using an appropriate statistical test if required.

2.3. Results.

2.3.1. Assessment of image analysis tool.

Across the thirteen treatment groups there was a wide range of symptom coverage, which was reflected in the disease severity scores (Figure 2.3). The control–no inoculant and the control–inoculated images were the only images where their identity was known prior to assessment, and except for a couple of expert scores were scored as having the lowest and highest symptom coverage, respectively. The level of agreement between the mean expert scores and the image analysis tool was high throughout, with the image analysis score always scoring the images within the range of the expert estimates. Once symptom coverage began to rise above 20 % (proline 6dpi in Figure 2.3) variability increased, with expert estimates showing the largest divergences from the expert mean. Image analysis outputs also diverged furthest from the expert mean in this range. In total, in all the assessments, 82 manual scores were received for symptom coverage that were less than 20%, and 74 scores were greater than 20 %. Of those below 20 %, 44 scores were non-divisible by 5, whereas when the scores were 20 % or higher only 3 of the 72 scores received a score non-divisible by 5. This reflects that once symptom coverage begins to exceed 20-25% scorers will automatically begin to band scores by intervals of 5 whereas below 20% they are able to offer more specific scores.

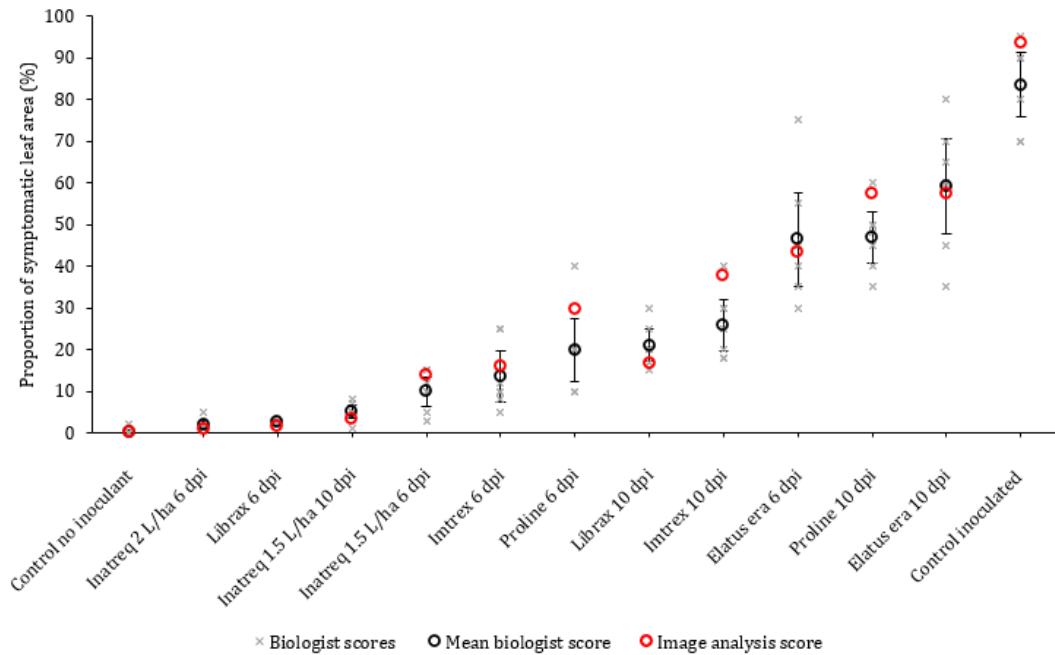


Figure 2.3: Comparison between the individual scores given by 7 industry experts (grey crosses), the mean score of the experts (black circle), and the score calculated using the image analysis tool (red circle). Error bars for mean expert score are $\pm 2SE$. Fungicides were applied either 6 days post-inoculation (dpi) or 10 days dpi. Analysed images taken from curative treatment data set (Section 2.2.2).

Inter-rater reliability.

Generally, inter-rater reliability was good between individual expert estimates, as well as between the image analysis tool and the expert estimates (Figure 2.4). All calculated R^2 values were above 0.8 showing strong positive relationships with minimal variation between estimates. The mean R^2 value of each scoring systems individual interactions with every other score (Table 2.3) were then compared using a one-way ANOVA. It was found that there was no significant difference between the mean R^2 values of any of the experts or the image analysis tool. The mean R^2 value of the image analysis results was 0.9317, higher than any of the experts when compared amongst each other, suggesting the image analysis tool had a greater level of agreement with each of the individual experts scores, than any of the experts had with each other.

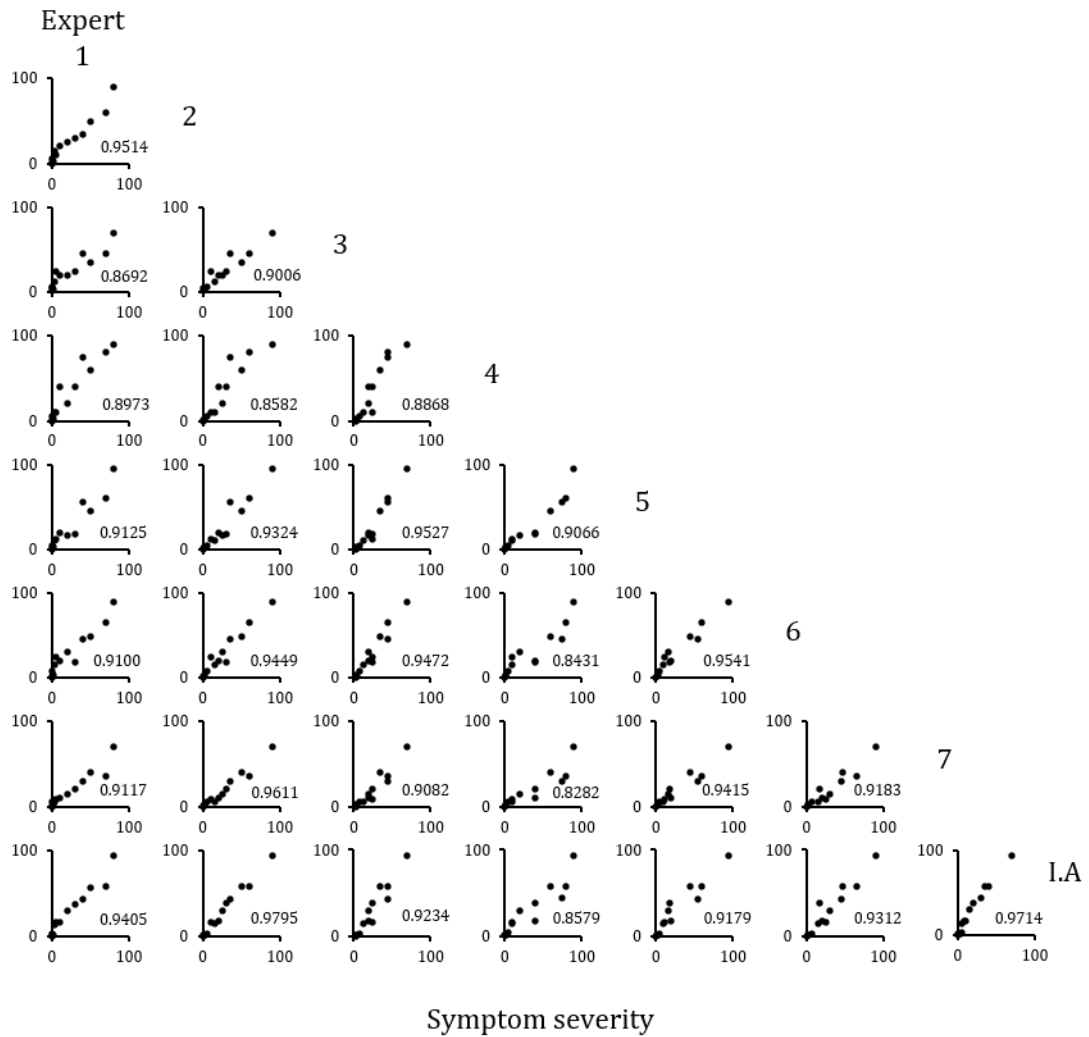


Figure 2.4: Linear regression matrix comparing all expert estimates to each other vertically and horizontally, as well as to the image analysis tools scores along the bottom (I.A.). All linear regressions feature R^2 values. Symptom severity scored as percentage coverage (0-100 %).

Table 2.3: Mean R^2 values from Figure 2.4 where each expert, or the scores from the image analysis tool, were compared to each other.

Expert	Expert	Expert	Expert	Expert	Expert	Expert	Image analysis
1	2	3	4	5	6	7	
0.9132	0.9208	0.9105	0.8905	0.9227	0.9143	0.9201	0.9317

Intra-rater reliability.

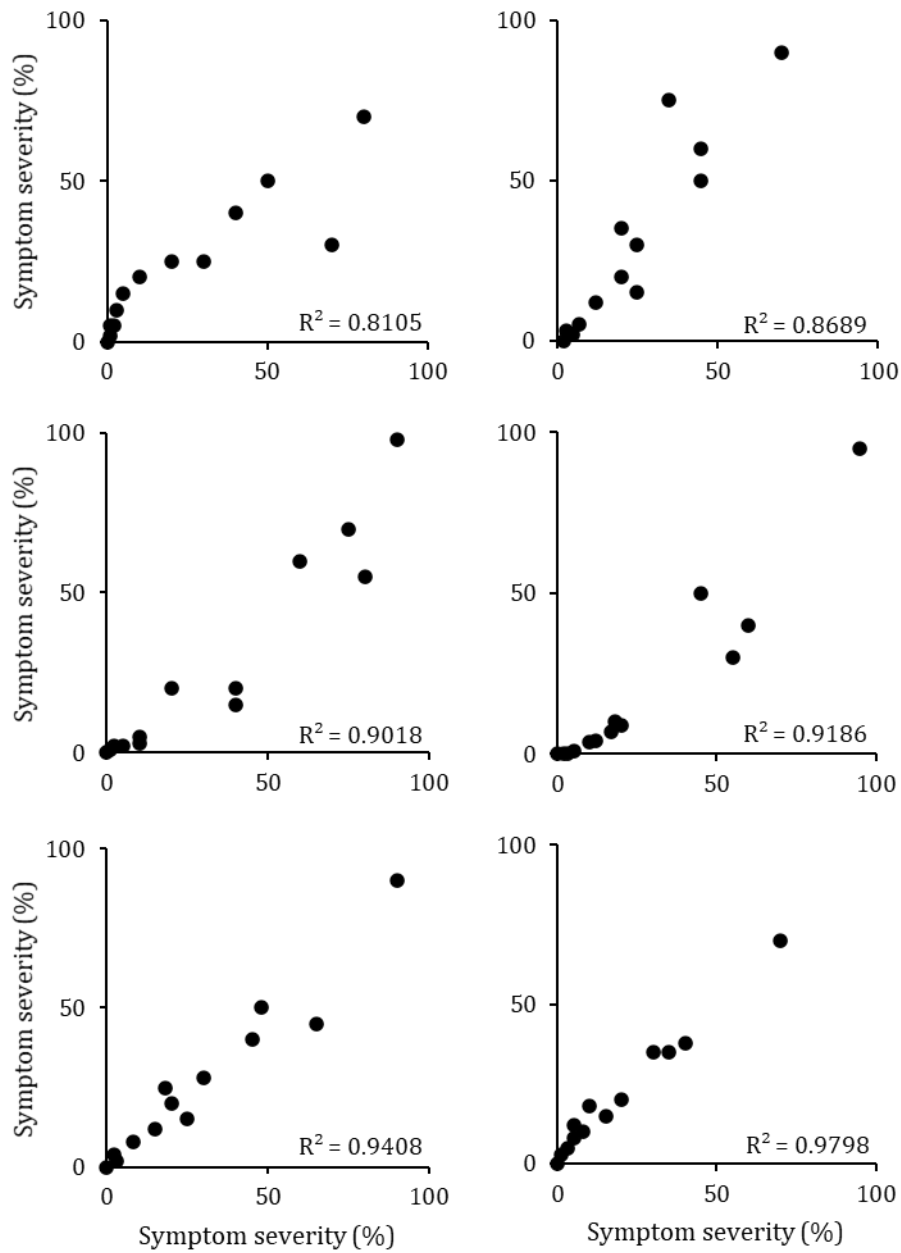


Figure 2.5: Intra-rater reliability comparing biologists first score (x-axis) to their second score (y-axis). Due to the automation of the image analysis tool, all repeats returned a score of 1.00.

Biologists received their second questionnaire featuring the same images, which had been edited to change the order of leaves in the images and the order of images within the questionnaire. Of the original 7 biologists to answer the first questionnaire, only 6 also completed the repeat questionnaire. A comparison of both their responses are represented in Figure 2.5, with their R^2 value in the bottom right of each graph. The R^2

values range from 0.81 to 0.98, suggesting all showed generally good correlation between the two scoring sessions, whilst the image analysis tool achieved an R^2 value of 1.0 due to the automated macro.

Accuracy.

Accuracy of the image analysis system was calculated by comparing the mean of all expert estimates to that of image analysis. This mean expert estimate score was considered the “ground truth” score. Figure 2.6 compares each individual expert’s estimates to the mean expert score whilst also featuring the image analysis tools scores against the expert mean for a reference of how the two compare. The concordance correlation coefficient (ρ_c) of the each of the experts and the image analysis tool is then listed below (Table 2.4). The ρ_c of the image analysis tool is 0.97, an extremely high accuracy.

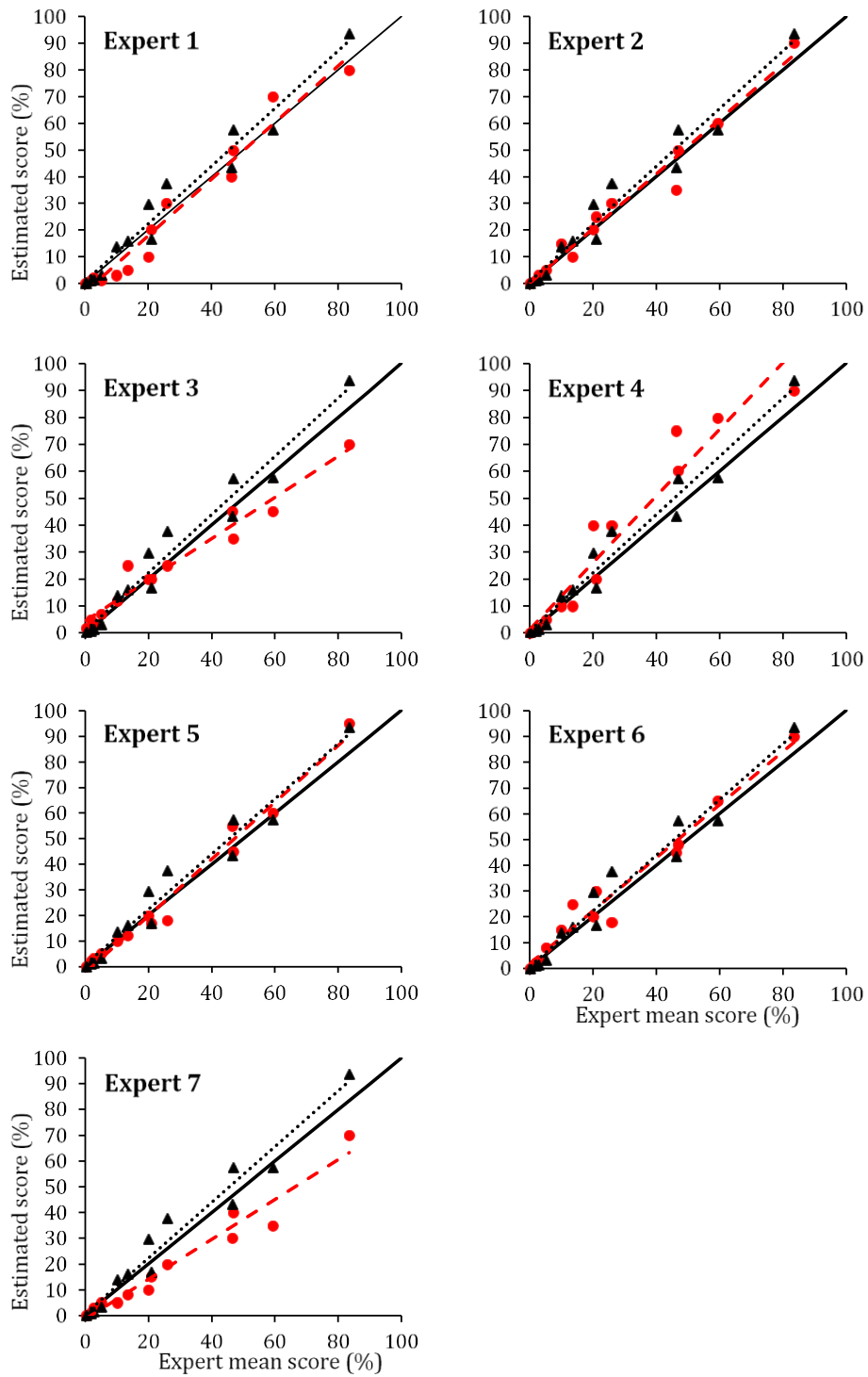


Figure 2.6: ● = Estimated disease symptom severity by individual experts plotted against the mean of all expert scores. ▲ = Image analysis symptom severity score plotted against mean expert score. — = solid line is the concordance line representing perfect agreement between the estimated and true value. Experts estimate and image analysis score each feature a red or black best fitting line by linear regression, respectively.

Table 2.4: Coefficients of determination (R^2 , testing reliability) and concordance correlation coefficient (ρ_c , measuring accuracy) compared between expert disease scores and image analysis scores, and between individual expert scores compared to the mean expert score (Expert \bar{x}). Assessments compared symptom coverage scores of leaves inoculated with *Z. tritici*, before being treated with a range of commercial fungicides at two separate timepoints.

Rater	Expert - Tool	Expert - Expert \bar{x}
	Interaction	Interaction
	R^2	ρ_c
Expert 1	0.9748	0.9557
Expert 2	0.9847	0.9848
Expert 3	0.9469	0.8913
Expert 4	0.9049	0.9041
Expert 5	0.9839	0.9545
Expert 6	0.9771	0.9637
Expert 7	0.9033	0.8572
I.A. tool	-	0.9730

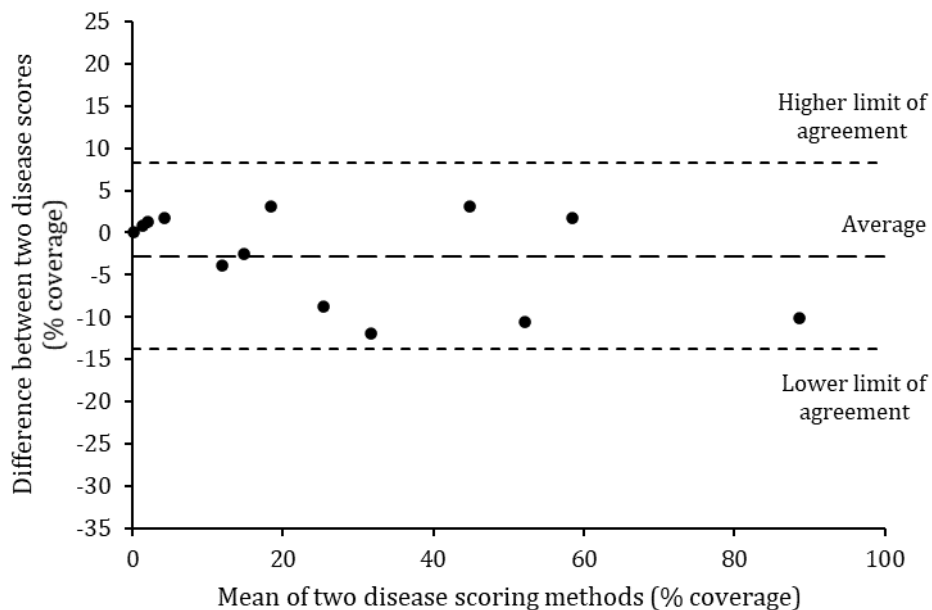


Figure 2.7: Bland-Altman plot visualising the difference in variance between the image analysis tool and Expert \bar{x} . The average difference in score coverage throughout was 2.7%, reflecting that the image analysis tool scored slightly higher than that of the experts mean score (Seen in Figure 2.5). The variance in scores from the mean error always fell within the 1.96 standard deviation.

2.3.2. Curative fungicidal efficacy of Inatreq.

Following the successful validation of the image analysis tool, the following results were derived using this technique (Figure 2.8).

Following the curative application of the panel of fungicides, the best performers were Inatreq and Librax, regardless of whether they were applied at 6 dpi or 10 dpi. All samples that had applications of Inatreq, irrespective of concentration or application timing, had a PLACN of below 20%. Imtrex and Librax both contain the same active ingredient; fluxapyroxad (SDHI) but Librax also contains prothioconazole (DMI), which may account for the improved performance. Elatus Era contains the SDHI benzovindflupyr, at a relatively low concentration alongside prothioconazole but seems to perform poorly when applied curatively. Proline purely contains prothioconazole and performs comparatively to Imtrex.

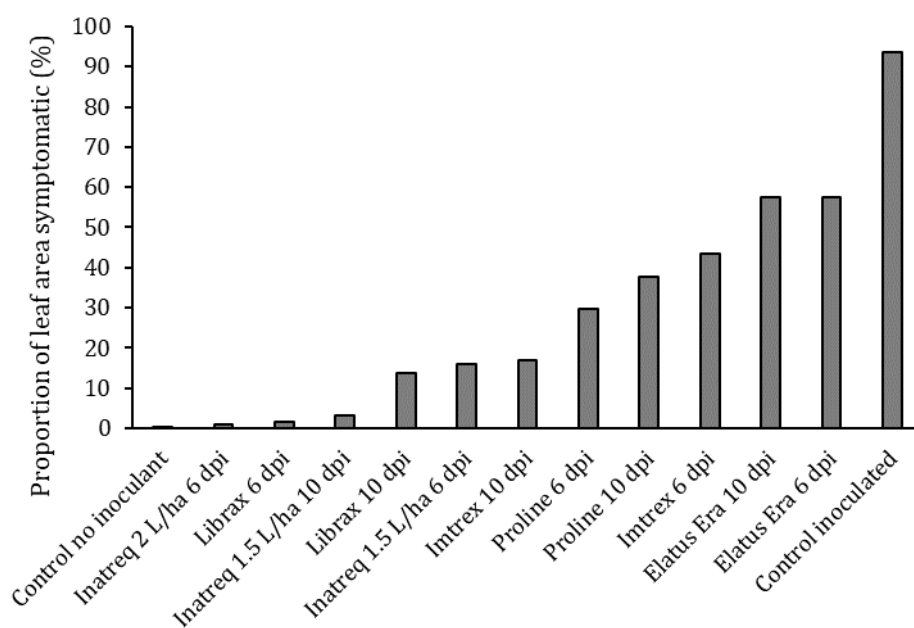


Figure 2.8: Percentage symptomatic leaf area, following the curative application of Inatreq active. Fungicides were applied at two time points: 6 days post-inoculation (dpi) or 10 dpi with *Z. tritici*. Each image had 8-12 leaves in, and the disease severity was calculated as a score of severity across all the leaves in the image.

2.3.4. Microscopy.

From the microscopy imaging data, the control group of leaf samples showed a higher total area of mycelia when compared to the panel of fungicides (Figure 2.9). There was no observed significant differentiation between the different fungicide treatments. The

logarithmic transformations of the measurements were used, as the variances were not equal.

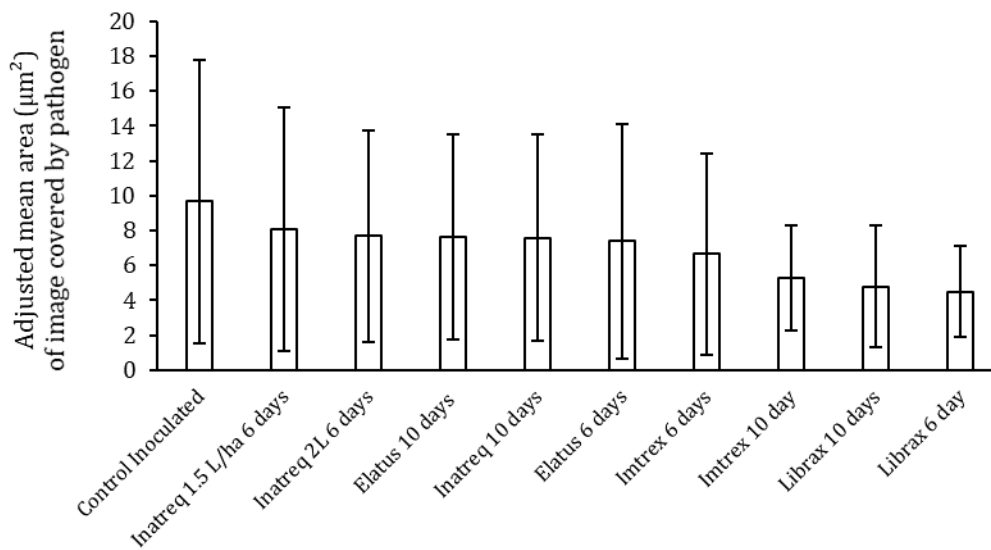


Figure 2.9: Total adjusted area of *Z. tritici* imaged on wheat samples treated with their respective fungicides. Variances were found to be unequal and therefore the log transformations were compared. Error bars = SE, $*=P<0.05$, $n=10$.

2.4. Discussion.

2.4.1. Development of a tool for disease assessment from images.

It is important that an unbiased scoring system is used for scoring plant disease symptoms. Commonly, severity is visually scored by experts within the field, as well as in the lab, and is a relatively quick and reliable system, with low costs. Using an image analysis-based approach, available on an open source image processing platform, allows for a potential alternative that is freer of inbuilt human bias (Stewart and McDonald, 2014a; Stewart *et al.*, 2016; Karisto *et al.*, 2018).

In the mid-range of severity (25-75 %), the variation in expert estimates varied much more than in the lower range (<25 %) (Figure 2.3). This phenomenon has been previously observed, with samples showing disease severity of 25%-75% having much larger variances in scores than those above or below these boundaries (Forbes and Jeger, 1987). Horsfall and Barratt developed an assessment scale (H-B scale) (Horsfall and Barratt, 1945) aimed to eradicate the ambiguity within this range, based upon the “Weber-Fechner law”. Weber’s law dictates that the “difference threshold” (the point at which a stimulus can be differentiated) is a constant proportion of the stimulus intensity. Fechner

accepted this but further suggested that the individuals acuity depends on the logarithm of the stimulus intensity (Horsfall and Barratt, 1945; Stevens, 1961; Nutter and Esker, 2006; Horsfall, 2012). However, the subsequently developed scale has been shown not to alleviate the difficulties associated with scoring within this range (Nita *et al.*, 2003). As well as the difficulty in scoring severity within this range, when scores were over 20 %, they were almost always scored towards the nearest 5 or 10 %, whereas below this range estimates were to the nearest 1 %. This behaviour has also been observed previously, where humans tend to prefer to score using certain values, such as in multiples of 5 or 10, causing disease scores to become “banded” and grouped together (Sherwood, 1983). Due to these factors, the use of an impartial tool, such as image analysis, may be valuable for scoring within this range and therefore circumvent the high levels of variance that may be observed.

Intra-rater reliability.

Observed intra-rater reliability was found to be high when expert’s repeat scores were compared, ranging from 0.81 to 0.97. This demonstrates that the experts can provide relatively consistent scores, for identical images on repeat occasions. However, the expert’s variability in scoring the same images will be dependent upon their level of experience and training.

Inter-rater reliability.

Inter-rater reliability was found to be very high when compared to each of the individual experts score. However, the image analysis tool was generally closer to each of the experts estimates than each of the experts were to each other. This suggests that the image analysis tool may be reliably used going forward, offering less variability in its scores when compared to the experts, than each of the experts were to each other.

Accuracy.

Accuracy was compared using the correlation concordance coefficients of the image analysis tool compared to that of the mean of 7 expert’s disease assessments. It was found that the scores produced by the image analysis tool were very close to that of the “ground truth” ($\rho_c = 0.9730$). Therefore, the tool may be considered very accurate, when aligned with expert opinion. However, despite this, it important to consider certain pitfalls of this technique when deciding upon scoring methods. This method relied on estimating the area of the leaf that was symptomatic, using lesions and necrosis as a marker for symptoms. In these experiments, the plants were grown in an environment where the only pathogen present was *Z. tritici* and the samples were inspected for other markers of

Z. tritici infection such as pycnidia. In an open environment however, these symptoms that have been scored may be the result of a variety of diseases, and not necessarily the target one. Senescence may also occur due to a range of abiotic factors such as drought or deficiencies in certain nutrients.

2.4.2. Fungicidal efficacy.

Following the successful validation of the image analysis tool, it was used to analyse Inatreq's curative performance against a panel of commercially available fungicides used in the prevention of STB. Inatreq was the best performing fungicide when applied curatively. It has previously performed well in experiments observing preventative application (Jackson *et al.*, 2018), but there has been little information available to date on its curative performance. It is reassuring to know that in future Inatreq has the flexibility to be applied in both manners. Librax also performed well and was directly comparable to Inatreq in curative results. However, Imtrex, which also contains fluxapyroxad did not quite perform as well as Librax which may highlight the importance of the metconazole included in Librax. Due to the traditional approaches to fungicide applications, where they are generally applied preventatively, there has been less focus on developing curative chemistries. Due to this, there are few commercial fungicides that have been shown to act effectively when applied curatively besides demethylation inhibitors (DMI's) (Tsuda *et al.*, 2004; Sanssené *et al.*, 2011). DMIs have generally shown to be effective when applied curatively, and therefore the addition of metconazole in combination with the SDHI fluxapyroxad to Librax may explain the superior performance when compared to the performance of Imtrex which only contains fluxapyroxad.

This work further highlights the efficacy of Inatreq as a fungicide, having been previously demonstrated strong preventative activity against *Zymoseptoria tritici* (Jackson *et al.*, 2018). The demonstration of effective curative activity means that Inatreq contains a particularly effective active ingredient, but it is also a product that offers producers a lot of flexibility in use. Due to restrictions on pesticide applications that has resulted from past mismanagement leading to resistance, contamination of water sources, and declining public interest in high chemical input agriculture, the opportunities for alternative application strategies will continue to grow. At present Inatreq has no cross resistance (Young *et al.*, 2018), and therefore if it is adopted in a low input strategy that focuses on curative application, may extend its usable lifespan, whilst maintaining popularity in the EU where pressure to reduce applications of pesticides are particularly strong.

Furthermore, the efficacious performance of Inatreq under both preventative and curative conditions, means fenpicoxamid will also offer an appealing co-formulant for future fungicides, and further reduce opportunities for resistance.

Chapter 3. Characterising the non-fungicidal effects of Inatreq on wheat.

3.1. Introduction and aims.

3.1.1. Introduction.

Recently there has been a trend to adopt an increasingly holistic approach to the characterisation of new fungicidal compounds, not only examining their performance against pathogens, but also investigating the impact these compounds may have on the plant itself. The characterisation of the impact of a new compound on the target plant is often limited and viewed purely from a phytotoxicity standpoint. The additional effects of pesticides, and how these may potentially benefit plants, are currently of great interest to producers and users. Table 3.1 highlights a selection of fungicides that have been identified to have beneficial non-fungicidal effects.

Early research into the potential beneficial side effects of fungicides reported the extension of green leaf area as well as delaying of senescence (Caldwell and Starratt, 1987; Wu and Von Tiedemann, 2001; Wu and von Tiedemann, 2002). Fungicides have since been associated with a variety of other physical and physiological effects, including increased grain set, improved phytochemistry and improved water use efficiency (Table 2.1). As the understanding of non-fungicidal effects of fungicides has improved, it has been observed that some associated effects may be able to alleviate stresses caused by abiotic factors, such as low water availability, and mitigate some of the losses. For example, it has been found that the application of the succinate dehydrogenase inhibitor (SDHI) benzovindiflupyr, was associated with better seed setting, and filling in wheat, particularly when the plants were grown under dry field conditions (Kuznetsov *et al.*, 2018). One of the observed effects following the application of benzovindiflupyr was a reduction in transpiration on the whole-plant scale, and it has consequently been hypothesised that this may have alleviated some of the losses from drought exposure. A controlled reduction of transpiration has long been recognised as a common stress mitigation strategy in plants, regulated by the hormone, abscisic acid (ABA) (Jones and Mansfield, 1970; Wilkinson and Davies, 2002). Traits such as this have recently garnered more interest as “added value” for the products, potentially offering solutions, or at least an extra benefit, when trying to secure higher yields.

These beneficial non-fungicidal effects can be referred to as “biostimulant-like” activity. Biostimulants are defined as substances and/or microorganisms that, when applied to plants, can stimulate natural processes to enhance or benefit nutrient uptake, efficiency, tolerance of abiotic stress and crop quality. Biostimulants do not act to directly fertilise the plant, nor have a direct action against pests, which is why these fungicides with associated beneficial effects can be considered to have biostimulative properties, but

cannot be classified as biostimulants (EBIC, 2012). Biostimulant products are still in their infancy but are now coming under stricter regulatory scrutiny due to growing interest and demand. This growing interest is reflected in the rapid increase in global market value to over \$2.91 billion in 2021, with a compound annual growth of 10.4% between 2016-2021 (Yakhin *et al.*, 2017; Madende and Hayes, 2020). Due to the nature of these being fungicides and having inherent fungicidal activity, non-fungicidal effects fall between the two classifications. The fungicidal activity of such compounds acts exclusively upon the pathogens and the non-fungicidal beneficial effects are initiating a response that is independent of the fungicidal activity, in the same way a biostimulant would. However, due to differing regulatory requirements, they will remain classified as fungicides. These beneficial non-fungicidal effects may offer opportunities for farmers to further improve their yields, and theoretically may one day influence the decisions, with chemistries that improve water use efficiency and tolerance to drought potentially being favoured in areas more prone to drought.

Table 3.1: Fungicides with observed non-fungicidal effects in the absence of disease.

Fungicide	Plant species	Side effect	Reference
Azoxystrobin	Wheat/ Barley (<i>Hordeum vulgare</i>)	Delayed senescence, > Chlorophyll content < Oxidative stress and electron leakage	(Wu and Von Tiedemann, 2001; Wu and von Tiedemann, 2002; Zhang <i>et al.</i> , 2010)
Benzovindiflupyr	Wheat	> Grain yield < Transpiration	(Kuznetsov <i>et al.</i> , 2018)
Bixafen	Wheat	Delayed senescence	(Berdugo <i>et al.</i> , 2012)
Carbendazim	Wheat	> Chlorophyll, < Oxidative stress and electron leakage	(Zhang <i>et al.</i> , 2010)
Epoxiconazole	Wheat/ Barley	> PSII efficiency > Biomass/ yield < Oxidative stress Delayed senescence	(Wu and Von Tiedemann, 2001; Wu and von Tiedemann, 2002; Ajigboye <i>et al.</i> , 2014b)
Fluxapyroxad	Wheat	< Transpiration > Water use efficiency > Yield under drought	(Smith <i>et al.</i> , 2013)
Hexaconazole	Chamomile (<i>Matricaria chamomilla</i> L.)	> Drought tolerance < Oxidative stress	(Hojati <i>et al.</i> , 2011)
Isopyrazam	Wheat	> PSII efficiency > Biomass/ yield	(Ajigboye <i>et al.</i> , 2014b)
Sedaxane	Wheat	> PSII efficiency > Biomass/ yield > Root growth	(Ajigboye <i>et al.</i> , 2017; Dal Cortivo <i>et al.</i> , 2017)
Trifloxystrobin	Red pepper (<i>Capsicum annuum</i> L.)	> Growth > Tolerance of a range of abiotic factors	(Han <i>et al.</i> , 2012)

3.1.2. Aims.

Preliminary research conducted by M. Walker and Dow agriscience (Walker, unpublished) suggested that the application of Inatreq may be associated with potentially beneficial side effects, particularly on plants grown under conditions with low water availability. The work described in this chapter aims to identify if there are any such effects associated with the application of Inatreq in the absence of disease. Plants were observed for general changes in growth and physiology parameters when grown under normal conditions, before being observed under conditions of limiting water availability. The difference in response between different winter wheat varieties, and different rates of application were examined. This work was conducted in controlled environment growth rooms, to provide consistent ambient conditions to enable accurate measurement of physiological processes such as transpiration rate, as well as providing consistent conditions across experiments to observe subtle differences in growth parameters, and better prevent the infection of plants.

3.2. Methods.

3.2.1. General plant material and growing conditions.

Two commercial wheat varieties (*Triticum aestivum* cv. 'RGT Skyfall', 'Extase') were used in all wheat experiments characterising the effects of Inatreq application. These varieties were selected owing to their relatively high resistance to powdery mildew and Septoria leaf blotch (STB), ensuring any differences observed would not be the result of fungicidal efficacy. Seeds of a uniform size were selected after passing through a set of calibrated, graduated sieves (Scientific Laboratory Supplies Ltd, Hessle, UK), collecting the seeds between 3.35 – 2.8 mm. These seeds were first sown in a cell tray (2 x 2 cm cells) filled with a peat-based compost (Levington M3) and placed within a growth room for two weeks at 16-18 °C with a 12-hour photoperiod to allow for germination. Seedlings were then transferred to a growth room set to 4-6 °C with an 8-hour photoperiod, where the seedlings were then left to vernalise for 7 weeks. Plants were then transferred into the growth room at 16-18 °C with a 12-hour photoperiod, ready for transplanting.

3.2.2. Comparing the root/ shoot biomass of mature plants treated with Inatreq under well-watered conditions.

Growth conditions.

Following vernalisation, the wheat plugs were transplanted into PVC columns (1 m tall, 15 cm OD) which could be split lengthways. These columns were fitted with a mesh at one end and filled with 10 mm diameter expanded hydroleca beads (Leca®, Specialist aggregates, Rugeley UK). The mesh, allowed for the hydroleca to be held within the tube, but for excess irrigation to pass freely through the column. Columns were maintained within a glasshouse and irrigated every two days with a commercial fertilizer mix (O-MIX 20-8-20 NPK feed, OMEX). The plants were grown between January – May 2018, in a glasshouse on Sutton Bonington campus (52°49'56.2"N 1°14'57.7"W). These glasshouses did not supply any supplementary lighting, as the day night cycles were representative of those the plants would experience in the field and only minimal supplementary heating was provided, preventing the temperatures decreasing below 0 °C.

Fungicide application.

Once plants reached growth stage 30-32 (BBCH cereal identification key) ten of each variety were treated with one of the fungicide treatments, Inatreq or a control solution. All treatments were applied using a calibrated handheld sprayer and applied in water at the recommended field rate of 200 L/ha. Inatreq active was applied at a rate of 2L/ha of concentrate, a rate of 100 g of active ingredient per hectare. The second treatment group were the control plants, which were treated with a control solution made up of water and Tween®20 spray adjuvant (Sigma-Aldrich) at a concentration of 0.01%. This was applied at the same rate as Inatreq active. All fungicide applications were made in the absence of noticeable fungal disease.

Data collection.

Plants were grown till BBCH growth stage 65 (all growth stages estimated onwards using the BBCH decimal code (Lancashire *et al.*, 1991)), when they were then harvested, to record fresh and dry weights of the roots and above ground biomass. Plants were excised at the base of the stem, tiller number counted, and placed in a paper bag, ready for drying. The root material was collected by splitting the columns lengthways, and removing the hydroleca by hand, and by triple washing in water. The roots were then also placed in a paper bag for drying. Root and above ground biomass samples were placed in a drying oven at 70 °C for 3 days before being weighed and their dry mass recorded. Figure 3.1 shows an example column (a), an opened column at growth stage 65 (b) and the root and shoot following excision and cleaning (c).

Statistical analysis.

Once the samples were dried and weighed the above ground and root samples were compared between the plants treated with Inatreq and the plants treated with the control solution using a student's *t*- test. These were conducted on the statistical software package SPSS v26 (SPSS, IBM corp).



Figure 3.1: Hydroleca column experimental set up. a) columns in-situ, b) a split column revealing the root system grown amongst the hydroleca, c) the root and shoot system following removal of the remaining hydroleca. A 1m rule is used for scale.

3.2.3. Effects of Inatreq on wheat grown under differential watering.

Growth conditions.

Following vernalising, plants that were to be grown to a mature growth stage were transplanted to 2 L pots filled with a mixture of 2/3 sandy loam topsoil (collected from a field site on Sutton Bonington campus 52°49'56.2"N 1°14'57.7"W) and 1/3 white sand. These plants were maintained in a controlled environment growth room, set to a 14- hour photoperiod, 60 % humidity and a 21/22 - 16/17 °C day – night temperature. In the room, light intensity was approximately 600 $\mu\text{mol m}^{-2} \text{s}^{-1}$ at plant level. The plants were watered daily and provided with commercial fertiliser mix (O-MIX 20-8-20 NPK feed, OMEX) once a week.

Fungicide applications.

Mature plants were treated with fungicides at BBCH growth stage 30-32, whereas the juvenile plants were treated with fungicides 1 week after transplanting to pots following vernalisation.

Plants were either treated with Inatreq or a control solution as outlined in Section 3.2.2. These were applied using a calibrated handheld sprayer, applying both fungicides at a rate equivalent to 200 L/ha. Inatreq was applied at a dose equivalent to 1 L of concentrate per 100 L of water, whilst the Tween-20 solutions were applied at a concentration of 0.01%. Plants were separated into their respective groups for fungicide application to eliminate any chances of application drift between the two sample groups and allowed to dry for 1 hour before being returned to their randomised positions.

Initiation of drought.

A preliminary experiment observed how soon after withholding water, under these environmental conditions, plants would exhibit reduced transpiration, an indication of drought stress. Significant reductions in transpiration were measured approximately 4-5 days after withholding water. Therefore, for droughted plants, water was withheld from 4 days prior to fungicide application, allowing the fungicides to be absorbed at the early onset of visual drought stress when the plant was reaching a severe stage of drought.

Transpiration measurements.

Transpiration measurements were only observed in mature leaves, as it can be difficult to obtain consistent results from smaller leaves that have not fully unrolled and matured. Transpiration was measured at the same time each day, 2 hours after the beginning of the photoperiod cycle. Measurements were recorded prior to fungicide application, and then every subsequent day after application. All measurements were recorded using a portable leaf porometer (Model SC-1, Decagon Devices, Inc. Washington, USA), taking care to consistently select the youngest, mature, fully unrolled leaf. To measure transpiration, plants were taken one at a time to a separate room, to avoid the local build-up of CO₂ which can adversely influence transpiration rate (Tausz-Posch *et al.*, 2013), before the sensor was placed on a central portion of a fully unrolled leaf, taking care not to be placed directly on a vein. The sensor then recorded the transpiration rate on the abaxial surface. Following observations, the plant was then taken back to its original room and returned to its position.

Recording relative water content and dry biomass.

Relative water content (RWC) was calculated at the end of the experiment when transpiration rate of the droughted plants fell below a recordable level. Sealable plastic bags were first weighed, before samples of leaf material were excised and placed inside. The bags were then re-weighed, giving the fresh weight (FW). Leaf samples were then fully submerged in water overnight, before again being weighed. This measurement is referred to as the turgid weight (TW). Finally, after recording the TW, leaf samples were then dried in a 70 °C drying oven for 3 days, before recording the dry weight (DW). These measurements were then able to be used to obtain the relative water content of the samples using Equation 1:

$$\frac{(FW - DW)}{(TW - DW)} \times 100$$

Equation 1: Calculation of relative water content (RWC).

FW= fresh weight, DW= dry weight, TW= turgid weight.

Statistical analysis.

The results of the control and treated plants in these experiments were compared using the two-sample *t*-test using the statistical software package SPSS v26 (SPSS, IBM corp)

3.2.4. Identifying if Inatreq reduces transpiration in a dose dependent manner.

Plants were cultivated, and transpiration observed in an identical manner to the well-watered plants outlined in Section 3.2.3.

Alongside the field equivalent rate of Inatreq applied in Section 3.2.2 & 3.2.3, an added dosage, equivalent to 200% of the usual field application dose (2 L of concentrate / 100 L water) was applied. Despite the increased concentration, both fungicides were applied at the same rate, equivalent to 200 L/ha.

Results were analysed using a one-way ANOVA in the statistical software package SPSS v26 (SPSS, IBM Corp.). Tukey's post-hoc test for statistical significance was used where appropriate.

3.3. Results.

3.3.1. Root/shoot biomass of mature wheat plants.

To identify if the application of Inatreq had any influence on biomass accumulation in the absence of disease plants were grown hydroponically, utilising the clay hydroleca beads as the growth medium. Plants were maintained with ample water and nutrient availability throughout this experiment, ensuring that although the growth medium was artificial, there were no obvious sources of abiotic stress, which may influence the plants growth rate or biomass accumulation. In this experiment, application of Inatreq to both varieties (Skyfall and Extase, lead to a significantly increased biomass in both roots and shoots (Figure 3.2). To ensure the impact observed was not merely a result of Inatreq's fungicidal efficacy, plants were inspected throughout their growing period, checking each leaf layer for any signs of common disease symptoms.

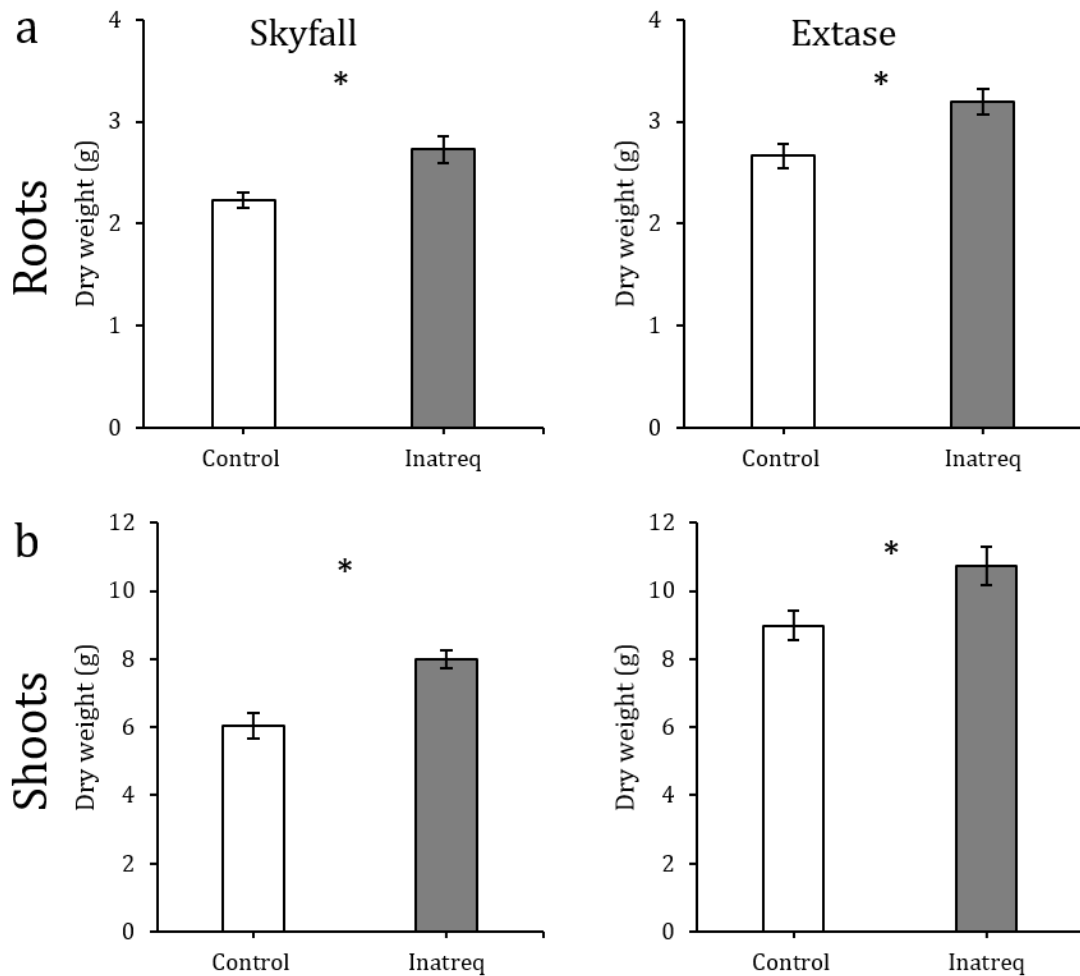


Figure 3.2: Mean root (a) and shoot (b) dry weights of two winter wheat varieties: Skyfall and Extase. $n=8$ Error bars = \pm SE, * = $P < 0.05$

3.3.2. Characterising the effects of Inatreq on wheat grown under differential watering.

In the plants that were watered freely throughout, there was an initial significant reduction in transpiration rate the first two days of post – Inatreq application of 10 and 5 % respectively, before the transpiration rates then began to rise, returning to a rate comparable to those treated with just the control solution (Figure 3.3b).

For droughted plants, both treatments reached the minimum transpiration rate recordable by the portable leaf porometer after 4 days post-application (Figure 3.3a). There was no discernible difference in transpiration the first day following the treatment, but by two days post-application, the plants that were treated with Inatreq had reduced their transpiration rate by 24% compared to the control plants, however this was not a significant reduction. By the third day post-application the treated plants had a significant

reduction in transpiration rate of 45% compared to control plants. On the final day of observations, the plants treated with Inatreq had a transpiration rate 33% lower than that of the control plants, however at this final timepoint, the reduction was again, not significant (Figure 3.3a).

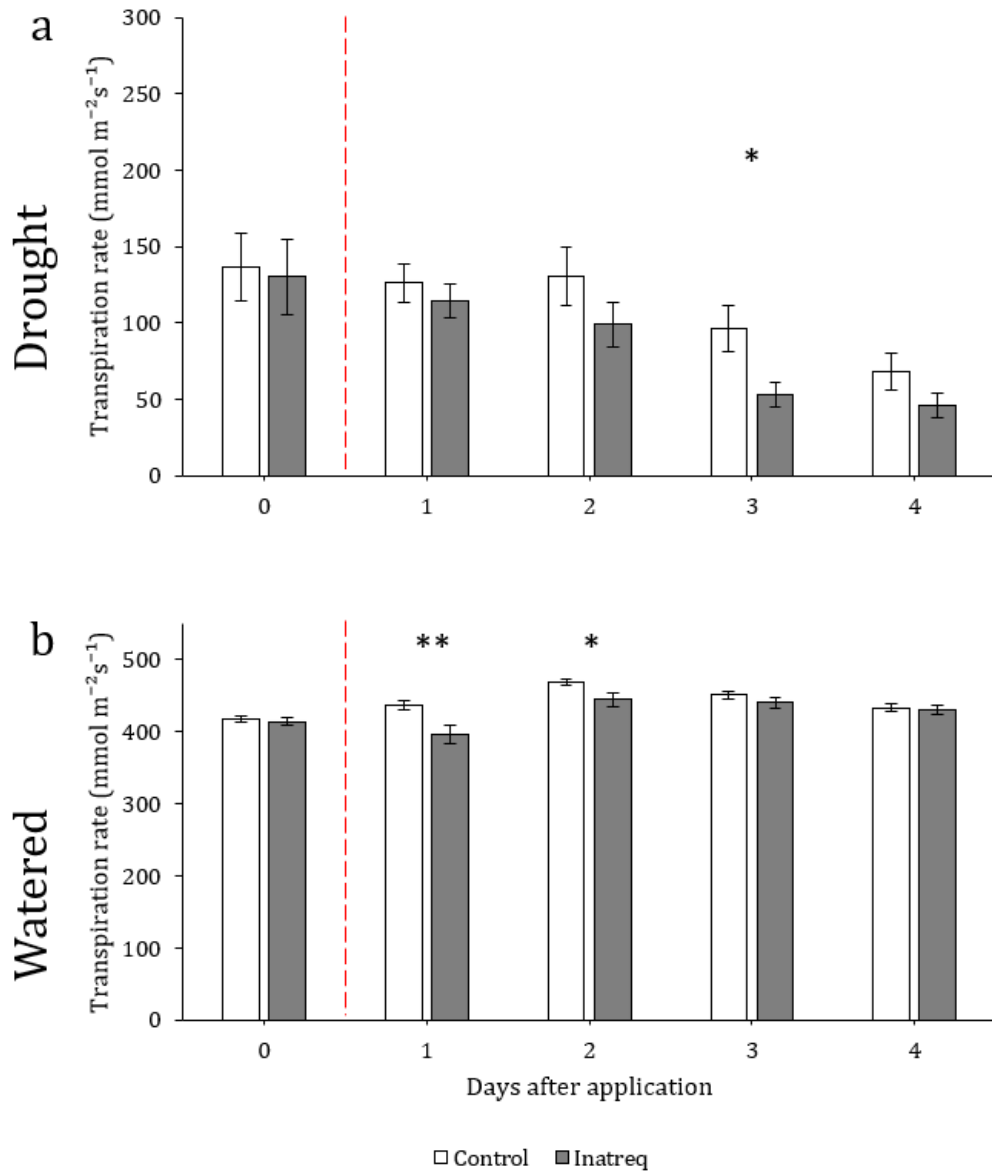


Figure 3.3: Comparison of transpiration rate in wheat plants (var. Skyfall) where (a) the water was withheld, and (b) where watering was maintained. Measurements were observed for 4 days following fungicide application (red line). $n = 30$, error bars = \pm SE, * = $P < 0.05$, ** = $P < 0.01$.

Following the transpiration observations, the plant material was harvested to measure the relative water content of the leaves. Plants that were treated with Inatreq and grown

under well-watered conditions were not significantly different from each other (Figure 3.4b). In the plants where water was withheld prior to the applications, the plants treated with Inatreq had a RWC that was significantly higher (5%) than that of the control solution treated plants (Figure 3.4a).

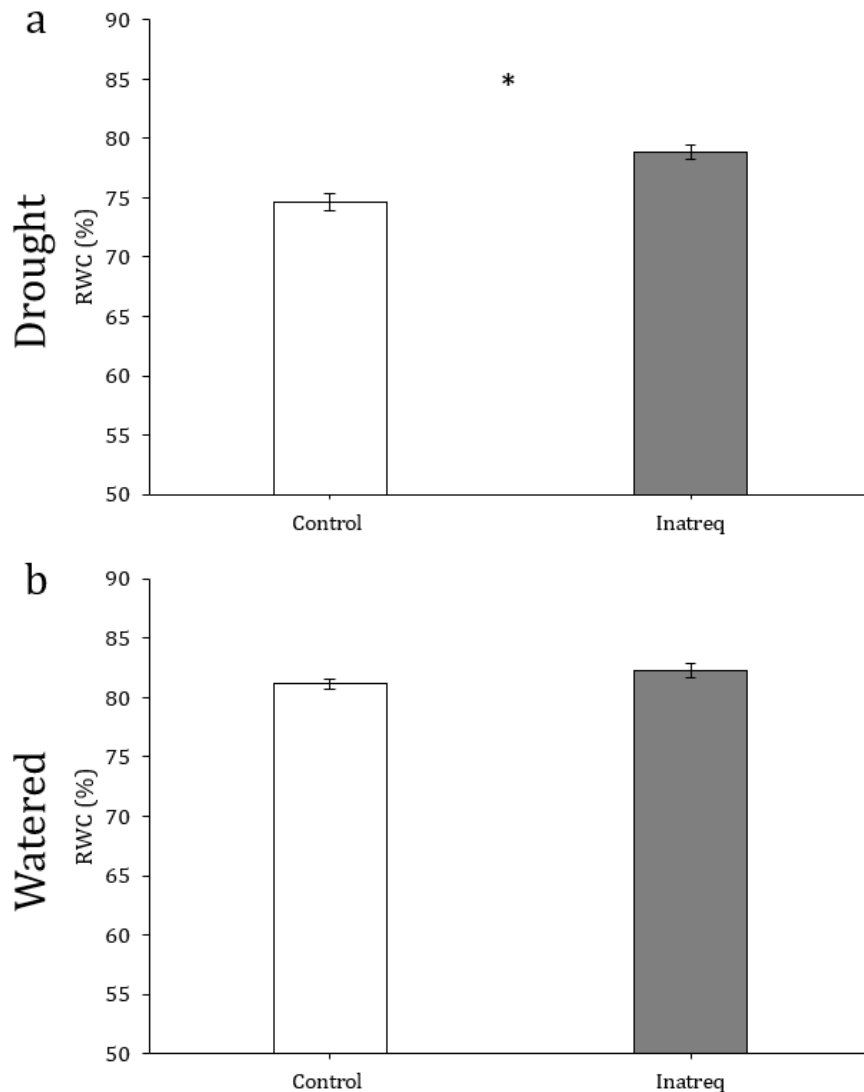


Figure 3.4: Mean relative water content (RWC) of mature wheat plants (var. Skyfall) treated with either Inatreq, or a control solution. The plants were grown under two different watering regimens, the drought condition where prior to the fungicide application watering was completely withheld (a), or the watered condition where regular watering to ensure the plants had a consistently high level of water availability throughout (b). $n = 30$, Error bars = \pm SE, * = $P < 0.05$.

3.3.3. Identifying if Inatreq reduces transpiration in a dose dependent manner.

There was no differential effect in the reduction of transpiration following the application of an increased dosage of Inatreq. Following fungicide application, there was no initial significant reduction in transpiration, however by the second day after fungicide application the transpiration of both dosages were significantly reduced when compared to the control plants, but there was no difference between the two dosages (Figure 3.5).

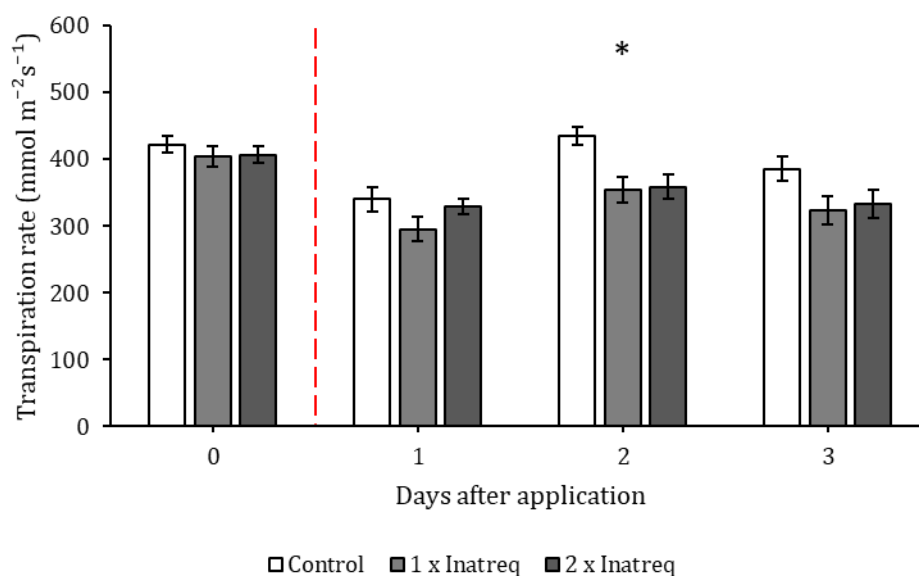


Figure 3.5: Dose response of transpiration rates of well-watered wheat plants (var. Skyfall) treated with either a control solution, 100 % field rate of Inatreq, or 200% field rate of Inatreq. Transpiration rates were observed prior to fungicide application, and subsequently each day for thereafter (red line represents fungicide application). $n=20$, error bars = \pm SE, * = $P<0.05$

3.4. Discussion

These results suggest that the application of Inatreq to both wheat varieties tested, Skyfall and Extase, resulted in significantly increased shoot and root dry weights (Figure 3.2). This increased accumulation of biomass is similar to that exhibited in previous observations of non-fungicidal effects of fungicides (Ajigboye *et al.*, 2017). The accumulation of increased biomass is also not dissimilar to the response following the application of various biostimulants (Calvo *et al.*, 2014), highlighting the similarity between this unintentional activity of certain fungicides and biostimulants. This finding also highlights that increased accumulation of biomass following the application of fungicides is not dependent upon similar chemical structures, as this response has been observed in a range of different classes, such as picolinamides, SDHIs (Ajigboye *et al.*,

2017), and DMIs (Lazo and Ascencio, 2014). This suggests that the compounds may be inducing a response from the target plants in multiple ways, rather than binding at a common binding site and initiating a specific pathway. Root development and growth is essential for plant development and plays roles in the retrieval and accumulation of water and nutrients, as well as interacting with microorganisms within the rhizosphere. Similarly, shoot growth is also vital for plant growth and development, acting as the site of photosynthesis among other biochemical processes.

Transpiration rates were measured in plants under two watering regimens: high water availability throughout, and reducing water availability, beginning prior to fungicide application. The aim of this study was to firstly identify if this trait occurred. Secondly, it aimed to identify whether plants that have naturally reduced transpiration rate, due to the reduced water available in the soil environment, had their transpiration rate reduction further accelerated. This is an important trait to observe, as plants utilise the regulation of their transpiration as a common water conservation strategy. The physiological observations revealed that the application of Inatreq reduced the rate of transpiration significantly in plants that were grown in ample water availability, as well in conditions where water was withheld prior to application. These reductions in transpiration do not appear to be the result of phytotoxicity, as the dry and fresh weights of both the droughted and watered plants that were treated with Inatreq were not reduced when compared to those treated with the control solution. Plants treated with Inatreq also had a significantly higher relative water content at the end of the experiment, suggesting they had improved water use efficiency and by reducing their rate of transpiration had conserved water for longer. The well-watered plants did not have significant differences in their RWC which may suggest that, despite the transpiration of the plants treated with Inatreq being significantly lowered for a time similar to those of the droughted plants, transpiration can be reduced to certain extent with no major detrimental effect on the RWC or dry weights, demonstrating that when plants are grown with ample water availability their transpiration is in excess of that required for effective gas exchange and photosynthesis. This supports previous observations that reductions in stomatal density of up to 50% have been reported to have no effect on yield, but have an intrinsic improvement in water use efficiency (Dunn *et al.*, 2019). Models have sought to identify the benefit that may be imparted by imposing a maximal transpiration rate, to identify future breeding traits, and found the imposition of a maximal transpiration rate can lead to an increased yield of 5 -7% across all conditions, but under dry yielding conditions this can increase further to 9 -13% (Sinclair *et al.*, 2005). The reduction of transpiration by means of partial closure of stomata is a quick and adaptive response to

variable drought, whereas a long-term mitigation strategy for drought is the reduction in stomatal density of the leaf (Buckley *et al.*, 2020). This reduction in transpiration following the application of a fungicides is a trait that has been previously observed in succinate dehydrogenase inhibitors (SDHIs) (Smith *et al.*, 2013; Kuznetsov *et al.*, 2018) and it was hypothesized that the response was due to SDHIs potentially interacting with the plant succinate dehydrogenase enzyme, due to high degree of homology in the structure of the SDH functional quinone-binding site across species (Maklashina and Cecchini, 2010). However, considering the findings in this chapter, this seems not to be the case as fenpicoxamid is a picolinamide, and targets the cytochrome *bc₁* complex at the Q_I site (Young *et al.*, 2018).

The reduction of transpiration rate observed after the application of Inatreq offers a potential solution to growers, or at least a stop-gap solution to an increasingly volatile climate. Genes that confer a reduced rate of transpiration have been highlighted as targets for breeding strategies (Yoo *et al.*, 2009) and therefore, if this trait may be imposed by a fungicide that would likely be applied regardless, it may offer growers a potential stop-gap solution until the breeding strategies begin to offer the long-term solution. Although reduction in transpiration following fungicide application appears to be transient (Figure 3.3), they are generally applied 1-3 times throughout a growing season: an early application, and more importantly once the flag leaf is unrolled. The health of the flag leaf has been highlighted as one of the most important factors influencing yield, and therefore disease control at this stage is vital (Pepler *et al.*, 2005). The additional improvement of the plants water use efficiency at this critical stage may also add a cumulative beneficial effect to ensure improved yields going forward. These biostimulant-like activities associated with the application of Inatreq also offer commercial benefits to the manufacturer. The fungicide market is a crowded sector, with several companies vying to produce the next widely adopted cereal fungicide. For Inatreq to offer beneficial effects that are unrelated to the fungicidal activity that it was designed for means that it offers further marketing opportunities, and a point of difference to the alternatives.

Chapter 4. High throughput glasshouse and field phenotyping.

4.1. Introduction and aims.

4.1.1. Introduction.

Controlled environment growth chambers offer researchers an opportunity to observe plant growth and physiology in an environment where they have control of extraneous variables, and conditions can be finely adjusted to experimental requirements. Growth chambers are also amenable to advanced phenotyping approaches due to the control of environmental variables and because they can easily house and facilitate sophisticated phenotyping tools. Many of these tools require defined environmental conditions, with minimal fluctuations, to give representative results across a set of plants, which may not be possible in more natural environments where conditions can be extremely variable. Controlled environment growth chambers also offer access to power sources and network access, which are increasingly necessary for many instruments. *Ex-situ* studies conducted in controlled environments can be used to identify a cause-and-effect relationship and are highly reproducible, detaching the observed phenotype from external influences. *In-situ* studies tend to be more descriptive, observing the phenotype whilst simultaneously contextualising them based upon the variable environmental conditions (Englund and Cooper, 2003; Irvine *et al.*, 2004).

Despite these benefits, most growth chambers are limited by their capability to house high sample numbers, particularly of larger plants such as cereals. Automated glasshouses allow for a greater sample size, but offer less fine control over environmental conditions than is possible in controlled environment growth rooms (although still more control than *in agri* (Limpens *et al.*, 2012)). Both glasshouses and growth chambers are ultimately limited in spatial scalability, and it is difficult to accurately generalise results from these studies to a field environment (Englund and Cooper, 2003). However, the environmental conditions inside glasshouses can reflect ambient environmental conditions, within a controllable range, utilising centrally controlled supplementary heating and lighting. Glasshouses, as with controlled environment growth rooms, can have tightly regulated watering and feeding regimes, and sufficient access to facilities such as network connections and mains power. With the increased capacity of glasshouses compared to growth rooms, they are popular housings for large scale, high throughput phenotyping systems (Jansen *et al.*, 2009; Golzarian *et al.*, 2011; Honsdorf *et al.*, 2014; Pavicic *et al.*, 2017; Roupael *et al.*, 2018).

Large-scale, high throughput (HTP) phenotyping generally tends to be image-based, using non-invasive techniques to quantify morphological and physiological traits. Such automated HTP systems circumvent the perceived phenotyping bottleneck due to lack of

replicate numbers as a result of labour and time costs associated with large scale phenotyping (Furbank and Tester, 2011). The adoption of image analysis also opens the potential to use a wide variety of imaging sensors, to not only measure physical traits, but also physiological characteristics. Due to the increased capacity for sample numbers, automated systems are often paired with software to analyse the images and extract a wide array of morphological, and physiological data sets from the captured images. The sensors that can be used to capture these images may include RGB cameras, (Rajendran *et al.*, 2009; Campbell *et al.*, 2015), thermal sensors (Merlot *et al.*, 2002; Sirault *et al.*, 2009; Munns *et al.*, 2010), and fluorescence imaging systems (Jansen *et al.*, 2009). The nature of image based analysis means that these systems are non-invasive, and individual plants may be extensively studied throughout their lifecycle without any damage, allowing for measurements, such as predictions of biomass to be used to generate growth rates, as well as understanding responses to a particular stimuli on a temporal scale (Jansen *et al.*, 2009; Berger *et al.*, 2010a; Campbell *et al.*, 2015; Sun *et al.*, 2019).

The final level of scalability of plant phenotyping is in the field. Experimental field sites have the highest capacity for samples and are capable of practically unlimited sample sizes. But, to preface this, they also have the lowest level of control over extraneous variables. *In-situ* field trials offer researchers the opportunity to observe plants in an agricultural setting and results are therefore more translatable to “real world” scenarios. As field trials are highly influenced by variable environmental conditions, studies need to be carefully considered in the context of the conditions the experiment was conducted in. Therefore, many field trials need to be repeated across multiple years and field sites to accommodate for varying environmental conditions before they can be truly generalised. Due to this, field trials are often less common due to their time consuming and unreliable nature, as well as associated costs. Academic research is often structured in a way that research is undertaken in cycles of 3- to 4-year projects, making multi-year, multi-site experiments challenging. Field trials are also often in remote locations, where access to power and network connection may not always be possible, limiting the phenotyping tools that may be used.

Of the environmental stresses that may impact crop productivity, drought is regarded as the most devastating (Aroca, 2013), as discussed in Chapters 1 and 3. Owing to the clear visual consequences of drought such as stunted growth, leaf rolling and wilting, it is amenable to image based HTP plant phenotyping. When plants are grown in conditions of drought, one of the main responses is for plants to reduce their stomatal conductance as a water preservation strategy. Stomatal conductance can be reduced by as much as

50% with no discernible detrimental effect on yield (Dunn *et al.*, 2019). However, sustained and severe reduction of stomatal conductance can not only reduce the rate of transpiration but also reduce the rate of gas exchange and consequently the absorption of CO₂. Due to the reduced CO₂ availability, photosynthesis is reduced and light energy then becomes in excess of what is required, and can lead to photodamage of the plants photosystem II (PSII) (Baker, 2004; Reddy *et al.*, 2004). Under normal conditions, where water is not limiting, light is absorbed by the light-harvesting antenna (LHA) of PSII, which initiates light reactions where the light energy is then converted into ATP and NADPH (Ashraf and Harris, 2013). To prevent this photodamage plants have evolved a variety of strategies to mitigate this, known as non-photochemical quenching (NPQ) (Müller *et al.*, 2001). When light is in excess of what is required, LHAs dissipate the absorbed light energy as heat, rather than initiating the production of ATP and NADPH (Ajigboye *et al.*, 2017). This is not the only strategy plants utilize to prevent photodamage during water stress, however, this dissipation of light energy as heat can be used to measure the degree of NPQ, and therefore be used to compare how plants tolerate stress. This is measured as chlorophyll fluorescence and represents the number of closed or damaged PSII reaction centres (Ruban *et al.*, 2012), with the low fluorescence suggesting that absorbed light energy is being either used or dissipated, whilst high fluorescence suggesting severe damage (Maxwell *et al.*, 2000).

It has been observed that particular fungicides have been shown to significantly improve photosynthetic efficiency (Fv/Fm) when the plants are grown under drought stress (Berdugo *et al.*, 2013; Ajigboye *et al.*, 2014a, 2017), and therefore may help plants mitigate the stress of drought.

4.1.2. Aims.

The work described in this chapter builds upon the findings in Chapter 3 and aims to better characterize the physiological and morphological effects of Inatreq, and how these may subsequently affect plants grown in varying levels of water availability. This utilised high-capacity studies in an automated glasshouse and field trial, to observe greater populations of plants than would be possible in a controlled growth room with traditional methods. Reduction of stomatal conductance, as reported in Chapter 3, has commonly been acknowledged as a drought mitigation strategy, increasing hydraulic resistance, and therefore reducing evapotranspiration. It is hypothesized that if Inatreq was to initiate this response before an enforced drought, treated plants may be better prepared and therefore be less affected by low water availability. It is important that findings derived from the studies in highly artificial settings are repeated in settings that are more

generalizable to natural conditions. Glasshouse trials offer a step towards a more natural setting, experiencing ambient conditions reflecting the outside, whilst offering the facilities to utilize highly sophisticated equipment on larger sample sizes. Field trials further increase the scalability of experiments, with almost unlimited sample sizes, but have very limited control of environmental conditions.

A large-scale glasshouse trial was conducted in collaboration with the National Plant Phenotyping Infrastructure (NaPPI) group at the University of Helsinki (<https://www.helsinki.fi/en/infrastructures/national-plant-phenotyping>). The “Large Plant” system is an automated HTP plant phenotyping platform, utilizing conveyor belts to transport plants between watering stations, as well as imaging stations where RGB and chlorophyll fluorescence images are recorded. The automated watering system allows individual plants to have bespoke watering regimens, enabling the imitation of varying water levels across the experiment. In this experiment, Inatreq was observed in two forms, as a whole product (as it has been observed in previous chapters), and the product without the active ingredient fenpicoxamid. This was to identify if the observed phenotype following the application of the fungicide was a result of the active ingredient itself, or the adjuvants also included in the product.

A field trial was conducted at the Corteva Agrisciences Wellesbourne field station, utilizing their automated rain-out shelter trial site. This facility enables the user to conduct a normal field trial, whilst offering partial control over the level of rainfall the trial receives. The field trial is vital in transitioning findings from the lab to the field. This trial was designed to characterize Inatreq in a field setting and compare it against a panel of other fungicides from a variety of different classes with differing modes of actions. This panel included fungicides with active ingredients that have previously been observed to have beneficial effects on wheat in the absence of disease. Physical and physiological observations were recorded throughout this trial, prior to and following the fungicide application. The automated rain out shelter was utilized to reduce rainfall.

4.2. Methods.

4.2.1. High-throughput glasshouse phenotyping.

Wheat varieties and growth conditions.

Two commercial wheat (*Triticum aestivum*) varieties were observed in this experiment, Skyfall (RGT-Seeds), and KWS Extase (KWS). Seeds were first germinated for two weeks in a cell tray containing Kekkilä mix W (Vantaa, Finland), composed of light peat and sand,

in March 2020 at the NaPPI ViGOR glasshouses. The ViGOR glasshouse day/night temperature and humidity conditions were controlled by a central control unit (Priva, De Lier, Netherlands) to approximately 21 °C/15 °C with a day length of 16 h. High-pressure sodium lamps (OSRAM 200 GmbH, Munchen, Germany) were used for any additional light requirements. Once the seedlings had germinated for two weeks the cell tray was moved to a cold room where temperatures were maintained at 4-6 °C and day length set to 8 h. They were kept under these conditions for 7 weeks to allow the seedlings to vernalise before transplantation from the cell tray into 3 litre rose pots (Sparco, 190 Conde-sur-Huisne, France) containing Kekkilä mix W (Vantaa, Finland) containing light peat and sand. The soil was fertilized with Yara Mila Y2 grains by mixing in the topsoil.

Large plant image-based phenotyping platform at the University of Helsinki.

The PlantScreen™ Modular System is installed within a plexiglass glasshouse with regulated temperatures and daylength. This system is made up of two robotic-assisted units for RGB and chlorophyll fluorescence imaging, as well as an automatic plant height measuring light curtain, an acclimation tunnel, and a weighing and watering unit. The plants are kept on individual transport disks and are moved between the individual imaging and handling stations by a conveyor belt. Chlorophyll fluorescence was measured using an enhanced version of the FluorCam FC-800MF pulse amplitude modulated (PAM) chlorophyll fluorometer (PSI, Czech Republic), with a top-down imaging view of 800 x 800 mm. The RGB imaging unit is an isolated box featuring a turntable with precision angled positioning, two RGB cameras capturing top-down and side-on images. Both camera orientations also featured supplementary LED lighting sources mounted on robotic arms to ensure each image was illuminated homogeneously. The imaging area in the top-down orientation was 800 x 800 mm, whilst the side-on orientation view area was 1205 x 1005 mm (height x width). Side view images were acquired from three separate angles. All RGB images were acquired using a GigE uEye UI-5580SE-C-5 Megapixels QSXGA Camera with ½" CMOS Sensor (IDS, Germany), with a resolution of 2560 x 1920 pixels for the top-down images, and a side on view with a resolution of 2560 x 2956 pixels. All lighting conditions, positions, and camera settings were maintained throughout the experiment.

Fungicide applications.

Plants were grown to growth stage 33 (BBCH), where they were then treated with their respective fungicide. The different treatments are listed in Table 4.1. All treatments were mixed in the equivalent of 200 L/ha of water, and were applied individually using a hand-held, calibrated sprayer. One of the formulations applied was the adjuvants that

accompany fenpicoxamid in Inatreq active and was observed to identify if the effects associated with Inatreq were due to the active ingredient fenpicoxamid or the accompanying adjuvant. This treatment was referred to as “blank”.

Table 4.1: Fungicide treatments for image-based phenotyping of the effects of fungicide application under varying water availability. Inatreq provided by Corteva Agriscience, Inatreq blank provided by Corteva Agriscience and Revystar ® XE provided by BASF.

Fungicide	Active ingredient	Application rate (L/ha)	Active ingredient per hectare (gai/ha)
Inatreq active	50 gai/L Fenpicoxamid	2	100
Revystar ® XE	47.5 gai/L Fluxapyroxad	1.5	71.25
	100 gai/L Mefentrifluconazole		150
Blank (Inatreq active adjuvant formulation)	N/A	2	N/A
Water (control)	N/A	2	N/A

Initiation and maintenance of variable water availability.

Two days before the fungicide application, plants began their individual watering regimens. Plants were divided into three separate regimens, representing: high, medium, or low water availability. Water availabilities were calculated as a proportion of the maximal field capacity (FC) of each pot of compost, with high medium and low representing 75%, 50% and 25% of the maximal FC, respectively. Maximal field capacity was calculated by recording the maximum water capacity a pot filled with compost could hold, compared to a completely dry pot. Once calculated for each of the pots, the automated watering system would weigh each pot and adjust the water provided accordingly throughout the experiment. Plants reached their respective water availability levels the day after fungicide application and were then maintained henceforth. Table 4.2 details the replicate number for each watering level as well as fungicide treatment.

Table 4.2: Experimental conditions and respective replicate numbers in HTP glasshouse trial

Extase	Water availability		
	High	Medium	Low
Inatreq	10	10	10
Inatreq Blank	10	10	10
Control	10	10	10
Skyfall	High	Medium	Low
Inatreq	10	10	10
Inatreq Blank	10	10	10
Control	10	10	10
Revystar	10	10	10

Table 4.3: Workflow of HTP glasshouse trial conducted at the NaPPI facility, part of The University of Helsinki.

Date	Timepoint	Event
05/05/2020		Seeds are sown
20/05/2020		Seedlings begin vernalising
01/07/2020		Plants removed from the cold room and transplanted to pots in the glasshouse
08/07/2020	1	RGB imaging
13/07/2020	2	RGB imaging
16/07/2020	3	RGB imaging
20/07/2020	4	RGB imaging
23/07/2020	5	RGB imaging
27/07/2020	6	RGB imaging
29/07/2020		Watering adjusted
30/07/2020	7	RGB imaging
31/07/2020		Fungicide application
01/08/2020		Differential water levels reached
03/08/2020	8	RGB imaging
06/08/2020	9	RGB imaging
13/08/2020	10	RGB imaging
14/08/2020		Fluorcam measurement
16/08/2020	11	RGB imaging

RGB imaging and processing.

Plants were periodically transported to the imaging cabinet of the PlantScreen™ system (see Table 4.3 for imaging dates), where plants were imaged by three RGB cameras positioned in three predefined orientations (two side on, one top down). To extract phenotypic data from the RGB images, the PlantScreen™ software first conducted basic processing of the images, correcting for fisheye distortion, cropping the region of interest in each image, removing the background as well as the filtration and removal of visible artefacts from images. Once the plants had undergone basic processing, the RGB images were converted to binary images before phenotypic data was extracted from them.

Observation of morphological parameters

To observe how the application of Inatreq may influence the growth of two wheat varieties, under varying water availability levels, plant height and the projected shoot area (PSA) were extracted from the calibrated images. PSA was estimated as the sum of the total plant area in three RGB images taken from different angles (2 side-on, 1 top-down), and has been found to be a reliable proxy for plant biomass (Berger *et al.*, 2010b; Campbell *et al.*, 2015). Plants were imaged and processed throughout the course of the experiment (Awlia *et al.*, 2016) (see Table 4.3. for imaging dates), comparing between both fungicide application and water availability. For each condition 10 plants were compared. The influence of fungicide application on plant growth parameters was compared using a one-way analysis of variance (ANOVA), and Tukey's *post-hoc* test of significance for each trait at each timepoint ($P < 0.05$) in the statistical analysis package SPSS 26 (IBM Corp).

Kinetic Chlorophyll Fluorescence Imaging and Processing.

To observe the effect of limited water availability, and the influence of different fungicides, chlorophyll fluorescence measurements were taken using a FluorCam FC-800MF system (PSI, Czech Republic). Plants were dark adapted for 30 minutes before passing through a whole plant measurement chamber equipped with a high sensitivity charge-coupled device (CCD) camera fitted with a Lensagon CY0314 lens. The camera captured images at a resolution of 720 x 560 pixels, a frame rate of 50 fps and a 12-bit depth. Light-emitting diodes (LEDs) surrounding the camera provided specific-wavelengths for pulse-amplitude modulated (PAM) short-duration measuring flashes (620 nm) and two treatments of photosynthetic photon flux density (PPFD); red orange (620 nm, max. PPFD of 289 $\mu\text{mol m}^{-2}\text{s}^{-1}$) and cool-white (480 – 720 nm, max. PPFD of 446 $\mu\text{mol m}^{-2}\text{s}^{-1}$).

After dark adaption, photochemical efficiency of PSII was calculated. To do this the standard Fv/Fm protocol associated with the FluorCam 7 software was run (see Appendix 2 for the protocol file). In brief, the weak measuring light ($\sim 0.09 \mu\text{mol m}^{-2}\text{s}^{-1}$) provides a measure of minimum fluorescence (Fo), which is then followed by a saturating pulse of $1312 \mu\text{mol m}^{-2}\text{s}^{-1}$ for 800 ms providing a measurement of maximum fluorescence (Fm). Variable fluorescence (Fv) is calculated as Fm - Fo (Baker, 2008). Once Fo was calculated, it was then possible to calculate the photochemical efficiency of PSII by calculating Fv/Fm.

To better calculate the maximum quantum efficiency of PSII, the images that were captured underwent post-hoc processing, with the green shoot area segmented from the main image using FluorCam 7.0 software (PSI, Czech Republic) by selecting the whole pixel range captured by the camera. The numeric average of this area was automatically calculated. Ten individual plants were imaged for each treatment. Plants from the highest and lowest water availability were compared 14 days after the initiation of the differential watering, when the differences in water availability were at their most severe. The influence of fungicide application on chlorophyll fluorescence was compared using a one-way analysis of variance (ANOVA), and then Tukey's *post-hoc* test of significance ($p < 0.05$) in the statistical analysis package SPSS 26 (IBM Corp).

4.2.2. Field trial.

Experimental Design.

To investigate the influence of Inatreq application on wheat drought tolerance and the onset of senescence, field trials were conducted in 2020 at the Corteva Agriscience field station, on the University of Warwick's Wellesbourne campus ($52^{\circ}12'24.4''\text{N}$ $1^{\circ}36'14.2''\text{W}$, an altitude of 46 m above sea level). Figures 4.1&2 show the weather data throughout the experimental period. This experiment utilised two rain-out shelters, which were activated to cover the experimental plots when they experienced rain, therefore enforcing a water limitation. In this study, the spring wheat variety Tybalt (Limagrain UK) was used due to adverse wet conditions preventing the sowing of winter wheat varieties in September 2019. Four replicate blocks were each divided into 12 microplots 1m x 2m in size (Figure 4.3), with approximately 250-300 plants per m^2 . The plots were treated with fungicides at growth stage 43 (BBCH), with a panel of 10 fungicide treatments and an untreated control. Each of the fungicide treatments and their respective producers are listed in Table 4.5 and 4.6.

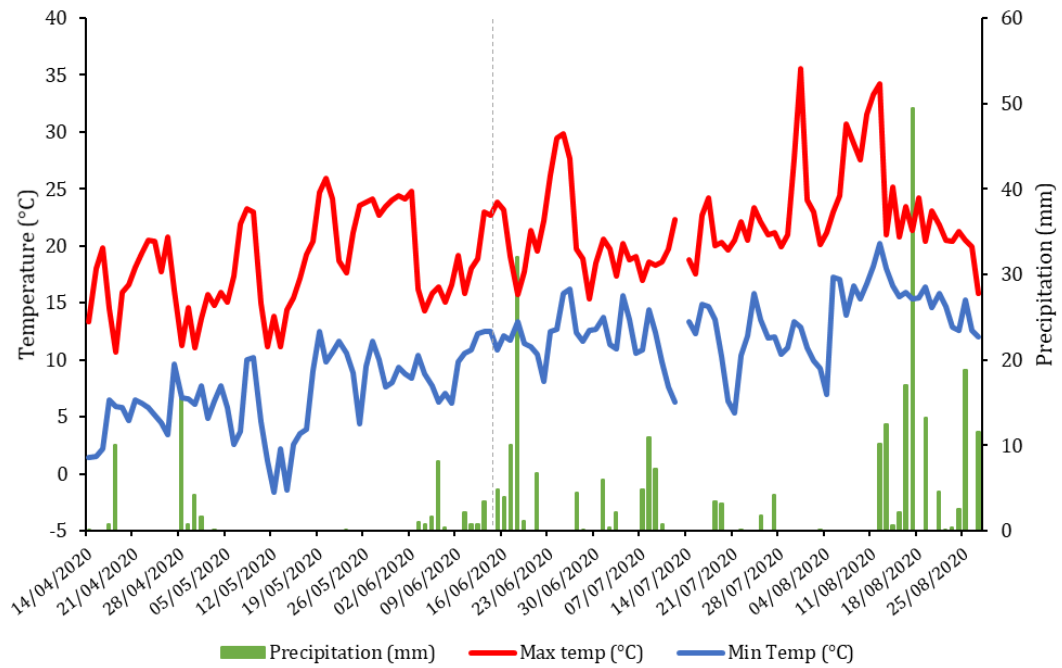


Figure 4.1: Weather data at Wellesbourne field trial site. Data collected daily over the course of the trial. Grey line represents fungicide application date (15/06/2020)

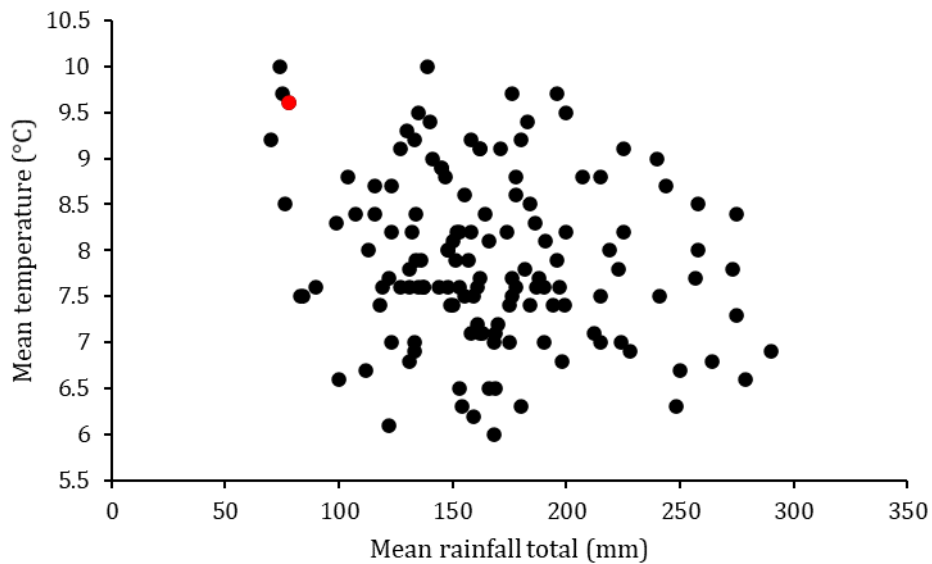


Figure 4.2: Annual spring rainfall and temperatures in the west-midlands, from 1862-2020. Red dot represents 2020 data. (Source: Met Office 'UK and Regional series' weather data).

Plot no. Treatment no.	107 7	108 8	109 9	110 10	111 11	112 12	Buffer	Plot no. Treatment no.	307 9	308 3	309 12	310 2	311 7	312 10	Buffer
Plot no. Treatment no.	101 1	102 2	103 3	104 4	105 5	106 6	Buffer	Plot no. Treatment no.	301 5	302 1	303 6	304 11	305 4	306 8	Buffer
Plot no. Treatment no.	207 7	208 6	209 11	210 12	211 10	212 1	Buffer	Plot no. Treatment no.	407 2	408 11	409 4	410 6	411 5	412 8	Buffer
Plot no. Treatment no.	201 2	202 9	203 3	204 5	205 8	206 4	Buffer	Plot no. Treatment no.	401 3	402 9	403 1	404 10	405 7	406 12	Buffer

Figure 4.3: Experimental design of field trials at the Wellesbourne field station 2020. 4 blocks, 12 treatments (listed in Table 4.5)

Table 4.4: Workflow of field experiment conducted at the Wellesbourne field station.

Date	Event	Product	Dose
14/04/2020	Drilling wheat cultivar Tybalt	N/A	300 kg/ha
16/04/2020	Herbicide application	Stomp	1.5 L/ha
28/04/2020	Fertiliser application	Aqua	1.5 L/ha
28/04/2020	Fertiliser application	Phosphorus	60 kg/ha
28/04/2020	Fertiliser application	Potassium	100 kg/ha
29/04/2020	Fertiliser application	Nitrogen	70 kg/ha
29/04/2020	Fertiliser application	Sulphur	31 kg/ha
29/04/2020	Fertiliser application	Nitrogen	65 kg/ha
29/05/2020	Herbicide application	Ally Max	35 g/ha
29/05/2020	Herbicide application	Pixxaro	0.5 L/ha
15/06/2020	Pre-treatment observations	-	-
15/06/2020	Fungicide applications	-	-
22/06/2020	Observations	-	-
29/06/2020	Observations	-	-
06/07/2020	Observations	-	-
13/07/2020	Observations	-	-
20/07/2020	Observations	-	-
27/08/2020	Harvest samples	-	-

Fungicide treatments.

In total 11 different fungicide treatments were applied with one non-sprayed control group. Each treatment is listed in Table 4.5 noting their active ingredient (a.i), and their respective contents and application rate. Table 4.6 lists the commercial names of each of the fungicides in Table 4.5. All fungicides were applied at a water volume equivalent to 175 L/ha, using a pressurized backpack sprayer with a 1 m boom and adjustable spray. All applications were made using size 3 Hypro® Guardian AIR™ nozzles. Fungicides were applied prior to the ear emergence at BBCH growth stage: 45-47.

Table 4.5: Panel of fungicides applied as part of the field trial at Wellesbourne field station, with respective application rates, and active ingredient content.

Treatment number	Active ingredient(s)	Application rate (% recommended dose)	dose Active ingredient applied
1	Fenpicoxamid	75%	75 g ai/ha
2	Fenpicoxamid	100%	100 g ai/ha
3	Fenpicoxamid + Prothioconazole	75%	
4	Fenpicoxamid + Prothioconazole	100%	50 + 175 g ai/ha
5	Prothioconazole	75%	150 g ai/ha
6	Prothioconazole	100%	200 g ai/ha
7	Benzovindiflupyr	75%	56.2 g ai/ha
8	Benzovindiflupyr	100%	75 g ai/ha
9	Mefentrifluconazole	75%	191.85 g ai/ha
10	Mefentrifluconazole	100%	145.5 g ai/ha
11	N/A	100%	50 g ai/ha
12	Untreated	N/A	-

Table 4.6: Commercial fungicide details, including active ingredient class, product name, and producer.

Treatment number	Active ingredient	Fungicide class	Fungicide name	Producer
1,2	Fenpicoxamid	Picolinamides	Inatreq™ active	Corteva Agriscience UK
3,4	Fenpicoxamid + Prothioconazole	Picolinamides Triazoles	Inatreq™ active	Corteva Agriscience UK
5,6	Prothioconazole	Triazole	Proline 250	Bayer Crop Science UK
7,8	Benzovindiflupyr	SDHI	Elatus™ Plus	Syngenta
9,10	Mefentrifluconazole	Triazole	Myresa	BASF

Data collection.

Data was collected immediately prior to fungicide application, and then every 7 days for the following 5 weeks.

Normalized difference vegetation index (NDVI) was measured using a handheld Trimble GreenSeeker® (Trimble Navigation Limited, Sunnyvale, CA, USA) optical sensor. These were collected by walking around trial plots whilst holding the GreenSeeker® approximately 80 cm over the crop. Two measurements were collected per plot and averaged across the study.

Relative water content data was only collected from plots where fungicides were applied at 100% field application rate. Two leaves were selected from each plot, and immediately placed inside a pre-weighed plastic bag and sealed. Selected samples were representative leaves from each plot, that were mature and fully unrolled when excised. Care was taken to ensure the leaf samples were placed within these bags as quickly as possible, to prevent any added losses due to evaporation/transpiration. These samples were then weighed to obtain their fresh weight (FW). The turgid weight (TW) was then obtained by submerging these leaf samples in water overnight, before blotting dry and re-weighing. Finally, the dry weight (DW) was then calculated by placing the leaf samples in a 50 °C oven for 3 days and recording the weight. Using these measurements, it was then possible to calculate the relative water content, using Equation 1 (Section 3.2.2).

To investigate the influence different fungicides, have upon the chlorophyll fluorescence of wheat grown in the field, a handheld FluorPen FP110 (Photon Systems Instruments, PSI, Czech Republic) was used to calculate photosystem II quantum yield (QY max). In this study, plants were light adapted and therefore QY represents F_v'/F_m' . For this, two measurements were taken per plot, and care was taken to select the youngest, fully unrolled leaves that were representative of the plants in the plot, clipping the Fluorpen on the middle section of the leaf, avoiding any large veins.

When plants had reached growth stage 99 two 50 cm² squares were randomly dropped in each plot and harvested. The ears were then counted, and the number was extrapolated to estimate the total ear number per plot. Following this the samples were threshed, and weighed, before extrapolating the total grain yield per plot. Subsets of these samples were taken to calculate thousand grain weight.

Statistical analysis.

Data was analysed using the statistical analysis package SPSS 26 (IBM Corp). The data was examined to observe its analysis of variance (ANOVA) as well as calculating the standard error of means (SE). Tukey's post-hoc test was used to compare means and separate subgroups at a 95% confidence limits.

54.3. Results.

4.3.1. High-throughput glasshouse phenotyping.

The effects of drought on wheat growth parameters

Drought had a significant influence on the growth parameters of both varieties of wheat observed in this experiment (Figures. 4.4, 4.5). When grown under equal watering conditions both varieties exhibited consistent growth, with the PSA of all treatment groups comparable. However, upon the onset of differential watering conditions, plants grown under "low water availability" had significant impairment of their growth rate and therefore PSA no longer increased at the same rate as the plants grown under the medium and high-water availabilities. For Extase, both PSA and height were significantly lower in the low water availability condition, when compared to the medium and high-water availabilities, by the first timepoint (5 days), whereas for Skyfall the PSA was significantly different but the height only became significantly different at the second time point after initiating differential watering conditions (8 days). Plants grown under all three watering conditions became significantly different from each other, in both varieties, by the third timepoint (15 days) after the initiation of differential watering. Although low water availability was the only watering condition that reduced height significantly in both varieties (Fig. 4.5). Extase and Skyfall exhibited slightly different responses to the onset of limited water availability. Extase exhibited a reduced PSA at timepoint 8 compared to 7 following the onset of water limitation (Figure 4.4a), whereas although Skyfall's growth rate did reduce when compared to the medium and high-water availability, the PSA did still increase between timepoint 7 and 8 (Figure 4.4b).

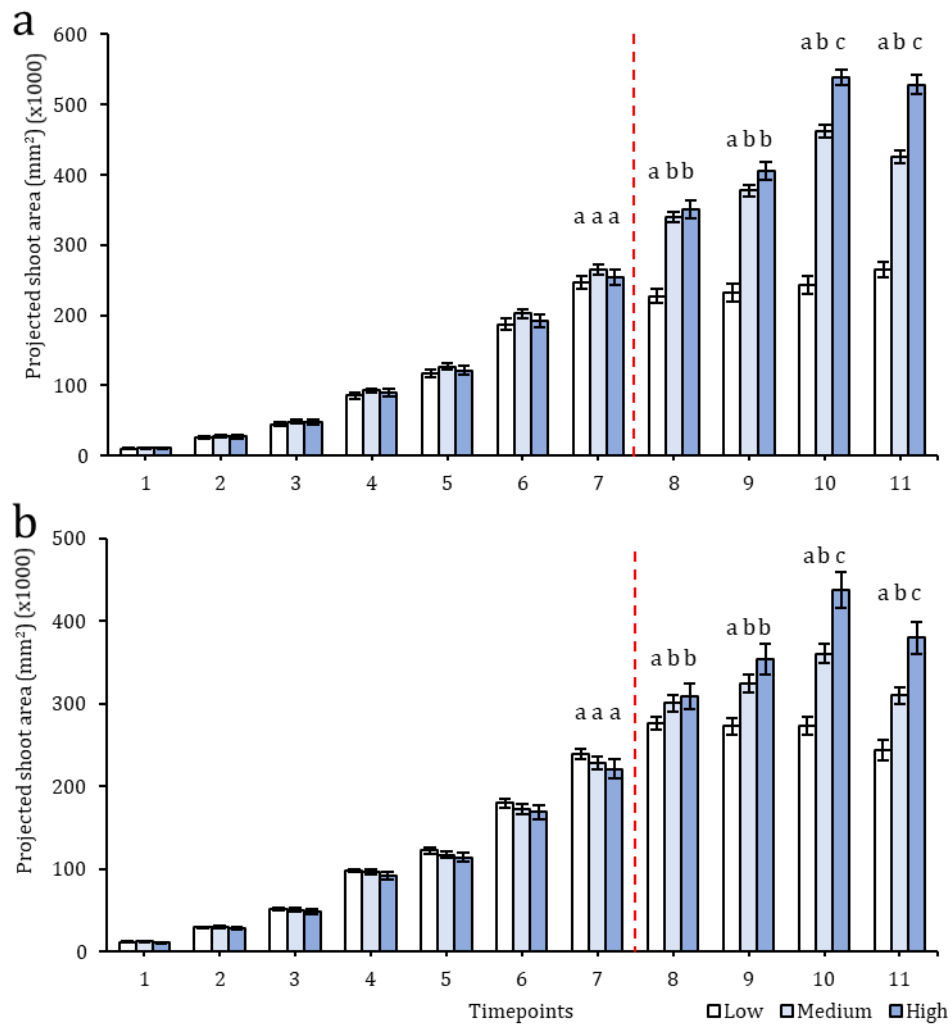


Figure 4.4: Comparison of untreated wheat PSA. Plants were grown until GS 33 (BBCH) with high water availability, before initiating differential watering to achieve three levels of water availabilities: low, medium, and high. This was observed in two different varieties: a) Extase and b) Skyfall. Initiation of differential watering represented by dashed red line (---). $n = 10$, error bars = \pm SE, a,b and c represent significant subsets ($P < 0.05$).

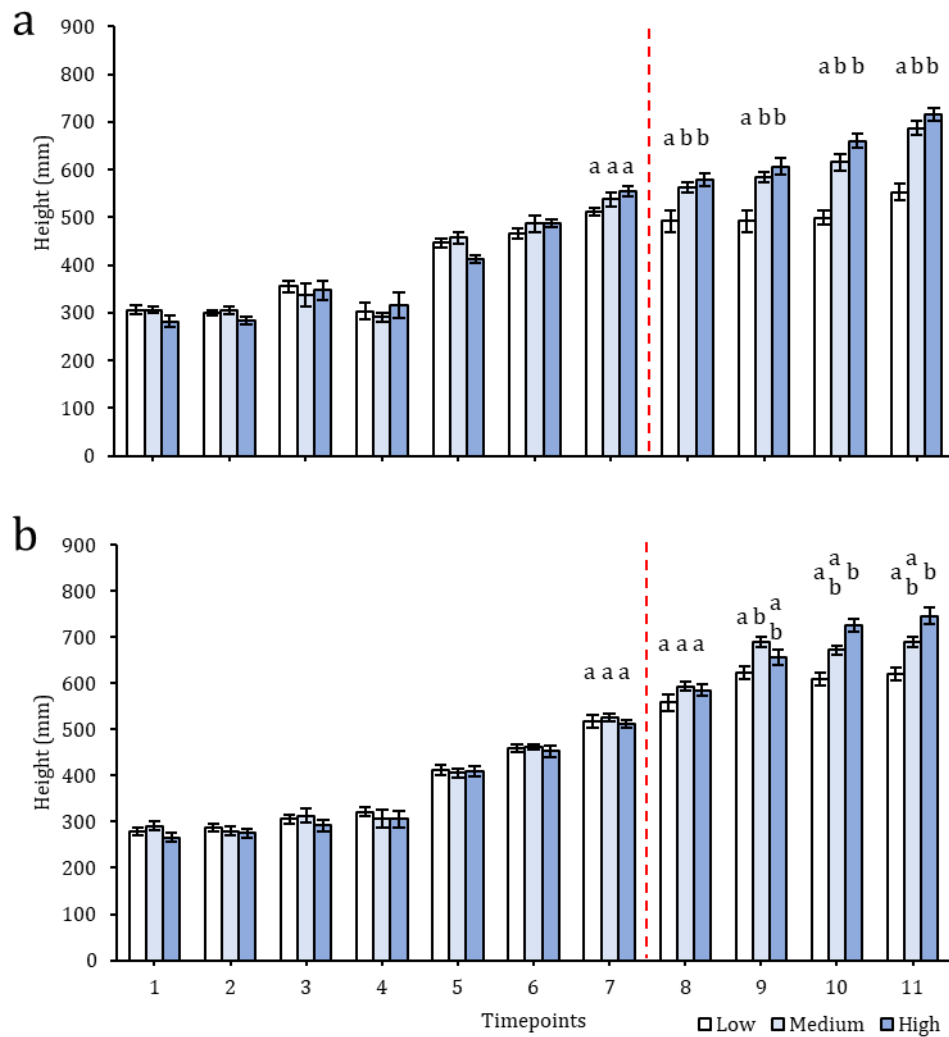


Figure 4.5: Comparison of untreated wheat height. Plants were grown until GS 33 (BBCH) with high water availability, before then initiating differential watering to achieve three levels of water availabilities: low, medium, and high. This was observed in two different varieties: a) Extase and b) Skyfall. Initiation of differential watering represented by dashed red line (---). $n = 10$, error bars = \pm SE, a, b, and c represent significant subsets ($P < 0.05$).

The effects of fungicides on growth parameters of wheat under differential water availabilities.

For Extase plants grown under low water availability, the application of Inatreq resulted in a significantly higher PSA, compared to plants treated with the control solution (Figure 4.6a). This increase in PSA was consistent over three imaging time points (15 days). At the final imaging point, the plants treated with Inatreq still had an increased PSA, however the difference was no longer significant. The plants treated with the blank solution grown in low water availability followed a similar trend to that of the Inatreq application,

however the PSA was not significantly higher than the control plant, or significantly lower than the plants treated with Inatreq.

When the plants were maintained under high and medium water availability the fungicide application had no impact on measured PSA (Figure 4.6b&c), and all groups increased at consistent rates to the other groups at their respective water availability. The differences in PSA were illustrated by the representative images in Figure 4.7.

Despite the differences exhibited in PSA due to following fungicide application under low watering conditions, height appeared to only be influenced by the water availability, and Inatreq and blank application appeared to have no discernible effect (Figure 4.9).

In contrast to the results seen in Extase plants, Skyfall plants did not show any differential response to drought depending upon the fungicide application (Figure 4.8&10). The PSA and height of all fungicide groups responded to their respective water availability at a similar rate, including an added fungicide with a differing mode of action, Revystar. As with Extase, drought-dependent height also did not appear to be influenced by their respective fungicide application (Figure 4.11).

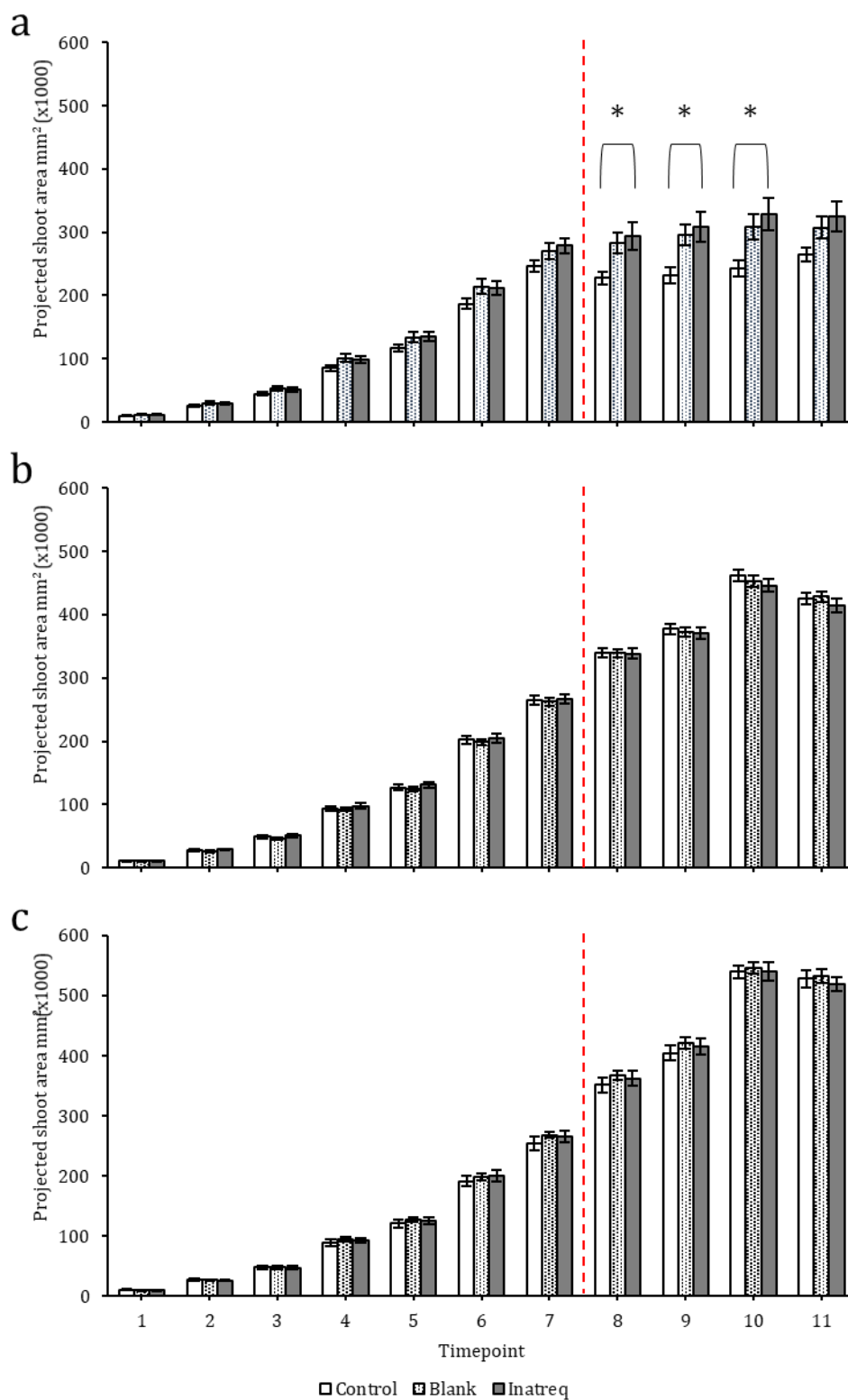


Figure 4.6: Projected shoot area (PSA) measurements in wheat variety Extase, treated with either: a) water control spray, blank solution or Inatreq. a) Plants grown under low water availability, b) plants grown under medium water availability, c) plants grown under high water availability. Spray date and drought initiation represented by dashed red line (---), $*=P < 0.05$, error bars = \pm SE, $n=10$.

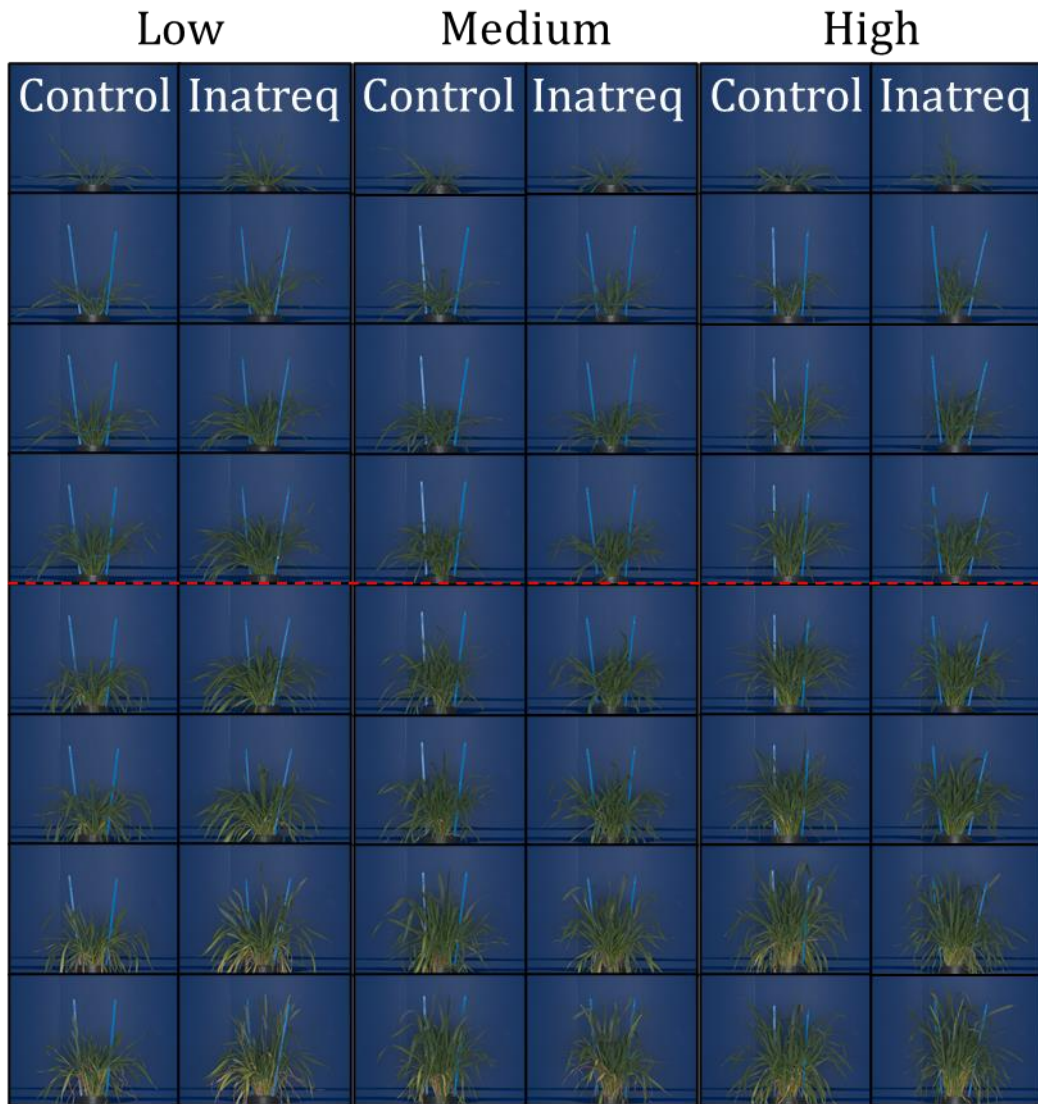


Figure 4.7: Raw images of wheat variety Extase, throughout growing season. Treated with the control solution or Inatreq, and grown under either low, medium, or high-water availability conditions. Spray date and drought initiation represented by dashed red line (---).

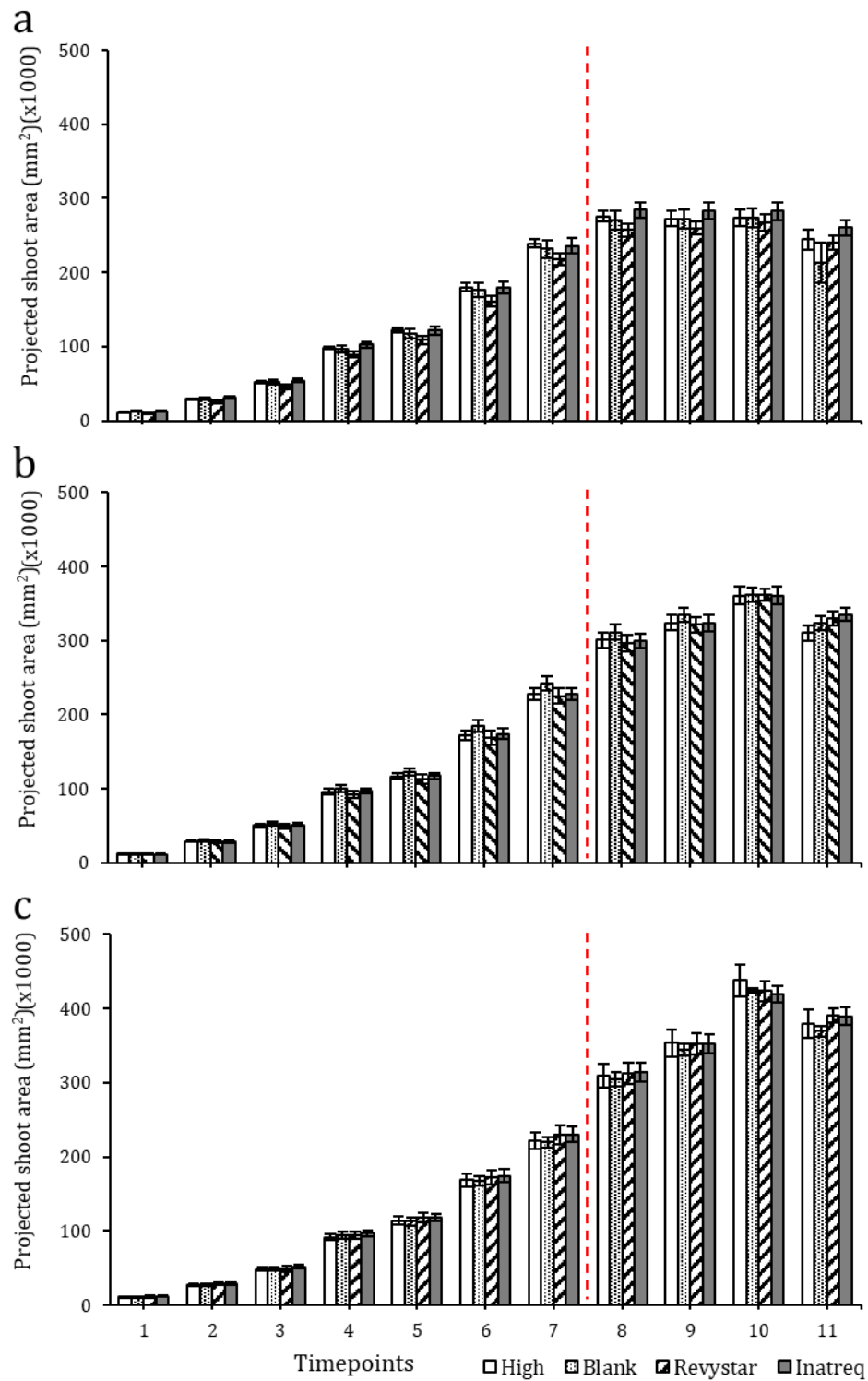


Figure 4.8: Projected shoot area (PSA) measurements in wheat variety Skyfall, treated with either: a) water control spray, blank solution, Revystar or Inatreq. a) Plants grown under low water availability, b) plants grown under medium water availability, c) plants grown under high water availability. Spray date and drought initiation represented by dashed red line (---), Error bars = \pm SE, $n=10$.

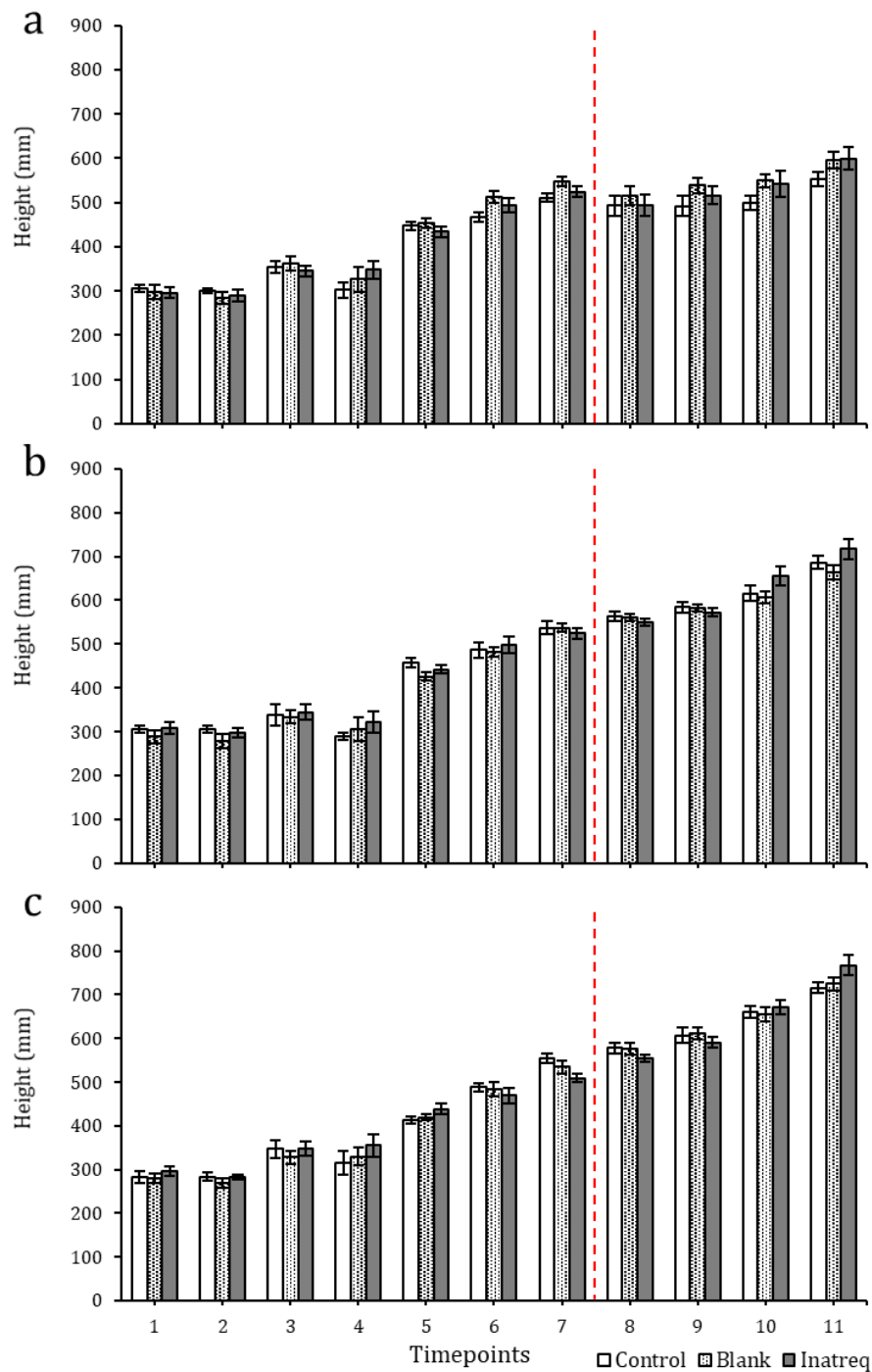


Figure 4.9: Height measurements in wheat variety Extase, treated with either: a water control spray, blank solution, or Inatreq. a) Plants grown under low water availability, b) plants grown under medium water availability, c) plants grown under high water availability. Spray date and drought initiation represented by dashed red line (---), error bars = \pm SE, $n=10$.

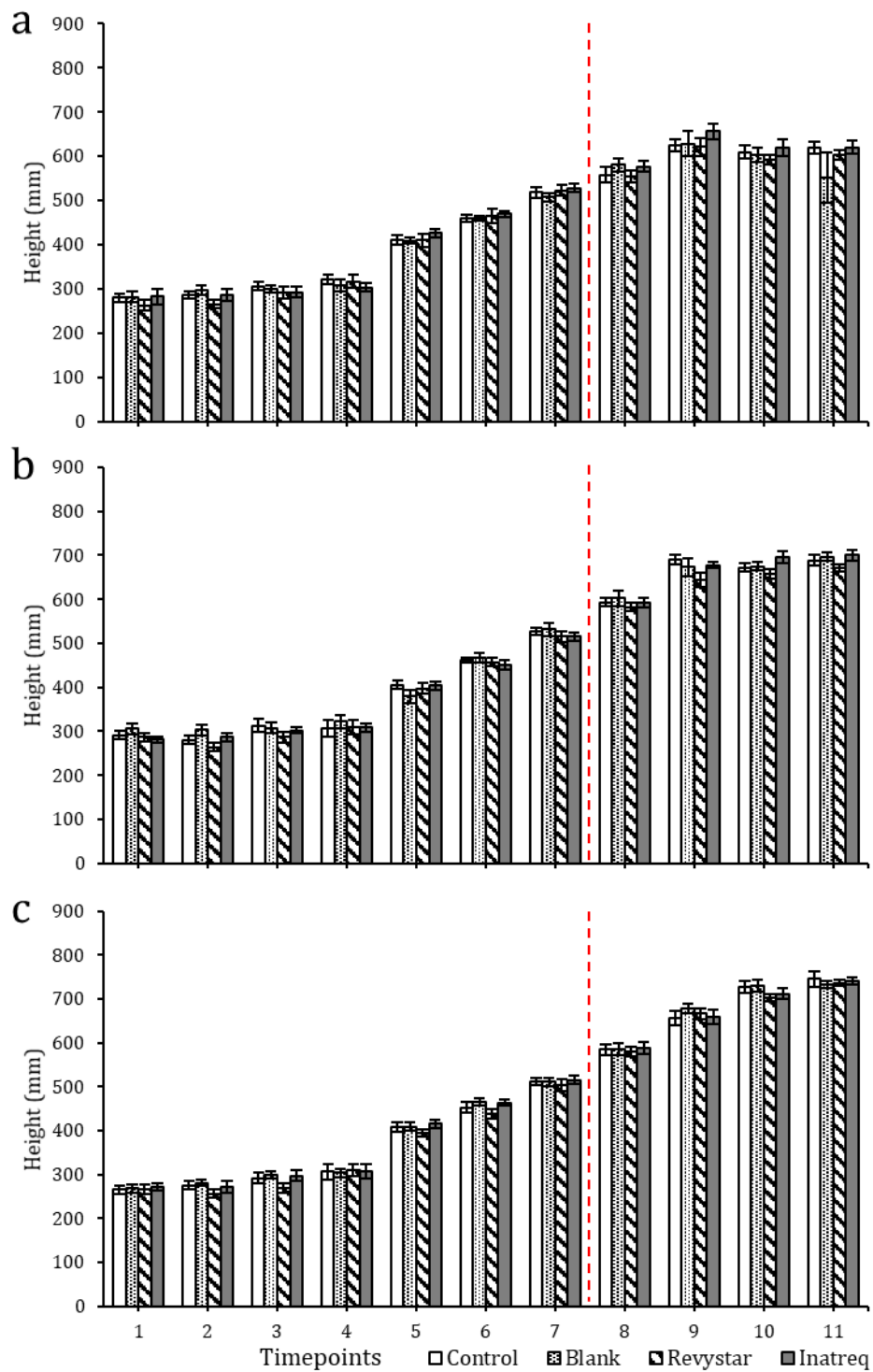


Figure 4.10: Height measurements in wheat variety Skyfall, treated with either: a water control spray, blank solution, Revystar, or Inatreq. a) Plants grown under low water availability, b) plants grown under medium water availability, c) plants grown under high water availability. Spray date and drought initiation represented by dashed red line (---), error bars = \pm SE, $n=10$.

After the final timepoint, inflorescence counts were observed of Extase, but were unable to be recorded in Skyfall, due to Gray Mold (*Botrytis cinerea*) infection requiring plants to be removed before counts could be made. The inflorescence count of plants treated with Inatreq and the blank solution were higher than the control plants at the lowest water availability, but not significantly so. The trend was the same for Inatreq at all water availabilities, whereas the blank solution did not have a consistent trend in comparison to the other treatments.

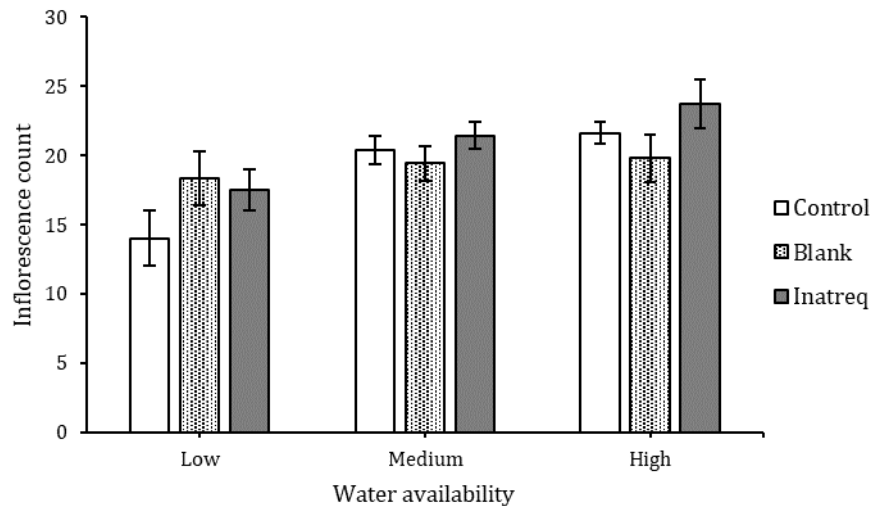


Figure 4.11: Inflorescence count for Extase plants treated with their respective fungicide application protocol. These plants were then grown under conditions of either high, medium, or low water availability. Error bars = \pm SE, $n = 10$.

Physiological parameters.

The control and blank-treated Extase plants, grown under low water availability, showed a significant decline in Fv/Fm compared the plants grown under high water availability (1.39% and 1.07% reduction in Fv/Fm and $P=0.002$ and $P=0.025$ respectively) (Table 4.7a). Plants that were treated with Inatreq and grown under low water availability had a Fv/Fm higher than the control and blank plants under low water availability, but lower than the ones grown under high water availability. Plants treated with Inatreq were not significantly different to either other treatment under high or low watering. Further to this, plants treated with Inatreq and grown under high water availability were significantly higher than the other two treatments groups grown at high water availability.

For Skyfall plants (Table 4.7b), it was found that many of the treatment groups performed similarly and were only affected by their water availability. The only result that differed

from this trend, was that plants treated with Inatreq and were grown under low water availability performed comparably to those treated with the control solution under high water availability, and therefore were not significantly different to each other. This was the only treatment group grown under low water availability that performed comparably to the control group grown under high water availability, as it did the in the Extase observations.

Table 4.7: Chlorophyll fluorescence parameters of dark-adapted plants under differential watering and fungicidal treatments. Table a) Extase variety, table b) Skyfall variety. \pm SE, a, b, and c = homogenous subsets derived by Tukey's post-hoc test for significance ($p < 0.05$).

a	Fungicide Application	Watering level	Fm	Fo	Fv	FV/FM
	Control	High-water		663.0 \pm 9.3	130.9 \pm 1.6	532.1 \pm 7.8
Drought			646.1 \pm 11.2	134.8 \pm 2.1	511.4 \pm 9.2	0.791 \pm 0.0012 (a)
Blank solution	High-water		662.0 \pm 19.9	130.6 \pm 2.7	531.4 \pm 17.3	0.802 \pm 0.0022 (b)
	Drought		684.6 \pm 16.5	141.1 \pm 2.6	543.5 \pm 14.1	0.794 \pm 0.0018 (a)
Inatreq	High-water		660.1 \pm 18.7	129.5 \pm 2.4	530.6 \pm 16.3	0.803 \pm 0.0023 (c)
	Drought		661.0 \pm 23.6	135.1 \pm 3.9	525.9 \pm 19.9	0.795 \pm 0.0023 (ab)

b	Fungicide Application	Watering level	Fm	Fo	Fv	FV/FM
	Control	High-water		569.1 \pm 9.0	111.0 \pm 1.8	458.1 \pm 7.4
Drought			595.7 \pm 6.8	122.0 \pm 2.0	473.7 \pm 5.6	0.789 \pm 0.0025 (a)
Blank solution	High-water		566.8 \pm 9.5	108.5 \pm 1.3	458.3 \pm 8.7	0.804 \pm 0.0025 (c)
	Drought		608.2 \pm 15.3	126.1 \pm 3.7	482.2 \pm 12.0	0.787 \pm 0.0026 (a)
Inatreq	High-water		577.6 \pm 11.5	111.4 \pm 1.3	466.2 \pm 10.5	0.803 \pm 0.0024 (c)
	Drought		603.5 \pm 11.0	123.8 \pm 3.1	479.7 \pm 8.4	0.789 \pm 0.0026 (ab)
Revystar	High-water		582.6 \pm 9.9	109.8 \pm 1.5	472.9 \pm 9.0	0.807 \pm 0.0027 (c)
	Drought		593.0 \pm 5.3	121.0 \pm 1.9	472.1 \pm 4.5	0.789 \pm 0.0030 (a)

4.3.2. Field trial.

During the field trial, measurements of QY max, NDVI and RWC were recorded immediately before the application of the respective fungicides, and then every 7 days for the proceeding 5 weeks. Plants were observed regularly to monitor disease status, to ensure any effects were not the result of disease symptomology. It is important to note that prior to the fungicide application, the abnormally reduced rainfall (<15 mm, Fig. 4.1&2) resulted in plants showing early symptoms of drought stress such as leaf rolling, stunted growth, and some wilting. Plants were visually examined for these symptoms at each timepoint before recording each of the physiological measurements and the symptoms were consistent throughout the plots, without any discernible distinctions between treatments. These pre-application drought symptoms are reflected in the pre-application measurements (15/06/2020, Table 4.8) of QY max, NDVI and RWC as well as in the measurements throughout. Following the application of the respective fungicides there was little differentiation between any of the treatments and the control treated plants throughout the rest of the remaining observation timepoints. One observation of note is the only plants treated with a fungicide to have an improved RWC following fungicide application are the samples treated with Inatreq and prothioconazole. However, the untreated plants also increased in RWC at the same timepoint. There were no significant differences in any of the measurement parameters at any time point throughout this trial. Recording of plant physiology parameters concluded when plants visually began to senesce, and measurements such as QY max and NDVI became negligible.

At the end of the trial, once plants had completely dried, they were harvested and the ear count, total yield and 1000 grain weight recorded. Again, there were no significant yield parameter differences between these treatments (Figure 4.12). There were also no consistent trends in each of the yield parameters and specific treatments.

Table 4.8: Mean effects of a panel of fungicides on wheat plants quantum yield (QY max, Fv'/Fm'), normalised difference vegetation index (NDVI), and relative water content (RWC %). Values with the same letter in the same column do not significantly differ from one another according to Tukey's post-hoc test ($P < 0.05$, $n = 8$).

	QY max						NDVI						RWC (%)					
	15/06/2020	22/06/2020	29/06/2020	06/07/2020	13/07/2020	20/07/2020	15/06/2020	22/06/2020	29/06/2020	06/07/2020	13/07/2020	20/07/2020	15/06/2020	22/06/2020	29/06/2020	06/07/2020	13/07/2020	20/07/2020
Inatreq 75%	0.66 (a)	0.62 (a)	0.76 (a)	0.73 (a)	0.69 (a)	0.31 (a)	0.50 (a)	0.48 (a)	0.43 (a)	0.39 (a)	0.33 (a)	0.28 (a)						
Inatreq 100%	0.66 (a)	0.65 (a)	0.77 (a)	0.73 (a)	0.73 (a)	0.26 (a)	0.50 (a)	0.48 (a)	0.42 (a)	0.39 (a)	0.34 (a)	0.28 (a)	87.55 (a)	86.97 (a)	86.87 (a)	77.68 (a)	78.60 (a)	76.98 (a)
Inatreq + Prothioconazole 75%	0.71 (a)	0.67 (a)	0.77 (a)	0.74 (a)	0.72 (a)	0.14 (a)	0.50 (a)	0.47 (a)	0.44 (a)	0.40 (a)	0.34 (a)	0.27 (a)						
Inatreq + Prothioconazole 100%	0.70 (a)	0.63 (a)	0.77 (a)	0.73 (a)	0.70 (a)	0.17 (a)	0.50 (a)	0.48 (a)	0.46 (a)	0.44 (a)	0.37 (a)	0.30 (a)	87.85 (a)	88.33 (a)	87.65 (a)	76.98 (a)	83.78 (a)	83.78 (a)
Proline 75%	0.69 (a)	0.68 (a)	0.76 (a)	0.73 (a)	0.74 (a)	0.33 (a)	0.49 (a)	0.49 (a)	0.46 (a)	0.41 (a)	0.35 (a)	0.29 (a)						
Proline 100%	0.63 (a)	0.72 (a)	0.79 (a)	0.74 (a)	0.73 (a)	0.20 (a)	0.51 (a)	0.51 (a)	0.46 (a)	0.43 (a)	0.36 (a)	0.28 (a)	90.65 (a)	86.14 (a)	88.09 (a)	79.21 (a)	80.91 (a)	80.91 (a)
Elatus Plus 75%	0.63 (a)	0.69 (a)	0.78 (a)	0.74 (a)	0.71 (a)	0.20 (a)	0.50 (a)	0.48 (a)	0.43 (a)	0.41 (a)	0.36 (a)	0.27 (a)						
Elatus Plus 100%	0.69 (a)	0.67 (a)	0.77 (a)	0.76 (a)	0.74 (a)	0.38 (a)	0.51 (a)	0.48 (a)	0.46 (a)	0.43 (a)	0.38 (a)	0.31 (a)	90.01 (a)	89.41 (a)	88.71 (a)	77.82 (a)	83.84 (a)	83.84 (a)
Myresa 75%	0.69 (a)	0.68 (a)	0.77 (a)	0.75 (a)	0.72 (a)	0.11 (a)	0.47 (a)	0.47 (a)	0.41 (a)	0.41 (a)	0.35 (a)	0.29 (a)						
Myresa 100%	0.66 (a)	0.62 (a)	0.76 (a)	0.75 (a)	0.73 (a)	0.23 (a)	0.51 (a)	0.51 (a)	0.47 (a)	0.44 (a)	0.38 (a)	0.29 (a)	91.74 (a)	87.37 (a)	86.51 (a)	77.34 (a)	82.94 (a)	82.94 (a)
Untreated	0.69 (a)	0.65 (a)	0.78 (a)	0.73 (a)	0.70 (a)	0.25 (a)	0.51 (a)	0.47 (a)	0.43 (a)	0.41 (a)	0.36 (a)	0.29 (a)	87.84 (a)	89.27 (a)	85.96 (a)	74.19 (a)	79.43 (a)	79.43 (a)

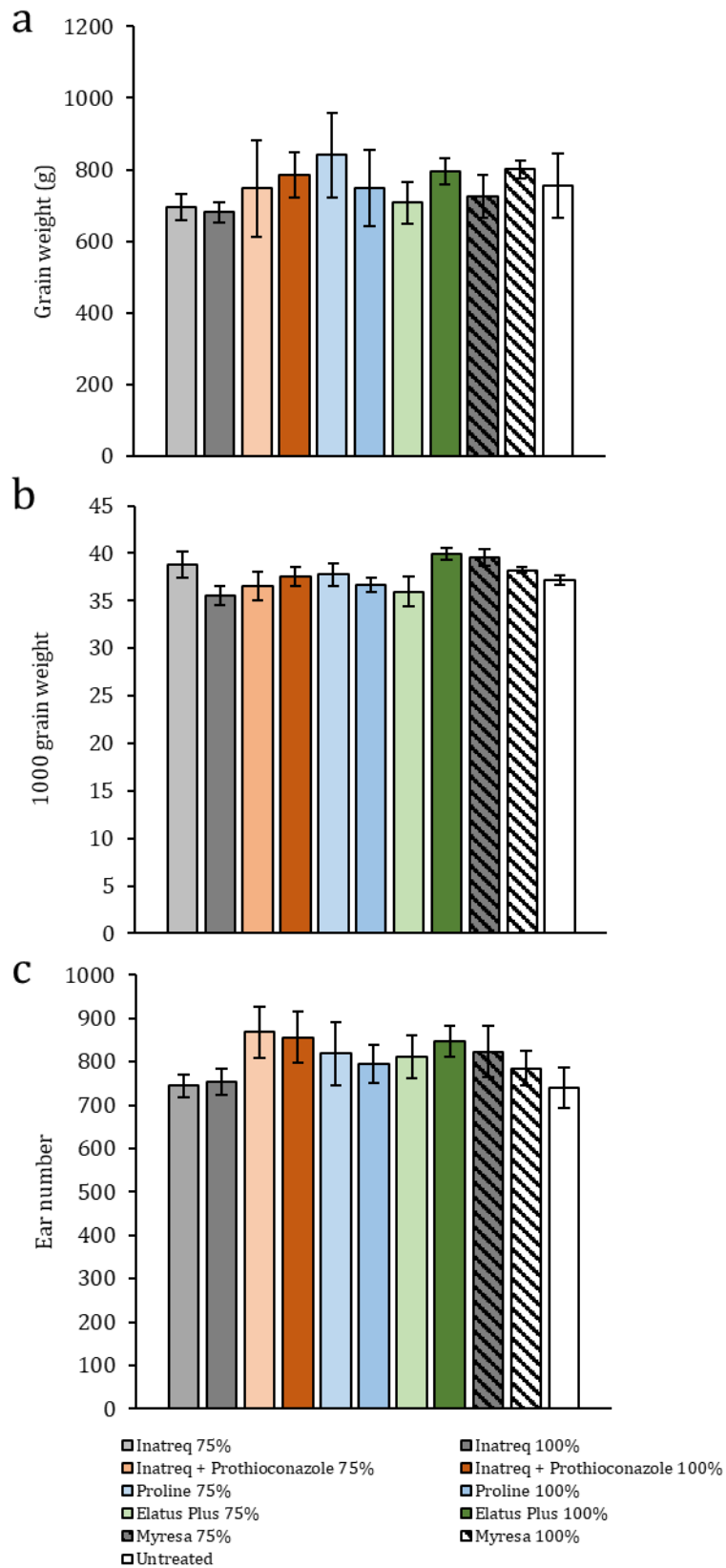


Figure 4.12: Yield data from the Wellesbourne field trial, comparing. a) Average total grain weight per plot, b) average 1000 grain weight, c) average total ear number per plot. Error bars = \pm SE.

4.4. Discussion.

4.4.1. High-throughput glasshouse phenotyping.

To observe the influence of drought upon winter wheat, and to determine if the application of Inatreq may alleviate some of the detrimental effects, plants were imaged throughout their life cycle, before and after the fungicide application under differential watering. The HTP imaging of these plants enabled the extraction of growth parameters including height and projected shoot area, on a temporal scale, which offers insight that would not be possible using traditional manual practices. To first quantify the severity of the effect of the experimental drought regimes, the control plants were observed at all three watering conditions. It was found that the most extreme level of drought resulted in a significantly lower biomass compared to the medium and well-watered plants within 3 days (Figure 4.4), with the high and medium water availability plants only becoming significantly different in PSA after 13 days. For Extase, at the first timepoint after the onset of differential watering, PSA was reduced in control plants grown under the low water regime. This measured reduction in PSA may be a result of drought symptoms such as leaf rolling, where the visual surface area will appear reduced. This phenomenon has been previously observed (Neilson *et al.*, 2015), where rolled leaves resulted in a significant decrease in PSA, when compared to unrolled leaves. Despite Skyfall plants grown under low water availability having significantly lower PSA when compared to the medium and high watering conditions, the PSA was not reduced when compared to the previous timepoint, suggesting it may not have experienced the degree of leaf rolling observed in Extase. This may suggest that Skyfall is potentially better adapted to lower water availabilities than Extase. Anecdotal observations have suggested that Skyfall performs excellently on lighter, more drought prone soil, whereas Extase has been suggested to perform fairly well, but being a new variety the data is not yet extensive (<https://www.agrii.co.uk/wp-content/uploads/2015/10/Skyfall.pdf>). This could be due to its reduced, more compact, size (Fig. 4.4b) when compared to Extase, meaning it has a lower water requirement, and therefore is able to conserve soil water for longer.

When observing how Inatreq may influence the response to low, medium, and high-water availability it was found that, for Extase, Inatreq was able to significantly alleviate the reduction in PSA in plants exposed to low-water availability (Fig. 4.6a). At the first timepoint after fungicide application, and the onset of differential watering, plants treated with Inatreq were found to not only have a significantly higher PSA than the other plants grown under low water availability, but the PSA was comparable to the plants grown under medium and high-water availability. Following the first timepoint after differential

watering, the plants treated with Inatreq maintained a significantly higher PSA (23-26%) than the control plants for a further two more imaging timepoints (14 days in total since fungicide application. However, the effects of Inatreq on Extase plants PSA were not observable in plants grown under medium and high-water availability (Figure 4.6b, 4.6c). The plants grown under low water availability, but were treated with the blank solution, were found to also show increased PSA when compared to the control group (15-20%), but the difference between them and the control plants were not significant (Fig. 4.6a). The resemblance between Inatreq and the blank solution in their effect upon Extase plants, grown under low water availability, may suggest that the response associated with Inatreq application may be an additive response to both the active ingredient fenpicoxamid and the adjuvants added to it. It is important to observe the influence of adjuvants and co-formulants independently, and previous studies have often overlooked these, instead comparing the fungicide application to plants sprayed with just water (Andres and Agudelo, 2013; Smith *et al.*, 2013; Ajigboye *et al.*, 2014a, 2017; Dal Cortivo *et al.*, 2017; Kuznetsov *et al.*, 2018), inferring the effect is due to the active ingredient, without consideration to the other compounds present in its formulation. Considering beneficial non-fungicidal effects have been observed after the application of a wide variety of fungicides, with active ingredients from a variety of different chemical classes, the role played by the adjuvants, which are more often more similar between products than the active ingredient, may have been downplayed.

For Extase, the application of either Inatreq or the blank solution had no measurable effect upon the height of the plant, which suggests it may not be a morphological parameter that is useful to observe when looking at these fine differences between plants. The effects of fungicide application on drought tolerance are likely to be small, incremental improvements, and not cause large-scale changes in morphology because, despite drought tolerance improvements, water availability is still limited.

For Skyfall, it was found that the morphological changes observed in Extase were not consistent. Neither PSA nor height was significantly influenced by the application of Inatreq, the blank or the additional fungicide Revystar. This lack of recognition of any morphological change may suggest that subtle changes in biomass may not be recognized so well in this variety, as changes in biomass have been previously observed when applying Inatreq to Skyfall (Chapter 3). Although PSA has been recognized as a reliable proxy for plant biomass, it has also been suggested that it can show biased estimations of biomass, particularly when observing responses to abiotic stress such as salt and drought (Golzarian *et al.*, 2011), and therefore may not be the best parameter to use in HTP

platforms observing these responses in the long term. A better model may instead also consider the age of the plant, and developmental stage, however these models for prediction of biomass are not as widely accepted as PSA (Golzarian *et al.*, 2011), and often are not as easily calculated, meaning the throughput may be impeded by having to manually, and subjectively define the plants growth stages. As mentioned, Skyfall has been noted to perform excellently when grown in light soils that are prone to drought, and therefore the lack of response to the application of Inatreq when grown under low water availability, may be due to Skyfall being inherently more drought tolerant. This is further supported by Skyfall plants PSA not being reduced at the first timepoint after transitioning to low water availability growing conditions, unlike Extase, which was likely the effect of fast response wilting and leaf rolling.

Plants were found to maintain a higher PSII efficiency (F_v/F_m) when they are grown under conditions with low water availability, following treatment with Inatreq, reflecting previous findings where other fungicides have elicited similar effects (Ajigboye *et al.*, 2014a, 2017). PSII efficiency was observed in this study, to monitor how plants were able to tolerate drought conditions, where reductions in water, and gas exchange following the reduction in stomatal conductance, can lead to excess excitation energy damaging PSII light harvesting complexes. The decline in F_v/F_m between the control plants under high and low drought conditions (Table. 4.7) is a result of the increasing minimal fluorescence (F_0), combined with the decreasing maximal fluorescence (F_m), and therefore also the maximal variable fluorescence ($F_v = F_m - F_0$). The increase in F_0 is a common characteristic in plants experiencing drought and is representative of PSII inactivation, whilst decreasing F_m and F_v are common indicators of an increase in non-photochemical quenching (NPQ) (Baker, 2008; Zlatev, 2009).

In the HTP screen of plants in the glasshouse, the plants grown under low water availability were maintained at 20% soil water capacity, which may not have been quite severe enough to elicit clearer responses, following the application of Inatreq. Further experiments with the complete withholding of water from treated and untreated plants may allow a clearer characterization of this effect, and therefore a clearer understanding on whether Inatreq may improve whole plant water use efficiency when experiencing limited water availability. Further to this, differences in photosynthetic efficiency were extremely small, and further drought stress would accentuate differences. Chlorophyll fluorescence has been previously used to detect the early signs of senescence and, the plants at the lowest water availability in this experiment may not have quite undergone

enough significant drought effects, as the photosynthetic efficiency of all plants were similar (Berdugo *et al.*, 2013).

The increased PSA observed in response to the application of Inatreq suggests that this fungicide has a role in improving plants water use efficiency (WUE). WUE can be defined as the amount of carbon assimilated as either plant biomass or yield, per unit of water used (Hatfield and Dold, 2019). Using PSA as a proxy for plant biomass suggests under conditions where water becomes limiting, Extase plants were better able to assimilate carbon following the application of Inatreq, than with the control solution alone.

4.4.2. Field trial.

The trial was drilled late in the 2019/2020 season due to an extremely wet winter, which was then followed by an abnormally dry spring season, with low precipitation (Fig. 4.1). Due to this, there were visible signs of drought before fungicide application, and throughout the season, therefore compromising the data gathered from this experiment. Furthermore, access to the trial site was limited due to restrictions on travel, therefore preventing additional irrigation being provided. The nature of these conditions may account for the similarities across observations due to all plants being under persistent stress from an early stage. These issues that were encountered further highlight that field trials are notoriously difficult to successfully execute and, for them to be reliably used to infer any cause and effect, they need to be repeated across a range of locations and under a range of conditions. This also reinforces the benefits offered by using facilities that offer elements of control over the conditions. Rather than field trials alone, a combination of methods in controlled conditions to identify the key elements for further investigation with field trials carried out in a range of conditions to test the model, taking into account year-to-year climatic changes (Tardieu, 2012).

Chapter 5. Studies using the model plant *Arabidopsis thaliana*.

5.1. Introduction and aims.

5.1.1. Introduction

Arabidopsis thaliana is one of the most thoroughly studied and characterized plant species. It was the first plant to have its entire genome sequenced (Kaul *et al.*, 2000), and has been considered one of the original model plant species. Between 1965 – 2015, there were over 53,000 scientific publications to feature *Arabidopsis* in the title, abstract and/or keywords (Provart *et al.*, 2016). *A. thaliana* was an appealing species to use as a model plant due to its ease of growth in an artificial environment, small size, the relative simplicity of its genome and its short generation time. Due to the extent of the research conducted on *A. thaliana*, and the degree to which its genome has been annotated, *A. thaliana* is often used in comparative studies (Parkin *et al.*, 2005). Despite *A. thaliana* being a dicotyledonous plant species, it can still serve as a useful model species for monocot cereal plants. For example, the gibberellin-insensitive dwarfing genes in *A. thaliana* (*GA1*) were found to be orthologs of the seminal reduced height genes (*Rht1*) in wheat, which were a central feature of the semi dwarf wheat ideotype developed as part of the Green Revolution (Peng *et al.*, 1999). Biotechnological tools are rapidly advancing and the understanding of the whole wheat genome and gene function are becoming more readily available, however complex biological processes such as stress signalling, and hormone interactions are still better understood in model species such as *A. thaliana* (Abhinandan *et al.*, 2018).

Plant phenotyping is a rapidly growing, transdisciplinary field, and is vital in bridging the gap in knowledge between genotype to phenotype (Pieruschka and Poorter, 2012; Großkinsky *et al.*, 2015; Pieruschka and Schurr, 2019). However, a bottleneck to the wider usage of large-scale phenotyping is that facilities that can offer a high throughput of sophisticated measurements are associated with high costs. This has led to an increase in alternative “affordable phenotyping” solutions (Minervini *et al.*, 2017; Reynolds *et al.*, 2019). These affordable solutions offer researchers the opportunity to invest more in the sensors they use, rather than the platform, meaning the data they collect may be more informative. Thermal infrared imaging is becoming an increasingly utilized as a remote sensing tool for water relations (Berger *et al.*, 2010b). Evapotranspiration from the leaf surface is a large determinant of the leaf surface temperature, and therefore any fluctuations in rates of transpiration and stomatal conductance are directly reflected in changes of temperature (Jones, 1999; Merlot *et al.*, 2002; Grant *et al.*, 2006; Jones *et al.*, 2009; Gómez-Bellot *et al.*, 2015; Elsayed *et al.*, 2017). Direct measurements of these traits in plants are generally not amenable to high throughput screening as they require manual

manipulation of the leaf, and in plants such as *A. thaliana* may result in damage of the leaf material, which may therefore affect measurements on a temporal scale.

Evapotranspiration is regulated by stomata on the leaf surface. Stomata are microscopic structures, ranging in length from 1-80 μm and up to 50 μm wide (Willmer and Fricker, 1996) located on most aerial plant material, in particular the abaxial surface of leaves (Driscoll *et al.*, 2006), serving as a gateway between the atmosphere into the intercellular space within the plant material. These pores are surrounded by two guard cells, which act to regulate the rate of transpiration and gas exchange that occurs through these pores, by changing their shape, either widening or narrowing the pore. These changes in conformation are caused by changes in turgor pressure within the guard cells, swelling with the osmosis of water into the guard cell causing the pore to widen, and osmosis out of the cell causing a decrease in turgor pressure and therefore the pore to narrow (Hetherington and Woodward, 2003). The degree of stomatal conductance is dependent upon a variety of signals, including environmental factors and cues regulated by the plant itself. ABA is a central regulator of abiotic stress responses, and directly influences adaptive responses to regulate plant water status (Sirault *et al.*, 2009; Raghavendra *et al.*, 2010; Verslues, 2016). Under stressful conditions, such as drought, ABA accumulates in the leaf material, initiating the reversible increase in the concentration of osmotically active solutes such as K^+ , Cl^- , malate and sucrose within the intracellular space, which causes the reduction in turgor of the stomatal guard cells, and therefore stomatal closure (Assmann, 2003). It has been found, using ABA mutants, that the plants that are unable to perceive or synthesise ABA are impaired in their adaptive responses to changes in abiotic stress (Merlot *et al.*, 2002; Acharya *et al.*, 2013). Due to the central role ABA plays in abiotic stress responses, it has now become a target for improvement of crop drought tolerance, either through genetic modification (Joo *et al.*, 2019) or the application of specific active compounds that may either mimic or induce ABA signal transduction (Cao *et al.*, 2013; Kim, 2014; Vaidya *et al.*, 2019).

If the effects that have been characterized in the previous chapters are consistent in *Arabidopsis thaliana*, it would offer the opportunity to investigate the underlying genetic mechanisms of the effect in a simpler genome. Once the effect is then characterized in this model species, a more targeted approach can then be taken in wheat, potentially identifying a select few select genes that may be homologous to those observed in *A. thaliana*.

5.1.2. Aims

The work in this chapter builds upon the observations reported in Chapters 3 and 4, that the application of Inatreq is associated with non-fungicidal benefits, potentially leading to improved drought tolerance. It is hypothesized that this improvement of drought tolerance may be associated with Inatreq initiating a reduction in stomatal conductance (Figure 3.3). The work reported in this chapter utilizes the model plant *A. thaliana*, and its extensively annotated genome to better understand the underlying genetic basis of this effect.

To first do this, it must first be established if *A. thaliana* responds to the application of Inatreq in a way that is comparable to the response in wheat. Traditionally a reduction in stomatal conductance would be measured utilizing tools such as handheld porometers, as in Chapter 3. However, these are often time consuming, laborious, and owing to having to physically clip these to the leaf, can result in damage to the plant material. Therefore it is becoming increasingly common that stomatal conductance is being compared by utilizing the leaf surface temperature as a proxy (Merlot *et al.*, 2002; Fiorani *et al.*, 2012; Klem *et al.*, 2017). Remote sensing, utilizing thermal sensors is amenable to automation, and the development of high throughput (HTP) phenotyping platforms. This chapter outlines the production of a bespoke, low-cost, automated, high throughput (HTP) thermal imaging platform. The use of temperature as a proxy for stomatal conductance in *A. thaliana* is first validated, before being used to observe if the application of Inatreq results in the reduction of stomatal conductance reported in wheat in Chapter 3. Further to this, the experiment will also observe any changes in water use efficiency, biomass accumulation, and response to drought following the application of Inatreq. This work will utilize wild type *A. thaliana*, as well as mutant varieties *aba2* and *ost1* which have mutations in their ABA biosynthesis and signalling pathways, respectively.

Finally, RNA sequencing will be used to identify the underlying genetic response to the application of Inatreq, to better understand the perceived improvement of drought tolerance. This was carried out to identify a potential subset of genes that are differentially expressed for future research.

5.2. Methods

5.2.1. Plant material and growth conditions

Two *A. thaliana* wildtype (WT) ecotypes, and two mutant lines were used in these experiments (Table 5.1). These were obtained from the National Arabidopsis Stock Centre (NASC). The ABA DEFICIENT 2 (*ABA2*) allele is involved in abscisic acid (ABA) biosynthesis – and the knockout (KO) plants, *aba2*, are therefore ABA-deficient (Mustilli *et al.*, 2002). The OPEN STOMATA 1 (*OST1-1*) allele is involved in ABA signalling and the KO is impaired in ABA signalling, particularly in the stomata (Merlot *et al.*, 2002).

Table 5.1: *A. thaliana* used in this study, including mutants with their genetic backgrounds listed.

Variety	Description/name
Col-0	Columbia-0 wildtype
<i>Ler</i>	Landsberg <i>erecta</i> wildtype
<i>ost1-1</i>	OST1 mutant knockout, ABA insensitive, Col-0 genetic background
<i>aba2</i>	ABA2 mutant ABA biosynthesis inhibition, <i>Ler</i> genetic background

For aseptic growth seeds were first surface sterilised using 5% (v/v) sodium hypochlorite before 5 sequential washes in sterile deionised water. The seeds were then sown onto 120 x 120 mm square plates containing half-strength Murashige and Skoog (MS) growth medium (Sigma) solidified with 1% (w/v) agar that had its pH adjusted to 6 with 1 M KOH. The plated seeds were then stratified in darkness at 4 °C for 48 hours. Following this, the plates were transferred to a controlled environment growth room with short day (8/16 hr photoperiod) conditions at 21 °C, 70% humidity and light intensity at plant level of 150 $\mu\text{mol m}^{-2} \text{s}^{-1}$. These seedlings were grown on their plates for a further 9 days before being transplanted to 50x50x50 mm cell trays filled with Levington M3 potting compost and kept in the same growth room. All plants then continued to be grown under the same conditions. Following transplanting to cell trays, plants were grown for a further two weeks before then being used for experimental observations.

5.2.2. Fungicide application

Plants were treated with either Inatreq or a control solution. Inatreq was applied at a rate equivalent to field concentration (75g active ingredient/ha⁻¹ in 200 L/ha⁻¹ of water). The control solution was 0.01% Tween-20 in water. These treatments were applied using clean, handheld sprayers that had been calibrated to the appropriate application rate. Following treatment application, plants were kept separate for 1 hour to allow the plants to dry, before being returned to their randomised positions.

5.2.3. Development of a high throughput thermal imaging platform.

This high throughput imaging platform consists of an infrared, thermal imaging sensor, mounted on a carriage fitted to a horizontally arranged aluminium carriage rail (Figure 5.1). This linear design positions a thermal sensor (FLIR A35 (60 Hz)) over the top of plant canopies that are grown in trays or pots grown within a controlled environment room. High throughput (HTP) imaging using such systems allows measurement of morphological properties including shape and size, as well as measuring these as they change over time (Tessmer *et al.*, 2013). The thermal sensor then enables surface temperatures of plants to be observed, as a proxy for transpiration rate and stomatal conductance (Leon-Kloosterziel *et al.*, 1996; Merlot *et al.*, 2002; Jones *et al.*, 2002, 2009; Chaerle *et al.*, 2009; Munns *et al.*, 2010; Jones, 2016; Mishra *et al.*, 2016). This system was designed to be customisable to the space available, in this instance its dimensions were selected to fit on a standard growth room shelf. A list of the components of the system are given in Table 5.2.



Figure 5.1: Bespoke HTP thermal imaging robot, *in situ*.

Table 5.2: Components of the HTP thermal imaging platform

Component	Specifications	Model/filename	Manufacturer
Stepper motor	Bipolar, 1.8°step angle, 1.68 A/phase	MT-1704HS168A	Motec
Microcontroller	16 MHz ATmega328P	Arduino Uno R3	Arduino
Driver Carrier	Arduino shield for removable drivers	CNC Shield V3	Various
Stepper driver	Max 32 microsteps, 2.5A, 12-40V	DRV8825	Texas Instruments
Drive belt	7mm width; 2mm pitch	GT2-2M	OpenBuilds
Timing Pulley	20 teeth; 2mm pitch	GT2-2M	OpenBuilds
Carriage Rail	V-slot profile	40 x 20	OpenBuilds
Carriage wheels	15.2 mm OD, Delrin	Mini V Wheel	OpenBuilds
Carriage plate	3D printed	therm_cm.stl ¹ , therm_cps.stl ¹	UoN ²
Sensor holder	3D printed	therm_s_flir.stl ¹	UoN
Electronics box	3D printed	therm_case.stl ¹	UoN
Limit switches	Hall-effect sensor, unipolar, 4.5-24V	MP101402	Cherry
Sensor	Thermal camera 19mm lens, 24° FOV	A35 (60 Hz)	FLIR

¹ Files available at: <https://github.com/UoNMakerSpace/thermal-imager-hardware>

² UoN: 3D printed at the University of Nottingham.

Mechanical components.

The imaging platform comprises of a horizontal aluminium carriage rail (V-slot profile, OpenBuilds) mounted on two support rails, made of the same aluminium profile. The height of these support rails can be customised to adjust the sensors field-of-view. The carriage is moved along the horizontal carriage rail using the “belt-and-pinion” linear drive principle, whereby a motor mounted on a wheeled carriage drives a timing belt that passes over the timing pulley and under the carriage wheels (Figure 5.2). The carriage itself, was made up of two custom designed, 3D printed plates, with mounting holes for a NEMA17 bipolar stepper motor on one plate, and for a custom 3D printed sensor mount on the other. All designs can be accessed via the repository in Table 5.2.

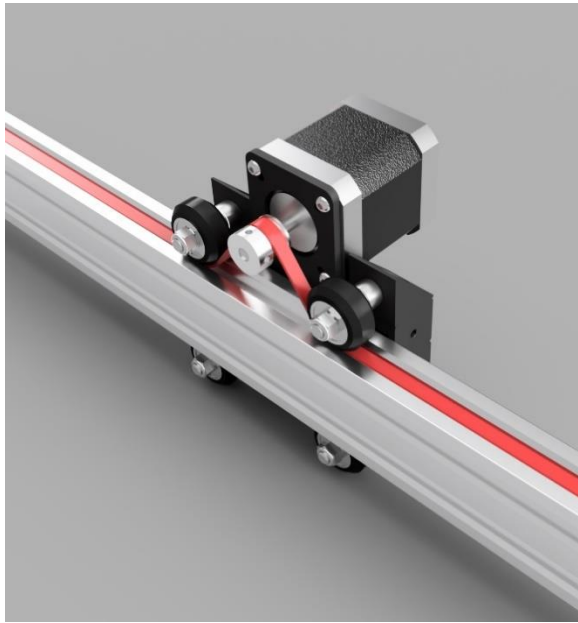


Figure 5.2: Belt-and-Pinion drive system

Electrical control components.

The motor control system is based on a microcontroller development board (Arduino Uno R3)—this incorporates a 16 MHz ATmega328P controller on an inexpensive breakout board with multiple input/output connections including a USB serial connection to a host PC or laptop. An expansion shield (CNC Shield V3) is connected to the board to allow deployment of up to three stepper motor drivers in the widely-used “StepStick” format (“StepStick - RepRap”) and multiple limit switches. The motor driver selected for this system (DRV8825, TI) can be configured to single stepping, 1/2, 1/4, 1/8, 1/16 or 1/32 microsteps and operates at a maximum drive current of 2.5 A at 24 V. Two unipolar Hall-effect sensors are wired to the shield and fixed at either end of the carriage plate. The sensors are triggered by magnets fixed to the carriage rail to act as home and limit switches. All electronic components are housed in a 3D-printed case with connectors for the stepper motor, Hall-effect sensors, and motor power. The motor is powered by a 24 V, 2.71 A power adaptor. A full wiring schematic is given in Figure 5.3. The microcontroller board is powered by a USB connection to the host computer, which also provides serial communication.

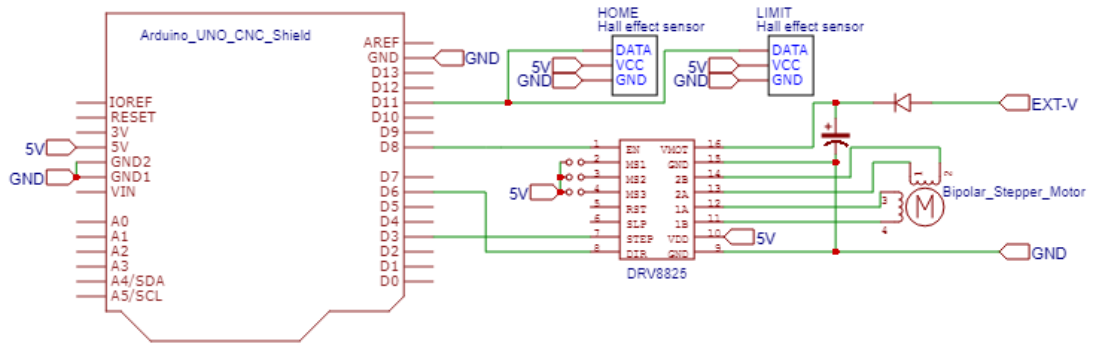


Figure 5.3: Wiring schematic of HTP thermal imaging platform

Software

The microcontroller runs a sketch written in the Arduino Integrated Development Environment that uses the AccelStepper library to control the stepper motor. This sketch allows setting of acceleration parameters for the motor, reads the state of the two limit switches and monitors the serial connection. The limit switch at the furthest extent of travel is an emergency stop, with the other sensor acting as a home switch—on triggering, it moves the carriage until the sensor is no longer active and sets the final position as zero (“home”). On receiving a serial string with positional information via the USB port, the carriage is moved to that position using the pre-defined acceleration parameters to ensure a smooth acceleration and deceleration before stopping and acquiring an image. Experimental parameters are set, and the imaging sensor controlled by a program written in the LabVIEW development environment (LabVIEW, National Instruments) running on the host computer. This provides a user-friendly graphical interface for control of the vector (distances moved, time-lapse parameters, etc.) and imaging sensor (Figure 5.4). The microcontroller sketch and LabVIEW software are available at <https://github.com/UoNMakerSpace/thermal-imager-software>. Once the experimental parameters had been entered, and the experiment initiated, images were captured in their predefined positions, and stored with a custom, predefined nomenclature.

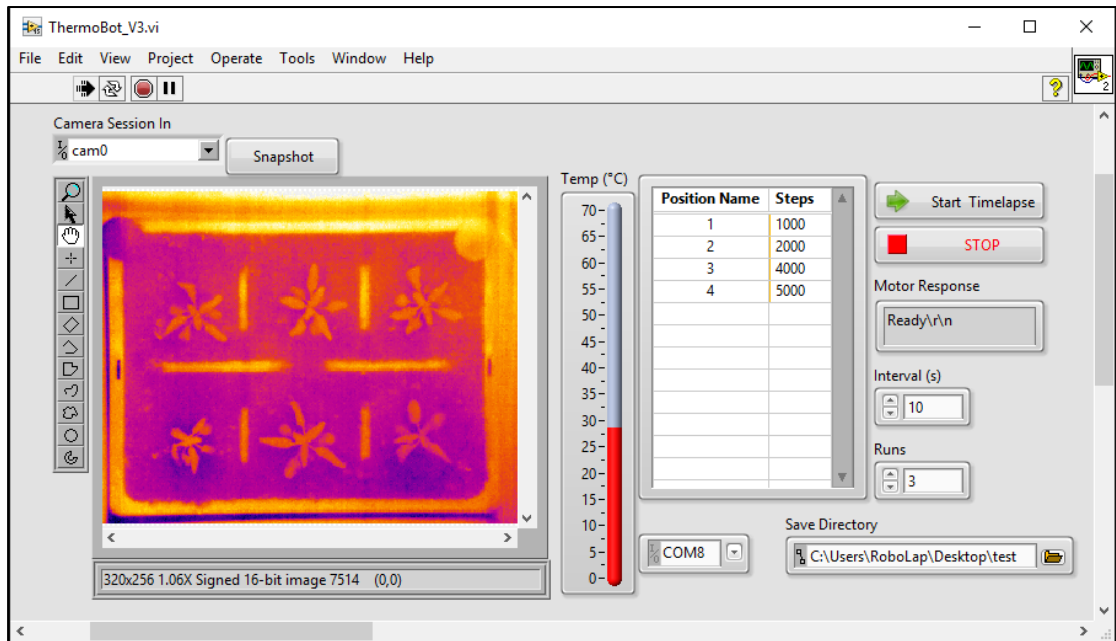


Figure 5.4: LabVIEW graphical interface for control of imaging vector with controls over various parameters

Image analysis

Once acquired, thermal images were analysed using FIJI image analysis software (Schindelin *et al.*, 2012, 2015). Pixel values (Pv) were measured at 4 points per plant, selected from the center of healthy leaves with no visible lesions, and avoiding major veins. Each point comprised of the mean score of 4-pixel values. The mean pixel value was then converted to Celsius using Equation 2:

$$((Pv - 32768)0.04) - 273.15$$

Experiments were organized to ensure that each image would contain plants for all test groups, as well as controls.

Validation of the HTP thermal imaging platform.

To validate the suitability of the custom built HTP thermal imaging platform as a proxy to measure stomatal conductance, 12 Col-0 plants had their rosette surface temperatures compared to measurements of stomatal conductance gathered from a hand-held portable leaf porometer (Model SC 1a, Decagon Devices Inc., Washington, USA) under light and dark growth conditions. Plants were maintained under light conditions for at least 2 hours prior to thermal images being captured, and transpiration rate (g_s) were recorded. This was then repeated once plants had been exposed to darkness for at least two hours. The

hand-held porometer was operated as per the protocol in Section 3.2.3, Chapter 3. Mean thermal and porometer recorded measurements were then compared by light condition and observed if light caused a significant difference in transpiration, and/or surface temperature. These gathered results were then also compared using a linear regression analysis to compare the thermal measurements to the transpiration measurements of the same plants. For the comparison of thermal measurements to those gathered using the porometer, data was compared using an independent student's *t*-test, to observe any difference using the SPSS v26 data analysis package (IBM corp.).

5.2.4. Observing the effect of application of Inatreq on stomatal conductance.

Following the validation of the HTP thermal imaging platform, it was then used to compare the transpiration rate of plants treated with either Inatreq, or the control solution. In this experiment, thermal images of wildtype (WT) ecotypes: Col-0, and *Ler* as well as two sets of mutant plants: *ost1* and *aba2* were taken prior to Inatreq application, and then 24 hours after application. Plant positions were randomized underneath the HTP thermal imaging robot, ensuring each image would have at least one plant of each test group. Thermal data was then extracted from the images, as outlined in Section 5.2.3, and compared between plants treated with Inatreq or the control solution. 48 hours after fungicide application the above ground plant material was excised, and RWC calculated, as outlined in Section 3.2.3 in Chapter 3.

A further experiment examined the effects of Inatreq application on WT plants when water was withheld. For this experiment, surface temperatures were observed for four groups: one treated with Inatreq and another with the control solution, both grown under either well-watered conditions, or had water permanently withheld 24 hours prior to fungicide application. Plants were first observed 1 hour prior to their respective applications, and then 24 and 48 hours after application.

All data was analysed using the SPSS v26 data analysis package (IBM corp.). All comparisons of the WT plants and mutant plants between control and Inatreq application were compared using student's *t*-test, whereas when the plants treated with Inatreq under differential watering were compared using an ANOVA, and Tukey's post-hoc test for significance.

5.2.5. Identifying the underlying genetic response to the application of Inatreq in *Arabidopsis*.

RNA sampling.

For all RNA sequencing the WT ecotype Col-0 was used. Rosettes were sampled at four different timepoints; pre-fungicide application, +1 hour after fungicide application, +4 hours, +8 hours, and +24 hours. The pre-fungicide application sampling was carried out at least two hours after the light cycle had begun, giving the plant time to acclimatise to the light condition. Samples at each timepoint consisted of 3 rosettes per technical replicate, and for each condition there were 5 technical replicates, giving a total of 45 samples. Samples were excised and stored in a 2 mL Eppendorf tube, before being flash frozen in liquid nitrogen and stored at -80 °C.

Total RNA was isolated from samples using the Monarch[®] Total RNA Miniprep Kit (New England Biolabs, MA USA), as per the manufacturer's instructions, including DNase treatment. For each sample approximately 100 mg of leaf tissue material was used. The sample was resuspended in 30 µL RNase free water for any further use and RNA quality was confirmed using a NanoDrop microvolume spectrophotometer (Thermo Scientific UK).

RNA sequencing and analysis.

Extracted and quantified RNA was used to generate first-strand specific mRNA libraries (TruSeq Stranded mRNA kit from Illumina) and loaded onto an S4 flow cell on 2 separate runs of an Illumina NovaSeq 6000 where paired-end 150bp sequencing was performed, producing at least 30 million reads per sample (+-3%) (2,381,480,384 reads, 1,190,740,192 read pairs, 357 Gbases) by Eurofins Genomics. FASTQ data from the sequencing runs was confirmed to pass initial quality controls by Fastqc (Andrews, 2010) and so gene expression was determined using Salmon (Patro *et al.*, 2017) in mapping based mode against a transcriptome index with genome-based decoys generated from the atRTD2 *Arabidopsis thaliana* transcriptome and TAIR10 genome reference (INSDC, 2008). Quantified transcript counts were imported into the R/Bioconductor environment (Gentleman *et al.*, 2004) using tximport (Soneson *et al.*, 2016) to create summarised per-gene abundances according to length scaled TPMs. A PCA was performed to ensure samples were appropriate for analysis with no confounding sample batch effects by PCAMethods (Stacklies *et al.*, 2007) and sample counts were filtered for samples with low per gene counts with edgeR, then normalised with mean-variance based modelling and contrasts statistically compared using an empirical Bayes moderated T-statistic with limma/voom (Law *et al.*, 2016) to produce lists of differentially expressed (DE)

genes (number). DE genes were filtered by Benjamini/Hochberg (Benjamini and Hochberg, 1995) false discovery rate corrected P value and fold change ($p < 0.05$, FC \pm 1 log₂ unit) and were clustered by Euclidian distance and Ward linkage (Ward, 1963) using fastcluster (Müllner, 2013) into 12 clusters, with differential gene expression Z-scores calculated and plotted as a heatmap by ComplexHeatmap (Gu *et al.*, 2016). Filtered genes for each differential contrast and identified cluster were analysed for overrepresented GO classifications by topGO (Alexa and Rahnenführer, 2020).

5.3. Results

5.3.1. HTP thermal imaging platform.

To validate the use of the HTP thermal imaging platform, leaf surface temperatures were compared to stomatal conductance (g_s) recorded using a porometer in Col-0 plants grown under light and dark conditions. Light and dark measurements were only recorded after the plants had been exposed to their respective lighting conditions for three hours, to allow the stomata to fully adjust. When measured during darkness, plants were found to have significantly higher mean surface temperatures and a significantly lower mean g_s (Figure 5.5). These findings support the use of surface temperatures as a proxy for transpiration rates. Reductions in leaf surface temperature are inversely related to transpiration rate, as a higher level of transpiration causes increases in evaporative cooling on the leaf surface, therefore reducing its temperature. This work reflects previous findings that have utilized thermal imaging as a tool to indirectly observe transpiration (Jones *et al.*, 2002; Cao *et al.*, 2017).

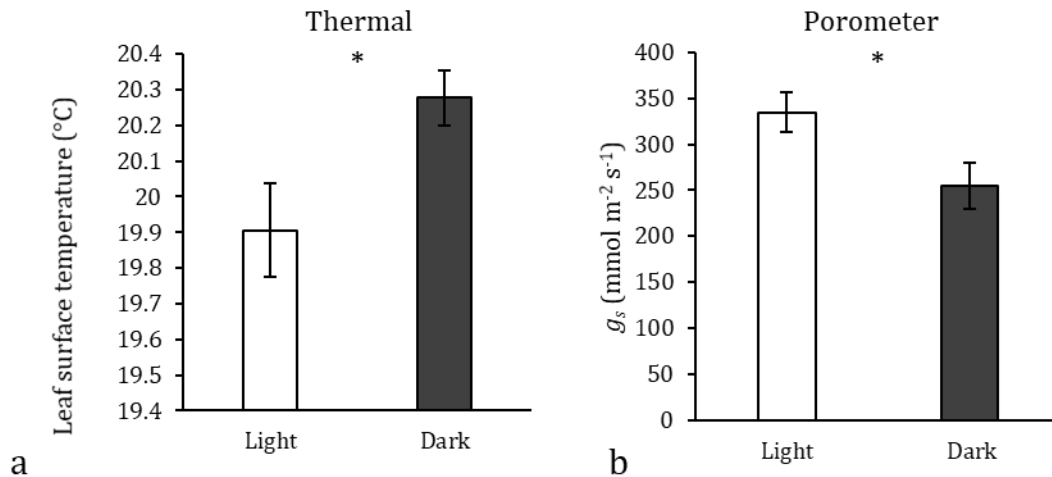


Figure 5.5: a) Comparison of thermal measurements between light/dark-adapted *A. thaliana* (Col-0) plants. b) Comparison of transpiration measurements derived from porometer measurements, between light-/dark-adapted plants, *= $P < 0.05$. $n=12$ error bars = 2SE

Temperatures and g_s of individual plants were then compared and analysed using a linear regression (Figure 5.6). It was found that the measurements recorded using the porometer and thermal camera did not align well when the plants were measured during the dark period ($R^2 = 0.0892$), whereas when the two were compared under light conditions there was a more linear relationship between the two ($R^2 = 0.4898$). During darkness, stomata close, and this leads to the grouping of measurements that had high temperatures and low stomatal conductance scores, whereas during light periods stomata are open and therefore temperature becomes more representative of the stomatal conductance rate are much more representative of the thermal temperature/low conductance region of the figure, whereas during the light stomata are open, and the importance stomatal conductance has on surface temperature is more pronounced. These findings will direct future usage of this tool, highlighting that it should use to compare stomatal conductance when the plants are light adapted rather than during the dark.

Despite the HTP thermal system only being able to give comparisons of transpiration rates, rather than directly quantifying stomatal conductance, its throughput far exceeds that of traditional porometers. The HTP robot can image up to 120 plants in ~40 s, in one cycle, and has the capability to begin a new cycle every minute. The traditional porometers can only facilitate ~ 1 measurement every 2 mins.

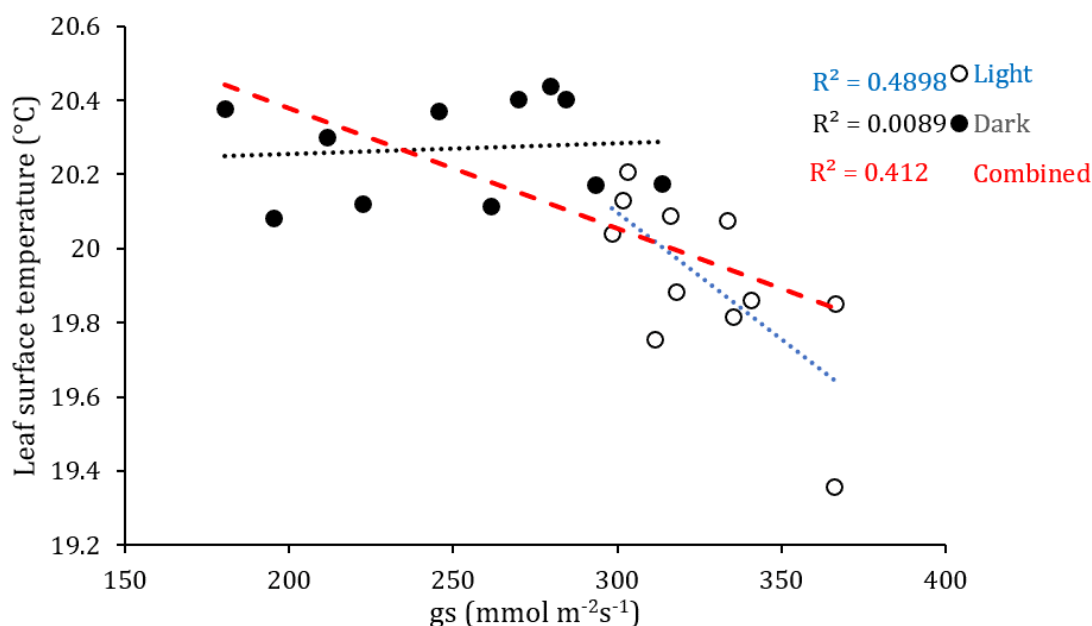


Figure 5.6: Regression analysis of thermal measurements compared to their respective transpiration score derived from porometer measurement. R^2 values are calculated for both light and dark groups individually as well as the combination between the two. $n=11$

5.3.2. Effects of Inatreq on transpiration rate in *Arabidopsis thaliana*

Following validation of the HTP thermal imaging platform, it was utilized to identify if *A. thaliana* transpiration rate responded in a similar way to wheat (Chapter 3) on application of Inatreq. It was found that when Inatreq was applied to the wildtype *A. thaliana* ecotypes, the surface temperature was significantly increased compared to the surface temperature of the control treated plants (Figure 5.7b). However, the ABA mutant ecotypes *ost1* and *aba2* showed no differences in surface temperature following the application of Inatreq, suggesting their respective stomatal conductances were unaffected.

Differences between the control treatments (Figure 5.7 a-b) were a result of natural room temperature variations. Due to this, it is important that when using thermal data for comparing stomatal conductance care is taken when comparing results across timepoints, as these will be heavily influenced by ambient temperatures, whereas data derived from the same timepoint can be more relied upon because the images captured not only contain both treatment groups in each image, but the rapid throughput means that up to 120 plants can be imaged within ~40 s, which should avoid any major temperature fluctuations.

Following the application of the fungicide to the plants in Figure 5.7, the plants were harvested 48 hours after treatment and their RWC calculated. It was found that both Col-0 and *Ler* showed significant increases in their respective RWCs, following the application of Inatreq, whilst the two ABA mutant varieties were unaffected.

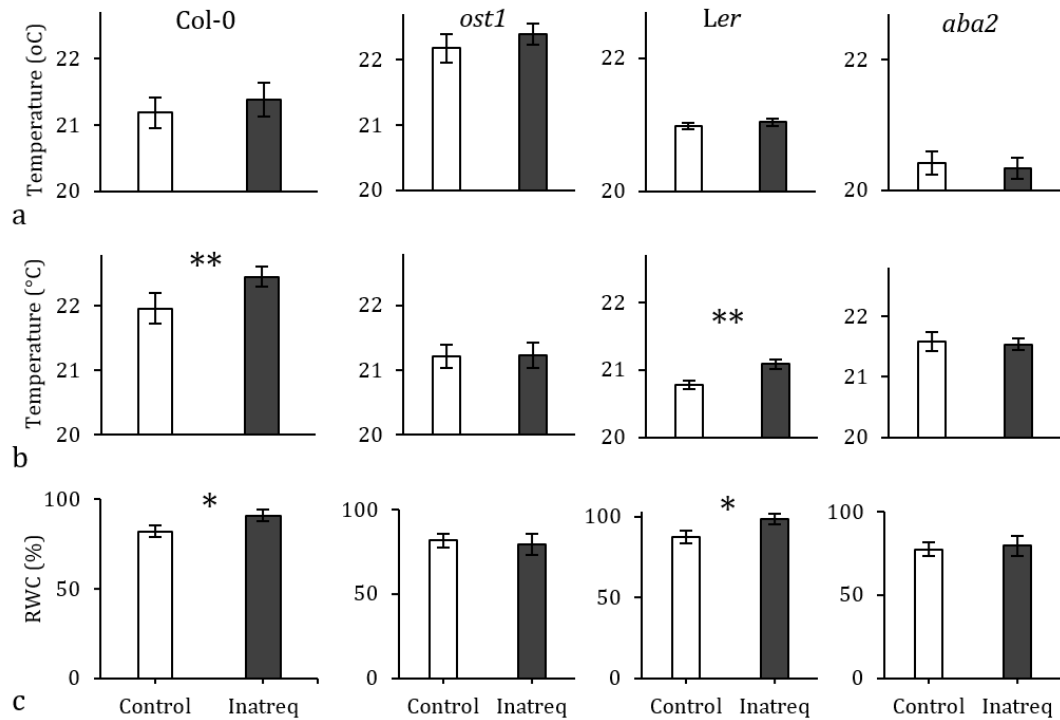


Figure 5.7: Comparison of surface temperatures following the application of Inatreq on four *Arabidopsis* lines: Wildtypes Col-0, and *Ler*, as well as ABA mutants *ost1* and *aba2*. a) 2 hours prior to Inatreq application, b) 24 hours after Inatreq application, c) relative water content (RWC) 48 hours after fungicide application. * = $P < 0.05$, ** = $P < 0.01$. $n = 8$, all error bars = $\pm 2SE$.

When observing the response of Col-0 to Inatreq, grown under conditions where water was withheld, it was found that Inatreq application was associated with a significant increase in surface temperature after 24h, and 48h and therefore can be assumed had caused a reduction in transpiration (Figure 5.8). The application of Inatreq to well-watered plants led to transpiration rates to be reduced to a level that was comparable to that of the control plants under low water availability at 24 hours (Figure 5.8). Therefore, the plants under well-watered conditions response to Inatreq application was a reduction in stomatal conductance that was comparable to control plants grown under limited water availability and therefore undergoing drought stress (Figure 5.8). As mentioned, in

reference to Figure 5.7, these temperature measurements are comparative to other measurements at the same timepoint, and due to fluctuations in growth room temperature cannot be compared across timepoints.

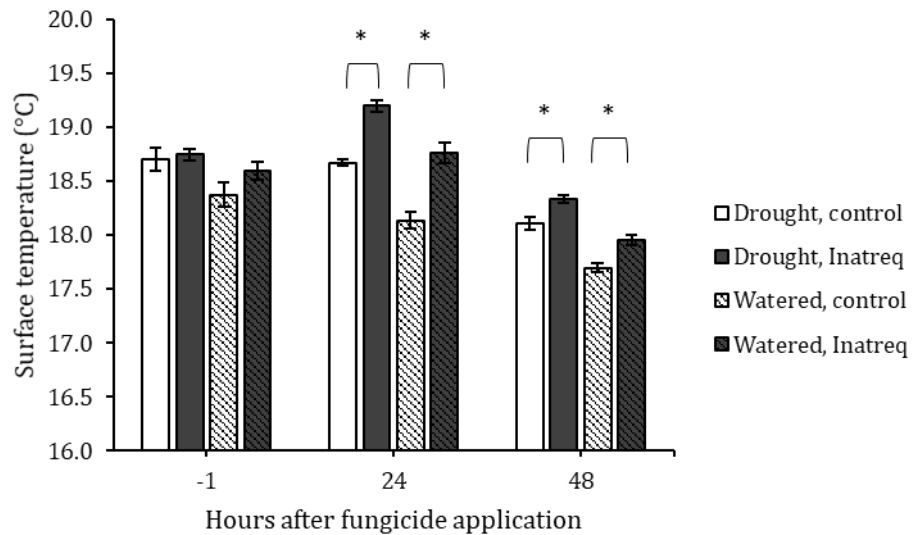


Figure 5.8: Comparison of surface temperatures of the WT ecotype Col-0. Plants were either grown under well-watered conditions or had water completely withheld 24 hours prior to their respective fungicide applications. $n=8$, error bars = SE, $*=P<0.05$

5.3.3. RNA sequencing analysis

Principal component analysis separated the sample groups into two “domains” - one representing a control domain over a 24-hour period, a second linear domain represents experimental effects (Figure 5.9).

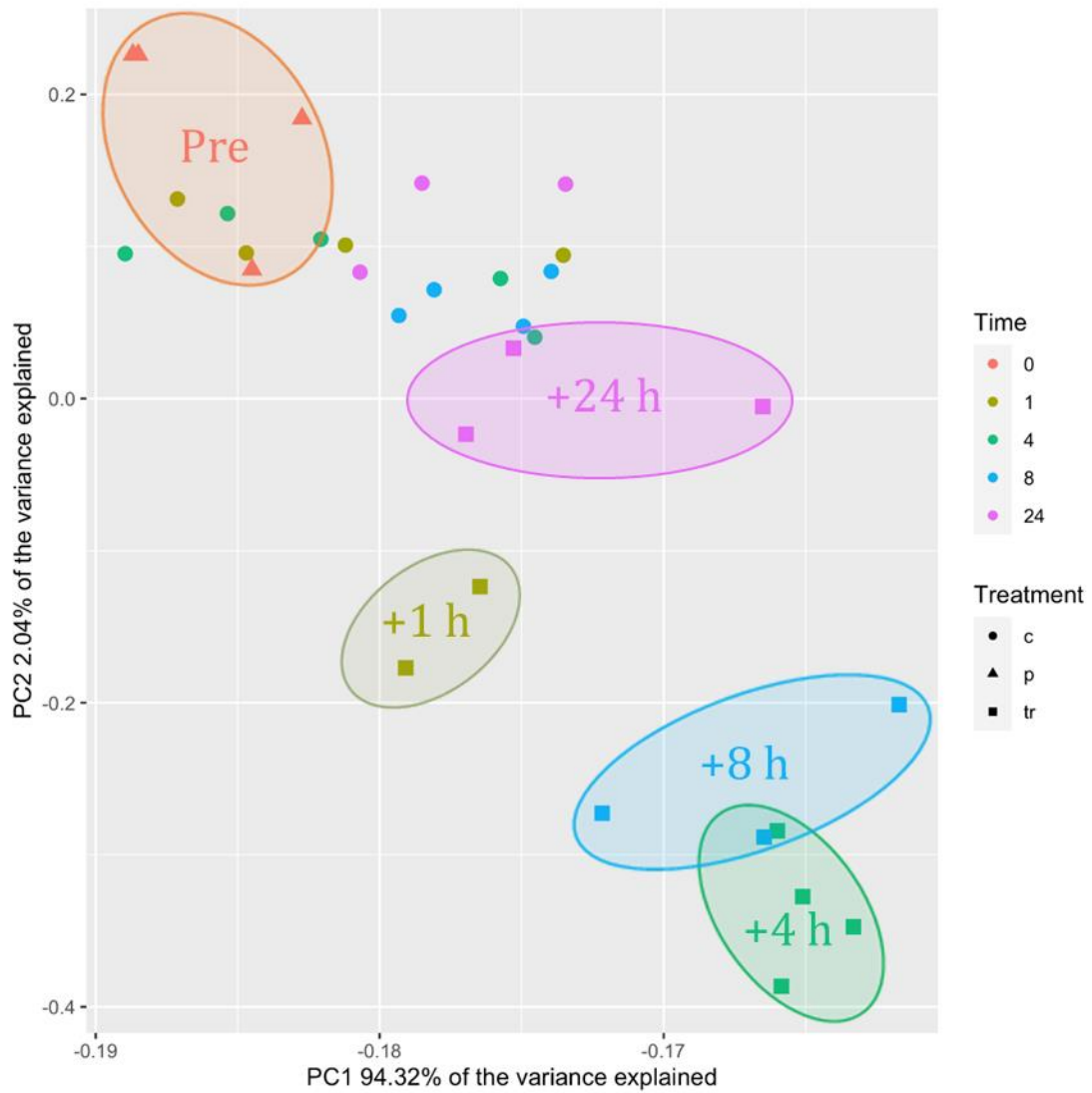


Figure 5.9: Principal components analysis. Data represents the pre-treated plants (p) ($n=4$), as well as the plants treated with either the control solution (c) or Inatreq (tr) at four timepoints: +1 hour after application ($n=4,2$), +4 hours ($n=5,4$), +8 hours ($n=4,3$), +24 hours ($n=3,3$). Treated samples have their timepoints indicated.

Hierarchical clustering of expression data was best described by dividing the data into 12 clades (Figure 5.10). A description of each of the clades is given in Table 5.3.

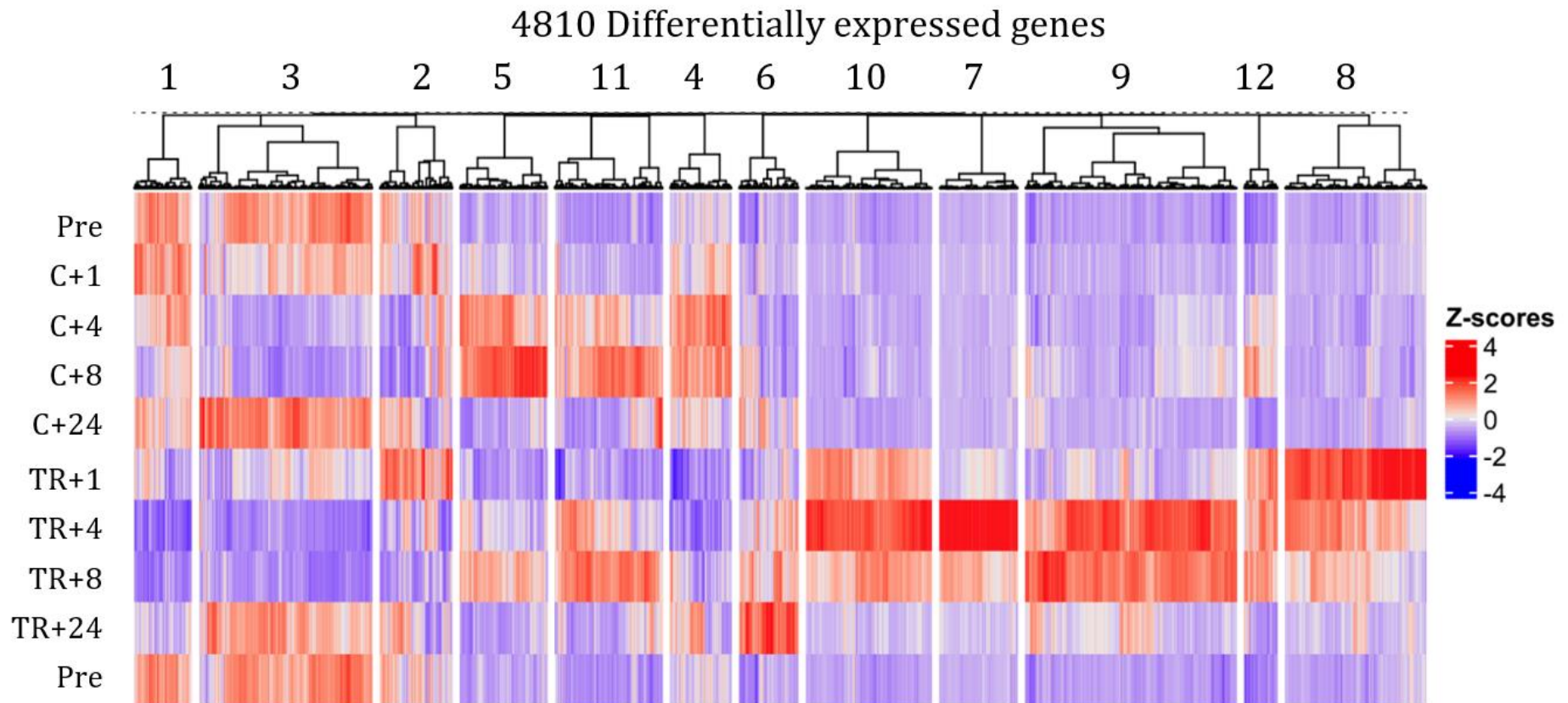


Figure 5.10: Heatmap and hierarchical clustering of 4810 *A. thaliana* genes showing differential expression, compared between 9 groups. These groups had either no treatment (pre-treated), treated with the control solution (C) or Inatreq (TR) and were analysed at 5 separate timepoints: 0 (pre-treatment group only), 1, 4, 8, and 24 hours after treatment application. Data was standardised to ensure a zero mean and unit variance. The scaled value (z-score) is plotted across a red-blue colour scale, red indicating a high score, and blue a low score.

Table 5.3: Description of differential expression (DE) within hierarchal clusters.

Cluster number	Number of genes	% of genes associated with circadian function	Description of cluster and treatment effect on DE genes
1	228	7%	Repressed by treatment from +1-+24 h after treatment.
2	289	19.4%	Background biological effect.
3	689	12.5%	Background biological effect.
4	244	3%	Repressed by treatment 1-8 h, control induced compared to pre-treatment, but not a circadian effect.
5	347	7.8%	Repression by treatment 1-4 h, and reduced induction at 8h compared to the control.
6	236	6.4%	Low induction by treatment at early stage before high level induction at a late stage.
7	312	3.2%	Very strong 4 h induction, reducing at 8 h and returns to normal by 24 h.
8	562	3.2%	Strong early induction and returns to normal by 24 h.
9	840	4.5%	4-8 h induction, before almost returning to normal by 24 h.
10	501	5.4%	General induction at early stages before returning to normal by 24 h.
11	429	7.7%	No strong differential effect.
12	133	9.8%	Induced at 1-8, but also some low-level induction in the control at 4-8 h.

Pairwise t-testing was used as an unbiased test to generate a contrast list of differentially expressed genes (Table 5.4 and Appendix 3.1).

Table 5.4: Number of differentially expressed (DE) genes found to be in contrast, using an unbiased pair-wise *t*-test.

Cluster	Genes	DE genes 1h	% contrast	DE genes 4h	% contrast	DE genes 8h	% contrast	DE genes 24h	% contrast
1	228	18	1.3%	160	6.2%	31	2.2%	4	3.3%
2	289	33	2.5%	55	2.1%	32	2.2%	2	1.7%
3	689	12	0.9%	110	4.3%	24	1.7%	7	5.8%
4	244	34	2.5%	196	7.6%	37	2.6%	2	1.7%
5	347	29	2.2%	99	3.8%	43	3.0%	0	0.0%
6	236	14	1.0%	93	3.6%	66	4.6%	31	25.8%
7	312	90	6.7%	308	12.0%	191	13.3%	11	9.2%
8	562	507	37.7%	373	14.5%	224	15.6%	16	13.3%
9	840	135	10.0%	683	26.5%	471	32.7%	31	25.8%
10	501	385	28.6%	465	18.1%	313	21.8%	15	12.5%
11	429	26	1.9%	19	0.7%	7	0.5%	1	0.8%
12	133	62	4.6%	15	0.6%	0	0.0%	0	0.0%
Total	4810	1345		2576		1439		120	

Gene ontology (GO) enrichment analysis was performed on the list of genes from each cluster and contrasts lists and identified as sets of genes associated with overrepresented biological processes (Table 5.5).

Table 5.6 lists the genes with the largest response in the contrast set in response to the application of Inatreq (Appendix 3.2 includes a larger subset of 100 of the highest responding genes).

Table 5.5: GO analysis of genes in each cluster of interest that were overrepresented in biological processes. Numbers of annotated genes associated with the process in brackets.

GO Term	GO Term
1 lipid catabolic process (98) cell wall organization (97) auxin-activated signalling pathway (1) wax biosynthetic process (1) long-chain fatty acid biosynthetic process (1) signal transduction (281) sterol biosynthetic process (3) root hair elongation (4) sexual reproduction (4) systemic acquired resistance (6)	6 lipid transport (78) regulation of photomorph (1) glutamine metabolic process (4) polysaccharide catabolic process (59) cellular response to salicylic acid stimulus (5) systemic acquired resistance (6) chitin catabolic process (7)
7 response to heat (19) response to hydrogen peroxide (4) response to high light intensity (5) response to abscisic acid (25) chitin catabolic process (7) cellular response to hypoxia (10) cell wall macromolecule catabolic process (13) response to herbivore (1) regulation of systemic acquired resistance (1) response to singlet oxygen (1) lignin biosynthetic process (16) malate transport (3) innate immune response (19) regulation of root development (5)	10 response to chitin (32) response to nitrate (4) tryptophan biosynthetic process (5) signal transduction (281) response to oomycetes (6) chitin catabolic process (7) defence response (442) pollen tube growth (11) root hair cell tip growth (1) cell wall macromolecule catabolism (13) response to oxidative stress (111) recognition of pollen (45) response to carbon dioxide (2) response to heat (19) response to osmotic stress (51) karyogamy (3) glycerol metabolic process (3)
8 response to wounding (19) response to chitin (32) response to oomycetes (6) defence response (442) signal transduction (281) response to karrikin (33) protein phosphorylation (258) response to other organism (255) response to oxidative stress (111) anaerobic respiration (8) ethylene-activated signaling pathway (30) fatty acid homeostasis (1) cellular response to chitin (1) intermembrane lipid transfer (1) phospholipid homeostasis (1) cellular response to jasmonic acid (1) triglyceride homeostasis (1) tryptophan catabolic process to kynurenine(1) integrin-mediated signaling pathway (2) response to arsenic-containing substance (2) plant-type hypersensitive response (2) response to symbiotic fungus (2) response to salt stress (48) inflammatory response (3) response to ozone (3)	9 alkaloid biosynthetic process (7) L-lysine catabolic process to acetyl-CoA via saccharopine (3) defence response to fungus, incompatible (5) response to virus (5) tricarboxylic acid cycle (7) trichome branching (1) defence response to nematode (1) cellular response to sucrose starvation (1) mitochondrial RNA catabolic process (1) nucleogenesis (1) regulation of cell division (1) response to absence of light (1) response to cadmium ion (55) embryo development - seed dormancy (14) pollen development (15) ribosomal large subunit export (2) response to arsenic-containing subst. (2) iron-sulfur cluster assembly (2) mitochondrial RNA processing (2) GMP biosynthetic process (2) DNA modification (2) ribosome assembly (2) ribosomal large subunit biogenesis (2) ubiquitin-dependent protein catabolism (61)

Table 5.6: The ten genes with the largest, most significant response (FDR $P \leq 10^{-7}$, except for 24hr where FDR $P \leq 0.05$), in each of the four contrast sets at t=1hr, t=4hr, t=8hr and t=24hr. FC= Log₂ fold change, FDR= False discovery rate corrected *p*-value, C= cluster membership. Genes were filtered to show only contrasts with an average expression greater than the set mean.

t	Gene code	FC	FDR	C	Gene description
+1	AT1G15520	6.66	1.95E-10	10	pleiotropic drug resistance 12 (PDR12)
	AT1G19020	5.62	3.61E-13	8	unknown protein
	AT1G05680	5.43	1.19E-11	7	UGT74E2
	AT3G25780	5.28	4.76E-14	8	AOC3; response to salt stress, fungus, JA biosyn
	AT5G59820	5.18	7.15E-13	10	RESPONSIVE TO HIGH LIGHT 41 (RHL41)
	AT2G29460	5.15	9.01E-11	10	glutathione S-transferase tau 4 (GSTU4)
	AT1G32960	5.04	1.11E-12	10	SBT3.3; proteolysis, neg regn catalytic activity
	AT1G66090	4.85	1.02E-13	8	Disease resistance protein (TIR-NBS class) prot serine/threonine kinase, sugar+ATP binding
	AT4G21390	4.80	2.11E-14	8	binding
	AT4G30280	4.72	2.83E-13	8	XTH18
+4	AT1G15520	7.50	4.44E-13	10	pleiotropic drug resistance 12 (PDR12)
	AT1G05680	6.68	1.90E-17	7	UGT74E2
	AT1G32350	6.57	1.23E-11	7	alternative oxidase 1D (AOX1D)
	AT2G41730	6.56	4.56E-18	7	unknown protein
	AT1G32960	6.55	3.87E-14	10	SBT3.3; proteolysis, neg regn catalytic activity
	AT2G34500	6.45	1.15E-10	7	CYP710A1
	AT2G04050	6.23	5.38E-18	7	MATE efflux family protein
	AT2G29460	6.12	2.71E-14	10	glutathione S-transferase tau 4 (GSTU4)
	AT1G17170	6.10	4.22E-17	7	glutathione S-transferase TAU 24 (GSTU24)
	AT2G29470	6.04	7.08E-08	10	glutathione S-transferase tau 3 (GSTU3) PMZ; response to abscisic acid stimulus and chitin
AT3G28210	6.00	1.94E-11	10	chitin	
+8	AT1G15520	6.02	1.19E-08	10	pleiotropic drug resistance 12 (PDR12)
	AT1G05680	5.72	1.52E-12	7	UGT74E2
	AT2G41730	5.63	5.17E-13	7	unknown protein
	AT1G32960	5.41	2.51E-10	10	SBT3.3; proteolysis, neg regn catalytic activity
	AT1G17170	5.04	2.92E-13	7	glutathione S-transferase TAU 24 (GSTU24)
	AT2G29460	4.95	8.00E-11	10	glutathione S-transferase tau 4 (GSTU4)
	AT3G26830	4.88	2.85E-08	10	PHYTOALEXIN DEFICIENT 3 (PAD3) PMZ; response to abscisic acid stimulus and chitin
	AT3G28210	4.87	6.52E-08	10	chitin
	AT2G04050	4.76	1.94E-13	7	MATE efflux family protein Bifunctional inhibitor/lipid-transfer/seed storage
AT3G22600	4.58	8.71E-08	9	storage	

Table 5.7: Lists the ten genes with the largest, most significant response (cont.)

t	Gene code	FC	FDR	C	Gene description
+24	AT4G12490	3.41	0.00097	6	Bifunctional inhibitor/lipid-transfer/seed storage
	AT3G57260	2.53	0.00540	6	beta-1,3-glucanase 2 (BGL2)
	AT1G32960	2.03	0.00540	10	SBT3.3; proteolysis, neg regn catalytic activity
	AT4G16260	1.95	0.00661	9	Glycosyl hydrolase superfamily protein
	AT1G21520	1.86	0.00302	9	unknown protein
	AT3G43270	1.75	0.00357	9	Plant invertase/pectin methylesterase inhibitor
	AT3G26210	1.72	0.00353	9	CYP71B23
	AT1G66920	1.59	0.00302	8	Protein kinase superfamily protein
	AT5G10380	1.44	0.00302	6	RING1
	AT5G46350	1.43	0.00522	9	WRKY DNA-binding protein 8 (WRKY8)

5.4. Discussion

5.4.1. Development of a HTP thermal imaging platform.

The HTP thermal imaging platform developed in this chapter was produced to offer an alternative methodology to observe and compare transpiration rate in plants exposed to differential watering and following the application of Inatreq. This was developed using low-cost components, and designed to be flexible to the user's needs, allowing the online instructions we have provided to be adjusted to the individual users' requirements. Mechanical and electrical components that were used in this have been popularized by the maker community and allows the deployment of bespoke systems at a fraction of the cost of "off the shelf" alternatives.

5.4.2. Non-fungicidal effects of Inatreq upon *A. thaliana*.

The application of Inatreq to the model plant *A. thaliana* produced many of the same effects as when applied to wheat (see Chapter 3). Reductions in transpiration can often be assumed as a function of reducing stomatal conductance, and the WT ecotypes responded in a similar way to wheat (Section 5.3.2). The improvement of RWC also reflects the findings in wheat, suggesting that the reduction of transpiration due to stomatal conductance acts to preserve water within the plants and improve its water use efficiency.

However, it was found using *A. thaliana* mutant plants that this response was not observed in plants that had mutations in either the perception of ABA or the biosynthesis

of ABA. ABA is a central regulator in the control of stomatal conductance under abiotic stress. The loss of effect in mutant varieties could potentially suggest that the effects associated with the application of ABA are linked to the ABA response pathway.

Controlling the rate of transpiration by regulating stomatal conductance has been highlighted as a target for improving drought tolerance in crop plants (Bertolino *et al.*, 2019). It has been found that the reduction of stomatal number itself can be reduced by up to 50%, dramatically reducing the potential transpiration rate, with little to no observable influence on plant growth parameters or yield (Dunn *et al.*, 2019). This was highlighted as a target for breeders to improve the water use efficiency of crops grown in drought-prone environments. Ultimately, short-term water loss is directly regulated by the degree of stomatal openness, whereas long-term water losses are more influenced by the stomatal number. Reducing the stomatal number can be associated with negative impacts on the plant, especially if heat sensitive, due to the reduction in evaporative cooling (Buckley *et al.*, 2020). However, being able to influence the stomatal conductance of a plant in a reversible manner may offer a more flexible opportunity, without the long-term damage that may result due to a reduced stomatal density. Due to these issues associated with reducing stomatal density, the length of time it would take to breed for lower stomatal density, or the low level of acceptance of genetic modification to use it as a tool to reduce stomatal conductance, it has been proposed that the development of compounds that may regulate stomatal conductance could be an invaluable tool in mitigating the effects of drought in the future (Kim, 2014). ABA mimics have presented an opportunity to offer short term control over stomatal conductance, utilizing the natural processes associated with abiotic stress (Cao *et al.*, 2013, 2017; Vaidya *et al.*, 2019). Due to Inatreq not influencing transpiration rate in *aba2*, an ABA biosynthesis mutant, it may be assumed that the structure of Inatreq does not mimic ABA.

5.4.3. RNA sequencing

The principal component analysis plot shows that the sequencing has successfully captured the expected experimental system, with no signs of batch effect. The samples in the control groups are closer to each other than to their respective treatment samples, and no closer to each other than to other control timepoints, suggesting that the variance in this meta-grouping represents the general, mixed, biological variation expected of *Arabidopsis* plants sampled over a 24hr circadian period. The pre-treatment, unsprayed samples grouping with the controls, agrees with this while their distinct but small difference specifically from the 24hr control group, sampled at the same point in the

circadian cycle, offers the possibility that there is a small residual effect from spraying. Touch response is a well-studied field, and plants have been found to have touch responses to the application of wider range of compounds (Braam, 2004) including the application of just water (Braam and Davis, 1990). The treatment samples show clear within-timepoint groupings advancing on the x-y diagonal with a maximal variance from the controls at 4hr then returning to close to control state at 24hr, suggesting that the dominant effect in the measured experimental system is from the application of the Inatreq treatment and not from the circadian clock.

Once it was confirmed that the application of Inatreq was the cause of differential expression of genes between the treated and control plants at different timepoints, these were then grouped based upon hierarchical clustering. GO analysis was conducted on clusters that showed differential expression profiles that were most likely to be associated with the application of Inatreq, to identify biological processes that may be associated with these DE genes. Of note, cluster 7 had the highest level of differential expression at any point (+4 hours, Figure 5.7). Two of the biological processes associated with the most differentially expressed genes in this cluster were: “response to ABA”, and “transport of Malate”. Both processes would potentially support the hypothesis that the application of Inatreq influences the ABA signalling pathway. “Response to ABA” is a clear indicator of influencing the ABA signalling pathway, but the transport and accumulation of malate is widely understood to act as an osmoticum and/or signalling molecule for guard cell turgor pressure (Hedrich *et al.*, 1994; Assmann, 2003; Dong *et al.*, 2018), which further supports the hypothesis. Further to these there were a variety of other biological processes within different clusters that may be associated with improved drought performance and the reduction of stomatal conductance. These include “response to hydrogen peroxide” (Cho *et al.*, 2013; Hossain *et al.*, 2015; Saruhan Guler and Pehlivan, 2016), and signalling responses to other phytohormones such as jasmonic acid and ethylene which are intrinsically linked to the ABA signalling pathway (Leung and Giraudat, 1998; Anderson *et al.*, 2004).

From the list of the most differentially expressed genes, there were also genes associated with ABA signalling. The zinc finger gene AT3G28210 has one of the most significant responses at t=4-8, and is known to be upregulated in transgenic *Arabidopsis* plants that have improved drought tolerance (Mei *et al.*, 2021). The most differentially expressed gene at three time points (+1, +4, +8 hrs) was pleiotropic drug resistance 12 (PDR12) (AT1G15520). This gene encodes the PDR12 ABC transporter in *A. thaliana* which has been reported to be a plasma membrane ABA uptake transporter. It has been shown that

this transporter is critical for rapid responses to ABA, and that *A. thaliana* plants with a loss of function mutation in this gene (*atabcg40*) have slower stomatal closure and reduced drought tolerance (Kang *et al.*, 2010). Considering this is a gene associated with rapid responses to ABA, it is of note that it was the most differentially expressed genes in the first three timepoints post Inatreq application. Other notable genes include the WRKY8 binding protein is associated with ABA signalling and abiotic stress response (Li *et al.*, 2020).

At timepoints +4 and +8 hours after Inatreq application, one of the most differentially expressed genes encodes an unknown protein, AT2G41730. Annotations of this gene suggest that it is primarily expressed in the sepal, stamen and in guard cells and potentially linked to calcium signalling. The plants that were harvested for RNA sequencing in this study were harvested before any flowers were able to form. Therefore, if the annotation is accurate, it suggests that this was primarily differentially expressed in the stomatal guard cell and provides an interesting target gene for future research.

Chapter 6. Conclusions and Future Work.

Fungicides are vital tools in modern day agriculture to protect yields from detrimental impacts of disease. In Northern Europe one of the most important diseases that requires control with fungicides is *Septoria tritici* blotch (STB), which can result in up to 50% yield losses in severe epidemics (Eyal, 1973; Eyal *et al.*, 1987). Due to this fungicides are critical in growers attaining the yield required to keep up with demand, with almost 40% of pesticide sales within the EU being for fungicides (Zubrod *et al.*, 2019). With increasing levels of resistance forming against previously-effective fungicides (Fraaije *et al.*, 2005, 2007, 2012; Cools and Fraaije, 2008; Brisson *et al.*, 2010; Cools *et al.*, 2011b), and increasing regulatory restrictions on pesticide products (Donley, 2019), the discovery and release of new fungicides with novel modes of action is vital. Fenpicoxamid, the active ingredient in Inatreq™ active is the first picolinamide fungicide to be commercially released and is an effective crop protectant from *Septoria tritici* blotch.

As well as the detrimental effects of crop disease that looks to threaten global crop production yields, abiotic stress such as drought is becoming more prominent, and increasing amounts of research is being directed towards its tolerance. One solution that has been identified is the application of biostimulants to help the plant mitigate the detrimental effects of drought (Fleming *et al.*, 2019). Preliminary research into Inatreq found that it had non-fungicidal effects upon the plant that behaved similarly to some fungicides.

The aims of this thesis were to:

- Investigate the curative fungicidal activity of Inatreq, using traditional and non-traditional assessment methodologies (Chapter 2).
- Characterising the non-fungicidal effects of Inatreq on wheat grown in glasshouses and controlled environment growth chambers (Chapter 3).
- Confirming the effects observed in Chapter 3 in large scale field and automated glasshouse trials (Chapter 4).
- Developing a high-throughput tool for assessment of non-fungicidal effects of Inatreq on a model species and investigate the underlying genetic basis of the response (Chapter 5).

6.1. Fungicidal activity of Inatreq

The work reported in Chapter 2 compared the curative activity of Inatreq to a variety of commercial alternatives. It was found that Inatreq performed extremely well, at both the full field application dosage, as well as at a reduced (75%) dosage, when compared to the panel of other fungicides (Figure 2.8). At present DMIs are one of the few classes of fungicides that offer effective curative activity to STB (Tsuda *et al.*, 2004; Sanssené *et al.*, 2011), which is confirmed in this work by Librax being one of the best performing products alongside Inatreq. In contrast to Inatreq, Librax contains two active ingredients, fluxapyroxad (SDHI) and metconazole (DMI). Despite the efficacy of DMIs, there are increasing instances of resistance beginning to occur (Heick *et al.*, 2017), highlighting the importance of developing alternatives.

Traditionally fungicides are applied preventatively and in excess, so much so that it is estimated that fungicide application can be reduced by as much as 47% without detriment, providing it is applied correctly (Lechenet *et al.*, 2017). With increasing regulatory pressure to reduce pesticide application and the adoption of IPM strategies, this will likely change. Decreased rates of pesticide application will therefore mean the integration of precision and variable rate applications will become more commonplace (Schirrmann *et al.*, 2016; Yang, 2020). For precision agriculture to be successful it requires tools that offer accurate detection of diseases (Oerke *et al.*, 2014; Mahlein, 2016) to be combined with effective curative fungicide chemistry. Inatreq is primarily targeted towards the control of *Septoria tritici* blotch, which asymptotically colonizes the leaf material for up to 21 days, before sudden onset of necrosis. This necrosis has the potential to reduce wheat yield by up to 50% (Fones and Gurr, 2015; Torriani *et al.*, 2015) and once symptoms become apparent, it is likely too late to prevent the losses curatively. Therefore, curative control will need to occur during the asymptomatic growth cycle.

Chemical fungicides are becoming increasingly unpopular, due to a variety of associated negative impacts upon the environment such as soil erosion and contamination of water supplies affecting aquatic ecosystems (Dale and Polasky, 2007; Zubrod *et al.*, 2019) as well as negative public perception (Saleh *et al.*, 2021). Due to these concerns there are increasing restrictions coming into place over the usage of certain pesticides, especially within the E.U. (Donley, 2019). Due to these restrictions the future of crop protection is changing, with emphasis on management strategies, such as integrated pest management (IPM), increased utilization of biological control agents (Leontopoulos, 2020), the integration of better resistance in crop plants and the reduced and more targeted chemical application (Barzman *et al.*, 2015). Another set of tools that are increasingly

being suggested as a solution, are natural products. These are products that are naturally produced by organisms and have naturally occurring pesticidal activity. These and offer a more appealing crop protection chemical than many synthesized chemicals (Gerwick and Sparks, 2014), and have been generally regarded as less concern and have easier pathways to market (Marchand, 2015). As one of the first new fungicide mode of actions to enter the market in the last 10 years, Inatreq and picolinamides therefore offer an example for the future of fungicide development, due to its source of discovery, and its amenability to a wide array of application strategies.

6.2. Non-fungicidal effects of Inatreq

The experiments reported in Chapter 3 showed that the application of Inatreq resulted in an increase in plant biomass accumulation, as well as reductions in stomatal conductance. These differences were observed in plants that were grown under ample watering, as well as plants that had their watering completely withheld. This effect was consistent across two different wheat varieties. The reduction in stomatal conductance associated with the application of Inatreq was hypothesized to improve the plants tolerance to drought, which was supported by the improved relative water content of plants grown with ample and limited water availability. These results reflect previous findings with other fungicides where they have been found to improve biomass accumulation, as well as tolerance of abiotic stresses (Hojati *et al.*, 2011; Ajigboye *et al.*, 2014b; Kuznetsov *et al.*, 2018). These findings also challenge the previously perceived hypothesis that this biostimulant-like effect was related to the active ingredients chemical class and specific binding (Kuznetsov *et al.*, 2018). To further characterize this effect, plants were observed in a HTP glasshouse trial and a field trial (Chapter 4). These experiments offered a step change in the translatability of their findings to a natural environment from those of Chapter 3. Where Chapter 3 was conducted in controlled environments, Chapter 4 was conducted in two environments where there was greater variability of environmental conditions, which would demonstrate if the traits in chapter 3 would still be apparent *in agri*. It was found that under low water availability, the variety Extase was able to demonstrate both an improved biomass accumulation, as well as photosynthetic efficiency. It was also of note that, although not statistically significant, applications of the adjuvants associated with Inatreq were associated with the accumulation of increased plant biomass. This highlights the importance of not attributing these non-fungicidal effects of fungicides directly to their active ingredients, as has been done in the past (Andres and Agudelo, 2013; Smith *et al.*, 2013; Ajigboye *et al.*, 2014a, 2017; Dal Cortivo *et*

al., 2017; Kuznetsov *et al.*, 2018). In the HTP glasshouse screen, there appeared to be varietal differences in plants response to Inatreq, as Skyfall did not show any physical response to the application of Inatreq, although it did appear to show a similar improvement of photosynthetic efficiency. This is in contrast to the observations reported in the previous chapter where Skyfall showed comparable changes to Extase. This may suggest a varietal response to Inatreq or highlight a difference in growth habit between the varieties leading to inaccuracies in inferring biomass from image data.

6.3. Model plant studies

A similar response to that seen in wheat was observed on Inatreq application to the model species *Arabidopsis thaliana*. This allowed the testing of responses in known mutants and an RNA-sequencing study in a better-annotated species (Chapter 5). Mutants in ABA biosynthesis and perception were insensitive to the application of Inatreq, suggesting the involvement of the ABA signalling pathway. Time-course RNA sequencing revealed processes and genes differentially expressed following Inatreq application (Chapter 5).

6.4. Phenotyping

Much of this work was focused on the characterization of Inatreq's effects, both fungicidal and non-fungicidal, and therefore phenotyping tools were important throughout. This work employed a wide range of phenotyping tools, able to characterize phenotypic data in a variety of settings and developed new methods where none were available.

To allow the characterisation of Inatreq's curative activity, the work reported in Chapter 2 included the validation of a simple disease scoring methodology based in the freely available image analysis tool ImageJ (Schindelin *et al.*, 2012). This tool was developed to remove inherent user bias from the traditional manual scoring protocols that are still widely used (Chiang *et al.*, 2016). This tool was shown to give comparable results to an expert panel and offers an unbiased method for future studies.

The increase in uptake of image-based phenotyping, and integration of these with highly automated systems has gone a long way in widening the perceived "phenotyping bottleneck" (Furbank and Tester, 2011). However, many of these sophisticated platforms now come with high upfront costs and therefore limits their availability and accessibility. The thermal imaging platform reported in Chapter 5 was built and developed using readily available, low-cost components and was found to be effective as a tool for

monitoring temperature as a proxy for stomatal conductance. Table 6.1 shows the costs of this system compared to equivalent commercial systems.

Table 6.1: List of specifications and cost of the HTP thermal imaging platform and commercial/research "off the shelf" alternatives. Taken from (Bagley *et al.*, 2020)

Specification	Thermal Imager	CPIB Imaging Robot ³	Commercial Actuator ¹
Drive	Belt and pinion	Toothed belt	Toothed belt
Travel	1.2 m	1.8 m	1.2 m
Step size	200 μm	300 μm	600 μm
Microstep size (minimum)	6.25 μm (32 microsteps)	300 μm (n/a)	9.4 μm (64 microsteps)
Maximum speed	125 mm/s	30 mm/s	5 m/s
Repeatability	$\sim 5 \mu\text{m}$	0.5 mm	200 μm
Temporal resolution	$\sim 40 \text{ s/run}$	$\sim 2 \text{ min/run}$	$\sim 8 \text{ s/run}$
Cost ²	€235	€1060	€3475

¹Model ZLW-1660, Igus GmbH

²Cost excludes camera and host PC.

³(French *et al.*, 2012)

The thermal imager can also be used for long-term studies (Figure 6.1), allowing responses to be monitored at a fine temporal resolution ($\sim 40\text{s}$ interval). This will be of great benefit when integrating responses to treatments with diurnal changes in transpiration.

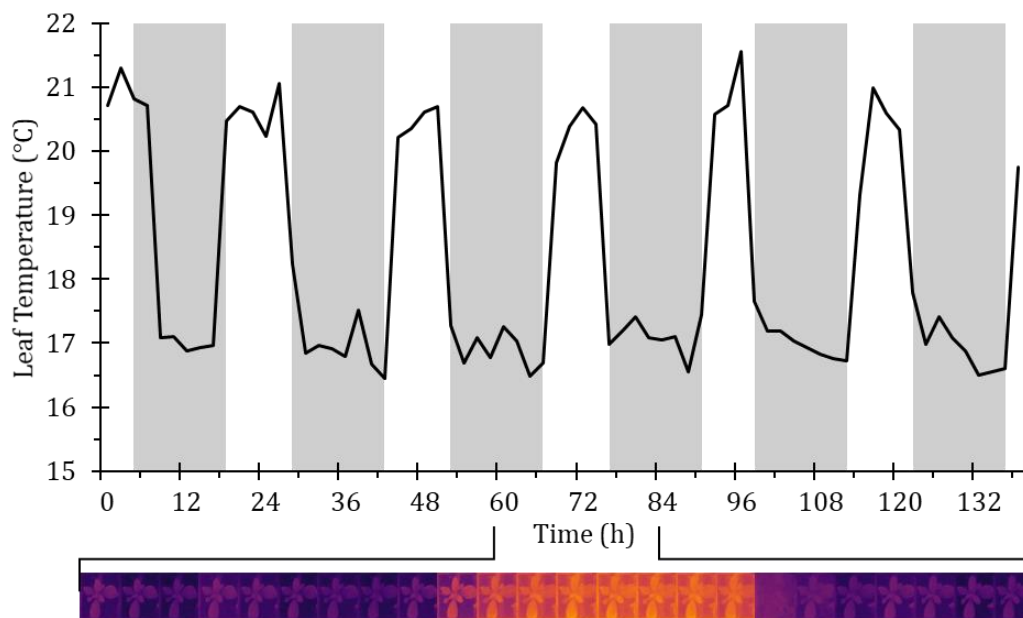


Figure 6.1: Time course of canopy temperatures taken using the Thermal Imager.

6.5. Future work

The initial aims of this thesis were met, and the findings presented offer valuable opportunities for future work to be carried out. Inatreq's efficacy as a curative fungicide was demonstrated in experiments reported in Chapter 2 that were mostly conducted in artificial environments. To build upon these findings, further work would need to be carried out in the field (over multiple sites and multiple seasons), to observe its curative efficacy in a more natural setting. As well as this, curative fungicides need to be better integrated with variable rate systems and precision application tools. Improvements in image-based assessment need to continue, but with images recorded in the field, rather than in the lab. These image analysis tools can be integrated with new spraying technology and may utilize alternative imaging sensors such as hyperspectral imaging, thermal, and chlorophyll fluorescence.

The automated glass house trial offered large amounts of data, on a temporal scale that would not be possible if using traditional phenotyping methods. Integrating alternative biomass predictors would be prudent to better understand the difference between Skyfall and Extase, for example using 3D canopy measurements.

Interaction analysis of the RNA-sequencing data that has been gathered in chapter 5 could be compared with published results using a tool such as MapMan (Thimm, 2004) may help to shed light on the specific responses to Inatreq application and compare it to other responses that have been observed. RNA sequencing should be repeated in wheat, and compared with the *A. thaliana* data, to find if there are any common orthologues. The results in *Arabidopsis* have provided a list of potential candidate genes and biological processes that could be further investigated to better dissect the mode of non-fungicidal activity. It appears from the data presented so far that this response involves the ABA pathway, but there are other stress related genes that were upregulated and candidates for future study. It would also be of interest to compare this response to the response to other fungicides with reported biostimulant-like effects, to better understand if this is a common mode of action between different fungicides, or if they each have unique modes of action. This mode of action may then be used as a start point for the design of future biostimulants. It is however still important to note that the ABA signalling pathway is complex, and not only effects abiotic stress responses, but also may influence responses to biotic stresses such as plant immune responses, as well as being intrinsically linked to other plant hormones associated with plant immune responses; salicylic acid, jasmonates and ethylene (Pieterse *et al.*, 2009) (Fig 6.2). This would therefore need to also be better understood, if being considered as a biostimulant target.

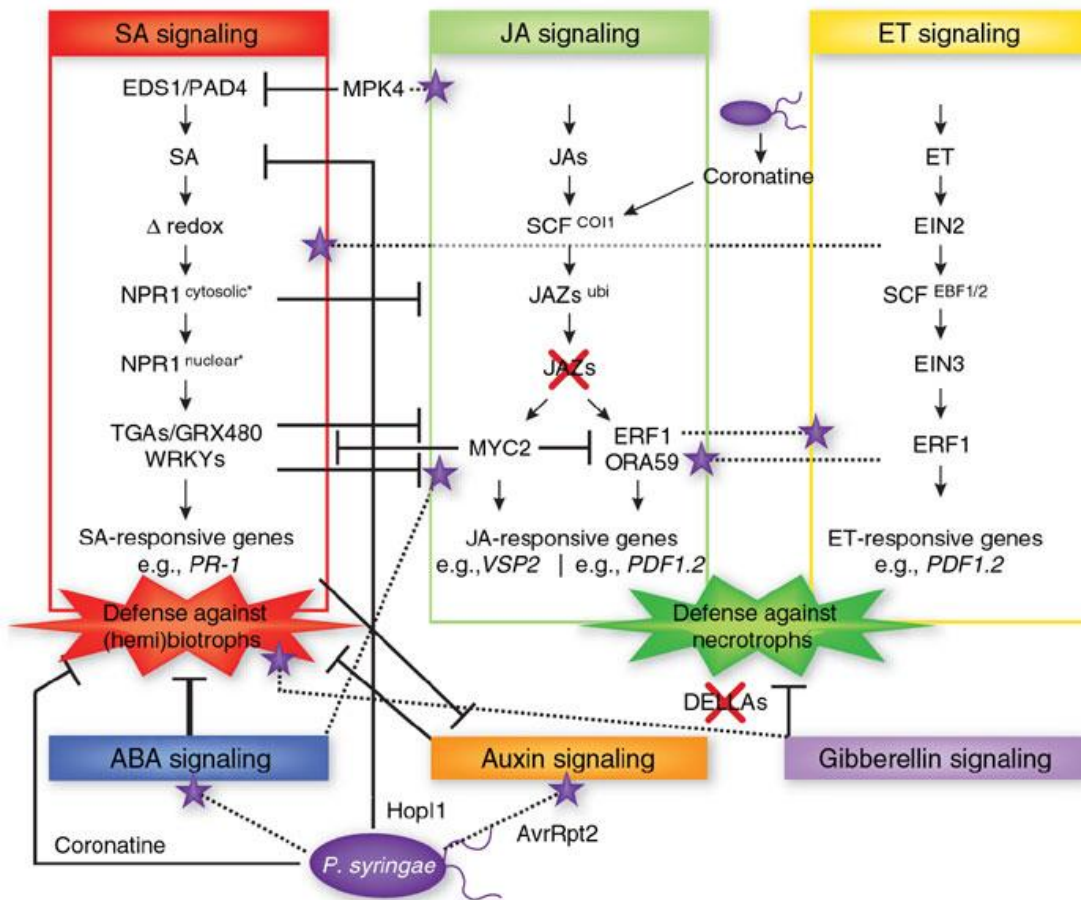


Figure 42: The networking of phytohormones involved in plant immune response, highlighting the role ABA plays and its interactions with other phytohormones. SA: Salicylic, JA: Jasmonates, ET: Ethylene. Figure taken from (Pieterse *et al.*, 2009)

References

- Abhinandan K, Skori L, Stanic M, Hickerson NMN, Jamshed M, Samuel MA.** 2018. Abiotic stress signaling in wheat – An inclusive overview of hormonal interactions during abiotic stress responses in wheat. *Frontiers in Plant Science* **9**, 734.
- Abunnour MA, Hashim NBM, Bin Jaafar M.** 2016. Agricultural water demand, water quality and crop suitability in Souk-Alkhamis Al-Khums, Libya. *IOP Conference Series: Earth and Environmental Science*. Institute of Physics Publishing, .
- Acharya BR, Jeon BW, Zhang W, Assmann SM.** 2013. Open Stomata 1 (OST1) is limiting in abscisic acid responses of Arabidopsis guard cells. *New Phytologist* **200**, 1049–1063.
- Ainsworth GC.** 2009. *Introduction to the history of mycology*. New York: Cambridge University Press.
- Ajigboye OO, Lu C, Murchie EH, Schlatter C, Swart G, Ray R V.** 2017. Altered gene expression by sedaxane increases PSII efficiency, photosynthesis and growth and improves tolerance to drought in wheat seedlings. *Pesticide Biochemistry and Physiology* **137**, 49–61.
- Ajigboye OO, Murchie E, Ray R V.** 2014a. Foliar application of isopyrazam and epoxiconazole improves photosystem II efficiency, biomass and yield in winter wheat. *Pesticide Biochemistry and Physiology* **114**, 52–60.
- Akpınar BA, Yuce M, Lucas S, Vrána J, Burešová V, Doležel J, Budak H.** 2015. Molecular organization and comparative analysis of chromosome 5B of the wild wheat ancestor *Triticum dicoccoides*. *Scientific Reports* **5**, 1–13.
- Alexa A, Rahnenführer J.** 2020. *topGO: Enrichment Analysis for Gene Ontology*. *R package version 2.42.0*.
- Anderson JP, Badruzsaufari E, Schenk PM, Manners JM, Desmond OJ, Ehlert C, Maclean DJ, Ebert PR, Kazan K.** 2004. Antagonistic interaction between abscisic acid and jasmonate-ethylene signaling pathways modulates defense gene expression and disease resistance in arabidopsis. *Plant Cell* **16**, 3460–3479.
- Andres C, Agudelo B.** 2013. Effects of fungicides on physiological parameters and yield formation of wheat assessed by non-invasive sensors.

Aroca R. 2013. *Plant responses to drought stress: From morphological to molecular features* (R Aroca, Ed.). Berlin: Springer-Verlag Berlin Heidelberg.

Ashraf M, Harris PJC. 2013. Photosynthesis under stressful environments: An overview. *Photosynthetica* **51**, 163–190.

Assmann SM. 2003. Open Stomata1 opens the door to ABA signaling in Arabidopsis guard cells. *Trends in Plant Science* **8**, 151–153.

Ault TR. 2020. On the essentials of drought in a changing climate. *Science* **368**, 256–260.

Awlia M, Nigro A, Fajkus J, Schmoeckel SM, Negrão S, Santelia D, Trtílek M, Tester M, Julkowska MM, Panzarová K. 2016. High-Throughput Non-destructive Phenotyping of Traits that Contribute to Salinity Tolerance in Arabidopsis thaliana. *Frontiers in Plant Science* **7**, 1414.

Andrews S. (2010). FastQC: a quality control tool for high throughput sequence data. Available online at: <http://www.bioinformatics.babraham.ac.uk/projects/fastqc>

Bacete L, Hamann T. 2020. The role of mechanoperception in plant cell wall integrity maintenance. *Plants* **9**.

Bagley SA, Atkinson JA, Hunt H, Wilson MH, Pridmore TP, Wells DM. 2020. Low-Cost Automated Vectors and Modular Environmental Sensors for Plant Phenotyping. *Sensors* **20**, 3319.

Baker NR. 2004. Applications of chlorophyll fluorescence can improve crop production strategies: an examination of future possibilities. *Journal of Experimental Botany* **55**, 1607–1621.

Baker NR. 2008. Chlorophyll Fluorescence: A Probe of Photosynthesis In Vivo. *Annual Review of Plant Biology* **59**, 89–113.

Bakker MM, Govers G, Jones RA, Rounsevell MDA. 2007. The effect of soil erosion on Europe's crop yields. *Ecosystems* **10**, 1209–1219.

Barba LA. 2018. Terminologies for Reproducible Research. Preprint <https://arxiv.org/abs/1802.03311arXiv>.

- Barzman M, Bàrberi P, Birch ANE, et al.** 2015. Eight principles of integrated pest management. *Agronomy for Sustainable Development* **35**, 1199–1215.
- Benjamini Y, Hochberg Y.** 1995. Controlling the False Discovery Rate: A Practical and Powerful Approach to Multiple Testing. *Journal of the Royal Statistical Society: Series B (Methodological)* **57**, 289–300.
- Berdugo CA, Mahlein A-K, Steiner U, Oerke E-C, Dehne H-W.** 2013. Use of non-invasive sensors to detect beneficial effects of fungicides on wheat physiology. XI international conference on precision agriculture. 135–139.
- Berdugo CA, Steiner U, Dehne HW, Oerke EC.** 2012. Effect of bixafen on senescence and yield formation of wheat. *Pesticide Biochemistry and Physiology* **104**, 171–177.
- Berger B, Parent B, Tester M.** 2010*a*. High-throughput shoot imaging to study drought responses. *Journal of Experimental Botany* **61**, 3519–3528.
- Berger B, Parent B, Tester M.** 2010*b*. High-throughput shoot imaging to study drought responses. *Journal of Experimental Botany* **61**, 3519–3528.
- Bertolino LT, Caine RS, Gray JE.** 2019. Impact of stomatal density and morphology on water-use efficiency in a changing world. *Frontiers in Plant Science* **10**, 6.
- Bland JM, Altman DG.** 2010. Statistical methods for assessing agreement between two methods of clinical measurement. *International Journal of Nursing Studies* **47**, 931–936.
- Bock CH, Parker PE, Cook AZ, Gottwald TR.** 2008. Characteristics of the perception of different severity measures of citrus canker and the relationships between the various symptom types. *Plant Disease* **92**, 927–939.
- Bockus WW, Bowden RL, Hunger RM, Murray TD, Smiley RW.** 2010. *Compendium of wheat diseases and pests*. St. Paul: American Phytopathological Society (APS Press).
- Borlaug NE.** 1972. Nobel Lecture: The Green Revolution, Peace, and Humanity. 'Speech delivered upon receipt of the 1970 Nobel Peace Prize'. Centro Internacional de Mejoramiento de Maiz y Trigo: El Batán, Mexico, .
- Braam J.** 2004. In touch: plant responses to mechanical stimuli. *New Phytologist* **165**, 373–389.

- Braam J, Davis RW.** 1990. Rain-, wind-, and touch-induced expression of calmodulin and calmodulin-related genes in Arabidopsis. *Cell* **60**, 357–364.
- Brent K, Hollomon D.** 2007. *Fungicide Resistance: The Assessment of Risk*. AImprint United Kingdom.
- Brisson N, Gate P, Gouache D, Charmet G, Oury FX, Huard F.** 2010. Why are wheat yields stagnating in Europe? A comprehensive data analysis for France. *Field Crops Research* **119**, 201–212.
- Brühl CA, Zaller JG.** 2019. Biodiversity Decline as a Consequence of an Inappropriate Environmental Risk Assessment of Pesticides. *Frontiers in Environmental Science* **7**, 177.
- Buckley CR, Caine RS, Gray JE.** 2020. Pores for Thought: Can Genetic Manipulation of Stomatal Density Protect Future Rice Yields? *Frontiers in Plant Science* **10**, 1.
- Caldwell CD, Starratt CE.** 1987. Response of max spring wheat to management inputs. *Canadian Journal of Plant Science* **67**, 645–652.
- Calvo P, Nelson L, Kloepper JW.** 2014. Agricultural uses of plant biostimulants. *Plant and Soil* **383**, 3–41.
- Campbell MT, Knecht AC, Berger B, Brien CJ, Wang D, Walia H.** 2015. Integrating image-based phenomics and association analysis to dissect the genetic architecture of temporal salinity responses in rice. *Plant Physiology* **168**, 1476–1489.
- Cao M, Liu X, Zhang Y, et al.** 2013. An ABA-mimicking ligand that reduces water loss and promotes drought resistance in plants. *Cell Research* **23**, 1043–1054.
- Cao MJ, Zhang YL, Liu X, et al.** 2017. Combining chemical and genetic approaches to increase drought resistance in plants. *Nature Communications* **8**, 1–12.
- Chaerle L, Lenk S, Leinonen I, Jones HG, Van Der Straeten D, Buschmann C.** 2009. Multi-sensor plant imaging: Towards the development of a stress-catalogue. *Biotechnology Journal* **4**, 1152–1167.
- Charmet G.** 2011. Wheat domestication: Lessons for the future. *Comptes Rendus - Biologies* **334**, 212–220.

- Chiang K-S, Bock CH, Lee I-H, El Jarroudi M, Delfosse P.** 2016. Plant Disease Severity Assessment—How Rater Bias, Assessment Method, and Experimental Design Affect Hypothesis Testing and Resource Use Efficiency. *Phytopathology* **106**, 1451–1464.
- Cho SM, Kim YH, Anderson AJ, Kim YC.** 2013. Nitric oxide and hydrogen peroxide production are involved in systemic drought tolerance induced by 2R,3R-butanediol in *Arabidopsis thaliana*. *Plant Pathology Journal* **29**, 427–434.
- Cools HJ, Fraaije BA.** 2008. Are azole fungicides losing ground against *Septoria* wheat disease? Resistance mechanisms in *Mycosphaerella graminicola*. *Pest Management Science* **64**, 681–684.
- Cools HJ, Mullins JGL, Fraaije BA, Parker JE, Kelly DE, Lucas JA, Kelly SL.** 2011a. Impact of recently emerged sterol 14 α -demethylase (CYP51) variants of *Mycosphaerella graminicola* on azole fungicide sensitivity. *Applied and environmental microbiology* **77**, 3830–7.
- Dai A.** 2013. Increasing drought under global warming in observations and models. *Nature Climate Change* **3**, 52–58.
- Dai A, Wigley TML.** 2000. Global patterns of ENSO-induced precipitation. *Geophysical Research Letters* **27**, 1283–1286.
- Dal Cortivo C, Conselvan GB, Carletti P, Barion G, Sella L, Vamerali T.** 2017. Biostimulant Effects of Seed-Applied Sedaxane Fungicide: Morphological and Physiological Changes in Maize Seedlings. *Frontiers in Plant Science* **8**, 2072.
- Dale VH, Polasky S.** 2007. Measures of the effects of agricultural practices on ecosystem services. *Ecological Economics* **64**, 286–296.
- Dean R, Van Kan JAL, Pretorius ZA, et al.** 2012. The Top 10 fungal pathogens in molecular plant pathology. *Molecular Plant Pathology* **13**, 414–430.
- Dong H, Bai L, Zhang Y, Zhang G, Mao Y, Min L, Xiang F, Qian D, Zhu X, Song CP.** 2018. Modulation of Guard Cell Turgor and Drought Tolerance by a Peroxisomal Acetate–Malate Shunt. *Molecular Plant* **11**, 1278–1291.
- Donley N.** 2019. The USA lags behind other agricultural nations in banning harmful pesticides. *Environmental Health: A Global Access Science Source* **18**, 44.

- Driscoll SP, Prins A, Olmos E, Kunert KJ, Foyer CH.** 2006. Specification of adaxial and abaxial stomata, epidermal structure and photosynthesis to CO₂ enrichment in maize leaves. *Journal of Experimental Botany* **57**, 381–390.
- Dubcovsky J, Dvorak J.** 2007. Genome plasticity a key factor in the success of polyploid wheat under domestication. *Science* **316**, 1862–1866.
- Duncan KE, Howard RJ.** 2000. Cytological analysis of wheat infection by the leaf blotch pathogen *Mycosphaerella graminicola*. *Mycological Research* **104**, 1074–1082.
- Dunn J, Hunt L, Afsharinafar M, Meselmani M Al, Mitchell A, Howells R, Wallington E, Fleming AJ, Gray JE.** 2019. Reduced stomatal density in bread wheat leads to increased water-use efficiency. *Journal of Experimental Botany* **70**, 4737–4747.
- Dvorak J, Luo MC, Yang ZL, Zhang HB.** 1998. The structure of the *Aegilops tauschii* genepool and the evolution of hexaploid wheat. *Theoretical and Applied Genetics* **97**, 657–670.
- Earl HJ, Davis RF.** 2003. Effect of Drought Stress on Leaf and Whole Canopy Radiation Use Efficiency and Yield of Maize. *Agronomy Journal* **95**, 688–696.
- EBIC.** 2012. About biostimulants and the benefits of using them. European Biostimulants Industry Consortium.
- Eliazer Nelson ARL, Ravichandran K, Antony U.** 2019. The impact of the Green Revolution on indigenous crops of India. *Journal of Ethnic Foods* **6**, 8.
- Elsayed S, Elhoweity M, Ibrahim HH, Dewir YH, Migdadi HM, Schmidhalter U.** 2017. Thermal imaging and passive reflectance sensing to estimate the water status and grain yield of wheat under different irrigation regimes. *Agricultural Water Management* **189**, 98–110.
- Englund G, Cooper SD.** 2003. Scale effects and extrapolation in ecological experiments. *Advances in Ecological Research* **33**, 161–213.
- Eriksen L, Shaw MW, Østergård H.** 2001. A model of the effect of pseudothecia on genetic recombination and epidemic development in populations of *Mycosphaerella graminicola*. *Phytopathology* **91**, 240–248.

- Evenson RE, Gollin D.** 2003. Assessing the Impact of the Green Revolution, 1960 to 2000. **758**.
- Eyal Z.** 1973. Physiologic Specialization of *Septoria tritici*. *Phytopathology* **63**, 1087.
- Eyal Z, Scharen AL, Prescott JM, Ginkel M van.** 1987. *The septoria diseases of wheat: concepts and methods of disease management*. Mexico: CIMMYT.
- Faiçal BS, Costa FG, Pessin G, et al.** 2014. The use of unmanned aerial vehicles and wireless sensor networks for spraying pesticides. *Journal of Systems Architecture* **60**, 393–404.
- Faiçal BS, Freitas H, Gomes PH, Mano LY, Pessin G, de Carvalho ACPLF, Krishnamachari B, Ueyama J.** 2017. An adaptive approach for UAV-based pesticide spraying in dynamic environments. *Computers and Electronics in Agriculture* **138**, 210–223.
- FAOSTAT.** 2014. FAOSTAT. Food and Agricultural Organization of the United Nations.
- Farooq M, Wahid A, Kobayashi N, Fujita D, Basra SMA.** 2009. Plant drought stress: Effects, mechanisms and management. *Agronomy for Sustainable Development*. *EDP Sciences*, 185–212.
- Feng S, Fu Q.** 2013. Expansion of global drylands under a warming climate. *Atmospheric Chemistry and Physics Discussions* **13**, 14637–14665.
- Fiorani F, Rascher U, Jahnke S, Schurr U.** 2012. Imaging plants dynamics in heterogenic environments. *Current Opinion in Biotechnology* **23**, 227–235.
- Fleming TR, Fleming CC, Levy CCB, Repiso C, Hennequart F, Nolasco JB, Liu F.** 2019. Biostimulants enhance growth and drought tolerance in *Arabidopsis thaliana* and exhibit chemical priming action. *Annals of Applied Biology* **174**, 153–165.
- Foley JA, DeFries R, Asner GP, et al.** 2005. Global consequences of land use. *Science* **309**, 570–574.
- Foley JA, Ramankutty N, Brauman KA, et al.** 2011. Solutions for a cultivated planet. *Nature* **478**, 337–342.

- Fones H, Gurr S.** 2015. The impact of *Septoria tritici* Blotch disease on wheat: An EU perspective. *Fungal Genetics and Biology* **79**, 3–7.
- Forbes G, Jeger M.** 1987. Factors affecting the estimation of disease intensity in simulated plant cultures. *Journal of Plant Diseases and Protect* **94**, 113–120.
- Forbes GA, Korva JT.** 1994. The effect of using a Horsfall-Barratt scale on precision and accuracy of visual estimation of potato late blight severity in the field. *Plant Pathology* **43**, 675–682.
- Fraaije BA, Bayon C, Atkins S, Cools HJ, Lucas JA, Fraaije MW.** 2012. Risk assessment studies on succinate dehydrogenase inhibitors, the new weapons in the battle to control *Septoria* leaf blotch in wheat. *Molecular Plant Pathology* **13**, 263–275.
- Fraaije BA, Cools HJ, Fountaine J, Lovell DJ, Motteram J, West JS, Lucas JA.** 2005. Role of Ascospores in Further Spread of QoI-Resistant Cytochrome b Alleles (G143A) in Field Populations of *Mycosphaerella graminicola*. *Phytopathology* **95**, 933–941.
- Fraaije BA, Cools HJ, Kim SH, Motteram J, Clark WS, Lucas JA.** 2007. A novel substitution I381V in the sterol 14 α -demethylase (CYP51) of *Mycosphaerella graminicola* is differentially selected by azole fungicides. *Molecular Plant Pathology* **8**, 245–254.
- FRAC.** 2017. FRAC (Fungicide Resistance Action Committee), Crop Life.
- de Fraiture C, Wichelns D.** 2010. Satisfying future water demands for agriculture. *Agricultural Water Management* **97**, 502–511.
- French A, Wells D, Everitt N, Pridmore T.** 2012. High-throughput quantification of root growth. *Measuring Roots: An Updated Approach*.
- Furbank RT, Tester M.** 2011. Phenomics - technologies to relieve the phenotyping bottleneck. *Trends in Plant Science* **16**, 635–644.
- Gate P, Brisson N, Charmet G, Gouache D, Oury F-X.** 2009. Les causes du plafonnement du rendement du blé en France? Changement climatique: conséquences et enseignements pour les grandes cultures et l'élevage herbivore. 23–34.

- Geiger F, Bengtsson J, Berendse F, et al.** 2010. Persistent negative effects of pesticides on biodiversity and biological control potential on European farmland. *Basic and Applied Ecology* **11**, 97–105.
- Gentleman RC, Carey VJ, Bates DM, et al.** 2004. Bioconductor: open software development for computational biology and bioinformatics. *Genome biology* **5**.
- Gerwick BC, Sparks TC.** 2014. Natural products for pest control: an analysis of their role, value and future. *Pest Management Science* **70**, 1169–1185.
- Godfray HCJ, Beddington JR, Crute IR, Haddad L, Lawrence D, Muir JF, Pretty J, Robinson S, Thomas SM, Toulmin C.** 2010. Food Security: The Challenge of Feeding 9 Billion People. *Science* **327**, 812–818.
- Godoy C V., Koga LJ, Canteri MG.** 2006. Diagrammatic scale for assessment of soybean rust severity. *Fitopatologia Brasileira* **31**, 63–68.
- Golzarian MR, Frick RA, Rajendran K, Berger B, Roy S, Tester M, Lun DS.** 2011. Accurate inference of shoot biomass from high-throughput images of cereal plants. *Plant Methods* **7**, 2.
- Gómez-Bellot MJ, Nortes PA, Sánchez-Blanco MJ, Ortuño MF.** 2015. Sensitivity of thermal imaging and infrared thermometry to detect water status changes in *Euonymus japonica* plants irrigated with saline reclaimed water. *Biosystems Engineering* **133**, 21–32.
- Grant OM, Chaves MM, Jones HG.** 2006. Optimizing thermal imaging as a technique for detecting stomatal closure induced by drought stress under greenhouse conditions. *Physiologia Plantarum* **127**, 507–518.
- Green H, Broun P, Cakmak I, et al.** 2016. Planting seeds for the future of food. *Journal of the Science of Food and Agriculture* **96**, 1409–1414.
- Großkinsky DK, Svensgaard J, Christensen S, Roitsch T.** 2015. Plant phenomics and the need for physiological phenotyping across scales to narrow the genotype-to-phenotype knowledge gap. *Journal of Experimental Botany* **66**, 5429–5440.
- Gu Z, Eils R, Schlesner M.** 2016. Complex heatmaps reveal patterns and correlations in multidimensional genomic data. *Bioinformatics* **32**, 2847–2849.

- Hamilton ES, Schlegel AM, Haswell ES.** 2015. United in diversity: mechanosensitive ion channels in plants. *Annual review of plant biology* **66**, 113–37.
- Han SH, Kang BR, Lee JH, Lee SH, Kim IS, Kim CH, Kim YC.** 2012. A trifloxystrobin fungicide induces systemic tolerance to abiotic stresses. *Plant Pathology Journal* **28**, 101–106.
- Hardwick N V., Jones DR, Slough JE.** 2001. Factors affecting diseases of winter wheat in England and Wales, 1989-98. *Plant Pathology* **50**, 650–652.
- Haswell ES, Verslues PE.** 2015. The ongoing search for the molecular basis of plant osmosensing. *Journal of General Physiology* **145**, 389–394.
- Hatfield JL, Dold C.** 2019. Water-use efficiency: Advances and challenges in a changing climate. *Frontiers in Plant Science* **10**, 103.
- Haudry A, Cenci A, Ravel C, et al.** 2007. Grinding up wheat: A massive loss of nucleotide diversity since domestication. *Molecular Biology and Evolution* **24**, 1506–1517.
- Hawkins NJ, Fraaije BA.** 2018. Fitness Penalties in the Evolution of Fungicide Resistance. *Annual Review of Phytopathology* **56**, 339–360.
- Hedrich R, Marten I, Lohse G, Dietrich P, Winter H, Lohaus G, Heldt H-W.** 1994. Malate-sensitive anion channels enable guard cells to sense changes in the ambient CO₂ concentration. *The Plant Journal* **6**, 741–748.
- Heick TM, Justesen AF, Jørgensen LN.** 2017. Resistance of wheat pathogen *Zymoseptoria tritici* to DMI and QoI fungicides in the Nordic-Baltic region - a status. *European Journal of Plant Pathology* **149**, 669–682.
- Helmer M, Hilhorst D.** 2006. Natural disasters and climate change. *Disasters* **30**, 1–4.
- Hetherington AM, Woodward FI.** 2003. The role of stomata in sensing and driving environmental change. *Nature* **424**, 901–908.
- Hoch HC, Staples RC, Whitehead B, Comeau J, Wolf ED.** 1987. Signaling for growth orientation and cell differentiation by surface topography in *Uromyces*. *Science* **235**, 1659–1662.

Hojati M, Modarres-Sanavy SAM, Ghanati F, Panahi M. 2011. Hexaconazole induces antioxidant protection and apigenin-7-glucoside accumulation in *Matricaria chamomilla* plants subjected to drought stress. *Journal of Plant Physiology* **168**, 782–791.

Hole DG, Perkins AJ, Wilson JD, Alexander IH, Grice P V., Evans AD. 2005. Does organic farming benefit biodiversity? *Biological Conservation* **122**, 113–130.

Honsdorf N, March TJ, Berger B, Tester M, Pillen K. 2014. High-Throughput Phenotyping to Detect Drought Tolerance QTL in Wild Barley Introgression Lines. *PLoS ONE* **9**, 97047.

Horsfall JG. 2012. *Plant Disease: An Advanced Treatise: How Disease Develops in Populations* (Horsfall J. G, Ed.). New York: Academic Press.

Horsfall JG, Barratt RW. 1945. An improved grading system for measuring plant diseases.(Abstract). *Phytopathology* **35**.

Hossain MA, Bhattacharjee S, Armin SM, Qian P, Xin W, Li HY, Burritt DJ, Fujita M, Tran LSP. 2015. Hydrogen peroxide priming modulates abiotic oxidative stress tolerance: Insights from ROS detoxification and scavenging. *Frontiers in Plant Science* **6**, 420.

Hunter MC, Smith RG, Schipanski ME, Atwood LW, Mortensen DA. 2017. Agriculture in 2050: Recalibrating targets for sustainable intensification. *BioScience* **67**, 386–391.

Irvine RL, Crone EE, Jackson LJ, MacIsaac EA. 2004. Does scale affect ecological model predictions? A test with lake responses to fertilization. *Ecological Applications* **14**, 1178–1188.

Jackson S, Fraser J, Leader A, Kemmitt G, Corrigan W. 2018. Efficacy of fenpicoxamid for the control of *Zymoseptoria tritici* (wheat leaf blotch). The Dundee Conference. Crop Production in Northern Britain 2018, Dundee, UK, 27-28 February 2018. The Association for Crop Protection in Northern Britain, 133–138.

Jansen M, Gilmer F, Biskup B, et al. 2009. Simultaneous phenotyping of leaf growth and chlorophyll fluorescence via Growscreen Fluoro allows detection of stress tolerance in *Arabidopsis thaliana* and other rosette plants. *Functional Plant Biology* **36**, 902–914.

Jones HG. 1999. Use of thermography for quantitative studies of spatial and temporal variation of stomatal conductance over leaf surfaces. *Plant, Cell and Environment* **22**,

1043–1055.

Jones AM. 2016. A new look at stress: abscisic acid patterns and dynamics at high-resolution. *New Phytologist* **210**, 38–44.

Jones RJ, Mansfield TA. 1970. Suppression of stomatal opening in leaves treated with abscisic acid. *Journal of Experimental Botany* **21**, 714–719.

Jones HG, Serraj R, Loveys BR, Xiong L, Wheaton A, Price AH. 2009. Thermal infrared imaging of crop canopies for the remote diagnosis and quantification of plant responses to water stress in the field. *Functional Plant Biology* **36**, 978.

Jones HG, Stoll M, Santos T, Sousa C de, Chaves MM, Grant OM. 2002. Use of infrared thermography for monitoring stomatal closure in the field: application to grapevine. *Journal of Experimental Botany* **53**, 2249–2260.

Joo J, Lee YH, Song SI. 2019. OsbZIP42 is a positive regulator of ABA signaling and confers drought tolerance to rice. *Planta* **249**, 1521–1533.

Kang J, Hwang J-U, Lee M, Kim Y-Y, Assmann SM, Martinoia E, Lee Y. 2010. PDR-type ABC transporter mediates cellular uptake of the phytohormone abscisic acid. *Proceedings of the National Academy of Sciences of the United States of America* **107**, 2355–60.

Karisto P, Hund A, Yu K, Anderegg J, Walter A, Mascher F, McDonald BA, Mikaberidze A. 2018. Ranking quantitative resistance to septoria tritici blotch in elite wheat cultivars using automated image analysis. *Phytopathology* **108**, 568–581.

Kaul S, Koo HL, Jenkins J, et al. 2000. Analysis of the genome sequence of the flowering plant *Arabidopsis thaliana*. *Nature* **408**, 796–815.

Kema G. 1996. Histology of the Pathogenesis of *Mycosphaerella graminicola* in Wheat. *Phytopathology* **86**, 777.

Kema GHJ, Verstappen ECP, Todorova M, Waalwijk C. 1996. Successful crosses and molecular tetrad and progeny analyses demonstrate heterothallism in *Mycosphaerella graminicola*. *Current Genetics* **30**, 251–258.

Kim TH. 2014. Mechanism of ABA signal transduction: Agricultural highlights for improving drought tolerance. *Journal of Plant Biology* **57**, 1–8.

King JE, Jenkins JEE, Morgan WA. 1983. The estimation of yield losses in wheat from severity of infection by Septoria species. *Plant Pathology* **32**, 239–249.

Klem K, Mishra KB, Novotná KI, Rapantová B, Hoda Ová P, Mishra A, Ková D, Urban O. 2017. Distinct growth and physiological responses of *Arabidopsis thaliana* natural accessions to drought stress and their detection using spectral reflectance and thermal imaging. *Functional Plant Biology* **44**, 312.

Kuznetsov D, Cazenave AB, Rambach O, Camblin P, Nina M, Leipner J. 2018. Foliar application of benzovindiflupyr shows non-fungicidal effects in wheat plants. *Pest Management Science* **74**, 665–671.

Lancashire PD, Bleiholder H, Boon T Van Den, Langeluddeke P, Stauss R, Weber E, Witzemberger A. 1991. A uniform decimal code for growth stages of crops and weeds. *Annals of Applied Biology* **119**, 561–601.

Law CW, Alhamdoosh M, Su S, Smyth GK, Ritchie ME. 2016. RNA-seq analysis is easy as 1-2-3 with limma, Glimma and edgeR. *F1000Research* **5**, 1408.

Lazo J V, and Ascencio J. 2014. Some morphometric and physiological responses induced by fungicide Opera (R) (Pyraclostrobin plus Epoxiconazole) in corn (*Zea mays* L.). *Rev. Fac. Agron* **31**, 39–59.

Lechenet M, Dessaint F, Py G, Makowski D, Munier-Jolain N. 2017. Reducing pesticide use while preserving crop productivity and profitability on arable farms. *Nature Plants* **3**, 17008.

Lehner F, Coats S, Stocker TF, Pendergrass AG, Sanderson BM, Raible CC, Smerdon JE. 2017. Projected drought risk in 1.5°C and 2°C warmer climates. *Geophysical Research Letters* **44**, 7419–7428.

Leon-Kloosterziel KM, Gil MA, Ruijs GJ, Jacobsen SE, Olszewski NE, Schwartz SH, Zeevaart JAD, Koornneef M. 1996. Isolation and characterization of abscisic acid-deficient *Arabidopsis* mutants at two new loci. *The Plant Journal* **10**, 655–661.

Leontopoulos S. 2020. Potential Use of Medicinal Plants as Biological Crop Protection Agents. *Biomedical Journal of Scientific & Technical Research* **25**.

- Leplat J, Mangin P, Falchetto L, Heraud C, Gautheron E, Steinberg C.** 2018. Visual assessment and computer-assisted image analysis of Fusarium head blight in the field to predict mycotoxin accumulation in wheat grains. *European Journal of Plant Pathology* **150**, 1065–1081.
- Leroux P, Albertini C, Gautier A, Gredt M, Walker A-S.** 2007. Mutations in the CYP51 gene correlated with changes in sensitivity to sterol 14 α -demethylation inhibitors in field isolates of *Mycosphaerella graminicola*. *Pest Management Science* **63**, 688–698.
- Leung J, Giraudat J.** 1998. Abscisic acid signal transduction. *Annual Review of Plant Biology* **49**, 199–222.
- Li W, Pang S, Lu Z, Jin B.** 2020. Function and Mechanism of WRKY Transcription Factors in Abiotic Stress Responses of Plants. *Plants* **9**, 1515.
- Limpens J, Granath G, Aerts R, et al.** 2012. Glasshouse vs field experiments: Do they yield ecologically similar results for assessing N impacts on peat mosses? *New Phytologist* **195**, 408–418.
- Lin LI-K.** 1989. A Concordance Correlation Coefficient to Evaluate Reproducibility. *Biometrics* **45**, 255.
- Lobell DB, Ortiz-Monasterio JI, Asner GP, Matson PA, Naylor RL, Falcon WP.** 2005. Analysis of wheat yield and climatic trends in Mexico. *Field Crops Research* **94**, 250–256.
- Loiseleur O.** 2017. Natural products in the discovery of agrochemicals. *Chimia* **71**, 810–822.
- Lovarelli D, Fiala M, Larsson G.** 2018. Fuel consumption and exhaust emissions during on-field tractor activity: A possible improving strategy for the environmental load of agricultural mechanisation. *Computers and Electronics in Agriculture* **151**, 238–248.
- Ludlow MM, Muchow RC.** 1990. A critical evaluation of the traits for improving crop yield in water limited environments. *Advances in Agronomy* **43**, 107–153.
- Luo MC, Yang ZL, You FM, Kawahara T, Waines JG, Dvorak J.** 2007. The structure of wild and domesticated emmer wheat populations, gene flow between them, and the site of emmer domestication. *Theoretical and Applied Genetics* **114**, 947–959.

Machida K, Takimoto H, Miyoshi H, Taniguchi M. 1999. UK-2A, B, C and D, novel antifungal antibiotics from *Streptomyces* sp. 517-02. V. Inhibition mechanism of bovine heart mitochondrial cytochrome bc1 by the novel antibiotic UK-2A. *Journal of Antibiotics* **52**, 748–753.

Madende M, Hayes M. 2020. Fish by-product use as biostimulants: An overview of the current state of the art, including relevant legislation and regulations within the EU and USA. *Molecules* **25**, 1122.

Mahlein AK. 2016. Plant disease detection by imaging sensors – Parallels and specific demands for precision agriculture and plant phenotyping. *Plant Disease* **100**, 241–254.

Maklashina E, Cecchini G. 2010. The quinone-binding and catalytic site of complex II. *Biochimica et Biophysica Acta - Bioenergetics* **1797**, 1877–1882.

Marchand PA. 2015. Basic substances: an opportunity for approval of low-concern substances under EU pesticide regulation. *Pest Management Science* **71**, 1197–1200.

Marshall R, Kombrink A, Motteram J, Loza-Reyes E, Lucas J, Hammond-Kosack KE, Thomma BPHJ, Rudd JJ. 2011. Analysis of Two in Planta Expressed LysM Effector Homologs from the Fungus *Mycosphaerella graminicola* Reveals Novel Functional Properties and Varying Contributions to Virulence on Wheat 1[W][OA]. *Plant Physiology* **156**, 756–769.

Maxwell K, Johnson GN. 2000. Chlorophyll fluorescence - a practical guide. *Journal of experimental botany*. **51**. 659-68.

Mei F, Chen B, Li F, Zhang Y, Kang Z, Wang X, Mao H. 2021. Overexpression of the wheat NAC transcription factor TaSNAC4-3A gene confers drought tolerance in transgenic *Arabidopsis*. *Plant Physiology and Biochemistry* **160**, 37–50.

Merlot S, Mustilli A-C, Genty B, North H, Lefebvre V, Sotta B, Vavasseur A, Giraudat J. 2002. Use of infrared thermal imaging to isolate *Arabidopsis* mutants defective in stomatal regulation. *The Plant Journal* **30**, 601–609.

Miles TD, Fairchild KL, Merlington A, Kirk WW, Rosenzweig N, Wharton PS. 2013. First Report of Boscalid and Penthiopyrad-Resistant Isolates of *Alternaria solani* Causing Early Blight of Potato in Michigan. *Plant Disease* **97**, 1655.

Minervini M, Giuffrida M V., Perata P, Tsiftaris SA. 2017. Phenotiki: an open software

and hardware platform for affordable and easy image-based phenotyping of rosette-shaped plants. *Plant Journal* **90**, 204–216.

Mishra KB, Mishra A, Klem K, Govindjee. 2016. Plant phenotyping: a perspective. *Indian Journal of Plant Physiology* **21**, 514–527.

Müller P, Li XP, Niyogi KK. 2001. Non-photochemical quenching. A response to excess light energy. *Plant Physiology* **125**, 1558–1566.

Müllner D. 2013. Fastcluster: Fast hierarchical, agglomerative clustering routines for R and Python. *Journal of Statistical Software* **53**, 1–18.

Munns R, James RA, Sirault XRR, Furbank RT, Jones HG. 2010. New phenotyping methods for screening wheat and barley for beneficial responses to water deficit. *Journal of Experimental Botany* **61**, 3499–3507.

Mustilli AC, Merlot S, Vavasseur A, Fenzi F, Giraudat J. 2002. Arabidopsis OST1 protein kinase mediates the regulation of stomatal aperture by abscisic acid and acts upstream of reactive oxygen species production. *Plant Cell* **14**, 3089–3099.

Neilson EH, Edwards AM, Blomstedt CK, Berger B, Møller BL, Gleadow RM. 2015. Utilization of a high-throughput shoot imaging system to examine the dynamic phenotypic responses of a C₄ cereal crop plant to nitrogen and water deficiency over time. *Journal of Experimental Botany* **66**, 1817–1832.

Newton AC. 2016. Exploitation of diversity within crops— the key to disease tolerance? *Frontiers in Plant Science* **7**.

Nita M, Ellis MA, Madden L V. 2003. Reliability and accuracy of visual estimation of phomopsis leaf blight of strawberry. *Phytopathology* **93**, 995–1005.

Nutter FW, Esker P. 2006. The Role of Psychophysics in Phytopathology: The Weber-Fechner Law Epidemiology of Black Sigatoka in Banana View project Improving production of horticultural crops in Costa Rica View project. Article in *European Journal of Plant Pathology* **114**, 119–213.

Nutter FW, Schultz PM. 1995. Improving the accuracy and precision of disease assessments: Selection of methods and use of computer-aided training programs. *Canadian Journal of Plant Pathology* **17**, 174–184.

Nutter FW, Teng P, Shokes F. 1991. Disease assessment terms and concepts. *Plant Disease* **75**, 1187–1188.

Nziguheba G, Zingore S, Kihara J, Merckx R, Njoroge S, Otinga A, Vandamme E, Vanlauwe B. 2016. Phosphorus in smallholder farming systems of sub-Saharan Africa: implications for agricultural intensification. *Nutrient Cycling in Agroecosystems* **104**, 321–340.

Oerke EC. 2006. Crop losses to pests. *Journal of Agricultural Science* **144**, 31–43.

Oerke EC, Mahlein AK, Steiner U. 2014. Proximal sensing of plant diseases. In: Gullino M, In: Bonants P, eds. *Detection and Diagnostics of Plant Pathogens. Plant Pathology in the 21st Century (Contributions to the 9th International Congress)*. Springer, Dordrecht Netherlands, 55–68.

Ortiz R, Trethowan R, Ferrara GO, Iwanaga M, Dodds JH, Crouch JH, Crossa J, Braun HJ. 2007. High yield potential, shuttle breeding, genetic diversity, and a new international wheat improvement strategy. *Euphytica*. Springer, 365–384.

Orton ES, Deller S, Brown JKM. 2011. *Mycosphaerella graminicola*: From genomics to disease control. *Molecular Plant Pathology* **12**, 413–424.

Owen WJ, Yao C, Myung K, Kemmitt G, Leader A, Meyer KG, Bowling AJ, Slanec T, Kramer VJ. 2017. Biological characterization of fenpicoxamid, a new fungicide with utility in cereals and other crops. *Pest Management Science* **73**, 2005–2016.

Palmer CL, Skinner W. 2002. *Mycosphaerella graminicola*: Latent infection, crop devastation and genomics. *Molecular Plant Pathology* **3**, 63–70.

Parkin IAP, Gulden SM, Sharpe AG, Lukens L, Trick M, Osborn TC, Lydiate DJ. 2005. Segmental Structure of the *Brassica napus* Genome Based on Comparative Analysis With *Arabidopsis thaliana*. *Genetics* **171**.

Patro R, Duggal G, Love MI, Irizarry RA, Kingsford C. 2017. Salmon provides fast and bias-aware quantification of transcript expression. *Nature Methods* **14**, 417–419.

Pavicic M, Mouhu K, Wang F, Bilicka M, Chovanček E, Himanen K. 2017. Genomic and phenomic screens for flower related ring type ubiquitin E3 ligases in *Arabidopsis*. *Frontiers in Plant Science* **8**, 416.

- Peng J, Richards DE, Hartley NM, et al.** 1999. 'Green revolution' genes encode mutant gibberellin response modulators. *Nature* **400**, 256–261.
- Pepler S, Gooding MJ, Ford KE, Ellis RH.** 2005. A temporal limit to the association between flag leaf life extension by fungicides and wheat yields. *European Journal of Agronomy*.
- Pieruschka R, Poorter H.** 2012. Phenotyping plants: genes, phenes and machines. *Functional Plant Biology* **39**, 813.
- Pieruschka R, Schurr U.** 2019. Plant Phenotyping: Past, Present, and Future. *Plant Phenomics* **2019**, 1–6.
- Pieterse, C., Leon-Reyes, A., Van der Ent, S., Van Wees, S.** 2009. Networking by small-molecule hormones in plant immunity. *Nat Chem Biol* **5**, 308–316.
- Pimentel D, Harvey C, Resosudarmo P, et al.** 1995. Environmental and economic costs of soil erosion and conservation benefits. *Science* **267**, 1117–1123.
- Pingali PL.** 2012. Green revolution: Impacts, limits, and the path ahead. *Proceedings of the National Academy of Sciences of the United States of America* **109**, 12302–12308.
- Pingali P.** 2015. Agricultural policy and nutrition outcomes – getting beyond the preoccupation with staple grains. *Food Security* **7**, 583–591.
- Power AG.** 2010. Ecosystem services and agriculture: tradeoffs and synergies. *Philosophical Transactions of the Royal Society B: Biological Sciences* **365**, 2959–2971.
- Provart NJ, Alonso J, Assmann SM, et al.** 2016. 50 years of Arabidopsis research: Highlights and future directions. *New Phytologist* **209**, 921–944.
- Raghavendra AS, Gonugunta VK, Christmann A, Grill E.** 2010. ABA perception and signalling. *Trends in Plant Science* **15**, 395–401.
- Rajendran K, Tester M, Roy SJ.** 2009. Quantifying the three main components of salinity tolerance in cereals.
- Ray DK, Mueller ND, West PC, Foley JA.** 2013. Yield Trends Are Insufficient to Double Global Crop Production by 2050 (JP Hart, Ed.). *PLoS ONE* **8**, e66428.

Reddy AR, Chaitanya KV, Vivekanandan M. 2004. Drought-induced responses of photosynthesis and antioxidant metabolism in higher plants. *Journal of Plant Physiology* **161**, 1189–1202.

Reif JC, Zhang P, Dreisigacker S, Warburton ML, Van Ginkel M, Hoisington D, Bohn M, Melchinger AE. 2005. Wheat genetic diversity trends during domestication and breeding. *Theoretical and Applied Genetics* **110**, 859–864.

Reynolds D, Baret F, Welcker C, et al. 2019. What is cost-efficient phenotyping? Optimizing costs for different scenarios. *Plant Science* **282**, 14–22.

Robinson RA, Sutherland WJ. 2002. Post-war changes in arable farming and biodiversity in Great Britain. *Journal of Applied Ecology* **39**, 157–176.

Rolfe SA, Scholes JD. 2010. Chlorophyll fluorescence imaging of plant-pathogen interactions. *Protoplasma* **247**, 163–175.

Rouphael Y, Spíchal L, Panzarová K, Casa R, Colla G. 2018. High-throughput plant phenotyping for developing novel biostimulants: from lab to field or from field to lab? *Frontiers in Plant Science* **9**.

Royle DJ. 1994. Understanding and predicting epidemics: a commentary based on selected pathosystems. *Plant Pathology* **43**, 777–789.

Ruban A V., Johnson MP, Duffy CDP. 2012. The photoprotective molecular switch in the photosystem II antenna. *Biochimica et Biophysica Acta - Bioenergetics* **1817**, 167–181.

Russell PE. 1995. Fungicide resistance occurrence and management. *The Journal of Agricultural Science* **124**, 317–323.

Russell PE. 2005. A century of fungicide evolution. *Journal of Agricultural Science* **143**, 11–25.

Saleh R, Bearth A, Siegrist M. 2021. How chemophobia affects public acceptance of pesticide use and biotechnology in agriculture. *Food Quality and Preference* **91**, 104197.

Sanssené J, Selim S, Roisin-Fichter C, Djerroud L, Deweer C, Halama P. 2011. Protective and curative efficacy of prothioconazole against isolates of *Mycosphaerella graminicola* differing in their *in vitro* sensitivity to DMI fungicides. *Pest Management Science* **67**, 1134–1140.

Saruhan Guler N, Pehlivan N. 2016. Exogenous low-dose hydrogen peroxide enhances drought tolerance of soybean (*Glycine max L.*) through inducing antioxidant system. *Acta Biologica Hungarica* **67**, 169–183.

Savary S, Willocquet L, Pethybridge SJ, Esker P, McRoberts N, Nelson A. 2019. The global burden of pathogens and pests on major food crops. *Nature Ecology and Evolution* **3**, 430–439.

Schindelin J, Arganda-Carreras I, Frise E, et al. 2012. Fiji: an open-source platform for biological-image analysis. *Nature methods* **9**, 676–82.

Schindelin J, Rueden CT, Hiner MC, Eliceiri KW. 2015. The ImageJ ecosystem: An open platform for biomedical image analysis. *Molecular Reproduction and Development* **82**, 518–529.

Schirrmann M, Giebel A, Gleiniger F, et al. 2016. Monitoring Agronomic Parameters of Winter Wheat Crops with Low-Cost UAV Imagery. *Remote Sensing* **8**, 706.

Schmidhuber J, Tubiello FN. 2007. Global food security under climate change. *Proceedings of the National Academy of Sciences of the United States of America* **104**, 19703–8.

Sharp RE. 2002. Interaction with ethylene: Changing views on the role of abscisic acid in root and shoot growth responses to water stress. *Plant, Cell and Environment* **25**, 211–222.

Sherwood RT. 1983. Illusions in Visual Assessment of *Stagonospora* Leaf Spot of Orchardgrass. *Phytopathology* **73**, 173.

Sherwood RT, Berg CC, Hoover MR, Zeiders KE. 1983. Illusions in Visual Assessment of *Stagonospora* Leaf Spot of Orchardgrass. *Phytopathology* **73**, 173.

Shetty NP, Kristensen BK, Newmana MA, Møller K, Gregersen PL, Jørgensen HJL. 2003. Association of hydrogen peroxide with restriction of *Septoria tritici* in resistant wheat. *Physiological and Molecular Plant Pathology* **62**, 333–346.

Shewry PR. 2009. Wheat. *Journal of Experimental Botany* **60**, 1537–1553.

Shiferaw B, Smale M, Braun HJ, Duveiller E, Reynolds M, Muricho G. 2013. Crops that feed the world 10. Past successes and future challenges to the role played by wheat in

global food security. *Food Security* **5**, 291–317.

Sinclair TR, Hammer GL, van Oosterom EJ. 2005. Potential yield and water-use efficiency benefits in sorghum from limited maximum transpiration rate. *Functional Plant Biology* **32**, 945.

Singh RP, Singh PK, Rutkoski J, Hodson DP, He X, Jørgensen LN, Hovmøller MS, Huerta-Espino J. 2016. Disease Impact on Wheat Yield Potential and Prospects of Genetic Control. *Annual Review of Phytopathology* **54**, 303–322.

Sirault XRR, James RA, Furbank RT. 2009. A new screening method for osmotic component of salinity tolerance in cereals using infrared thermography. *Functional Plant Biology* **36**, 970.

Smale M. 1997. The Green Revolution and Wheat Genetic Diversity: Some Unfounded Assumptions. *World Development* **25**, 1257–1269.

Smith J, Grimmer M, Waterhouse S, Paveley N. 2013. Quantifying the non-fungicidal effects of foliar applications of fluxapyroxad (Xemium) on stomatal conductance, water use efficiency and yield in winter wheat. *Communications in agricultural and applied biological sciences* **78**, 523–35.

Solomon S. 2007. *Climate Change 2007: The Physical Science Basis. Contribution of Working Group I to the Fourth Assessment Report of the Intergovernmental Panel on Climate Change.* *Climate Change 2007: The Physical Science Basis. Contribution of Working Group I to the Fourth Assessment Report of the Intergovernmental Panel on Climate Change.* Cambridge: Cambridge University Press, 996.

Soneson C, Love MI, Robinson MD. 2016. Differential analyses for RNA-seq: Transcript-level estimates improve gene-level inferences. *F1000Research* **4**.

Sparks TC, Hahn DR, Garizi N V. 2017. Natural products, their derivatives, mimics and synthetic equivalents: role in agrochemical discovery. *Pest Management Science* **73**, 700–715.

Stacklies W, Redestig H, Scholz M, Walther D, Selbig J. 2007. *pcaMethods* - A bioconductor package providing PCA methods for incomplete data. *Bioinformatics* **23**, 1164–1167.

Steinberg G. 2015. Cell biology of *Zymoseptoria tritici*: Pathogen cell organization and wheat infection. *Fungal Genetics and Biology* **79**, 17–23.

StepStick - RepRap.

Stevens SS. 1961. To honor Fechner and repeal his law. *Science* **133**, 80–86.

Stewart EL, Hagerty CH, Mikaberidze A, Mundt CC, Zhong Z, McDonald BA. 2016. An Improved Method for Measuring Quantitative Resistance to the Wheat Pathogen *Zymoseptoria tritici* Using High-Throughput Automated Image Analysis.

Stewart EL, McDonald BA. 2014*a*. Measuring quantitative virulence in the wheat pathogen *Zymoseptoria tritici* using high-throughput automated image analysis. *Phytopathology* **104**, 985–92.

Stewart EL, McDonald BA. 2014*b*. Measuring Quantitative Virulence in the Wheat Pathogen *Zymoseptoria tritici* Using High-Throughput Automated Image Analysis. *Phytopathology* **104**, 985–992.

Sun D, Zhu Y, Xu H, He Y, Cen H. 2019. Time-Series Chlorophyll Fluorescence Imaging Reveals Dynamic Photosynthetic Fingerprints of *sos* Mutants to Drought Stress. *Sensors* **19**, 2649.

Tackenberg M, Volkmar C, Dammer KH. 2016. Sensor-based variable-rate fungicide application in winter wheat. *Pest management science* **72**, 1888–1896.

Talaviya T, Shah D, Patel N, Yagnik H, Shah M. 2020. Implementation of artificial intelligence in agriculture for optimisation of irrigation and application of pesticides and herbicides. *Artificial Intelligence in Agriculture* **4**, 58–73.

Tardieu F. 2012. Any trait or trait-related allele can confer drought tolerance: just design the right drought scenario. *Journal of Experimental Botany* **63**, 25–31,

Tausz-Posch S, Norton RM, Seneweera S, Fitzgerald GJ, Tausz M. 2013. Will intra-specific differences in transpiration efficiency in wheat be maintained in a high CO₂ world? A FACE study. *Physiologia Plantarum* **148**, 232–245.

Tessmer OL, Jiao Y, Cruz JA, Kramer DM, Chen J. 2013. Functional approach to high-throughput plant growth analysis. *BMC Systems Biology* **7**, 1–13.

Thimm O, Bläsing O, Gibon Y, Nagel A, Meyer S, Krüger P, Selbig J, Müller L. A, Rhee S. Y, Stitt M. 2004. MAPMAN: a user-driven tool to display genomics data sets onto diagrams of metabolic pathways and other biological processes. *The Plant journal : for cell and molecular biology*, **37**(6), 914–939.

Tian J (Jingxin), Bryksa BC, Yada RY. 2016. Feeding the world into the future – food and nutrition security: the role of food science and technology. *Frontiers in Life Science* **9**, 155–166.

Tilman D. 1998. The greening of the green revolution. *Nature* **396**, 211–212.

Tilman D. 1999. Global environmental impacts of agricultural expansion: the need for sustainable and efficient practices. *Proceedings of the National Academy of Sciences of the United States of America* **96**, 5995–6000.

Tilman D, Balzer C, Hill J, Befort BL. 2011. Global food demand and the sustainable intensification of agriculture. *Proceedings of the National Academy of Sciences of the United States of America* **108**, 20260–20264.

Torriani SF, Brunner PC, McDonald BA, Sierotzki H. 2009. QoI resistance emerged independently at least 4 times in European populations of *Mycosphaerella graminicola*. *Pest Management Science* **65**, 155–162.

Torriani SFF, Melichar JPE, Mills C, Pain N, Sierotzki H, Courbot M. 2015. Zymoseptoria tritici: A major threat to wheat production, integrated approaches to control. *Fungal Genetics and Biology* **79**, 8–12.

Tsuda M, Itoh H, Kato S. 2004. Evaluation of the systemic activity of simeconazole in comparison with that of other DMI fungicides. *Pest Management Science* **60**, 875–880.

Ueki M, Abe K, Hanafi M, Shibata K, Tanaka T, Taniguchi M. 1996. UK-2A, B, C and D, novel antifungal antibiotics from Streptomyces sp. 517-02. I. Fermentation, isolation, and biological properties. *The Journal of antibiotics* **49**, 639–43.

United Nations. 2015. United Nations, Department of Economic and Social Affairs, Population Division (2015). *World Population Prospects: The 2015 Revision, custom data acquired via website.* , 1.

- Vaidya AS, Helander JDM, Peterson FC, et al.** 2019. Dynamic control of plant water use using designed ABA receptor agonists. *Science* **366**.
- Verslues PE.** 2016. ABA and cytokinins: challenge and opportunity for plant stress research. *Plant Molecular Biology* **91**, 629–640.
- Wang Y, Meyer TJ.** 2019. A Route to Renewable Energy Triggered by the Haber-Bosch Process. *Chem* **5**, 496–497.
- Ward JH.** 1963. Hierarchical Grouping to Optimize an Objective Function. *Journal of the American Statistical Association* **58**, 236–244.
- Watson DJ, Thorne GN, French SAW.** 1963. Analysis of growth and yield of winter and spring wheats. *Annals of Botany* **27**, 1–22.
- Wichelns D, Oster JD.** 2006. Sustainable irrigation is necessary and achievable, but direct costs and environmental impacts can be substantial. *Agricultural Water Management* **86**, 114–127.
- Wilkinson S, Davies WJ.** 2002. ABA-based chemical signalling: the co-ordination of responses to stress in plants. *Plant, Cell and Environment* **25**, 195–210.
- Willmer C, Fricker M.** 1996. *Stomata*. Springer Netherlands.
- Wu C, Chen X.** 2004. Impact of pesticides on biodiversity in agricultural areas. *Chinese Journal of Applied Ecology* **15**, 341–344.
- Wu YX, von Tiedemann A.** 2002. Impact of fungicides on active oxygen species and antioxidant enzymes in spring barley (*Hordeum vulgare* L.) exposed to ozone. *Environmental Pollution* **116**, 37–47.
- Wu YX, Von Tiedemann A.** 2001. Physiological effects of azoxystrobin and epoxiconazole on senescence and the oxidative status of wheat. *Pesticide Biochemistry and Physiology* **71**, 1–10.
- Wuepper D, Borrelli P, Finger R.** 2020. Countries and the global rate of soil erosion. *Nature Sustainability* **3**, 51–55.
- Yakhin OI, Lubyantsov AA, Yakhin IA, Brown PH.** 2017. Biostimulants in plant science: A global perspective. *Frontiers in Plant Science* **7**, 2049.

- Yang C.** 2020. Remote Sensing and Precision Agriculture Technologies for Crop Disease Detection and Management with a Practical Application Example. *Engineering* **6**, 528–532.
- Yoo CY, Pence HE, Hasegawa PM, Mickelbart M V.** 2009. Regulation of transpiration to improve crop water use. *Critical Reviews in Plant Sciences* **28**, 410–431.
- Young DH, Wang NX, Meyer ST, Avila-Adame C.** 2018. Characterization of the mechanism of action of the fungicide fenpicoxamid and its metabolite UK-2A. *Pest Management Science* **74**, 489–498.
- Zhan J, Pettway RE, McDonald BA.** 2003. The global genetic structure of the wheat pathogen *Mycosphaerella graminicola* is characterized by high nuclear diversity, low mitochondrial diversity, regular recombination, and gene flow. *Fungal Genetics and Biology* **38**, 286–297.
- Zhang Y-J, Zhang X, Chen C-J, Zhou M-G, Wang H-C.** 2010. Effects of fungicides JS399-19, azoxystrobin, tebuconazole, and carbendazim on the physiological and biochemical indices and grain yield of winter wheat. *Pesticide Biochemistry and Physiology* **98**, 151–157.
- Zhu J-K.** 2002. Salt and Drought Stress Signal Transduction in Plants. *Annual Review of Plant Biology* **53**, 247–273.
- Zlatev Z.** 2009. Drought-Induced Changes in Chlorophyll Fluorescence of Young Wheat Plants. *Biotechnology & Biotechnological Equipment* **23**, 438–441.
- Zubrod JP, Bundschuh M, Arts G, et al.** 2019. Fungicides: An Overlooked Pesticide Class? *Environmental Science and Technology* **53**, 3347–3365.

Appendices

Appendix 1

A1.1 Image analysis symptom selection macro




```
run("Color Threshold...");
// Color Thresholder 2.0.0-rc-67/1.52e
// Autogenerated macro, single images only!
min=newArray(3);
max=newArray(3);
filter=newArray(3);
a=getTitle();
run("HSB Stack");
run("Convert Stack to Images");
selectWindow("Hue");
rename("0");
selectWindow("Saturation");
rename("1");
selectWindow("Brightness");
rename("2");
min[0]=0;
max[0]=35;
filter[0]="pass";
min[1]=0;
max[1]=255;
filter[1]="pass";
min[2]=125;
max[2]=255;
filter[2]="pass";
for (i=0;i<3;i++){
  selectWindow(""+i);
  setThreshold(min[i], max[i]);
  run("Convert to Mask");
  if (filter[i]=="stop") run("Invert");
}
imageCalculator("AND create", "0","1");
imageCalculator("AND create", "Result of 0","2");
for (i=0;i<3;i++){
  selectWindow(""+i);
  close();
}
selectWindow("Result of 0");
close();
selectWindow("Result of Result of 0");
rename(a);
// Colour Thresholding-----
run("Close");
run("Analyze Particles...", " circularity=0.00-0.60 show=[Overlay Masks] display summarize
in_situ");
```

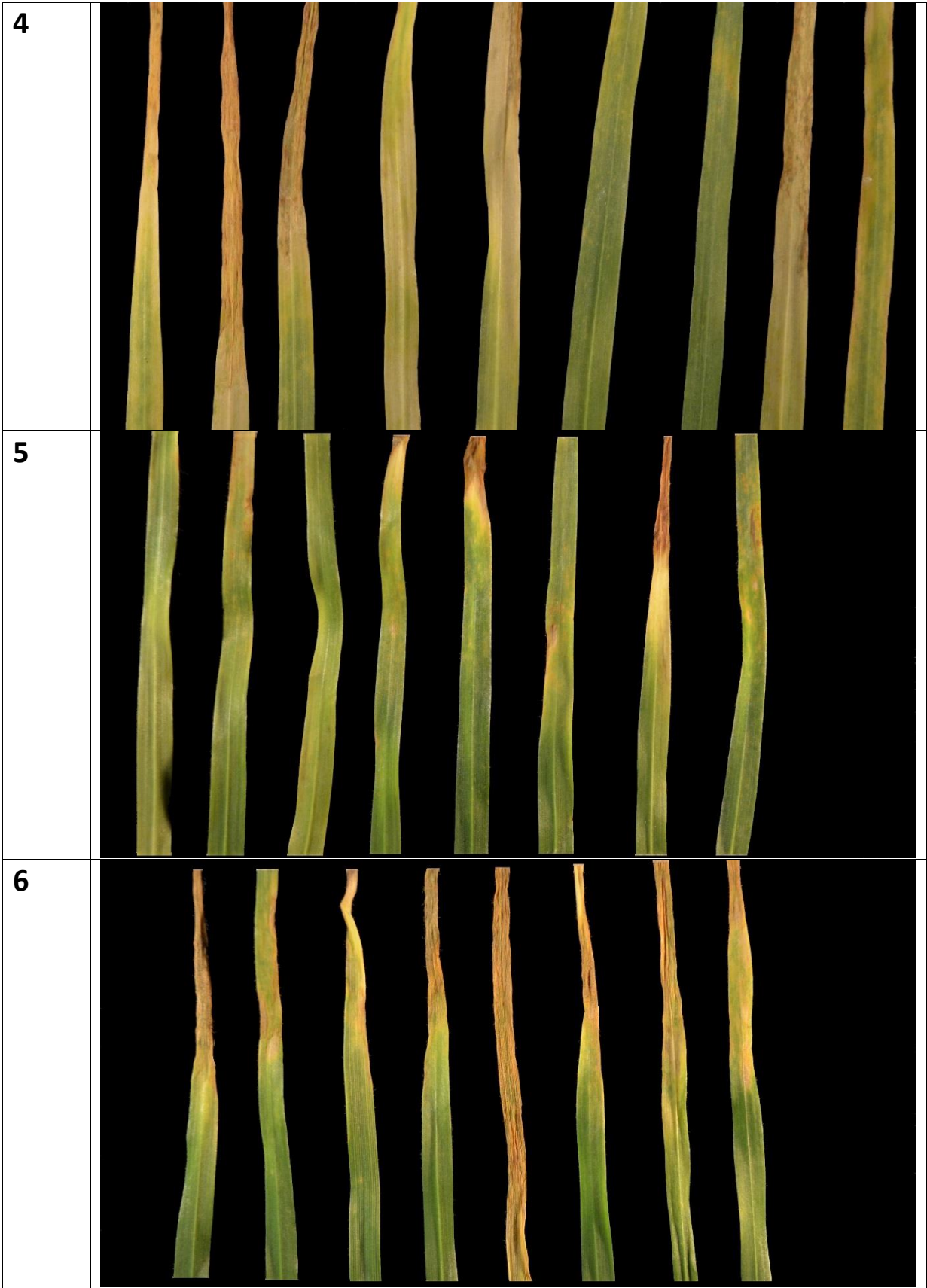
A1.2 Total leaf area selection macro

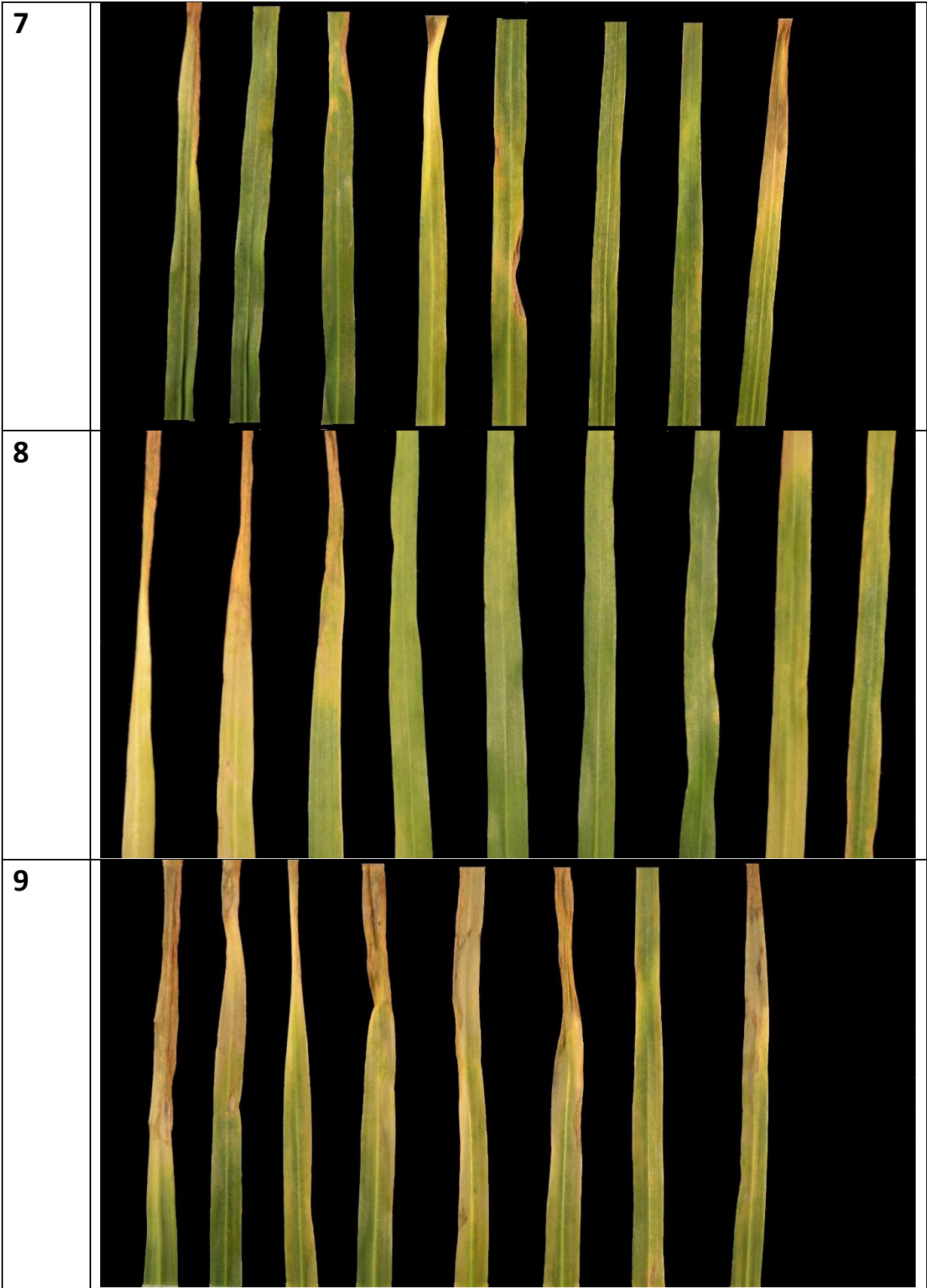
```
// Color Thresholder 2.0.0-rc-43/1.50e
// Autogenerated macro, single images only!
dir = getDirectory("image");
min=newArray(3);
max=newArray(3);
filter=newArray(3);
a=getTitle();
run("HSB Stack");
run("Convert Stack to Images");
selectWindow("Hue");
rename("0");
selectWindow("Saturation");
rename("1");
selectWindow("Brightness");
rename("2");
min[0]=0;
max[0]=255;
filter[0]="pass";
min[1]=0;
max[1]=255;
filter[1]="pass";
min[2]=62;
max[2]=255;
filter[2]="pass";
for (i=0;i<3;i++){
  selectWindow(""+i);
  setThreshold(min[i], max[i]);
  run("Convert to Mask");
  if (filter[i]=="stop") run("Invert");
}
imageCalculator("AND create", "0","1");
imageCalculator("AND create", "Result of 0","2");
for (i=0;i<3;i++){
  selectWindow(""+i);
  close();
}
selectWindow("Result of 0");
close();
selectWindow("Result of Result of 0");
rename(a);
run("Analyze Particles...", "size=1000-Infinity circularity=0.00-0.6 show=[Overlay] display
in_situ");
index = lastIndexOf(a, ".");
if (index!=-1) a = substring(a, 0, index);
b = a;
a = a + ".csv";
saveAs("Measurements", dir+a);
//selectWindow(b + ".jpg");
//saveAs("PNG",dir+b);
run("Clear Results");
```




```
//close();
```

A1.3 First disease severity scoring questionnaire

<p>1</p> <p>No Fungicide, Inoculated</p>	
<p>2</p> <p>No Fungicide, Not Inoculated</p>	
<p>3</p>	





10	
11	
12	



Plant Image	% coverage of disease symptoms	Ranking 1 = worst 13 = best
1 No fungicide inoculated		1
2 No fungicide or inoculation		13
3		
4		
5		
6		
7		
8		
9		
10		
11		
12		
13		

Aims:

For each image please give an estimated % disease coverage (leaves within one image may vary so give an approximate average of them all.) The first two were control plants, so may be good to act as standards for the worst/ best you will see.



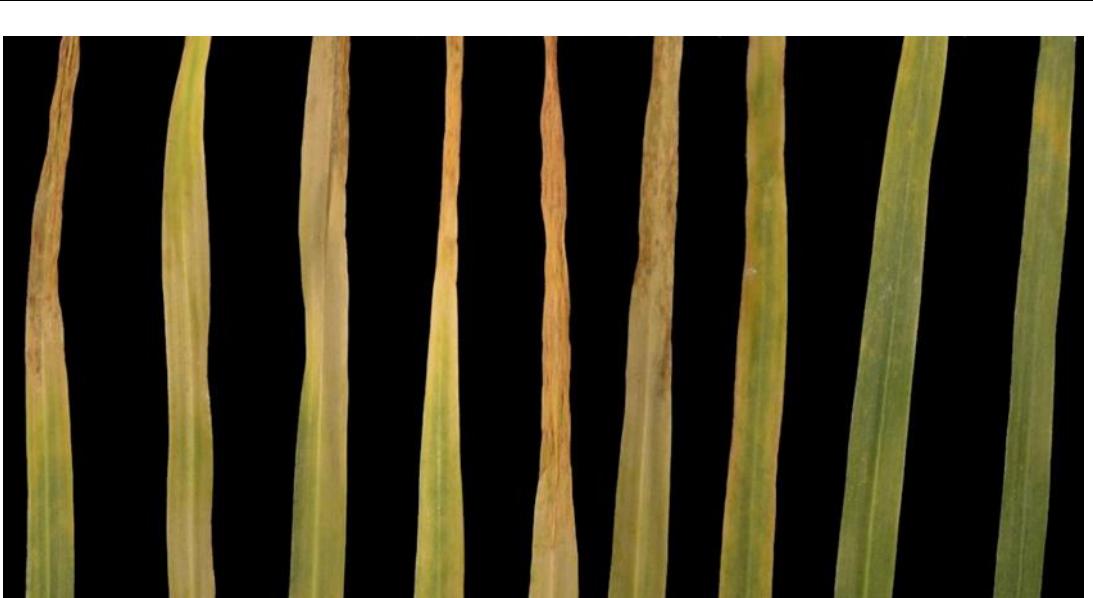
Please fill in the % coverage in the table above when you have finished, and then their respective rank from worst to best in the right hand column.




Please remember to estimate the coverage of disease, rather than the other way around.




Respective treatments for images in questionnaire 1.




1	Control
2	Control no inoculation
3	Inatreq 1.5 6dpi
4	Elatus era 6dpi
5	Librax 10dpi
6	Proline 10dpi
7	Imtrex 10dpi
8	Proline 6dpi
9	Elatus era 10 dpi
10	Inatreq 2l 6dpi
11	Librax 6dpi
12	Inatreq 1.5 10 dpi
13	Imtrex 6dpi

A1.4 Expert disease severity questionnaire 2

<p>1</p> <p>No Fungicide, Inoculated</p>	
<p>2</p> <p>No Fungicide, Not Inoculated</p>	
<p>3</p>	

4	
5	
6	

7	
8	
9	

10	
11	
12	



Plant Image	% coverage of disease symptoms	Ranking 1 = worst 13 = best
1 No fungicide inoculated		1
2 No fungicide or inoculation		13
3		
4		
5		
6		
7		
8		
9		
10		
11		
12		
13		

Aims:

The first two images are reused from the previous questionnaire, and still act as a worst and best standard. For this questionnaire it would be preferable if you did not look at the previous one, so as not to affect estimates.

For each image, please give an estimated % disease coverage (leaves within one image may vary so give an approximate average of them all.) The first two were control plants, so may be good to act as standards for the worst/ best you will see.

Please fill in the % coverage in the table above when you have finished, and then their respective rank from worst to best in the right-hand column.

Please remember to estimate the coverage of disease, rather than the other way around.

Questionnaire 2 results

No fungi inoc	1
No fungi no inoc	2
Elatus era 6dpi	3
Inatreq 2l 6dpi	4
Proline 10dpi	5
Librax 6dpi	6
Imtrex 10dpi	7
Proline 6dpi	8
Imtrex 6dpi	9
Inatreq 1.5 6dpi	10
Elatus era 10dpi	11
Inatreq 1.5 10 dpi	12
Librax 10dpi	13

Appendix 2

A2.1 FvFm protocol

```
;FvFm protocol
;protocol body - modified by ZB
;version November 18, 2010
;high-resolution CCD
;estimated time: app. 4 s
;
TS=20ms
FAR=0
Act2=40.4
Act1=40.4
include default.inc ;Includes standard options, do not remove it !
include light.inc ;Includes standard options, do not remove it !
Shutter=1
Sensitivity=20.2
Super=20
;-----
;*** Fo Measurement
;*****
;-----
F0duration=2s;
F0period = 200ms
<0,F0period..F0duration>=>mfmsub
;
;Fo definition
<TS>=>checkPoint,"startFo"
<F0duration - F0period>=>checkPoint,"endFo"
;
;-----
;*** Saturating Pulse & Fm Measurement
;*****
;-----
PulseDuration=800ms; ##
a1=F0duration + 2*mfmsub_length; ##
;
<a1>=>SatPulse(PulseDuration)
;
<a1>=>mpulse
;
;Fm definition
<a1 + PulseDuration/2>=>checkPoint,"startFm"
<a1 + PulseDuration - mfmsub_length>=>checkPoint,"endFm"
;
;Visual frame definition - image shown in pre-processing window
<a1 + PulseDuration/2 + TS>=>checkPoint,"timeVisual"
```

Appendix 3

A3.1 Contrast list

Cluster Number	number of genes in this cluster	1hr Tr vs Control number significant DE		Percentage of contrast in this cluster		4hr Tr vs Control number significant DE		Percentage of contrast in this cluster		8hr Tr vs Control number significant DE		Percentage of contrast in this cluster		24hr Tr vs Control number significant DE		Percentage of contrast in this cluster	
1	228	18	1.3%	7.9%	160	6.2%	70.2%	31	2.2%	13.6%	4	3.3%	1.8%				
2	289	33	2.5%	11.4%	55	2.1%	19.0%	32	2.2%	11.1%	2	1.7%	0.7%				
3	689	12	0.9%	1.7%	110	4.3%	16.0%	24	1.7%	3.5%	7	5.8%	1.0%				
4	244	34	2.5%	13.9%	196	7.6%	80.3%	37	2.6%	15.2%	2	1.7%	0.8%				
5	347	29	2.2%	8.4%	99	3.8%	28.5%	43	3.0%	12.4%	0	0.0%	0.0%				
6	236	14	1.0%	5.9%	93	3.6%	39.4%	66	4.6%	28.0%	31	25.8%	13.1%				
7	312	90	6.7%	28.8%	308	12.0%	98.7%	191	13.3%	61.2%	11	9.2%	3.5%				
8	562	507	37.7%	90.2%	373	14.5%	66.4%	224	15.6%	39.9%	16	13.3%	2.8%				
9	840	135	10.0%	16.1%	683	26.5%	81.3%	471	32.7%	56.1%	31	25.8%	3.7%				
10	501	385	28.6%	76.8%	465	18.1%	92.8%	313	21.8%	62.5%	15	12.5%	3.0%				
11	429	26	1.9%	6.1%	19	0.7%	4.4%	7	0.5%	1.6%	1	0.8%	0.2%				
12	133	62	4.6%	46.6%	15	0.6%	11.3%	0	0.0%	0.0%	0	0.0%	0.0%				
		1345			2576			1439			120						
number of genes in contrast																	

A3.2 Complete gene list.

1hr	logFC	CI	AveExpr	FDR P	Cluster	Description
AT1G15520	6.66	(6.50-6.82)	3.77	1.95E-10	10	pleiotropic drug resistance 12 (PDR12)
AT1G19020	5.62	(5.32-5.93)	2.97	3.61E-13	8	unknown protein
AT1G05680	5.43	(5.22-5.63)	3.29	1.19E-11	7	Uridine diphosphate glycosyltransferase 74E2 (UGT74E2)
AT3G25780	5.28	(5.07-5.49)	3.21	4.76E-14	8	allene oxide cyclase 3 (AOC3)
AT5G59820	5.18	(4.96-5.40)	2.92	7.15E-13	10	RESPONSIVE TO HIGH LIGHT 41 (RHL41)
AT2G29460	5.15	(4.97-5.32)	3.95	9.01E-11	10	glutathione S-transferase tau 4 (GSTU4)
AT1G32960	5.04	(4.25-5.84)	2.95	1.11E-12	10	SBT3.3
AT1G66090	4.85	(4.46-5.25)	2.63	1.02E-13	8	Disease resistance protein (TIR-NBS class)
AT4G21390	4.80	(4.37-5.24)	2.32	2.11E-14	8	B120 xyloglucan endotransglucosylase/hydrolase 18 (XTH18)
AT4G30280	4.72	(4.42-5.02)	2.35	2.83E-13	8	(XTH18)
AT3G50930	4.62	(4.31-4.93)	3.24	2.80E-13	10	cytochrome BC1 synthesis (BCS1)
AT2G41730	4.60	(4.18-5.03)	3.05	1.34E-12	7	unknown protein
AT3G23550	4.51	(4.37-4.65)	2.65	2.54E-12	8	MATE efflux family protein
AT5G25930	4.43	(4.24-4.61)	3.82	1.27E-14	8	Protein kinase family protein with leucine-rich repeat domain
AT4G03450	4.42	(3.78-5.06)	2.71	2.41E-10	10	Ankyrin repeat family protein
AT4G02380	4.30	(3.79-4.82)	5.03	5.02E-10	8	senescence-associated gene 21 (SAG21) receptor-like protein kinase-related family protein
AT5G48540	4.28	(4.07-4.49)	3.63	1.27E-14	8	protein
AT4G37370	4.27	(3.74-4.81)	3.99	1.07E-13	10	cytochrome P450, family 81, subfamily D, polypeptide 8 (CYP81D8)
AT3G22060	4.21	(3.53-4.89)	4.28	2.49E-12	8	Receptor-like protein kinase-related family protein
AT2G15480	4.11	(3.89-4.33)	2.63	5.85E-13	8	UDP-glucosyl transferase 73B5 (UGT73B5)
AT5G27420	4.11	(3.94-4.27)	3.30	8.99E-13	8	carbon/nitrogen insensitive 1 (CNI1)
AT2G02010	4.05	(3.79-4.31)	3.04	1.06E-10	8	glutamate decarboxylase 4 (GAD4)
AT4G34135	4.02	(3.75-4.29)	4.42	4.35E-14	10	UDP-glucosyltransferase 73B2 (UGT73B2)
AT3G15356	3.95	(2.92-4.97)	4.94	4.76E-14	8	Legume lectin family protein
AT2G41100	3.92	(3.71-4.12)	5.68	5.12E-09	8	TOUCH 3 (TCH3)
AT4G01870	3.84	(3.64-4.04)	3.90	5.80E-12	10	tolB protein-related
AT2G18690	3.84	(3.58-4.09)	3.74	1.07E-09	10	unknown protein
AT1G76600	3.74	(3.59-3.89)	2.59	1.29E-11	8	unknown protein
AT5G18470	3.70	(2.76-4.63)	2.37	7.17E-10	8	Curculin-like (mannose-binding) lectin family protein
AT1G28480	3.63	(3.25-4.02)	2.38	1.33E-08	10	GRX480
AT2G15390	3.63	(2.81-4.45)	2.70	1.53E-10	8	fucosyltransferase 4 (FUT4)
AT5G41750	3.60	(3.44-3.76)	2.47	3.48E-10	8	Disease resistance protein (TIR-NBS-LRR class) family
AT4G20830	3.59	(3.41-3.77)	6.75	4.46E-14	8	FAD-binding Berberine family protein
AT1G74360	3.59	(3.39-3.78)	2.67	9.01E-11	10	Leucine-rich repeat protein kinase family protein
AT2G03760	3.58	(3.22-3.95)	4.60	9.97E-16	7	sulphotransferase 12 (SOT12)
AT4G20860	3.58	(2.79-4.37)	4.67	5.02E-10	8	FAD-binding Berberine family protein

AT3G25610	3.52 (3.27-3.78)	4.32	7.58E-15	10	ATPase E1-E2 type family protein / haloacid dehalogenase-like hydrolase family protein
AT2G47000	3.50 (2.86-4.14)	4.40	2.80E-13	7	ATP binding cassette subfamily B4 (ABCB4)
AT1G07135	3.45 (2.69-4.20)	2.53	6.69E-12	8	glycine-rich protein
AT4G22530	3.44 (3.24-3.63)	2.95	1.12E-13	10	S-adenosyl-L-methionine-dependent methyltransferases superfamily protein
AT3G52400	3.39 (1.99-4.79)	4.05	2.79E-11	8	syntaxin of plants 122 (SYP122)
AT1G17170	3.36 (3.07-3.65)	3.23	2.17E-09	7	glutathione S-transferase TAU 24 (GSTU24)
AT4G14365	3.34 (2.10-4.58)	4.38	4.01E-09	10	XB3 ortholog 4 in Arabidopsis thaliana (XBAT34)
AT5G01540	3.31 (3.12-3.49)	2.39	9.03E-10	8	lectin receptor kinase a4.1 (LECRKA4.1)
AT2G29720	3.30 (3.10-3.50)	3.85	1.81E-15	8	CTF2B
AT4G23190	3.28 (3.14-3.43)	3.11	1.73E-11	8	cysteine-rich RLK (RECEPTOR-like protein kinase) 11 (CRK11)
AT5G19230	3.28 (3.02-3.54)	2.76	5.93E-10	8	Glycoprotein membrane precursor GPI-anchored
AT5G57560	3.25 (3.03-3.47)	3.82	3.77E-13	8	Touch 4 (TCH4)
AT1G28190	3.24 (2.95-3.54)	2.80	2.75E-12	8	unknown protein
AT5G51440	3.23 (2.22-4.25)	4.83	3.31E-13	7	HSP20-like chaperones superfamily protein
AT1G09970	3.21 (1.57-4.85)	7.21	3.32E-13	8	LRR XI-23
AT4G23810	3.16 (2.78-3.54)	2.60	1.27E-10	8	WRKY53
AT1G18300	3.14 (1.03-5.25)	2.67	2.14E-13	8	nudix hydrolase homolog 4 (NUDT4)
AT3G01290	3.13 (2.80-3.46)	5.34	3.27E-08	8	SPFH/Band 7/PHB domain-containing membrane-associated protein family
AT2G38470	3.11 (2.94-3.28)	4.09	1.57E-11	8	WRKY DNA-binding protein 33 (WRKY33)
AT1G76680	3.09 (2.91-3.28) (-4.80-	7.13	4.53E-14	8	12-oxophytodienoate reductase 1 (OPR1)
AT2G29490	3.07 10.94)	4.22	2.15E-10	10	glutathione S-transferase TAU 1 (GSTU1)
AT1G51760	3.06 (2.72-3.41)	6.66	2.23E-10	10	IAA-ALANINE RESISTANT 3 (IAR3)
AT5G25250	3.04 (2.83-3.25)	3.37	2.41E-08	10	SPFH/Band 7/PHB domain-containing membrane-associated protein family
AT2G36790	3.00 (2.73-3.26)	2.51	1.44E-10	7	UDP-glucosyl transferase 73C6 (UGT73C6)
AT3G09405	2.99 (1.30-4.67)	2.78	1.17E-10	10	Pectinacetyltransferase family protein
AT5G10695	2.93 (2.75-3.12)	2.53	4.45E-09	8	unknown protein
AT1G63840	2.93 (0.99-4.87)	4.33	5.07E-14	10	RING/U-box superfamily protein
AT1G52200	2.91 (2.67-3.15)	3.53	2.47E-09	8	PLAC8 family protein
AT2G25735	2.89 (2.51-3.27)	2.39	8.28E-11	8	unknown protein
AT4G13180	2.86 (2.60-3.12)	5.01	9.90E-13	8	NAD(P)-binding Rossmann-fold superfamily protein
AT5G39050	2.84 (2.65-3.03)	5.33	7.26E-13	10	HXXXD-type acyl-transferase family protein
AT1G76970	2.83 (2.46-3.21)	3.52	1.02E-13	10	Target of Myb protein 1
AT1G72520	2.82 (2.29-3.35)	4.04	1.54E-09	8	PLAT/LH2 domain-containing lipoxigenase family protein
AT3G57450	2.82 (2.50-3.14)	4.86	3.23E-08	8	unknown protein
AT1G22400	2.82 (2.44-3.19)	5.15	9.01E-11	10	UGT85A1
AT3G28340	2.82 (2.58-3.06)	2.55	2.58E-13	8	galacturonosyltransferase-like 10 (GATL10)
AT5G08790	2.82 (2.47-3.17)	5.76	7.35E-13	10	ATAF2
AT3G09010	2.80 (2.14-3.46)	3.02	4.92E-14	8	Protein kinase superfamily protein

AT3G62150	2.79	(2.31-3.28)	4.18	2.10E-11	8	P-glycoprotein 21 (PGP21)
AT1G30755	2.77	(2.55-2.99)	3.11	1.32E-14	8	Protein of unknown function (DUF668)
AT1G07400	2.77	(2.54-2.99)	3.15	8.99E-09	10	HSP20-like chaperones superfamily protein
AT2G26560	2.76	(2.57-2.96)	3.65	7.64E-09	8	phospholipase A 2A (PLA2A)
AT4G25810	2.71	(2.47-2.96)	3.20	2.45E-11	10	xyloglucan endotransglycosylase 6 (XTR6)
AT5G19240	2.70	(2.41-3.00)	4.72	9.77E-08	8	Glycoprotein membrane precursor GPI-anchored
AT1G66160	2.69	(2.07-3.31)	2.33	3.23E-09	10	CYS, MET, PRO, and GLY protein 1 (CMPG1)
AT2G36750	2.69	(2.44-2.93)	2.92	1.35E-10	9	UDP-glucosyl transferase 73C1 (UGT73C1)
AT5G41740	2.68	(2.06-3.31)	3.38	2.56E-11	8	Disease resistance protein (TIR-NBS-LRR class) family
AT5G13190	2.68	(2.44-2.92)	4.89	7.40E-13	8	CONTAINS InterPro DOMAIN/s: LPS-induced tumor necrosis factor alpha factor (InterPro:IPR006629)
AT1G70140	2.66	(2.43-2.89)	3.00	6.97E-12	8	formin 8 (FH8)
AT3G11840	2.64	(2.43-2.85)	2.78	1.48E-10	8	plant U-box 24 (PUB24)
AT1G21550	2.63	(1.47-3.78)	3.04	8.44E-11	8	Calcium-binding EF-hand family protein
AT1G32870	2.60	(2.38-2.81)	4.35	4.92E-14	10	NAC domain protein 13 (NAC13)
AT1G72900	2.59	(2.32-2.87)	4.67	2.11E-11	10	Toll-Interleukin-Resistance (TIR) domain-containing protein
AT2G30250	2.57	(2.38-2.75)	4.25	1.41E-10	10	WRKY DNA-binding protein 25 (WRKY25)
AT4G05020	2.56	(2.31-2.81)	5.02	5.99E-12	9	NAD(P)H dehydrogenase B2 (NDB2)
AT3G13080	2.54	(2.40-2.68)	5.19	9.33E-13	9	multidrug resistance-associated protein 3 (MRP3)
AT3G04000	2.53	(2.35-2.72)	4.88	5.59E-09	9	NAD(P)-binding Rossmann-fold superfamily protein
AT4G27410	2.53	(2.22-2.84)	3.93	1.01E-08	10	RESPONSIVE TO DESICCATION 26 (RD26)
AT2G23680	2.50	(1.80-3.21)	3.58	3.48E-11	8	Cold acclimation protein WCOR413 family
AT2G26530	2.50	(2.27-2.73)	3.88	2.39E-11	8	AR781
AT3G55980	2.50	(2.29-2.70)	4.09	2.39E-11	8	salt-inducible zinc finger 1 (SZF1)
AT1G17420	2.49	(2.29-2.68)	5.62	2.05E-10	8	lipoxygenase 3 (LOX3)
AT5G03610	2.48	(2.26-2.70)	4.03	3.83E-10	10	GDSL-like Lipase/Acylhydrolase superfamily protein
AT3G22370	2.48	(2.20-2.75)	6.64	1.08E-13	10	alternative oxidase 1A (AOX1A)

4hr	logFC	CI	AveExpr	FDR P	Cluster	Description
AT1G15520	7.496316	(7.12-7.88)	3.77	4.44E-13	10	pleiotropic drug resistance 12 (PDR12)
AT1G05680	6.676783	(6.42-6.94)	3.29	1.90E-17	7	Uridine diphosphate glycosyltransferase 74E2 (UGT74E2)
AT1G32350	6.569313	(5.64-7.50)	2.36	1.23E-11	7	alternative oxidase 1D (AOX1D)
AT2G41730	6.563677	(6.37-6.76)	3.05	4.56E-18	7	unknown protein
AT1G32960	6.554764	(5.73-7.38)	2.95	3.87E-14	10	SBT3.3
AT2G34500	6.44694	(6.08-6.82)	2.04	1.15E-10	7	cytochrome P450, family 710, subfamily A, polypeptide 1 (CYP710A1)
AT2G04050	6.234417	(5.91-6.56)	2.19	5.38E-18	7	MATE efflux family protein
AT2G29460	6.117762	(5.96-6.28)	3.95	2.71E-14	10	glutathione S-transferase tau 4 (GSTU4)
AT1G17170	6.1027	(5.99-6.22)	3.23	4.22E-17	7	glutathione S-transferase TAU 24 (GSTU24)
AT2G29470	6.038117	(5.90-6.18)	2.03	7.08E-08	10	glutathione S-transferase tau 3 (GSTU3)
AT3G28210	5.995403	(5.53-6.47)	2.12	1.94E-11	10	PMZ

AT2G47000	5.898895	(5.57-6.23)	4.40	5.38E-21	7	ATP binding cassette subfamily B4 (ABCB4)
AT1G19020	5.880246	(5.67-6.09)	2.97	1.11E-14	8	unknown protein
AT2G30770	5.858055	(5.12-6.60)	2.43	2.61E-09	9	cytochrome P450, family 71, subfamily A, polypeptide 13 (CYP71A13)
AT4G04490	5.855806	(5.48-6.23)	2.03	1.27E-15	7	cysteine-rich RLK (RECEPTOR-like protein kinase) 36 (CRK36)
AT2G36800	5.845767	(5.65-6.04)	2.34	2.64E-11	9	don-glucosyltransferase 1 (DOGT1)
AT2G18690	5.831285	(5.64-6.02)	3.74	6.15E-14	10	unknown protein
AT4G37990	5.721909	(5.39-6.06)	4.23	8.54E-08	9	elicitor-activated gene 3-2 (ELI3-2) ATPase E1-E2 type family protein / haloacid dehalogenase-like hydrolase
AT3G63380	5.720463	(4.71-6.73)	2.16	4.56E-11	10	family protein
AT1G05340	5.670602	(4.79-6.55)	2.31	1.89E-09	9	unknown protein
AT2G03760	5.640804	(5.51-5.77)	4.60	2.22E-23	7	sulphotransferase 12 (SOT12)
AT1G10585	5.603245	(5.47-5.73)	2.74	1.92E-12	7	basic helix-loop-helix (bHLH) DNA-binding superfamily protein
AT3G26830	5.598814	(4.52-6.68)	4.67	1.96E-11	10	PHYTOALEXIN DEFICIENT 3 (PAD3)
AT5G59820	5.541545	(5.40-5.69)	2.92	1.27E-15	10	RESPONSIVE TO HIGH LIGHT 41 (RHL41)
AT5G03210	5.512064	(5.40-5.63)	2.77	8.35E-10	10	unknown protein
AT2G36790	5.454545	(5.11-5.80)	2.51	4.20E-19	7	UDP-glucosyl transferase 73C6 (UGT73C6)
AT1G21240	5.331844	(4.98-5.69)	2.52	1.69E-12	7	wall associated kinase 3 (WAK3)
AT4G37370	5.205332	(4.69-5.72)	3.99	3.46E-18	10	cytochrome P450, family 81, subfamily D, polypeptide 8 (CYP81D8)
AT5G25250	5.177363	(4.88-5.48)	3.37	1.62E-13	10	SPFH/Band 7/PHB domain-containing membrane-associated protein family
AT3G22600	5.17591	(5.00-5.35)	3.16	1.01E-10	9	Bifunctional inhibitor/lipid-transfer protein/seed storage 2S albumin superfamily protein
AT3G50930	5.068567	(4.92-5.22)	3.24	2.22E-17	10	cytochrome BC1 synthesis (BCS1)
AT5G38900	5.034125	(4.86-5.21)	2.75	3.62E-11	9	Thioredoxin superfamily protein
AT2G29500	4.98314	(4.88-5.09)	4.21	3.44E-13	7	HSP20-like chaperones superfamily protein
AT1G61120	4.962667	(4.72-5.20)	3.93	1.90E-08	10	terpene synthase 04 (TPS04)
AT2G24850	4.955134	(4.56-5.35)	5.53	8.15E-09	9	tyrosine aminotransferase 3 (TAT3)
AT4G11890	4.949196	(4.77-5.13)	2.49	2.64E-12	7	Protein kinase superfamily protein
AT3G49620	4.810415	(4.61-5.01)	3.19	1.90E-08	10	DARK INDUCIBLE 11 (DIN11)
AT5G27420	4.648111	(4.20-5.09)	3.30	1.65E-14	8	carbon/nitrogen insensitive 1 (CNI1)
AT2G21640	4.596978	(3.26-5.94)	4.98	2.90E-18	7	unknown protein
AT1G26420	4.559704	(4.36-4.76)	2.19	3.15E-11	7	FAD-binding Berberine family protein
AT5G43450	4.558359	(4.42-4.70)	5.08	5.27E-22	7	2-oxoglutarate (2OG) and Fe(II)-dependent oxygenase superfamily protein
AT3G15356	4.464197	(3.61-5.32)	4.94	1.83E-17	8	Legume lectin family protein
AT3G14440	4.425239	(2.77-6.08)	2.21	1.51E-10	9	nine-cis-epoxycarotenoid dioxygenase 3 (NCED3)
AT1G02920	4.42408	(4.25-4.60)	6.46	2.31E-10	7	glutathione S-transferase 7 (GSTF7)
AT2G39030	4.370298	(4.14-4.60)	4.93	8.35E-08	6	Acyl-CoA N-acyltransferases (NAT) superfamily protein
AT1G14870	4.349677	(3.89-4.81)	2.30	1.46E-09	10	PLANT CADMIUM RESISTANCE 2 (PCR2)
AT2G29350	4.337107	(4.23-4.44)	5.82	2.88E-08	9	senescence-associated gene 13 (SAG13)
AT5G25930	4.320281	(4.12-4.52)	3.82	5.11E-17	8	Protein kinase family protein with leucine-rich repeat domain
AT5G27060	4.314913	(4.04-4.59)	2.02	1.70E-09	9	receptor like protein 53 (RLP53)

AT5G20230	4.303031	(4.06-4.54)	5.49	3.91E-11	10	blue-copper-binding protein (BCB)
AT4G02380	4.287602	(3.84-4.73)	5.03	2.64E-12	8	senescence-associated gene 21 (SAG21)
AT5G51440	4.232328	(3.69-4.77)	4.83	1.22E-18	7	HSP20-like chaperones superfamily protein
AT2G29490	4.213626	(3.96-4.47)	4.22	1.80E-15	10	glutathione S-transferase TAU 1 (GSTU1) NAC domain containing protein 19
AT1G52890	4.203555	(3.62-4.79)	3.62	1.44E-09	9	(NAC019)
AT1G32940	4.181399	(2.29-6.08)	4.65	6.44E-16	9	SBT3.5 Uncharacterised conserved protein
AT5G13210	4.153175	(3.11-5.20)	2.70	2.32E-16	7	UCP015417, vWA Leucine-rich repeat protein kinase family
AT1G74360	4.144223	(3.63-4.66)	2.67	8.51E-13	10	protein
AT4G01870	4.135477	(3.95-4.32)	3.90	1.20E-14	10	tolB protein-related
AT1G59590	4.121444	(3.57-4.67)	2.59	9.94E-13	10	ZCF37 Leucine-rich repeat protein kinase family
AT1G51890	4.116104	(3.74-4.50)	2.13	2.70E-10	7	protein
AT1G02930	4.077867	(3.92-4.24)	6.73	3.32E-09	10	glutathione S-transferase 6 (GSTF6)
AT4G05020	4.076501	(3.92-4.23)	5.02	1.22E-18	9	NAD(P)H dehydrogenase B2 (NDB2) FAD/NAD(P)-binding oxidoreductase
AT5G22140	4.075168	(1.30-6.85)	1.97	4.80E-11	7	family protein
AT3G61630	4.064541	(3.84-4.29)	2.94	3.71E-16	7	cytokinin response factor 6 (CRF6) receptor-like protein kinase-related family
AT5G48540	4.030286	(3.85-4.21)	3.63	1.60E-15	8	protein
AT3G22370	4.019228	(3.85-4.18)	6.64	5.27E-21	10	alternative oxidase 1A (AOX1A)
AT3G52400	4.014732	(3.71-4.32)	4.05	6.01E-14	8	syntaxin of plants 122 (SYP122)
AT4G03450	4.012474	(3.88-4.15)	2.71	2.18E-12	10	Ankyrin repeat family protein HXXXD-type acyl-transferase family
AT5G39050	3.984604	(3.87-4.10)	5.33	1.41E-18	10	protein Late embryogenesis abundant (LEA)
AT1G65690	3.950116	(3.78-4.12)	2.68	2.55E-10	9	hydroxyproline-rich glycoprotein family
AT2G36750	3.930753	(3.77-4.10)	2.92	5.37E-18	9	UDP-glucosyl transferase 73C1 (UGT73C1) SPFH/Band 7/PHB domain-containing
AT5G54100	3.922593	(3.63-4.21)	4.02	1.27E-19	7	membrane-associated protein family
AT4G34131	3.915374	(2.95-4.88)	2.11	5.65E-15	10	UDP-glucosyl transferase 73B3 (UGT73B3)
AT3G47480	3.86859	(3.34-4.39)	2.07	3.93E-09	9	Calcium-binding EF-hand family protein
AT4G21390	3.862777	(3.38-4.34)	2.32	1.45E-14	8	B120
AT2G29440	3.855386	(3.72-3.99)	2.28	5.78E-09	9	glutathione S-transferase tau 6 (GSTU6)
AT5G14730	3.836249	(3.17-4.50)	2.17	3.52E-15	10	unknown protein
AT1G28480	3.808738	(3.50-4.12)	2.38	3.02E-11	10	GRX480
AT2G15480	3.711684	(3.46-3.96)	2.63	2.91E-13	8	UDP-glucosyl transferase 73B5 (UGT73B5)
AT1G52200	3.696754	(3.58-3.81)	3.53	4.47E-11	8	PLAC8 family protein xyloglucan endotransglucosylase/hydrolase 18
AT4G30280	3.69262	(3.48-3.91)	2.35	3.17E-10	8	(XTH18) Regulator of Vps4 activity in the MVB
AT1G13340	3.691131	(3.52-3.86)	3.93	1.07E-14	7	pathway protein XB3 ortholog 4 in Arabidopsis thaliana
AT4G14365	3.680406	(3.56-3.80)	4.38	1.98E-12	10	(XBAT34)
AT5G67340	3.672311	(3.51-3.84)	2.19	2.91E-13	10	ARM repeat superfamily protein
AT2G43570	3.667181	(3.56-3.78)	3.82	6.20E-09	9	chitinase, putative (CHI) Curculin-like (mannose-binding) lectin
AT5G18470	3.649259	(3.38-3.92)	2.37	7.63E-11	8	family protein Pentatricopeptide repeat (PPR)
AT2G20720	3.639154	(3.48-3.80)	2.87	2.37E-16	7	superfamily protein

AT5G59220	3.632514	(2.88-4.38)	3.42	2.23E-10	9	highly ABA-induced PP2C gene 1 (HAI1) Disease resistance protein (TIR-NBS-LRR class) family
AT5G41750	3.625983	(3.36-3.89)	2.47	2.71E-11	8	Methylenetetrahydrofolate reductase
AT5G38710	3.611066	(2.98-4.24)	2.30	6.42E-10	10	family protein
AT3G03270	3.605856	(2.72-4.49)	3.79	6.62E-17	7	Adenine nucleotide alpha hydrolases-like superfamily protein
AT1G68620	3.603339	(2.96-4.25)	3.52	1.84E-10	9	alpha/beta-Hydrolases superfamily protein
AT3G04000	3.587551	(3.38-3.80)	4.88	5.19E-15	9	NAD(P)-binding Rossmann-fold superfamily protein
AT2G41380	3.578858	(3.36-3.79)	2.19	9.71E-14	7	S-adenosyl-L-methionine-dependent methyltransferases superfamily protein
AT4G20830	3.573235	(3.33-3.82)	6.75	1.63E-17	8	FAD-binding Berberine family protein
AT4G20860	3.533156	(2.69-4.38)	4.67	7.46E-12	8	FAD-binding Berberine family protein
AT4G22980	3.527206	(2.75-4.30)	1.95	8.06E-18	10	FUNCTIONS IN: molecular_function unknown
AT1G10140	3.527155	(3.01-4.04)	3.18	8.73E-12	8	Uncharacterised conserved protein UCP031279
AT2G15390	3.505529	(3.36-3.65)	2.70	7.49E-11	8	fucosyltransferase 4 (FUT4)
AT4G16260	3.503084	(3.35-3.66)	3.81	1.14E-09	9	Glycosyl hydrolase superfamily protein
AT3G47780	3.496231	(3.26-3.73)	2.11	5.37E-12	7	ABC2 homolog 6 (ATH6)

8hr	logFC	CI	AveExpr	FDR P	Cluster	Description
AT1G15520	6.018873	(5.74-6.30)	3.77	1.19E-08	10	pleiotropic drug resistance 12 (PDR12) Uridine diphosphate glycosyltransferase
AT1G05680	5.721463	(5.36-6.09)	3.29	1.52E-12	7	74E2 (UGT74E2)
AT2G41730	5.630134	(5.19-6.07)	3.05	5.17E-13	7	unknown protein
AT1G32960	5.412545	(4.28-6.54)	2.95	2.51E-10	10	SBT3.3
AT1G17170	5.042179	(4.78-5.31)	3.23	2.92E-13	7	glutathione S-transferase TAU 24 (GSTU24)
AT2G29460	4.948735	(4.76-5.13)	3.95	8.00E-11	10	glutathione S-transferase tau 4 (GSTU4)
AT3G26830	4.883133	(4.61-5.16)	4.67	2.85E-08	10	PHYTOALEXIN DEFICIENT 3 (PAD3)
AT3G28210	4.86694	(4.66-5.07)	2.12	6.52E-08	10	PMZ
AT2G04050	4.76234	(4.58-4.94)	2.19	1.94E-13	7	MATE efflux family protein Bifunctional inhibitor/lipid-transfer protein/seed storage 2S albumin superfamily protein
AT3G22600	4.579629	(4.36-4.80)	3.16	8.71E-08	9	superfamily protein
AT2G18690	4.513375	(4.24-4.79)	3.74	5.81E-10	10	unknown protein
AT4G04490	4.464969	(3.96-4.97)	2.03	8.36E-11	7	cysteine-rich RLK (RECEPTOR-like protein kinase) 36 (CRK36)
AT2G47000	4.433739	(3.88-4.99)	4.40	5.17E-16	7	ATP binding cassette subfamily B4 (ABCB4)
AT1G21240	4.296755	(4.13-4.46)	2.52	1.11E-08	7	wall associated kinase 3 (WAK3)
AT2G03760	4.130841	(3.92-4.34)	4.60	1.14E-17	7	sulphotransferase 12 (SOT12) basic helix-loop-helix (bHLH) DNA-binding superfamily protein
AT1G10585	4.117584	(3.84-4.40)	2.74	1.42E-08	7	superfamily protein
AT5G38900	4.087763	(2.01-6.16)	2.75	8.18E-08	9	Thioredoxin superfamily protein
AT5G59820	4.043397	(3.62-4.47)	2.92	1.88E-11	10	RESPONSIVE TO HIGH LIGHT 41 (RHL41)
AT1G67810	3.999699	(3.73-4.27)	1.95	8.23E-11	10	sulfur E2 (SUFE2)
AT1G02920	3.968062	(3.51-4.42)	6.46	8.18E-08	7	glutathione S-transferase 7 (GSTF7)
AT2G36790	3.923326	(3.75-4.10)	2.51	5.88E-14	7	UDP-glucosyl transferase 73C6 (UGT73C6)
AT1G19020	3.919349	(3.72-4.12)	2.97	6.82E-10	8	unknown protein

AT5G25250	3.862626	(2.14-5.59)	3.37	3.97E-09	10	SPFH/Band 7/PHB domain-containing membrane-associated protein family
AT4G11890	3.843449	(3.53-4.16)	2.49	1.91E-08	7	Protein kinase superfamily protein
AT2G21640	3.742093	(3.33-4.15)	4.98	4.11E-14	7	unknown protein
AT4G37370	3.727984	(3.54-3.92)	3.99	1.42E-12	10	cytochrome P450, family 81, subfamily D, polypeptide 8 (CYP81D8)
AT1G32940	3.636863	(3.39-3.88)	4.65	2.43E-12	9	SBT3.5
AT5G27420	3.549876	(1.94-5.16)	3.30	6.23E-10	8	carbon/nitrogen insensitive 1 (CNI1)
AT3G26210	3.481119	(1.95-5.01)	3.51	4.86E-09	9	cytochrome P450, family 71, subfamily B, polypeptide 23 (CYP71B23)
AT5G25930	3.454355	(3.25-3.65)	3.82	3.67E-12	8	Protein kinase family protein with leucine-rich repeat domain
AT4G03450	3.452719	(3.03-3.88)	2.71	2.39E-08	10	Ankyrin repeat family protein
AT5G43450	3.377382	(2.93-3.82)	5.08	5.54E-17	7	2-oxoglutarate (2OG) and Fe(II)-dependent oxygenase superfamily protein
AT3G54420	3.334729	(3.15-3.52)	1.72	6.42E-11	9	homolog of carrot EP3-3 chitinase (EP3)
AT1G47510	3.322031	(3.03-3.62)	1.87	8.77E-08	10	inositol polyphosphate 5-phosphatase 11 (5PTASE11)
AT1G80840	3.319682	(3.17-3.47)	1.78	1.36E-08	8	WRKY DNA-binding protein 40 (WRKY40)
AT3G50930	3.299901	(3.04-3.56)	3.24	9.10E-12	10	cytochrome BC1 synthesis (BCS1)
AT5G39050	3.23693	(3.00-3.48)	5.33	2.10E-14	10	HXXXD-type acyl-transferase family protein
AT4G02520	3.19181	(2.62-3.76)	7.88	1.51E-10	9	glutathione S-transferase PHI 2 (GSTF2)
AT4G34131	3.174877	(2.90-3.45)	2.11	2.51E-10	10	UDP-glucosyl transferase 73B3 (UGT73B3)
AT1G68620	3.172418	(2.90-3.45)	3.52	8.18E-08	9	alpha/beta-Hydrolases superfamily protein
AT4G02380	3.152784	(2.51-3.79)	5.03	3.09E-08	8	senescence-associated gene 21 (SAG21)
AT2G29490	3.143949	(2.91-3.37)	4.22	1.01E-10	10	glutathione S-transferase TAU 1 (GSTU1)
AT4G05020	3.137831	(2.52-3.75)	5.02	2.53E-14	9	NAD(P)H dehydrogenase B2 (NDB2)
AT4G01870	3.10265	(2.91-3.29)	3.90	1.83E-09	10	tolB protein-related receptor-like protein kinase-related family
AT5G48540	3.0892	(2.96-3.21)	3.63	1.88E-11	8	protein
AT4G14365	3.06074	(2.71-3.41)	4.38	7.52E-09	10	XB3 ortholog 4 in Arabidopsis thaliana (XBAT34)
AT3G22370	3.002939	(2.79-3.21)	6.64	2.71E-16	10	alternative oxidase 1A (AOX1A)
AT5G26340	2.952252	(2.75-3.15)	5.97	1.79E-13	10	MSS1
AT5G54100	2.892913	(2.25-3.54)	4.02	2.10E-14	7	SPFH/Band 7/PHB domain-containing membrane-associated protein family
AT3G52400	2.87332	(2.59-3.15)	4.05	9.23E-09	8	syntaxin of plants 122 (SYP122)
AT5G51440	2.869234	(2.70-3.04)	4.83	2.73E-13	7	HSP20-like chaperones superfamily protein
AT2G36750	2.861142	(0.75-4.97)	2.92	2.01E-13	9	UDP-glucosyl transferase 73C1 (UGT73C1)
AT5G04340	2.819139	(2.51-3.13)	2.28	8.78E-09	8	zinc finger of Arabidopsis thaliana 6 (ZAT6)
AT1G59590	2.807727	(2.22-3.40)	2.59	2.97E-08	10	ZCF37
AT5G17330	2.770793	(2.53-3.02)	1.90	3.28E-12	9	glutamate decarboxylase (GAD)
AT4G27410	2.750317	(2.49-3.01)	3.93	1.63E-09	10	RESPONSIVE TO DESICCATION 26 (RD26)
AT3G04000	2.747145	(0.66-4.83)	4.88	8.82E-11	9	NAD(P)-binding Rossmann-fold superfamily protein
AT5G67340	2.719258	(2.07-3.37)	2.19	1.75E-08	10	ARM repeat superfamily protein
AT4G22980	2.713528	(2.03-3.40)	1.95	1.08E-12	10	FUNCTIONS IN: molecular_function unknown
AT4G18360	2.701	(2.53-2.87)	2.33	8.18E-08	9	Aldolase-type TIM barrel family protein
AT4G22530	2.694058	(2.51-2.88)	2.95	4.66E-11	10	S-adenosyl-L-methionine-dependent methyltransferases superfamily protein

AT3G61630	2.668754	(2.51-2.83)	2.94	4.14E-10	7	cytokinin response factor 6 (CRF6)
AT5G54610	2.627083	(2.28-2.97)	5.17	6.74E-08	9	ankyrin (ANK)
AT4G04220	2.623803	(2.36-2.89)	2.06	1.08E-08	9	receptor like protein 46 (RLP46)
AT4G38540	2.607574	(2.40-2.81)	3.94	1.24E-09	10	FAD/NAD(P)-binding oxidoreductase family protein
AT4G21390	2.59954	(1.85-3.35)	2.32	5.76E-09	8	B120
AT1G60730	2.568419	(1.58-3.56)	5.41	3.67E-12	10	NAD(P)-linked oxidoreductase superfamily protein
AT1G13340	2.56666	(2.06-3.07)	3.93	9.25E-10	7	Regulator of Vps4 activity in the MVB pathway protein
AT5G14730	2.563201	(2.29-2.84)	2.17	8.05E-08	10	unknown protein
AT3G51660	2.550242	(2.37-2.73)	4.56	1.61E-09	8	Tautomerase/MIF superfamily protein
AT1G63840	2.523232	(2.35-2.70)	4.33	1.43E-13	10	RING/U-box superfamily protein
AT4G20830	2.503913	(-0.90-5.90)	6.75	3.09E-12	8	FAD-binding Berberine family protein
AT4G34135	2.493799	(2.28-2.71)	4.42	3.86E-12	10	UDP-glucosyltransferase 73B2 (UGT73B2)
AT3G03270	2.485933	(2.16-2.81)	3.79	4.45E-11	7	Adenine nucleotide alpha hydrolases-like superfamily protein
AT5G46350	2.451479	(1.93-2.97)	2.99	1.02E-08	9	WRKY DNA-binding protein 8 (WRKY8)
AT1G66090	2.448118	(2.17-2.73)	2.63	1.82E-08	8	Disease resistance protein (TIR-NBS class)
AT1G62570	2.434013	(1.46-3.41)	2.90	1.24E-10	9	flavin-monoxygenase glucosinolate S-oxygenase 4 (FMO GS-OX4)
AT3G43270	2.389945	(1.81-2.97)	4.31	4.95E-08	9	Plant invertase/pectin methylesterase inhibitor superfamily
AT1G66880	2.351568	(2.23-2.48)	4.13	2.11E-09	7	Protein kinase superfamily protein
AT5G13210	2.34655	(2.13-2.56)	2.70	9.54E-10	7	Uncharacterised conserved protein
AT4G03320	2.328348	(2.02-2.64)	2.73	1.96E-11	7	UCP015417, vWA translocon at the inner envelope
AT2G38470	2.316956	(2.13-2.50)	4.09	4.20E-08	7	membrane of chloroplasts 20-IV (tic20-IV)
AT5G57480	2.315655	(2.09-2.54)	2.44	5.57E-09	8	WRKY DNA-binding protein 33 (WRKY33)
AT2G35480	2.306058	(1.57-3.04)	2.23	1.00E-10	10	P-loop containing nucleoside triphosphate hydrolases superfamily protein
AT2G20720	2.290357	(2.11-2.47)	2.87	1.65E-09	7	unknown protein
AT1G70800	2.289543	(2.00-2.58)	3.10	3.19E-11	7	Pentatricopeptide repeat (PPR) superfamily protein
AT4G36040	2.285891	(1.89-2.69)	6.56	1.63E-12	9	Calcium-dependent lipid-binding (CaLB domain) family protein
AT3G22060	2.284538	(2.00-2.57)	4.28	1.84E-08	2	Chaperone DnaJ-domain superfamily protein
AT1G15670	2.277779	(1.66-2.89)	4.24	3.95E-09	8	Receptor-like protein kinase-related family protein
AT2G31865	2.268588	(2.03-2.51)	2.92	4.40E-09	7	Galactose oxidase/kelch repeat superfamily protein
AT3G11840	2.253553	(1.99-2.52)	2.78	2.65E-08	7	poly(ADP-ribose) glycohydrolase 2 (PARG2)
AT5G05410	2.227377	(1.60-2.85)	3.21	7.54E-08	8	plant U-box 24 (PUB24)
AT3G25610	2.22233	(2.08-2.36)	4.32	3.81E-12	10	DRE-binding protein 2A (DREB2A)
AT3G15356	2.220339	(2.00-2.44)	4.94	4.77E-10	8	ATPase E1-E2 type family protein / haloacid dehalogenase-like hydrolase family protein
AT5G20960	2.220078	(0.87-3.57)	4.62	2.45E-09	8	Legume lectin family protein
AT1G21390	2.216816	(1.62-2.81)	3.12	3.08E-11	7	aldehyde oxidase 1 (AO1)
AT2G37770	2.203823	(1.61-2.80)	4.97	5.37E-08	7	embryo defective 2170 (emb2170)
AT5G01100	2.203531	(1.92-2.49)	2.19	7.81E-09	10	NAD(P)-linked oxidoreductase superfamily protein
					8	O-fucosyltransferase family protein

24hr	logFC	CI	AveExpr	FDR P	Cluster	Description
AT4G13180	2.201902	(2.07-2.33)	5.01	4.52E-11	8	NAD(P)-binding Rossmann-fold superfamily protein
AT2G41380	2.188104	(2.03-2.35)	2.19	3.52E-08	7	S-adenosyl-L-methionine-dependent methyltransferases superfamily protein
AT3G22840	2.167033	(1.95-2.38)	2.37	2.73E-09	9	EARLY LIGHT-INDUCIBLE PROTEIN (ELIP1)
AT4G12480	3.667419	(3.47-3.87)	4.47	0.00021	6	pEARLI 1 Bifunctional inhibitor/lipid-transfer protein/seed storage 2S albumin superfamily protein
AT4G12490	3.41195	(2.85-3.98)	3.40	0.000974	6	superfamily protein
AT1G61120	3.315336	(3.08-3.56)	3.93	0.023625	10	terpene synthase 04 (TPS04)
AT3G24982	3.060724	(2.49-3.64)	3.03	0.034094	9	receptor like protein 40 (RLP40)
AT3G57260	2.527588	(2.11-2.95)	4.07	0.005398	6	beta-1,3-glucanase 2 (BGL2) Acyl-CoA N-acyltransferases (NAT) superfamily protein
AT2G39030	2.43073	(2.19-2.67)	4.93	0.020814	6	superfamily protein
AT4G12470	2.266506	(2.12-2.42)	3.00	0.027413	9	azelaic acid induced 1 (AZI1)
AT1G32960	2.033252	(1.77-2.30)	2.95	0.005398	10	SBT3.3
AT4G16260	1.948638	(1.32-2.58)	3.81	0.006607	9	Glycosyl hydrolase superfamily protein
AT1G02930	1.881566	(1.63-2.14)	6.73	0.039613	10	glutathione S-transferase 6 (GSTF6)
AT5G38900	1.880627	(1.66-2.11)	2.75	0.019902	9	Thioredoxin superfamily protein
AT1G21520	1.862671	(1.35-2.37)	3.88	0.003018	9	unknown protein Bifunctional inhibitor/lipid-transfer protein/seed storage 2S albumin superfamily protein
AT3G22600	1.852751	(1.48-2.22)	3.16	0.036885	9	superfamily protein
AT2G41730	1.852115	(1.67-2.04)	3.05	0.024352	7	unknown protein
AT4G02330	1.851061	(1.60-2.10)	3.26	0.024811	9	ATPMEPCRB
AT1G02920	1.842689	(1.31-2.38)	6.46	0.029983	7	glutathione S-transferase 7 (GSTF7)
AT1G76930	1.822018	(1.46-2.19)	4.44	0.011398	6	extensin 4 (EXT4)
AT2G43570	1.777326	(1.62-1.94)	3.82	0.015589	9	chitinase, putative (CHI)
AT1G68620	1.766339	(-2.33-5.86)	3.52	0.019141	9	alpha/beta-Hydrolases superfamily protein
AT5G64120	1.758863	(0.91-2.60)	4.17	0.045844	8	Peroxidase superfamily protein
AT5G59820	1.756683	(1.59-1.92)	2.92	0.029983	10	RESPONSIVE TO HIGH LIGHT 41 (RHL41) Plant invertase/pectin methylesterase inhibitor superfamily
AT3G43270	1.748004	(0.80-2.69)	4.31	0.003575	9	inhibitor superfamily
AT2G29460	1.744203	(1.53-1.96)	3.95	0.045826	10	glutathione S-transferase tau 4 (GSTU4) Late embryogenesis abundant (LEA)
AT1G65690	1.738373	(1.42-2.06)	2.68	0.012675	9	hydroxyproline-rich glycoprotein family cytochrome P450, family 71, subfamily B, polypeptide 23 (CYP71B23)
AT3G26210	1.718122	(0.32-3.12)	3.51	0.003533	9	polypeptide 23 (CYP71B23)
AT1G21310	1.710229	(1.44-1.98)	5.13	0.021881	6	extensin 3 (EXT3)
AT1G66920	1.585531	(1.36-1.81)	3.49	0.003018	8	Protein kinase superfamily protein
AT5G27420	1.565104	(1.29-1.84)	3.30	0.011727	8	carbon/nitrogen insensitive 1 (CNI1)
AT1G75040	1.534614	(1.34-1.73)	4.21	0.030567	9	pathogenesis-related gene 5 (PR5)
AT1G76960	1.49243	(0.66-2.33)	5.10	0.025347	6	unknown protein
AT5G10380	1.438718	(0.79-2.09)	4.56	0.003018	6	RING1
AT5G46350	1.430903	(0.63-2.23)	2.99	0.005216	9	WRKY DNA-binding protein 8 (WRKY8)
AT3G04720	1.398543	(0.71-2.08)	7.23	0.005216	6	pathogenesis-related 4 (PR4)
AT1G28400	1.359684	(0.60-2.12)	5.06	0.005398	6	unknown protein

AT1G15125	1.325205	(0.65-2.00)	3.77	0.023768	2	S-adenosyl-L-methionine-dependent methyltransferases superfamily protein
AT4G34135	1.297406	(1.12-1.48)	4.42	0.023116	10	UDP-glucosyltransferase 73B2 (UGT73B2)
AT4G37370	1.26071	(1.02-1.50)	3.99	0.019902	10	cytochrome P450, family 81, subfamily D, polypeptide 8 (CYP81D8)
AT3G25610	1.248882	(0.83-1.67)	4.32	0.003018	10	ATPase E1-E2 type family protein / haloacid dehalogenase-like hydrolase family protein
AT4G34230	1.226628	(1.06-1.40)	5.56	0.019902	9	cinnamyl alcohol dehydrogenase 5 (CAD5)
AT1G17860	1.215674	(1.01-1.42)	4.09	0.020599	8	Kunitz family trypsin and protease inhibitor protein
AT2G38870	1.214024	(0.96-1.47)	5.80	0.017777	8	Serine protease inhibitor, potato inhibitor I-type family protein
AT1G66880	1.200647	(0.56-1.84)	4.13	0.007189	7	Protein kinase superfamily protein ATP binding cassette subfamily B4 (ABC B4)
AT2G47000	1.190454	(-0.13-2.51)	4.40	0.020623	7	(ABC B4)
AT1G32940	1.164453	(1.00-1.33)	4.65	0.009686	9	SBT3.5
AT5G25930	1.150021	(0.99-1.31)	3.82	0.030157	8	Protein kinase family protein with leucine-rich repeat domain
AT3G15356	1.146637	(0.83-1.46)	4.94	0.003741	8	Legume lectin family protein
AT2G29490	1.135999	(0.81-1.47)	4.22	0.046544	10	glutathione S-transferase TAU 1 (GSTU1)
AT3G12500	1.132742	(0.13-2.14)	2.68	0.016293	6	basic chitinase (HCHIB)
AT2G31880	1.130578	(0.81-1.45)	5.73	0.012086	9	SUPPRESSOR OF BIR1 1 (SOBIR1)
AT2G25000	1.126296	(0.46-1.79)	3.09	0.003018	6	WRKY DNA-binding protein 60 (WRKY60)
AT4G02520	1.118406	(0.79-1.45)	7.88	0.02816	9	glutathione S-transferase PHI 2 (GSTF2)
AT1G62300	1.117637	(0.65-1.59)	3.55	0.020599	10	WRKY6
AT5G12050	-1.11096	(-2.61-0.38)	3.76	0.003662	1	unknown protein
AT4G13180	1.09606	(0.65-1.54)	5.01	0.003533	8	NAD(P)-binding Rossmann-fold superfamily protein
AT5G48540	1.078589	(0.83-1.32)	3.63	0.005664	8	receptor-like protein kinase-related family protein
AT1G60730	1.077874	(0.68-1.48)	5.41	0.003018	10	NAD(P)-linked oxidoreductase superfamily protein
AT3G49120	1.047862	(0.57-1.52)	8.51	0.010019	9	peroxidase CB (PRXCB)
AT4G37800	-1.00604	(-1.38--0.63)	9.08	0.003018	4	xyloglucan endotransglucosylase/hydrolase 7 (XTH7)
AT5G03120	-1.00095	(-1.36--0.64)	5.25	0.024773	1	unknown protein

Appendix 4



A4.1 Publication

The following paper was based on the work presented in Chapter 5.

Bagley SA, Atkinson JA, Hunt H, Wilson MH, Pridmore TP, Wells DM. 2020. Low-Cost Automated Vectors and Modular Environmental Sensors for Plant Phenotyping. *Sensors* **20**, 3319.

Article

Low-Cost Automated Vectors and Modular Environmental Sensors for Plant Phenotyping

Stuart A. Bagley ¹, Jonathan A. Atkinson ², Henry Hunt ³, Michael H. Wilson ² ,
Tony P. Pridmore ³ and Darren M. Wells ^{1,*} 

¹ Integrated Phenomics Group, School of Biosciences, University of Nottingham, Sutton Bonington Campus, Sutton Bonington LE12 5RD, UK; stuart.bagley1@nottingham.ac.uk

² Future Food Beacon, School of Biosciences, University of Nottingham, Sutton Bonington Campus, Sutton Bonington LE12 5RD, UK; jonathan.atkinson@nottingham.ac.uk (J.A.A.); michael.wilson@nottingham.ac.uk (M.H.W.)

³ School of Computer Science, University of Nottingham, Nottingham NG8 1BB, UK; psyhh2@nottingham.ac.uk (H.H.); psztpp@exmail.nottingham.ac.uk (T.P.P.)

* Correspondence: darren.wells@nottingham.ac.uk

Received: 9 May 2020; Accepted: 9 June 2020; Published: 11 June 2020



Abstract: High-throughput plant phenotyping in controlled environments (growth chambers and glasshouses) is often delivered via large, expensive installations, leading to limited access and the increased relevance of “affordable phenotyping” solutions. We present two robot vectors for automated plant phenotyping under controlled conditions. Using 3D-printed components and readily-available hardware and electronic components, these designs are inexpensive, flexible and easily modified to multiple tasks. We present a design for a thermal imaging robot for high-precision time-lapse imaging of canopies and a Plate Imager for high-throughput phenotyping of roots and shoots of plants grown on media plates. Phenotyping in controlled conditions requires multi-position spatial and temporal monitoring of environmental conditions. We also present a low-cost sensor platform for environmental monitoring based on inexpensive sensors, microcontrollers and internet-of-things (IoT) protocols.

Keywords: phenotyping robots; 3D printing; phenomics vectors; IoT sensors

1. Introduction

Plant phenotyping—the assessment of complex plant traits (architecture, growth, development, physiology, yield, etc.) and quantification of parameters underlying those traits [1–3]—is a rapidly developing transdiscipline of vital importance when addressing issues of global food security [4,5]. High-throughput phenotyping in controlled environments (growth chambers and glasshouses) is often delivered via large, expensive installations, leading to limited access and an increased relevance of “affordable phenotyping” solutions [6,7]. The availability of low-cost microcontrollers and automation components developed for the Maker community, combined with the ease of fabrication of 3D-printed parts allows low-cost, flexible phenotyping vector platforms to be designed for more widespread adoption [8]. We present two robotic vectors that carry sensors for plant phenotyping under controlled conditions—a linear actuator to position a thermal camera and a plate imaging robot designed to carry an RGB camera to image plate-grown plants such as the model species *Arabidopsis thaliana*. Each vector is designed for a specific task and is of inexpensive, modular construction, allowing re-design and re-purposing for other phenotyping activities as necessary.

When phenotyping in controlled conditions, spatial and temporal environmental sensor data are essential for correct interpretation of results [9]. We also present a low-cost sensor platform for

monitoring environmental conditions over a range of phenotyping setups based on inexpensive sensors, microcontrollers and internet-of-things (IoT) protocols.

2. Automated Vectors

Both vectors are based on the “belt-and-pinion” linear drive principle, whereby a motor mounted on a wheeled carriage drives a timing belt that passes over the timing pulley and under the carriage wheels. The wheels then act as idler pulleys to prevent the belt losing tension (Figure 1). For increased torque and positional accuracy, a stepper motor is employed to propel the carriage and payload along a rigid drive rail. This simple configuration allows longer travel lengths and rapid carriage movement compared to leadscrew designs.

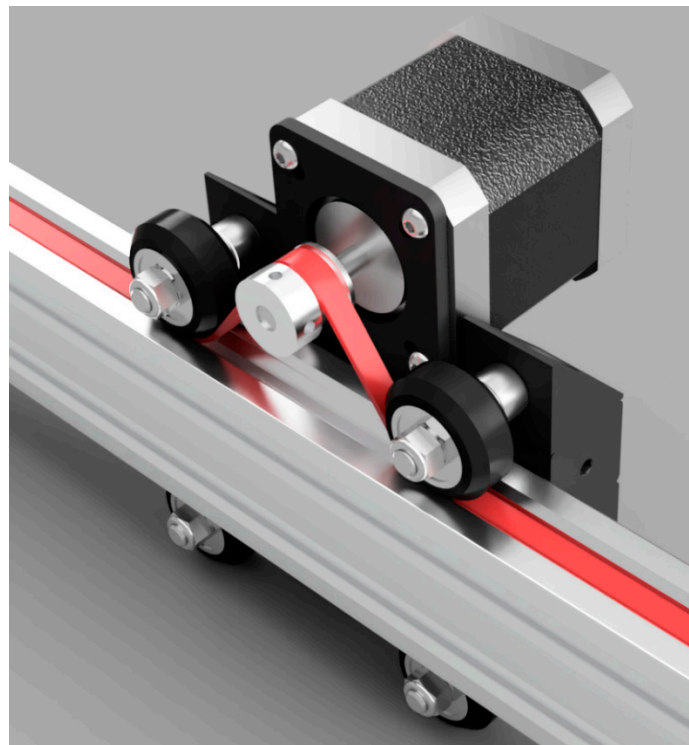


Figure 1. Belt-and-pinion drive system. The timing belt (red) passes under the drive wheels and over the timing pulley to maintain tension in the belt. Drawing files from [10].

This design has been developed and adopted by the Maker community for home-built computer numerical control (CNC) machines and plotters [10] and compatible parts are readily available. A list of components used in each design is given in Table 1. Custom parts are 3D printed to reduce cost and allow flexibility and re-configuration for alternative sensor payloads or additional deployment modes. Files for all 3D-printed components are available at <https://github.com/UoNMakerSpace/>. All parts were printed using a fused filament fabrication 3D printer (Model S5, Ultimaker) using tough polylactic acid (PLA) filament.

Both designs utilize microcontrollers to generate the signals to the drivers that control the stepper motor—these controllers also provide input/output signals for limit switches used as both emergency stops and home sensors. The microcontrollers themselves also trigger, configure and collect data from the sensor and provide a user-friendly interface to set experimental acquisition parameters. Microcontroller sketches and control software examples are available at <https://github.com/UoNMakerSpace/>.

Table 1. Components for the automated plant phenotyping vectors.

Component	Specifications	Model/File name	Manufacturer
Thermal Imager			
Stepper motor	Bipolar, 1.8° step angle, 1.68 A/phase	MT-1704HS168A	Motec
Microcontroller	16 MHz ATmega328P	Arduino Uno R3	Arduino
Driver carrier	Arduino shield for removable drivers	CNC Shield V3	Variuos
Stepper driver	Max 32 microsteps, 2.5 A, 12–40 V	DRV8825	Texas Instruments
Drive belt	7 mm width; 2 mm pitch	GT2-2M	OpenBuilds
Timing pulley	20 teeth; 2 mm pitch	GT2-2M	OpenBuilds
Carriage rail	V-slot profile	40 × 20	OpenBuilds
Carriage wheels	15.2 mm outside diameter (OD), Delrin	Mini V Wheel	OpenBuilds
Carriage plate	3D printed	therm_cm.stl ¹ , therm_cps.stl	UoN ²
Sensor holder	3D printed	therm_s_flir.stl	UoN
Electronics box	3D printed	therm_case.stl	UoN
Limit switches	Hall-effect sensor, unipolar, 4.5–24 V	MP101402	Cherry
Sensor	Thermal camera 19 mm lens, 24° field of view	A35 (60 Hz)	FLIR
Plate Imager			
Stepper motor	Bipolar, 1.8° step angle, 1.68 A/phase	MT-1704HS168A	Motec
Microcontroller	72 MHz Cortex-M4	Teensy 3.2	PJRC
Stepper driver	Max 32 microsteps, 3.5 A, 8–45 V	TB6600	Toshiba
Drive belt	7 mm width; 2 mm pitch	GT2-2M	OpenBuilds
Timing pulley	20 teeth; 2 mm pitch	GT2-2M	OpenBuilds
Carriage rail	V-slot profile	40 × 20	OpenBuilds
Carriage wheels	15.2 OD, Delrin	Mini V Wheel	OpenBuilds
Carriage plate	3D printed	plate_carriage.stl ³	UoN
Sensor holder	3D printed	plate_sm.stl	UoN
Light baffle	3D printed	plate_baffle(1–3).stl	UoN
Electronics box	3D printed	plate_case(1–3).stl	UoN
Limit switches	Hall-effect sensor, omnipolar, 2.5–5 V	AH180	Diodes Inc.
Sensor	FireWire camera, 8 mm lens	Stingray	AVT

¹ Files available at: <https://github.com/UoNMakerSpace/thermal-imager-hardware>. ² UoN: 3D printed at the University of Nottingham. ³ Files available at: <https://github.com/UoNMakerSpace/plate-imager-hardware>.

2.1. Thermal Imager

The Thermal Imager is a simple linear robot designed to position a thermal camera (FLIR A35 (60 Hz)) over the canopies of plants grown in trays or pots on a standard controlled environment room shelf (Figure 2). High-throughput top-view imaging of plants can be used to measure morphological properties, such as shape and size and how these parameters develop over time [11]. The use of thermal sensors enables the measurement of physiological processes such as stomatal function [12] and responses to disease [13]. With a 19 mm lens, the field of view of the sensor is approximately 220 × 300 mm when mounted 80 cm above the canopy to be imaged.

2.1.1. Mechanical Components

The Thermal Imager comprises a horizontally-arranged aluminium carriage rail (V-slot profile, OpenBuilds) onto which is located a wheeled carriage assembled from two carriage plates. The carriage plates are 3D-printed parts with mounting holes for a NEMA17 bipolar stepper motor on one plate and a sensor attachment fitting on the other. Guide wheels are mounted between the plates and locate in the slot of the carriage rail (see Figure 1). The carriage rail is mounted on two supports fabricated from the same aluminium profile but any sturdy support will suffice. The use of aluminium profile allows easy adjustment of both carriage rail height (to adjust the sensor field-of-view) and orientation of the carriage rail (for example to a side-imaging mode to allow use with non-rosette species such as wheat, rice and barley). Files for the 3D-printed components are available at: <https://github.com/UoNMakerSpace/thermal-imager-hardware>.



Figure 2. Thermal Imager. For scale, the drive rail is 1.2 m in length.

2.1.2. Electrical/Control Components

The motor control system is based on a microcontroller development board (Arduino Uno R3)—this incorporates a 16 MHz ATmega328P controller on an inexpensive breakout board with multiple input/output connections including a USB serial connection to a host PC or laptop [14]. An expansion shield (CNC Shield V3) is connected to the board to allow deployment of up to three stepper motor drivers in the widely-used “StepStick” format [15] and multiple limit switches. The motor driver selected for this system (DRV8825, TI) can be configured to single stepping, 1/2, 1/4, 1/8, 1/16 or 1/32 microsteps and operates at a maximum drive current of 2.5 A at 24 V. Two unipolar Hall-effect sensors are wired to the shield and fixed at either end of the carriage plate. The sensors are triggered by magnets fixed to the carriage rail to act as home and limit switches. All electronic components are housed in a 3D-printed case with connectors for the stepper motor, Hall-effect sensors and motor power. The motor is powered by a 24 V, 2.71 A power adaptor. A full wiring schematic is given as Figure S1.

The microcontroller board is powered by a USB connection to the host computer, which also provides serial communication.

2.1.3. Software

The microcontroller runs a sketch written in the Arduino Integrated Development Environment [16] that uses the AccelStepper library [17] to control the stepper motor. This sketch allows setting of acceleration parameters for the motor, reads the state of the two limit switches and monitors the serial connection. The limit switch at the furthest extent of travel is an emergency stop, with the other sensor acting as a home switch—on triggering, it moves the carriage until the sensor is no longer active and sets the final position as zero (“home”). On receiving a serial string with positional information via the USB port, the carriage is moved to that position using the pre-defined acceleration parameters to ensure a smooth acceleration and deceleration before stopping and acquiring an image. Experimental parameters are set and the imaging sensor controlled by a program written

in the LabVIEW development environment [18] running on the host computer. This provides a user-friendly graphical interface for control of the vector (distances moved, time-lapse parameters, etc.) and imaging sensor (Figure 3). The microcontroller sketch and LabVIEW software are available at <https://github.com/UoNMakerSpace/thermal-imager-software>. Once acquired, image sets are processed for leaf temperature values at multiple points on each rosette using macros written for the ImageJ/FIJI image analysis platforms [19,20].

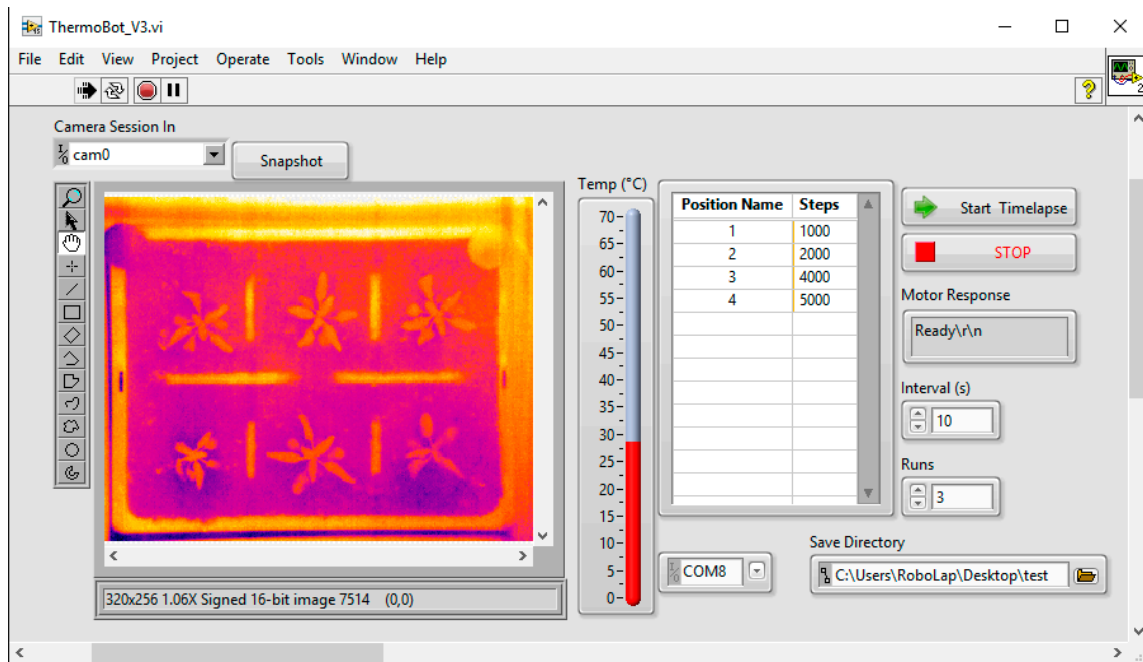


Figure 3. Thermal Imager control software user interface.

2.1.4. Performance and Results

Operating characteristics of the Thermal Imager are given in Table 2. For comparison, characteristics of a previously published research system [21] and a commercially available actuator are also given. A standard experimental run with five imaging positions along the travel distance and a microstepping size of 4 is completed in 38 s including the homing sequence (which runs at each timepoint to improve repeatability). These settings give a positional accuracy of $\sim 500 \mu\text{m}$ during extended running, no measurable discrepancy in positioning was found. We estimate the repeatability of positioning at $\sim 5 \mu\text{m}$. Compared to the CPIB Imaging Robot [21], the Thermal Imager has improved repeatability, speed, and temporal resolution, completing each imaging run in less than half the time. This can be attributed to the use of microstepping by the Thermal Imager driver board—the Imaging Robot does not use microstepping (cost-effective drivers were not available at the time of design), which impacts resolution and repeatability. Despite the components costing only 20% of those used in the Imaging Robot, the Thermal Imager design is thus an improvement in all operating characteristics. A typical commercial actuator (Table 2) operating at the highest level of microstepping outperforms the Thermal Imager in terms of speed and temporal resolution but at the cost of positional accuracy and hence repeatability. Importantly, current commercial systems of this specification are relatively expensive, in this case nearly 15 times more expensive than the system presented here.

Table 2. Comparison of Thermal Imager specifications with competing (research and commercial) robots.

Specification	Thermal Imager	CPIB Imaging Robot [21]	Commercial Actuator ¹
Drive	Belt and pinion	Toothed belt	Toothed belt
Travel	1.2 m	1.8 m	1.2 m
Step size	200 μm	300 μm	600 μm
Microstep size (minimum)	6.25 μm (32 microsteps)	300 μm (n/a)	9.4 μm (64 microsteps)
Maximum speed	125 mm/s	30 mm/s	5 m/s
Repeatability	$\sim 5 \mu\text{m}$	0.5 mm	200 μm
Temporal resolution	$\sim 40 \text{ s/run}$	$\sim 2 \text{ min/run}$	$\sim 8 \text{ s/run}$
Cost ²	€235	€1060	€3475

¹ Model ZLW-1660, Igus GmbH. ² Cost excludes camera and host PC.

An example output from the Thermal Imager is shown in Figure 4.

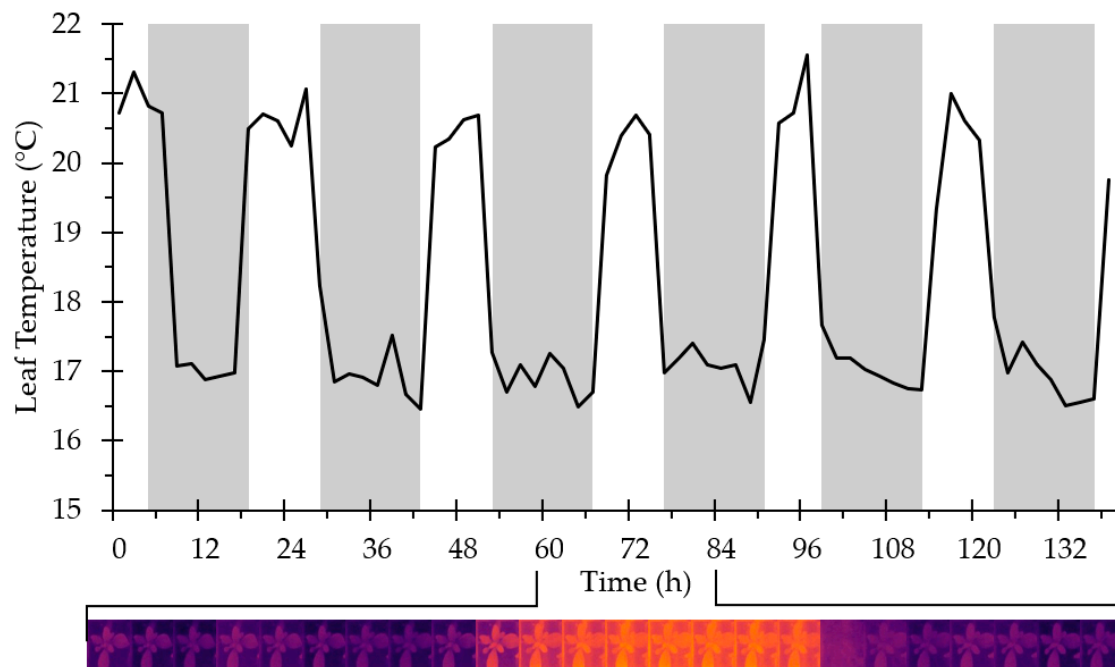


Figure 4. Leaf temperatures of *Arabidopsis thaliana* rosettes recorded using the Thermal Imager. In total, 48 plants were imaged every 30 min for 136 h. For clarity, data for a single plant are shown (mean of three spot measurements) at 2 h intervals. Dark bars show the night photoperiod. Inset: hourly thermographs for the marked 24 h period.

2.2. Plate Imager

The Plate Imager is designed for the automated high-throughput imaging of plate-grown plants in a standard growth room (Figure 5). Rather than continuous operation, it was designed for users to bring multiple plates for imaging at discrete time points. This approach allows different users to image many hundreds of plants using a single shared machine. With this in mind, the design focuses on throughput rather than absolute positional accuracy. Once acquired, images are processed for root system architectural traits using the RootTrace and RootNav analysis software suites [22–24].

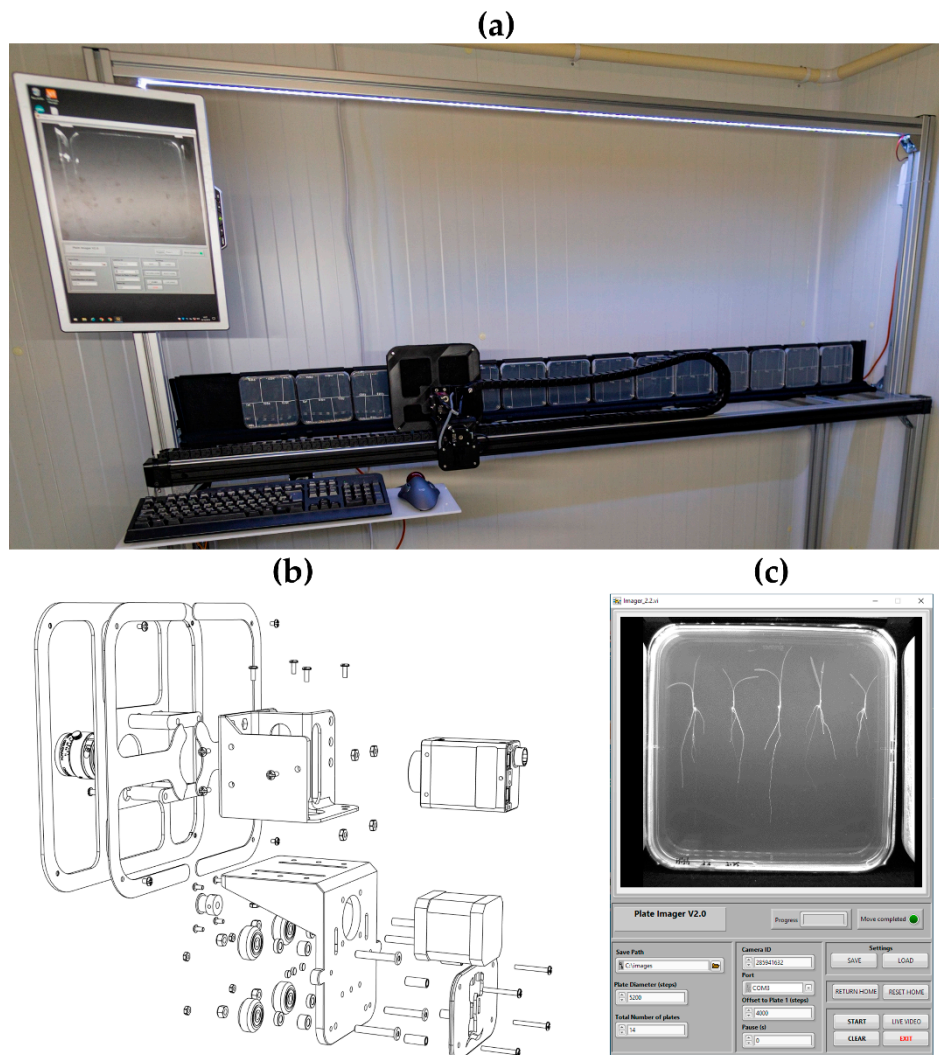


Figure 5. (a) Plate Imager robot. (b) Carriage plate, sensor holder and baffle assembly. (c) Plate Imager control software user interface.

2.2.1. Mechanical Components

Using a similar drive system to the Thermal Imager, the Plate Imager is composed of a carriage rail on which a belt and pinion-driven carriage translocates a machine vision RGB camera (Stingray, AVT). The rail is 2 m in length, giving a working travel of 1.8 m, and allowing 14 standard 125 mm square plates to be imaged in a run. The carriage plate assembly (Figure 5b) is made from 3D-printed components and consists of a carriage plate to which is connected a sensor holder. When imaging plates, reflections from the plate lid often obscure details—to lessen this effect, a baffle plate is fitted over the front of the carriage with a cut-out for the imaging lens. This is covered in blackout material to remove reflections from the lid of the plate. Plates are mounted using 3D-printed clips against a aluminium profile bracket (covered in blackout material to provide contrast to plant roots). The carriage rail is mounted to a free-standing frame constructed from aluminium profile with an LED lighting array mounted above the drive rail to provide imaging illumination. Files for the 3D-printed components are available at: <https://github.com/UoNMakerSpace/plate-imager-hardware>.

2.2.2. Electrical/Control Components

A limitation of the AccelStepper library and relatively low clock speed processors such as the ATmega328P used by the Arduino Uno in the Thermal Imager is motor speed. The maximum steps

per second at a clock frequency of 16 MHz is estimated at 4000 but in practice, this is difficult to achieve [17]. To achieve higher motor speeds (and still utilize acceleration and deceleration), the Plate Imager uses a development board with a processor than runs at a much higher clock speed (72 MHz Cortex-M4 microcontroller; Arm Ltd). This board (Teensy 3.2, PJRC) uses 3.3 V signal voltages (rather than the 5 V of the Arduino Uno) but is 5 V tolerant, so some common parts can be used in both systems). Again, Hall-effect sensors are used as limit and home switches. In this design, the sensors are connected at the extremes of the carriage rail and triggered by magnets fitted to the carriage. For this device, 3.3 V-tolerant omnipolar sensors are used. Omnipolar sensors are advantageous in high-speed systems as the sensor will be triggered by the opposite pole of the carriage magnet in the case of an overrun. The stepper motor driver used in the Plate Imager is based on the TB6600 chip (Toshiba) that allows a higher maximum motor current. The microcontroller and stepper driver boards are housed in a 3D-printed enclosure with connectors for power, limit switches and a USB connection to the host computer mounted in the support frame. The motor is powered by a 31 V, 2.4 A power adaptor. A full wiring schematic is given as Figure S2.

2.2.3. Software

To exploit the faster clock frequency of the Cortex-M4 microcontroller, a high-speed driver library (TeensyStep, [25]) was used in the microcontroller sketch software. This allows a theoretical motor speed of 300,000 steps per second with acceleration/deceleration control. User control of experimental parameters (plate diameter, delay between images, save directory) is via a LabVIEW program running on the host PC. This interface also allows monitoring and setting of camera attributes. Images are saved in individual directories for each plate position with unique filenames including acquisition time and date. Experimental settings can be saved as a configuration file and re-loaded on subsequent experimental runs, ensuring that image sets are appended to the same directory. The microcontroller sketch and LabVIEW code are available at <https://github.com/UoNMakerSpace/plate-imager-software>.

2.2.4. Performance

Characteristics of the Plate Imager are given in Table 3. For comparison, characteristics of a previously published research system [26] and a typical commercially-available actuator are also given.

Table 3. Comparison of Plate Imager specifications with competing (research and commercial) robots.

Specification	Plate Imager	CPIB Imaging Platform [26]	Commercial Actuator ¹
Drive	Belt and pinion	Leadscrew	Toothed belt
Travel	1.5 m	1.5 m	1.495 m
Step size	200 μm	31.75 μm	270 μm
Microstep size (minimum)	6.25 μm (32 microsteps)	0.5 μm (64 microsteps)	4.2 μm (64 microsteps)
Maximum speed	300 mm/s	60 mm/s	2000 mm/s
Repeatability	$\sim 5 \mu\text{m}$	$< 2 \mu\text{m}$	$< 20 \mu\text{m}$
Temporal resolution	68 s/run	~ 5 mins/run	~ 20 s/run
Cost ²	€780	€4560	€2904

¹ Model X-BLQ1495-E01, Zaber Technologies, Inc. ² Cost excludes camera and host PC.

The Plate Imager outperforms the CPIB Imaging Robot (see Table 2) in all measured parameters. Compared to a research unit for plate imaging based on a leadscrew design [26], the new design has a slightly lower repeatability due to the larger microstep size (Table 3). However, the higher positional accuracy of a leadscrew design results in a slower system and the maximum speed of the Imaging Platform is 20% of that of the Plate Imager, leading to a similar increase in the time required for an experimental run. Leadscrew systems are also relatively expensive—components

for the Imaging Platform cost nearly 6 times as much as the Plate Imager (Table 3). Compared to a belt-driven commercial design, the Plate Imager has a smaller minimum microstep size and thus improved repeatability. The commercial model is capable of higher maximum speeds, reflected in an improved temporal resolution. Although the commercial model is cheaper than the leadscrew platform, it is nearly 4 times more expensive than the Plate Imager.

3. IoT Environmental Sensor Logger

Network-enabled wireless sensor devices are a rapidly expanding market, found throughout homes [27], businesses, and agriculture [28] and increasingly in research environments [29]. This has led to a number of readily available, low-cost IoT components with a rich ecosystem of hardware components and software libraries. We have taken advantage of this expansion to design a highly modular platform that can host a range of environmental sensors from subdollar to highly-calibrated domain specific sensors costing tens to hundreds of dollars. The platform is also modular with respect to communication platform, designed to operate in its default instance with readily available WiFi but able to be adapted to long-range radio systems (XBee/LoRa/GSM) and deployed into remote locations.

3.1. Hardware

The initially developed unit (Figure 6) is a low-cost instantiation of the platform designed to be deployed at high numbers into plant growth facilities in a large academic department. The core of the unit is an ESP32-based microprocessor [30] which allows data from sensors connected via multiple devices busses to be relayed over built-in WiFi hardware. The sensor module is an ultra-low-power unit that measures ambient temperature, relative humidity, barometric pressure and air quality (model BME680 [31]). This sensor can be interfaced with using I2C or SPI serial communication protocols and is widely available on breakout boards to simplify deployment (Figure 6a). The utility of pressure and air quality logging is limited in phenotyping installations and a cheaper sensor (BME280 [32]) is available with similar characteristics for temperature and humidity measurement (Table 4). For comparison, specifications of a commercial standalone sensor and a WiFi-enabled datalogger are also shown.

Table 4. Sensor and logging characteristics.

Specification	BME680	BME280 [32]	TinyTag Ultra ²	WiFi Logger ¹ [33]
Humidity range	0–100% rh	20–80% rh	0 to 95% rh	0–100% rh
Humidity accuracy	±3% rh	±3% rh	±3% rh	±4.0% rh
Humidity response time	8 s	1 s	~10 s	n/a
Temperature range	−40 to 85 °C	−40 to 85 °C	−25 to +85 °C	−20 to 60 °C
Temperature accuracy (25 °C)	±0.5 °C	±0.5 °C	±0.4 °C	±0.8 °C
Minimum time between readings		10 ² s	1 s	10 s
Maximum readings		250,000 ³	32,000	500,000
Battery life		1 month ⁴	1 year	1 year
Online reporting		yes	no	yes
Cost	€19	€11	€135	€133

¹ Model OM-EL-WIFI-TH-PLUS, OMEGA Engineering, Inc. ² This figure represents the minimum duty cycle time of the unit to read the sensors, store the results and relay over WiFi to a test connection; in network connected mode readings are batched and sent to the network with WiFi authentication time dependent on network configuration (connection to WPA2-Enterprise networks can take up to 20 s). ³ This figure is for permanent storage on the unit, acting in logging mode or when not connected to the network. ⁴ This is at a logging interval of 60 s with a 1500 mAh battery.

A printed circuit board (PCB) was designed for deployment of the sensor unit assembly to allow the use of inexpensive, pre-soldered components. The board consists of headers for the

ESP32 development board, RTC module, sensor module, and a battery holder for an 18650 LiFePO₄ battery. Headers are included for a voltage divider circuit to monitor battery voltage, two i2c bus connections for additional sensors and diagnostic unit connection, and serial device headers for connection of future domain specific hardware. Electrical schematics are shown in Figure S3 and a populated PCB in Figure 6. Schematics and fabrication files for the PCB are available at <https://github.com/UoNMakerSpace/sensor-platform-hardware>.

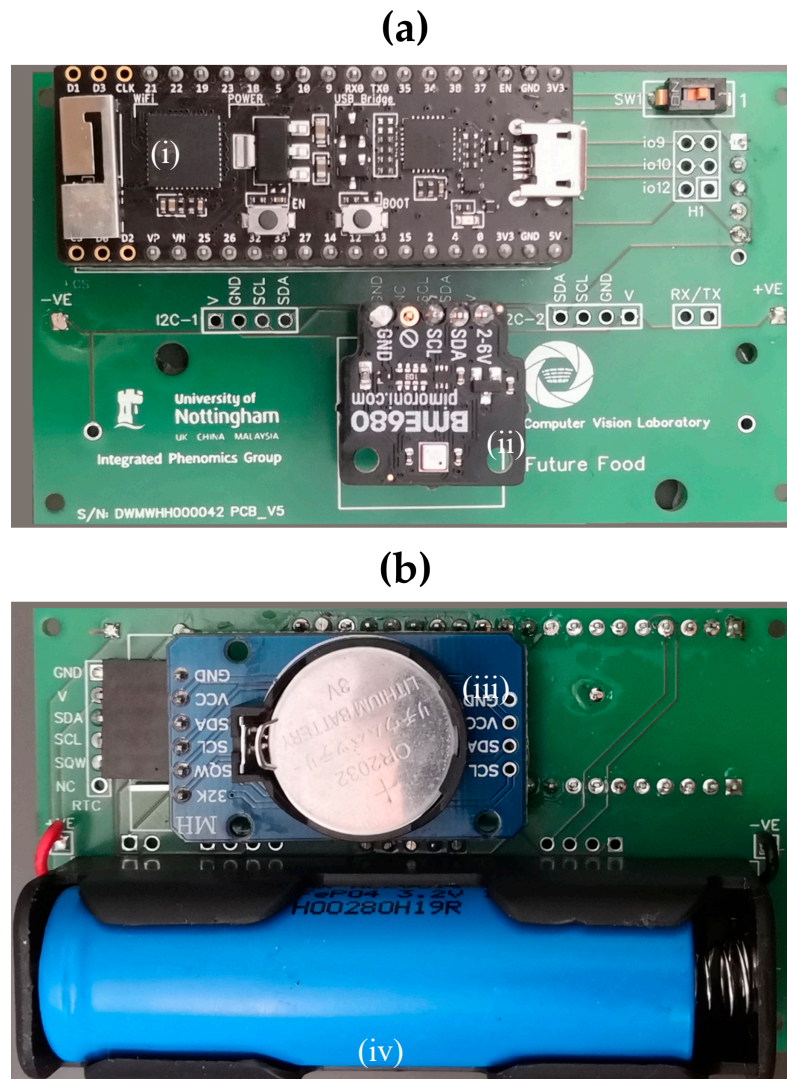


Figure 6. (a) Sensor printed circuit board (PCB) top side. (b) Bottom side. Main components: (i) ESP32 development board, (ii) sensor daughter board, (iii) real-time clock module, and (iv) LiFePO₄ rechargeable battery.

3.2. Software

The ESP32 hosts a range of runtime environments with their own system libraries and languages, including JavaScript, Python, Lua, and C++. Our platform is environment and language agnostic, requiring only that the chosen suite can provide a network interface via MQTT(S) and HTTP(S) and can connect to a WiFi network via the security mechanism in place in the monitored environment. The test instantiation is written in C++ using the manufacturer default operating system with Arduino libraries (<https://github.com/UoNMakerSpace/psn-node>) compiled and uploaded via PlatformIO. The ESP32, like most true IoT units is headless, communicating bidirectionally with host development platforms over serial connections. For this reason, unit administration of the devices, such as maintaining

WiFi credentials and server addresses, is generally a laborious task requiring either a development platform or an insecure setup mode accessible with local, private Bluetooth or WiFi networks. We have developed for the platform a simple administration app, written in C# and using WPF libraries (<https://github.com/UoNMakerSpace/psn-node-admin>), to provide an administration interface for effective, secure, off-line administration. Given the austere locations the units are planned to be deployed into, the variability of wireless communication, and the necessity to conserve battery life, if a connection attempt fails the unit will rapidly timeout, and store the sensor data with the timestamp and send the data on the next successful connection. Units can relay simple debugging messages, such as battery strength, connection signal strength, and number of failed network connections to the server for online monitoring purposes. A simple administration unit can also be connected to the unit for in-field interrogation of debug messages, in the unlikely event of an edge-case connection issue.

3.3. Network

Deployed devices relay sensor readings and diagnostic messages in a common, self-describing format using JSON to backend server-side software components (Figure 7). These consist of a message router which processes MQTT PubSub messages and relays them, again using a common described format to a database interface layer, where messages are written into a backend datastore. We have found MQTT to be highly efficient on units with limited processing power, offering reliable probe-driven bi-directional communication, with the backend. In the event of an issue with MQTT communication, the unit can fall back to classic HTTP-POST communication, using the same message format.

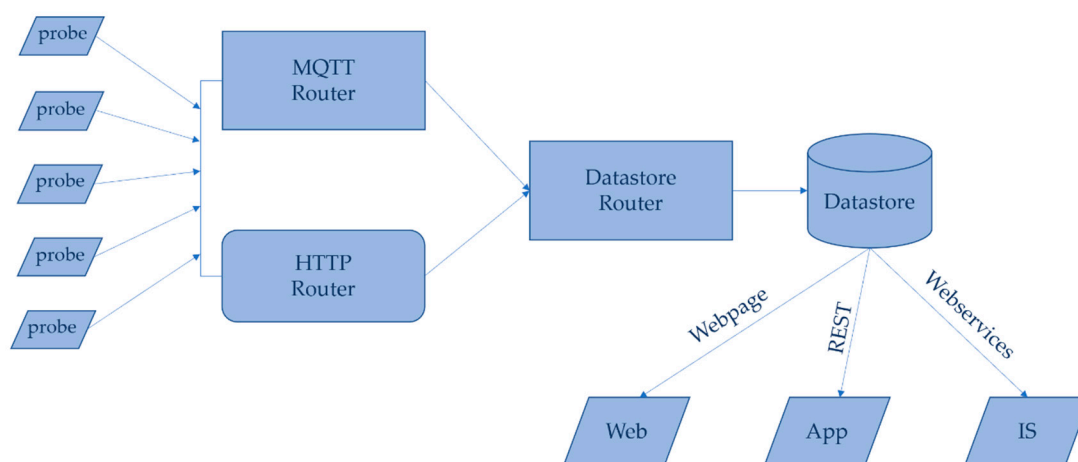


Figure 7. Network architecture of the platform showing flow of measurements and data through the routing layers to end users via web pages, web apps and associated integrative stores (IS).

The platform does not proscribe the backend datastore, offering flexibility to integrate with existing deployed technologies. For ease of deployment and testability, the initial instantiation combines message routing and data layer into a self-contained unit, backed by a SQL database (<https://github.com/UoNMakerSpace/psn-logger>, <https://github.com/UoNMakerSpace/psn-server>). Data are made accessible to the end users by a web server component, written in PHP, which allows a user to interrogate probe data using a web browser. Other dissemination routes are planned, using access to the datastore via REST to provide live feed and notifications via a web or mobile app, or using webservices to provide the logged environmental conditions for phenotyping experiments into integrative stores (IS) such as PHIS [34] and PIPPA [35].

The server-side programs can run on the same hardware, but they can also be modified to allow the message router to run on cheap frontend hardware—for instance, a RaspberryPi as in [36]—while the database and webserver run in either dedicated server hardware, or a low-cost virtual machine either on site or in the cloud. This provides a reliability advantage, with server components running in

a datacentre overseen by IT administrators whilst allowing the bespoke IoT-specific functionality to be run closer to the units on the same network (with failover capability), and a cost advantage, as specific server hardware need not be purchased and the frontend is running on low-cost hardware.

3.4. Performance

An example sensor log is shown in Figure 8.

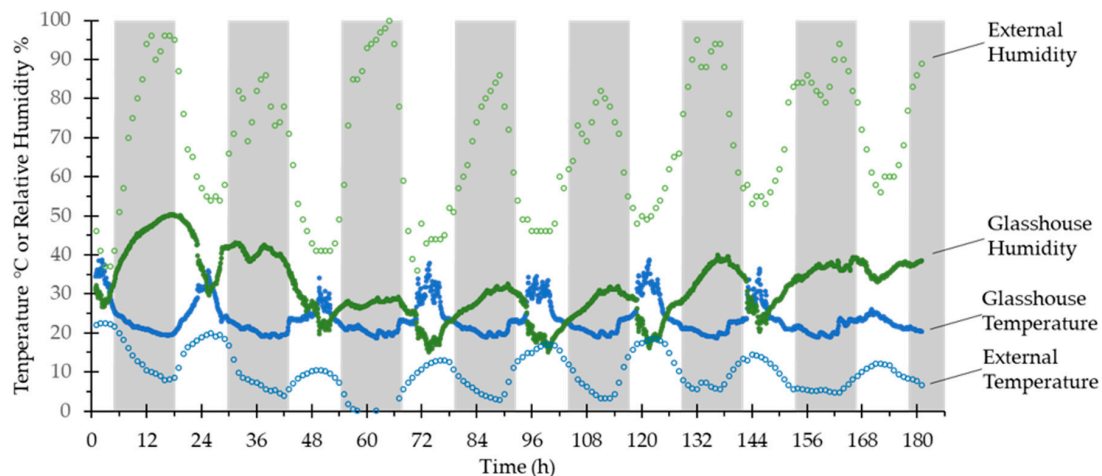


Figure 8. Data recorded by a probe over 182 h in a glasshouse. Green circles are percentage relative humidity, blue circles are temperature ($^{\circ}\text{C}$). Filled circles are data gathered by the probe in the glasshouse (readings every 5 mins), open circles are from a calibrated weather station approximately 300 m away (readings every 60 mins) for the same period showing external environmental conditions. 0 h was 12 pm on a Saturday afternoon. Dark bars show the period after sunset, light bars the period after sunrise.

In Table 4, the platform, configured with two commonly available temperature sensors (Bosch Sensortech BME680 and BME280, a 1500 mAh LiFePO₄ rechargeable battery, and set to 1 min recording interval), is compared to two popular commercially available environmental sensor units: Tinytag Ultra 2 (Gemini Data Loggers TGU-4017) and OM-EL-WIFI-TH-PLUS (Omega Engineering). All the units have similar operating ranges and accuracy, appropriate for their role measuring variables in large environments. The platform developed here shows that despite its low cost, it is competitive with more expensive commercial units in terms of numbers of readings that can be logged and in mode of operation, the trade off with battery life as presented is due to a design requirement for the test unit to log standard experimental runs, which in this case are a few weeks in duration. The run duration is a factor of the logging interval, which, as tested here, is at a high frequency (60 h^{-1})—the unit can perform approximately 30,000 measurements on a standard battery, or 60,000 on a large capacity battery, which would see a lifetime in the several month range at a standard 10 minute logging interval. Minimum reading time is controlled by two figures: the time to wake the unit, read the sensors and determine the median reading for each (approximately 3 s), and a longer period connecting to WiFi and a very rapid delay to relay signals (approximately 0.9 s). The connection to WiFi is a complicated variable—simple secure authentication systems found on home-type routers or WiFi hotspots can be connected to in $<5\text{ s}$ (95th percentile), but complex WPA2-Enterprise based systems, such as the academic eduroam system, can take 2-fold longer (90th percentile) or even 4-fold longer (99th percentile) (data not shown). For this reason, to save power, the unit saves readings and connects to WiFi at a regular frequency determined by a user-specified batching number. The unit could be redesigned to step around the delay induced by WiFi connection time with an event based loop, but we do not believe any of these sensors would accurately identify gross environmental parameters in a large monitored space at subminute temporal resolution, and at this sampling frequency any unit would quite rapidly deplete its battery.

Figure 8 shows the performance of the test unit with a BME680 sensor and 5 min logging interval over a week in a glasshouse, along with external measurements at 1 h logging intervals from a calibrated weather station on the same campus. As can be seen, the temperature and humidity sensors perform as expected for an environmental sensor, with little variability, and demonstrate how the glasshouse environment is affected by external conditions.

4. Discussion

The vector platforms presented here are inexpensive and easily adapted for multiple use cases. The use of readily-available mechanical and electronic components popularized by the Maker community allows the deployment of bespoke systems at a fraction of the cost of the off-the-shelf platforms. The platforms offer improvements to existing research designs and are comparable in key performance characteristics to commercial models. The modular nature of the designs and the extensive use of 3D-printed components means that the vectors can easily be re-purposed if required.

The sensor platform provides logging of low-cost environmental probes which can be deployed at scale to provide complete fine-granularity coverage over a range of plant phenotyping facilities with designed-in management and administration, and user-targeted distribution of real-time environmental conditions. The platform is low cost, offers comparable features to commercial alternatives, and has been designed to be as modular as possible, while retaining ease of deployment and management, to ensure that it does not restrict deployment to measure any feasible environmental parameter or growth environment.

Supplementary Materials: The following are available online at <http://www.mdpi.com/1424-8220/20/11/3319/s1>, Figure S1: Thermal Imager wiring schematic; Figure S2: Plate Imager wiring schematic; Figure S3: Sensor platform PCB Schematic.

Author Contributions: Conceptualization, M.H.W., T.P.P. and D.M.W.; data curation, M.H.W.; funding acquisition, T.P.P. and D.M.W.; investigation, S.A.B., J.A.A., H.H., M.H.W. and D.M.W.; methodology, S.A.B., J.A.A., H.H., M.H.W. and D.M.W.; project administration, J.A.A., T.P.P. and D.M.W.; resources, T.P.P. and D.M.W.; software, S.A.B., J.A.A., H.H., M.H.W., T.P.P. and D.M.W.; supervision, M.H.W., T.P.P. and D.M.W.; writing—original draft, S.A.B., J.A.A., M.H.W., T.P.P. and D.M.W.; writing—review and editing, S.A.B., J.A.A., H.H., M.H.W., T.P.P. and D.M.W. All authors have read and agreed to the published version of the manuscript.

Funding: This research was supported by the Biotechnology and Biological Sciences Research Council [grant numbers BB/L026848/1, BB/S020551/1, BB/T001437/1, BB/P026834/1, and BB/M008770/1] and the University of Nottingham Future Food Beacon of Excellence (J.A.A., M.H.W. and D.M.W.). The APC was funded by the Biotechnology and Biological Sciences Research Council.

Acknowledgments: The authors wish to acknowledge the support of Corteva (UK) Ltd. to S.A.B and D.M.W.

Conflicts of Interest: The authors declare no conflict of interest.

References

1. Pieruschka, R.; Poorter, H. Phenotyping plants: Genes, phenes and machines. *Funct. Plant. Biol.* **2012**, *39*, 813–820. [[CrossRef](#)] [[PubMed](#)]
2. Pieruschka, R.; Schurr, U. Plant Phenotyping: Past, Present, and Future. Available online: <https://spj.science.org/plantphenomics/2019/7507131/> (accessed on 28 May 2020).
3. Großkinsky, D.K.; Svendsgaard, J.; Christensen, S.; Roitsch, T. Plant phenomics and the need for physiological phenotyping across scales to narrow the genotype-to-phenotype knowledge gap. *J. Exp. Bot.* **2015**, *66*, 5429–5440. [[CrossRef](#)] [[PubMed](#)]
4. Atkinson, J.A.; Jackson, R.J.; Bentley, A.R.; Ober, E.; Wells, D.M. Field Phenotyping for the future. In *Annual Plant Reviews Online*; American Cancer Society: Atlanta, GA, USA, 2018; pp. 719–736. ISBN 978-1-119-31299-4.
5. Walter, A.; Liebisch, F.; Hund, A. Plant phenotyping: From bean weighing to image analysis. *Plant. Methods* **2015**, *11*, 14. [[CrossRef](#)] [[PubMed](#)]
6. Reynolds, D.; Baret, F.; Welcker, C.; Bostrom, A.; Ball, J.; Cellini, F.; Lorence, A.; Chawade, A.; Khafif, M.; Noshita, K.; et al. What is cost-efficient phenotyping? Optimizing costs for different scenarios. *Plant. Sci.* **2019**, *282*, 14–22. [[CrossRef](#)]

7. Minervini, M.; Giuffrida, V.; Perata, P.; Tsaftaris, S.A. Phenotiki: An open software and hardware platform for affordable and easy image-based phenotyping of rosette-shaped plants. *Plant. J.* **2017**, *90*, 204–216. [[CrossRef](#)] [[PubMed](#)]
8. Fahlgren, N.; Gehan, M.A.; Baxter, I. Lights, camera, action: High-throughput plant phenotyping is ready for a close-up. *Curr. Opin. Plant. Biol.* **2015**, *24*, 93–99. [[CrossRef](#)]
9. Fiorani, F.; Schurr, U. Future scenarios for plant Phenotyping. *Annu. Rev. Plant. Biol.* **2013**, *64*, 267–291. [[CrossRef](#)]
10. V-Slot™ Belt & Pinion Example Build. Available online: <https://openbuilds.com/builds/v-slot%E2%84%A2-belt-pinion-example-build.97/> (accessed on 19 December 2019).
11. Tessmer, O.L.; Jiao, Y.; Cruz, J.A.; Kramer, D.M.; Chen, J. Functional approach to high-throughput plant growth analysis. *BMC Syst. Biol.* **2013**, *7*, S17. [[CrossRef](#)]
12. Sirault, X.; James, R.; Furbank, R.T. A new screening method for osmotic component of salinity tolerance in cereals using infrared thermography. *Funct. Plant. Biol.* **2009**, *36*, 970–977. [[CrossRef](#)]
13. Mahlein, A.-K.; Oerke, E.-C.; Steiner, U.; Dehne, H.-W. Recent advances in sensing plant diseases for precision crop protection. *Eur. J. Plant. Pathol.* **2012**, *133*, 197–209. [[CrossRef](#)]
14. Badamasi, Y.A. The working principle of an Arduino. In Proceedings of the 2014 11th International Conference on Electronics, Computer and Computation (ICECCO), Abuja, Nigeria, 29 September–1 October 2014; pp. 1–4.
15. StepStick—RepRap. Available online: <https://reprap.org/wiki/StepStick> (accessed on 19 December 2019).
16. Arduino—Software. Available online: <https://www.arduino.cc/en/main/software> (accessed on 19 December 2019).
17. AccelStepper: AccelStepper Library for Arduino. Available online: <https://www.airspayce.com/mikem/arduino/AccelStepper/index.html> (accessed on 19 December 2019).
18. Travis, J.; Kring, J. *LabVIEW for Everyone: Graphical Programming Made Easy and Fun*; Prentice Hall: Upper Saddle River, NJ, USA, 2007; ISBN 978-0-13-185672-1.
19. Schindelin, J.; Rueden, C.T.; Hiner, M.C.; Eliceiri, K.W. The ImageJ ecosystem: An open platform for biomedical image analysis. *Mol. Reprod. Dev.* **2015**, *82*, 518–529. [[CrossRef](#)]
20. Schindelin, J.; Arganda-Carreras, I.; Frise, E.; Kaynig, V.; Longair, M.; Pietzsch, T.; Preibisch, S.; Rueden, C.; Saalfeld, S.; Schmid, B.; et al. Fiji: An open-source platform for biological-image analysis. *Nat. Methods* **2012**, *9*, 676–682. [[CrossRef](#)]
21. French, A.P.; Wells, D.M.; Everitt, N.M.; Pridmore, T.P. High-throughput quantification of root growth. In *Measuring Roots: An Updated Approach*; Springer: Berlin/Heidelberg, Germany, 2012; pp. 109–126. ISBN 978-3-642-22066-1.
22. Naeem, A.; French, A.P.; Wells, D.M.; Pridmore, T.P. High-throughput feature counting and measurement of roots. *Bioinformatics* **2011**, *27*, 1337–1338. [[CrossRef](#)] [[PubMed](#)]
23. Pound, M.P.; French, A.P.; Atkinson, J.A.; Wells, D.M.; Bennett, M.J.; Pridmore, T.P. RootNav: Navigating images of complex root architectures. *Plant. Physiol.* **2013**, *162*, 1802–1814. [[CrossRef](#)]
24. Yasrab, R.; Atkinson, J.A.; Wells, D.M.; French, A.P.; Pridmore, T.P.; Pound, M.P. RootNav 2.0: Deep learning for automatic navigation of complex plant root architectures. *GigaScience* **2019**, *8*, 8. [[CrossRef](#)]
25. Niggel, L. TeensyStep. Available online: <https://luni64.github.io/TeensyStep/> (accessed on 20 December 2019).
26. Wells, D.M.; French, A.P.; Naeem, A.; Ishaq, O.; Traini, R.; Hijazi, H.; Bennett, M.J.; Pridmore, T.P. Recovering the dynamics of root growth and development using novel image acquisition and analysis methods. *Philos. Trans. R. Soc. B Biol. Sci.* **2012**, *367*, 1517–1524. [[CrossRef](#)]
27. Haase, J.; Alahmad, M.; Nishi, H.; Ploennigs, J.; Tsang, K.-F. The IOT mediated built environment: A brief survey. In Proceedings of the 2016 IEEE 14th International Conference on Industrial Informatics (INDIN), Poitiers, France, 18–21 July 2016; pp. 1065–1068.
28. Tzounis, A.; Katsoulas, N.; Bartzanas, T.; Kittas, C. Internet of things in agriculture, recent advances and future challenges. *Biosyst. Eng.* **2017**, *164*, 31–48. [[CrossRef](#)]
29. Stankovic, J.A. Research directions for the internet of things. *IEEE Internet Things J.* **2014**, *1*, 3–9. [[CrossRef](#)]
30. Maier, A.; Sharp, A.; Vagapov, Y. Comparative analysis and practical implementation of the ESP32 microcontroller module for the internet of things. *Internet Technol. Appl.* **2017**, 143–148. [[CrossRef](#)]
31. BME680. Available online: <https://www.bosch-sensortec.com/products/environmental-sensors/gas-sensors-bme680/> (accessed on 7 May 2020).

32. BME280. Available online: <https://www.bosch-sensortec.com/products/environmental-sensors/humidity-sensors-bme280/> (accessed on 2 June 2020).
33. Temperature and Humidity Wireless Data Logger. Available online: https://www.omega.co.uk/pptst/om-el-wifi_series.html (accessed on 2 June 2020).
34. Neveu, P.; Tireau, A.; Hilgert, N.; Nègre, V.; Mineau-Cesari, J.; Brichet, N.; Chapuis, R.; Sanchez, I.; Pommier, C.; Charnomordic, B.; et al. Dealing with multi-source and multi-scale information in plant phenomics: The ontology-driven Phenotyping Hybrid Information System. *New Phytol.* **2018**, *221*, 588–601. [[CrossRef](#)] [[PubMed](#)]
35. Coppens, F.; Wuyts, N.; Inzé, D.; Dhondt, S. Unlocking the potential of plant phenotyping data through integration and data-driven approaches. *Curr. Opin. Syst. Biol.* **2017**, *4*, 58–63. [[CrossRef](#)]
36. Ferdoush, S.; Li, X. Wireless sensor network system design using raspberry Pi and arduino for environmental monitoring applications. *Procedia Comput. Sci.* **2014**, *34*, 103–110. [[CrossRef](#)]



© 2020 by the authors. Licensee MDPI, Basel, Switzerland. This article is an open access article distributed under the terms and conditions of the Creative Commons Attribution (CC BY) license (<http://creativecommons.org/licenses/by/4.0/>).